THE FORMATION OF HIGH-MASS STARS AND STELLAR CLUSTERS

Suinan Zhang

A Thesis Submitted for the Degree of PhD
at the
University of St Andrews

2023

Full metadata for this thesis is available in
St Andrews Research Repository
at:
http://research-repository.st-andrews.ac.uk/

Identifiers to use to cite or link to this thesis:

DOI: https://doi.org/10.17630/sta/618
http://hdl.handle.net/10023/28438

This item is protected by original copyright

This item is licensed under a
Creative Commons License

https://creativecommons.org/licenses/by-nc-nd/4.0

The formation of high-mass stars and stellar clusters

Suinan Zhang

University of
St Andrews

This thesis is submitted in partial fulfilment for the degree of

Doctor of Philosophy (PhD)

at the University of St Andrews

February 2023

Candidate's declaration

I, Suinan Zhang, do hereby certify that this thesis, submitted for the degree of PhD, which is approximately 33,200 words in length, has been written by me, and that it is the record of work carried out by me, or principally by myself in collaboration with others as acknowledged, and that it has not been submitted in any previous application for any degree. I confirm that any appendices included in my thesis contain only material permitted by the 'Assessment of Postgraduate Research Students' policy.

I was admitted as a research student at the University of St Andrews in August 2018.

I, Suinan Zhang, received assistance in the writing of this thesis in respect of language, grammar and spelling, which was provided by Janice Deary.

I received funding from an organisation or institution and have acknowledged the funder(s) in the full text of my thesis.

Date Signature of candidate

February 21 2023

Supervisor’s declaration

I hereby certify that the candidate has fulfilled the conditions of the Resolution and Regulations appropriate for the degree of PhD in the University of St Andrews and that the candidate is qualified to submit this thesis in application for that degree. I confirm that any appendices included in the thesis contain only material permitted by the ‘Assessment of Postgraduate Research Students’ policy.

Date 21 February 2023 Signature of supervisor

Date 21 February 2023 Signature of supervisor

Permission for publication

In submitting this thesis to the University of St Andrews we understand that we are giving permission for it to be made available for use in accordance with the regulations of the University Library for the time being in force, subject to any copyright vested in the work not being affected thereby. We also understand, unless exempt by an award of an embargo as requested below, that the title and the abstract will be published, and that a copy of the work may be made and supplied to any bonafide library or research worker, that this thesis will be electronically accessible for personal or research use and that the library has the right to migrate this thesis into new electronic forms as required to ensure continued access to the thesis.

I, Suinan Zhang, confirm that my thesis does not contain any third-party material that requires copyright clearance.

The following is an agreed request by candidate and supervisor regarding the publication of this thesis:

Printed copy

No embargo on print copy.

Electronic copy

No embargo on electronic copy.

Date Signature of candidate

February 21 2023

Date 21 February 2023 Signature of supervisor

Date 21 February 2023 Signature of supervisor

Underpinning Research Data or Digital Outputs

Candidate's declaration

I, Suinan Zhang, understand that by declaring that I have original research data or digital outputs, I should make every effort in meeting the University's and research funders' requirements on the deposit and sharing of research data or research digital outputs.

Date Signature of candidate

February 21 2023

Permission for publication of underpinning research data or digital outputs

We understand that for any original research data or digital outputs which are deposited, we are giving permission for them to be made available for use in accordance with the requirements of the University and research funders, for the time being in force.

We also understand that the title and the description will be published, and that the underpinning research data or digital outputs will be electronically accessible for use in accordance with the license specified at the point of deposit, unless exempt by award of an embargo as requested below.

The following is an agreed request by candidate and supervisor regarding the publication of underpinning research data or digital outputs:

No embargo on underpinning research data or digital outputs.

Date Signature of candidate

February 21 2023

Date 21 February 2023 Signature of supervisor

Date 21 February 2023 Signature of supervisor

Abstract

The earliest phase of high-mass star formation has remained a challenging topic. The distinguishing feature between competing theoretical models is the prediction for the high-mass prestellar cores. This thesis presents (sub)arcsecond-resolution interferometric observations in conjunction with synthetic observations at submillimeter wavelengths towards high-mass pre-/proto-stellar objects, for the purpose of characterising the physical and kinematic properties of the early stages of high-mass star formation.

Chapter two showcases deep ALMA 0.82 mm observations ($\theta \sim 0.5''$) towards the high-mass prestellar core candidate G11.92-0.61 MM2. Extensive N_2H^+ (4-3) emission is detected around MM2, displaying complex spectra with multiple velocity components present. Gaussian decomposition and hierarchical clustering are performed to the N_2H^+ data cube to investigate the kinematics of the N_2H^+-emitting gas, which reveals a hierarchical system with filamentary substructures showing velocity gradients. The most dominant N_2H^+ substructure probably traces the accretion flows towards MM2. A mass inflow rate of $2 \times 10^{-4} \sim 1.2 \times 10^{-3}$ $M_\odot$ yr^{-1} is derived with the hypothesis of filamentary accretion flows.

Chapter three presents synthetic 1.3 mm dust continuum images of high-mass star-forming clumps generated with analytic prescriptions and radiative transfer modelling. 432 models with different combinations of stellar masses, separations of sources, and beam sizes are considered. This parametric study predicts that the low-mass objects with masses $\leqq 1$ $M_\odot$ will not be detected if located $\leqq 0.1$ pc from a 50 $M_\odot$ protostar in $0.5''$observations.

Chapter four summarises the SMA 1.3 mm observations towards the high-mass protostellar object G34.24+0.13MM. The $1''$ 1.3 mm continuum image reveals that G34.24+0.13MM is a single compact core, with a size of 4700 AU and a mass of 12.5 $M_\odot$. Molecular lines are detected towards the source, possibly indicating ordered motions of the gaseous envelope or unresolved multiplicity. The uniquely high luminosity-mass ratio of G34.24+0.13MM requires future higher-resolution multi-wavelength observations to properly explain.

Acknowledgements

General acknowledgements

I would like to express my deepest appreciation to the University of St Andrews and the China Scholarship Council (CSC) for supporting my PhD from Aug 2018 to Feb 2023. This endeavour would not have been possible without being funded by them.

I would like to express my deepest gratitude to my supervisors, Dr Claudia Cyganowski and Professor Ian Bonnell, for their generous help in both academic and non-academic aspects throughout my PhD journey. I wanted to thank my principal supervisor, Dr Claudia Cyganowski, for always being patient and incredibly supportive to me for the past five years. I also wanted to thank my secondary supervisor, Prof. Ian Bonnell, for inspiring me (by delivering modern art lectures and sharing hiking photos) and supporting me to get through the hardest times.

I would like to express my sincere thanks to my collaborators, Dr Jonathan Henshaw, Dr Crystal Brogan, Dr Todd Hunter, Dr Rachel Friesen, Dr Camilo Cabrera, and Dr John Ilee, for their insightful suggestions for my PhD projects and fruitful discussions during the work.

I am grateful to the members of the star formation group meeting at the astronomy department of the University of St Andrews, for regular communication and useful discussion as a research community. I wanted to thank my office mates in the Astro Suite for creating and maintaining an inspirational and supportive working environment.

I am thankful to Janice Deary, the tutor at the Academic English Service (AES) of the University of St Andrews, for the language tutorials that helped me to write a PhD thesis in my second language.

I would like to thank my family for understanding and supporting me to do a PhD in a distant country, especially throughout the Covid. I would like to thank my best friend, Chenhan Tang, for understanding, supporting, and inspiring me for every single decision that I have made for the past years. I would also like to thank my friends from undergrad, for supporting each other throughout the Covid years.

Funding

This work was supported by the University of St Andrews [ID 180023582]; and the China Scholarship Council [ID 201806190010].

Research Data/Digital Outputs access statement

Research data underpinning Chapter 2 of this thesis are available at the ALMA Science Archive at `https://almascience.nrao.edu/aq/?result_view=observations`. The project codes are 2015.1.00827.S and 2017.1.01373.S.

Digital outputs underpinning Chapter 3 of this thesis are available at `https://doi.org/10.17630/74981de8-9380-41cd-a384-81f73f7b13b3`.

Research data underpinning Chapter 4 of this thesis are available at the SMA Science Archive at `https://lweb.cfa.harvard.edu/cgi-bin/sma/smaarch.pl`. The project code is 2014B-S032.

Contents

Abstract **vii**

Acknowledgements **ix**

1 Introduction **1**

1.1 The formation of high-mass stars 1

1.1.1 Monolithic collapse models 2

1.1.2 Competitive accretion models 3

1.2 Formation of stellar clusters 4

1.3 Observations: history and prospect 6

1.3.1 Ultra-compact H II regions 6

1.3.2 Infrared bright protostars 6

1.3.3 Infrared dark clouds (IRDCs) and filamentary structures 7

1.3.4 Search for massive prestellar cores 7

1.4 A brief introduction to submillimeter interferometry 10

1.4.1 Basics of interferometry 10

1.4.2 Limitation: short spacing and missing flux problems 11

1.4.3 (Sub)millimeter interferometers: SMA and ALMA 11

1.5 Thesis plan 12

2 Gas kinematics around the high-mass prestellar core candidate G11.92-0.61 MM2 **15**

2.1 Background 15

2.1.1 How do high-mass stars assemble their masses? 15

2.1.2 G11.92-0.61 MM2: a massive prestellar core candidate 16

2.2 Observations and data reduction 18

2.2.1 ALMA 0.82 mm observations 18

2.3 Results 19

2.4 N_2H^+ (4-3) kinematics . . . 24
  2.4.1 Gaussian Decomposition using SCOUSEPY . . . 24
  2.4.2 Hierarchical Clustering using ACORNS . . . 30
2.5 Filamentary accretion flows . . . 34
  2.5.1 Velocity gradient . . . 34
  2.5.2 Mass . . . 36
  2.5.3 Mass inflow rate . . . 40
2.6 Discussions . . . 41
  2.6.1 Filamentary accretion flows feeding the protobinary system . . . 41
  2.6.2 Non-detection of $H_2D^+(1_{1,0}-1_{1,1})$ . . . 42
  2.6.3 Impact of protostellar feedback traced by N_2H^+ (4-3) . . . 43
2.7 Conclusions . . . 44

3 A parametric study of the observability of low-mass cores in massive protoclusters 45
3.1 Background . . . 45
  3.1.1 Isolated high-mass star formation . . . 45
  3.1.2 Synthetic Observations . . . 47
3.2 Methodology . . . 51
  3.2.1 Model construction . . . 51
  3.2.2 Radiative transfer modelling . . . 54
  3.2.3 Parameter space . . . 56
3.3 Results . . . 56
  3.3.1 A one-dimensional overview . . . 56
  3.3.2 Excess Flux . . . 82
  3.3.3 Contrast . . . 86
3.4 Discussion . . . 88
  3.4.1 Radiative transfer modelling vs. optically-thin calculation . . . 88
  3.4.2 Observability of prestellar cores . . . 92
  3.4.3 Caveats and future work . . . 94
3.5 Conclusions . . . 95

4 Resolving the high-mass protostellar object G34.24+0.13 MM 97
4.1 Background . . . 97

4.2 Observations and data reduction 101
4.2.1 SMA 1.3 mm observations 101
4.2.2 Archive data 102
4.3 Results 102
4.3.1 1.3mm continuum 102
4.3.2 Spectral lines 103
4.4 Discussions and future work 105
4.4.1 Mass calculation 105
4.4.2 L_{bol}/M ratio of G34.24+0.13MM 106
4.4.3 Kinematics 109
4.4.4 Fragmentation and multiplicity 112

5 Summary and Future Work **115**
5.1 Summary 115
5.2 Future Work 117

Bibliography **124**

List of Figures

1.1 Snapshots from the simulation of monolithic core collapsing carried out by Krumholz et al. (2009). Left panels show the column densities in colorscale from the perspective that is perpendicular to the rotation axis of the core. The colour scales are logarithmic, with the minimum in black (10^0 g cm^{-2}) and the maximum in red ($10^{2.5}$ g cm^{-2}). Right panels show the volume density along the rotation axis (logarithmic colorscale: black 10^{-18} g cm^{-3}, red 10^{-14} g cm^{-3}). Row A are taken at the time of 1.75 $\times 10^4$ yr; row B are taken at 2.5 $\times 10^4$ yr. The white crossings show the positions of forming stars. 3

1.2 Snapshots of the gas distribution at different times of the simulation presented by Bonnell et al. (2004). The colorscale shows the column density distribution of the gas that is ultimately accreted onto the most massive star. The upper-left panel shows the gas distribution at the time that the star forms: 0.66 $t_{\rm ff}$, $\sim 1.26 \times 10^5$ yr, with the upper-right panel for 1 t_{ff}, lower-left for 1.15 t_{ff}, and lower-right for 1.3 t_{ff}. Each panel has a size of 0.8 pc with the concerned star in the centre. 5

1.3 The Infrared Dark Clouds (IRDCs) presented in Peretto & Fuller (2010). Left panel shows the Spitzer IRAC three-colour image, where the IRDCs structure is indicated by extinction. Right panel shows the molecular hydrogen column density map of the IRDCs, which is inferred from the 8 micron extinction. 8

1.4 A schematic diagram taken from Motte et al. (2018) displaying the evolutionary track of high-mass star formation proposed by Tigé et al. (2017). 9

1.5 The PdBI 1.2 mm dust continuum image of CygX-N53 overlaid with the blue and red contours of the CO emission (adapted from Duarte-Cabral et al. 2013). The green star symbols mark the locations of the massive protostar CygXN53-MM1 and the high-mass prestellar core candidate CygXN53-MM2. The arrows indicate the directions of the CO outflows driven by CygXN53-MM1. 10

1.6 A schematic plot showing the spatial scales that a single dish telescope and an interferometer are sensitive to (adapted from Faridani et al. 2018). The shadowed area represents the overlapping region of spatial scales that both a single dish and an interferometer are sensitive to. 12

2.1 SMA 1.3 mm observations of the high-mass prestellar core candidate G11MM2 presented by Cyganowski et al. (2014). Panel (a): Spitzer three-color image (RGB: 8.0, 4.5, 3.6 μm) overlaid with continuum contours (black) and outflow contours (blue and red). The magenta and diamond markers indicate the locations of Class I and II CH_3OH masers. Panel (b) - (f): integrated intensity maps of submillimeter spectral lines (as marked on the top of each panel) overlaid with the SMA 1.3 mm continuum contours (white), with the VLA 1.3 cm continuum contours (grey) in Panel (f) only. Panel (g) and (h) show the observed MM2 SED overplotted with graybody fits. Panel (i) shows the χ^2 surface plot, where the black line indicates the 4σ 1.3 cm limit. 17

2.2 A summary of the observed results. Panel (a): the 0.8 mm continuum data in colorscale overlaid with the contours of the integrated N_2H^+(4-3) emission (velocity range: 27.0 - 42.0 km s^{-1}; contour levels: 0.06 × [5,10,15,20] Jy km s^{-1}). Panel (b): the integrated $H_2D^+(1_{1,0}\text{-}1_{1,1})$ emission (velocity range: 29.0 - 41.8 km s^{-1}) in colorscale overlaid with the 0.8 mm continuum contours (contour levels: 0.5 × [5,15,40,160,280] mJy beam^{-1}). Panel (c): the integrated DCO^+(5-4) emission (velocity range: 32.6 - 38.4 km s^{-1}) in colorscale overlaid with the 0.8 mm continuum contours. Panel (d): the integrated N_2H^+ emission in colorscale overlaid with continuum contours. Panel (e): the peak intensity map (i.e. moment 8 map) of the N_2H^+ emission in colorscale with continuum contours. Panel (f): the intensity-weighted velocity field map (i.e. moment 1 map) of the N_2H^+ emission in colorscale with continuum contours (velocity range: 27.0 - 42.0 km s^{-1}; cutoff: $4 \times \sigma^*$, where $\sigma^* = 4.7$ mJy beam^{-1} is measured with the N_2H^+ cube before primary beam correction). 21

2.3 Top-left panel: integrated N_2H^+ (4-3) emission overlaid with the 0.82 mm continuum contours (velocity range: 27.0 - 42.0 km s^{-1}; contour levels: 0.06 × [5,10,15,20] Jy km s^{-1}). The right and bottom panels show the N_2H^+ (4-3) spectra extracted at the local peaks of the integrated intensity map to the north (labelled as A) and south (C) of MM2, the continuum peak of MM2 (B) and one of the negative bowls (D). The red vertical lines indicate the relative intensities of the hyperfine structures of this transition. The grey dashed contours show the negative bowls. 22

2.4 An example of performing Gaussian Decomposition to a N_2H^+ (4-3) spectrum with two velocity components. The observed spectrum is plotted in black, with the best-fitting Gaussian models in blue (individual) and red (overall). The best-fitting parameters along wih associated uncertainties are shown on the top right of the figure: peak intensity in Jy beam^{-1} ("A"), centroid velocity in km s^{-1} ("Δx"), and velocity dispersion in km s^{-1} (σ). The numbers in brackets refer to the indices of individual Gaussian models, which increases with ascending centroid velocities. 23

2.5 Left: the version of the best-fitting models employed in the final compiled solution. Different versions of tolerance levels are coded by color/number: dark-blue/0 represents version 0; yellow/1 for version 1; pink/2 for version 2. Overlaid are the continuum contours. Right: the distribution of the number of velocity components of the best-fitting models. The cyan filled circles overlaid indicate the locations of the 10 spectra that are selected for hyperfine structure fitting. 27

2.6 (a) Top panel: the histogram of centroid velocities for the best-fitting components (bin size: 0.25 km s^{-1}). Bottom panel: the amplitude of velocity components versus centroid velocity. (b) Top panel: the histogram of velocity dispersion for the best-fitting components (bin size: 0.06 km s^{-1}). Bottom panel: the amplitude of velocity components versus velocity dispersion. 28

2.7 A one-component N_2H^+ (4-3) spectrum fitted with a single set of hyperfine structures. The spectrum is plotted in black, with the model in red. The fitted parameters are listed on the top right corner. 29

2.8 The comparison of the fitted parameters from Gaussian Decomposition (plotted with black circles) and hyperfine structure fitting (plotted with red squares). The y axis shows the velocity dispersion; the x axis shows the centroid velocity; the associated error is indicated by the length of the line. 31

2.9 The dendrogram showing the structure of the ACORNS forest. The forest consists of 70 trees (i.e. the ACORNS clusters). ∼23% (16/70) of the trees have branches or leaves (i.e. substructure). The substructure is indicated by the short horizontal lines. The highest points of the leaves represent their peak intensities. The eight most dominant trees are plotted in rainbow colours (as labelled). The red rectangle marks Branch 8. 33

2.10 Tree 0 in Position-Position-Velocity (PPV) space. Each velocity component that is clustered into Tree 0 is plotted with a filled circle. The colours indicate the peak intensities of the velocity components. The 0.8 mm continuum emission is plotted in colourscale on the bottom, with a cutoff of $5 \times \sigma_{cont}$ ($\sigma_{cont} = 0.5$ mJy beam^{-1}) applied. 35

2.11 Left panel: the distribution of the peak intensities of the velocity components of Tree 0; black contours show the 0.8 mm continuum emission (contour levels: $0.5 \times [5,15,40,160,280]$ mJy beam^{-1}). Mid panel: the centroid velocity map of Tree 0 overlaid with the continuum contours. Right panel: the velocity dispersion map of Tree 0 with the contours. 36

2.12 The filled circles show the Probability Distribution Function (PDF) of the centroid velocities of the components in Tree 0. The dashed lines represent the best-fitting Gaussian model to the velocity PDF. 37

2.13 The centroid velocity map of Branch 8, overlaid with the 0.8 mm continuum contours (black; contour levels: $0.5 \times [5,15,40,160,280]$ mJy beam^{-1}), and the 1.3 mm continuum contours (grey; contour levels: $0.06 \times [10,50,150]$ mJy beam^{-1}). The synthesised beams of the 0.8 mm and 1.3 mm data are illustrated in the bottom left and right corners, respectively. 38

2.14 Left panel: the distribution of the peak intensities of the velocity components of Tree 7; black contours show the 0.8 mm continuum emission (contour levels: 0.5 × [5,15,40,160,280] mJy beam^{-1}). Mid panel: the centroid velocity map of Tree 7 overlaid with the continuum contours. Right panel: the velocity dispersion map of Tree 7 with the contours. The magenta crosses mark the locations of the class II 6.7 GHz methanol masers; the cyan diamonds mark the locations of the class I 44 GHz methanol masers (Cyganowski et al. 2009). 43

3.1 An example of synthetic observations of an accretion disk around a young high-mass star (Meyer et al. 2018). Left panel shows the synthetic image of dust continuum emission; Mid panel shows the continuum image that is expected if it is observed with ALMA; Right panel shows the CH_3CN velocity map that would appear in ALMA observations. 49

3.2 Synthetic ALMA observations of the CO(1-0) and [CI](1-0) emission from a typical Milky Way (MW) GMC (Haworth et al. 2018). Their models consider that the GMC is irradiated by an MW-average isotropic Far-UV radiation field and cosmic rays with a cosmic ray ionisation rate equal to 1 and 10 times the MW average. The top row shows the fluxes of CO(1-0) (left) and [CI](1-0) (right) with different cosmic ray ionisation rates (as labelled). Bottom left panel shows the true distribution of the molecular hydrogen column density of the GMC. The four small panels on the lower right show the distributions of the molecular hydrogen column density that are derived using the CO-to-H_2 and CI-to-H_2 conversion factors. 50

3.3 A cartoon showing the gas sphere described by a 3D Cartesian grid. The locations of protostars are plotted with orange stellar markers encompassed by black circles. The line of sight is parallel to the y axis. 51

3.4 One-dimensional slices crossing the locations of the high- and low-mass sources extracted from the synthetic continuum images (where $m_a = 8\ M_\odot$). The intensities are plotted in units of Jansky per square arcsecond area. Results with different resolution are plotted in different columns (left: $0.6'' \times 0.4''$; middle: $3.0'' \times 2.0''$; right: $6.0'' \times 5.0''$). Results with different separation are shown in rows (from top to bottom: 0.05 pc, 0.10 pc, 0.15 pc, 0.20 pc, 0.25 pc, 0.30 pc). The masses of the low-mass source (m_b) are colour-coded (black: 0.1 $M_\odot$; blue: 0.25 $M_\odot$; red: 0.5 $M_\odot$; lime: 1.0 $M_\odot$; magenta: 2.0 $M_\odot$; green: 5.0 $M_\odot$). 58

3.5 As Fig.3.4 with $m_a = 15\ M_\odot$. 59

3.6 As Fig.3.4 with $m_a = 25\ M_\odot$. 60

3.7 As Fig.3.4 with $m_a = 50\ M_\odot$. 61

3.8 One-dimensional slices crossing the locations of the high- and low-mass sources extracted from the synthetic continuum images (where $m_b = 0.1$ M$_\odot$). The intensities are plotted in units of Jansky per square arcsecond area. Results with different resolution are plotted in different columns (left: $0.6'' \times 0.4''$; middle: $3.0'' \times 2.0''$; right: $6.0'' \times 5.0''$). Results with different separation are shown in rows (from top to bottom: 0.05 pc, 0.10 pc, 0.15 pc, 0.20 pc, 0.25 pc, 0.30 pc). The masses of the high-mass source (m_a) are colour-coded (magenta: 8 M$_\odot$;blue: 15 M$_\odot$; red: 25 M$_\odot$; green: 50 M$_\odot$). 64

3.9 As Fig.3.8 with $m_b = 0.25$ M$_\odot$. 65

3.10 As Fig.3.8 with $m_b = 0.5$ M$_\odot$. 66

3.11 As Fig.3.8 with $m_b = 1.0$ M$_\odot$. 67

3.12 As Fig.3.8 with $m_b = 2.0$ M$_\odot$. 68

3.13 As Fig.3.8 with $m_b = 5.0$ M$_\odot$. 69

3.14 One-dimensional slices crossing the locations of the high- and low-mass sources extracted from the synthetic continuum images (where $m_a = 8$ M$_\odot$). The intensities are plotted in units of Jansky per beam. Results with different resolution are plotted in different columns (left: $0.6'' \times 0.4''$; middle: $3.0'' \times 2.0''$; right: $6.0'' \times 5.0''$). Results with different separation are shown in rows (from top to bottom: 0.05 pc, 0.10 pc, 0.15 pc, 0.20 pc, 0.25 pc, 0.30 pc). The masses of the low-mass source are colour-coded (black: 0.1 M$_\odot$; blue: 0.25 M$_\odot$; red: 0.5 M$_\odot$; lime: 1.0 M$_\odot$; magenta: 2.0 M$_\odot$; green: 5.0 M$_\odot$). The grey dotted lines show the 5σ threshold in practical ALMA, SMA and ACA observations (taken from literature, see details in section 4.3.1). 72

3.15 As Fig.3.14 with $m_a = 15$ M$_\odot$. 73

3.16 As Fig.3.14 with $m_a = 25$ M$_\odot$. 74

3.17 As Fig.3.14 with $m_a = 50$ M$_\odot$. 75

3.18 One-dimensional slices crossing the locations of the high- and low-mass sources extracted from the synthetic continuum images (where $m_b = 0.1$ M$_\odot$). The intensities are plotted in units of Jansky per square arcsecond area. Results with different resolution are plotted in different columns (left: $0.6'' \times 0.4''$; middle: $3.0'' \times 2.0''$; right: $6.0'' \times 5.0''$). Results with different separation are shown in rows (from top to bottom: 0.05 pc, 0.10 pc, 0.15 pc, 0.20 pc, 0.25 pc, 0.30 pc). The masses of the high-mass source (m_a) are colour-coded (magenta: 8 M$_\odot$;blue: 15 M$_\odot$; red: 25 M$_\odot$; green: 50 M$_\odot$). The grey dotted lines show the 5σ threshold in practical ALMA, SMA and ACA observations (taken from literature, see details in section 4.3.1). 76

3.19 As Fig.3.18 with $m_b = 0.25$ M$_\odot$. 77

3.20 As Fig.3.18 with $m_b = 0.5$ M$_\odot$. 78

3.21 As Fig.3.18 with $m_b = 1.0$ M$_\odot$. 79

3.22 As Fig.3.18 with $m_b = 2.0$ M$_\odot$. 80

3.23 As Fig.3.18 with m$_b$ = 5.0 M$_\odot$. 81

3.24 colourscale: the excess flux versus the mass of the low-mass source (y axis) and the separation (x axis) for different masses of the high-mass source (each row). The excess flux is calculated by the secondary peak minus the valley between the two sources, with a unit of Jansky per square arcsecond area. The cases where the calculated excess flux equals zero are marked with "x" symbols. The upward triangles mark the boundary above which the excess flux values are greater than 5 $\times\sigma_{rms}$. 83

3.25 This figure is the same as Fig.3.24 but the excess flux is in unit of Jansky per beam. The lightblue circles mark the cases where the intensity at the location of the low-mass source is above the 5 $\times\sigma_{rms}$ threshold. The upward triangles mark the boundary above which the Excess Flux values are greater than 5 $\times\sigma_{rms}$. 87

3.26 colourscale: the contrast versus the mass of the low-mass source (y axis) and the separation (x axis) for different masses of the high-mass source (each row). The contrast is given by (the secondary peak - the valley)/the valley, where the intensity is in unit of Jansky per beam. The black filled circles mark the cases where the contrast of the secondary peak is greater than that converted from 5σ noise. Cases where the secondary peak equals the valley are marked with X symbols. 89

3.27 colourscale: the contrast versus the mass of the low-mass source (y axis) and the separation (x axis) for different masses of the high-mass source (each row). The contrast is given by (the secondary peak - the valley)/the valley, where the intensity is in unit of Jansky per square arcsecond area. The black filled circles mark the cases where the contrast of the secondary peak is greater than that converted from 5σ noise. Cases where the secondary peak equals the valley are marked with X symbols. 90

3.28 The distribution of optical depth on the projection plane for the case with m$_a$ = 50 M$_\odot$, m$_b$ = 5 M$_\odot$, separation = 0.15 pc. 91

3.29 The fractional difference of the 1D slices between the optically-thin calculation and the RT modelling. The fraction is given by (OT - RT)/RT. 92

3.30 The 1D slices along the locations of high- and low-mass sources (red: with a uniform density sphere; blue: without). The separation is set to 0.1 pc, with m$_a$ = 25 M$_\odot$ and m$_b$ = 2 M$_\odot$. The three panels show the three different beam sizes (from left to right: 0.6″ × 0.4″, 3.0″ × 2.0″, 6.0″ × 5.0″). 93

4.1 Spitzer IRAC 3-color image (red 8 μm, green 4.5 μm, blue 3.6 μm) overlaid in the left panel with Herschel 70μm contours and 6 cm contours (6, 15, 75, 300 mJy beam^{-1}) from the VLA CORNISH survey (Hoare et al. 2012) showing the UCHII region G34.26+0.15 located 1.5 pc from the target. The right panel is a zoomed view to the white rectangular area targeted by the SMA primary beam, overlaid with contours from the SMA 1.3 mm observations (resolution$\sim$1 $''$, red), OVRO 1.3 mm data from Hunter et al. (1998) (resolution $\sim$2.5 $''$, black) and 870 μm contours (400, 900, 1750 mJy beam^{-1}) from the ATLASGAL survey (resolution $\sim$19.2 $''$, blue, Csengeri et al. 2014). The 6.7 GHz methanol maser position from Bartkiewicz et al. (2016) is marked by a green cross. 100

4.2 A zoom-in view of the SMA 1.3 mm dust continuum emission from G34.24+0.13MM (left panel), the best-fitting 2D Gaussian model (mid panel), and the residual image (right panel). 102

4.3 Moment maps of H_2CO $3_{1,2}-2_{1,1}$ (225.698 GHz, E_{upper} =33.4 K) emission overlaid with SMA 1.3 mm continuum contours: **Left:** moment 0 (integrated intensity), **Center:** moment 1, **Right:** moment 8 (peak map). Continuum contour levels: (0.2, 0.4, 0.6, 0.8)×peak intensity (=55.5 mJy beam^{-1}). 103

4.4 Moment maps of HC_3N (J = 25-24) emission overlaid with SMA 1.3 mm continuum contours: **Left:** moment 0 (integrated intensity), **Center:** moment 1, **Right:** moment 8 (peak map). Continuum contour levels: (0.2, 0.4, 0.6, 0.8)×peak intensity (=55.5 mJy beam^{-1}). The velocity range is 53.7-59.2 km s^{-1}.105

5.1 Left panel: the distribution of the peak intensities of the velocity components of Tree 9; black contours show the 0.8 mm continuum emission (contour levels: 0.5 × [5,15,40,160,280] mJy beam^{-1}). Mid panel: the centroid velocity map of Tree 9 overlaid with the continuum contours. Right panel: the velocity dispersion map of Tree 9. 119

5.2 An example of the synthetic 1.3 mm continuum images generated by RADMC-3D. This image shows the result of the model with separation = 0.3 pc, the mass of the high-mass protostar $m_a = 50\ M_\odot$, and the mass of the low-mass protostar $m_b = 2\ M_\odot$. The high-mass source is located in the centre, while the low-mass source is 0.3 pc above. 120

5.3 A synthetic ALMA 1.3 mm dust continuum image simulating 43-antenna observations using the CASA task *simobserve*. The model is set up with separation = 0.1 pc, the mass of the high-mass protostar $m_a = 25\ M_\odot$, and the mass of the low-mass protostar $m_b = 2\ M_\odot$. The simulations consider single pointing observations centred at 231 GHz with a bandwidth of 1.875 GHz at the C43-4 configuration of ALMA Cycle 6. The assumed phase centre is (18h13m58.11s, -18d54m22.141s). 121

List of Tables

1.1 A summary of the key information about the SMA and ALMA. 13

2.1 A summary of the three sets of tolerance levels used in stage 3). 25

3.1 A summary of parameters. 52

3.2 A summary of the parameter space we explore in this work. 56

3.3 A summary of the representative ALMA, SMA, and ACA 1.3 mm continuum observations. 71

4.1 A summary of the fitted parameters of the 1.3 mm SMA continuum image for G34.24+0.13MM. 103

4.2 A summary of the observational parameters of recently published far-infrared and submillimeter data that is available for the SED fitting for G34.24+0.13MM. 110

1

Introduction

1.1 The formation of high-mass stars

Massive stars, also known as OB stars, are stars with masses $\gtrsim 8$ $M_\odot$. Massive stars are of vital significance in galaxy evolution and shaping the universe. Strong stellar winds are generated while massive stars evolve, profoundly affecting surrounding environments. High-energy UV radiation from inner massive stars can ionize outer neutral gas clouds, creating HII regions and driving their expansion. High-mass stars are massive enough to synthesise heavy elements, and finally disperse them via supernova explosions. The interaction between these feedback activities and nearby molecular clouds produce mixing and turbulence in the interstellar medium (ISM), which can possibly trigger the formation of next generations of stars.

Due to the important role that massive stars play in the evolution of galaxies and the universe, a comprehensive understanding of the processes of massive star formation (MSF) is required. However, compared to low-mass stars, massive stars are rare and short-lived. The progenitors of massive stars are deeply embedded in their parental molecular clouds.

Observations of early formation phases are thus impeded by high dust extinction. Moreover, massive stars form mostly in clusters and/or associations, where the formation of a single massive star can be affected by other high-mass (proto)stars. Hence, a widely accepted picture of massive star formation has not yet been established.

The major problems in the field of massive star formation include: what are the initial conditions of MSF? What are the factors which dominate the fragmentation of molecular clouds? What is the evolution path leading from molecular clouds to newly-born massive stars? How does the massive stellar feedback influence the environment of massive stars?

1.1.1 Monolithic collapse models

Currently theoretical work explaining high-mass star formation can be divided into two main classes: core accretion models (or monolithic collapse models; McKee & Tan 2002, McKee & Tan 2003) and competitive accretion models (Bonnell et al. 2001, Bonnell et al. 2003, Bonnell et al. 2004, Bonnell & Bate 2006). In the context of core accretion models, high-mass star formation is a scaled-up version of low-mass star formation. It is proposed that the initial condition of massive star formation is a massive, coherent, gravitationally bound, starless core, which is the analog of a low-mass prestellar core. A massive prestellar core is expected to have a high gas surface density Σ of ~ 1 g cm^{-2}, without hosting a hydrostatic protostar inside (Tan et al. 2014). Massive prestellar cores can be more massive than the thermal Jeans mass but will not fragment into smaller cores, due to the support of strong turbulence and/or magnetic fields. When prestellar cores gain the necessarily high mass, gravitation overcomes the effects of turbulence and magnetic fields and they start to collapse, entering the protostellar phase. The prestellar core mass function (CMF) is thus speculated to be similar in shape to the stellar initial mass function (IMF). Sources with small sizes (e.g. $\sim$0.01 - 0.1 pc), high densities ($n_{H_2} \sim 10^6$ cm^{-3}), and low temperatures ($\sim 10\ K$) are expected to be potential candidates of massive prestellar cores (André et al. 2010, Tan et al. 2014). Krumholz et al. (2009) perform a hydrodynamic simulation to model the collapse of a single massive prestellar core. They set up the initial conditions to be 100M$_\odot$, 0.1 pc, and density profile of r$^{-1.5}$ to keep the simulation consistent with the models in McKee & Tan (2003) and McKee & Tan (2002). Their results support that high-mass stars can form via monolithic collapses, as shown in Figure 1.1.

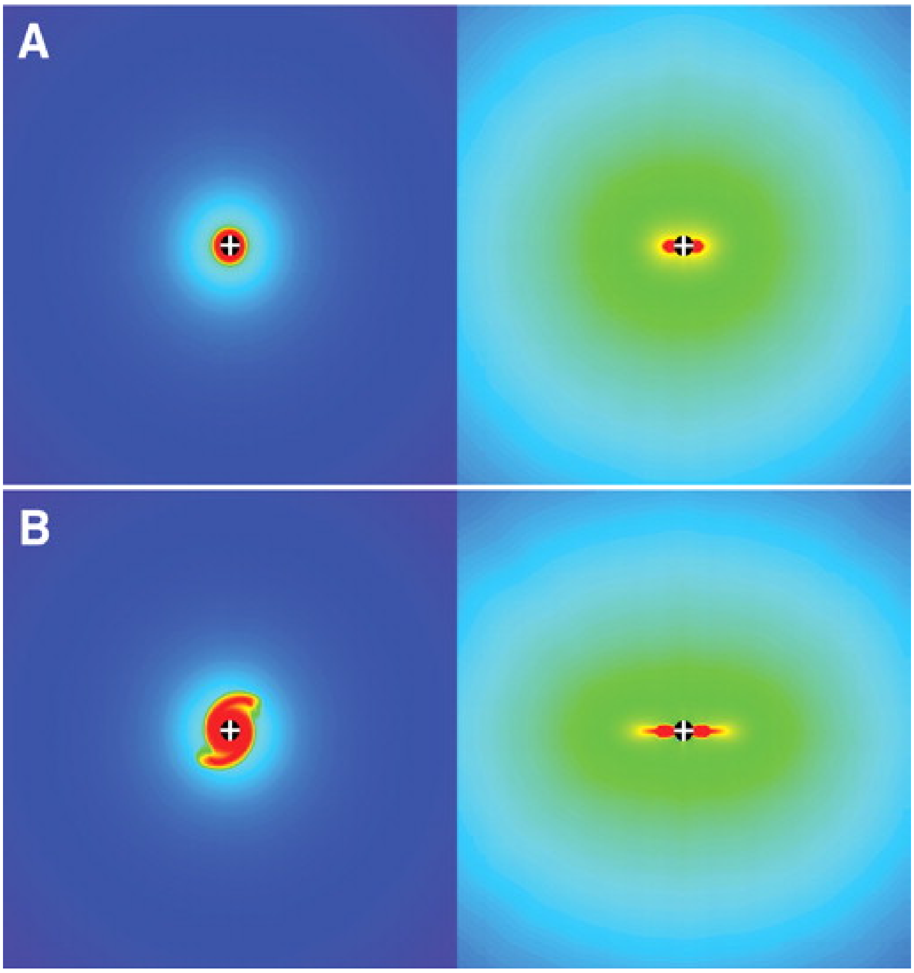

Figure 1.1: Snapshots from the simulation of monolithic core collapsing carried out by Krumholz et al. (2009). Left panels show the column densities in colorscale from the perspective that is perpendicular to the rotation axis of the core. The colour scales are logarithmic, with the minimum in black (10^0 g cm^{-2}) and the maximum in red ($10^{2.5}$ g cm^{-2}). Right panels show the volume density along the rotation axis (logarithmic colorscale: black 10^{-18} g cm^{-3}, red 10^{-14} g cm^{-3}). Row A are taken at the time of 1.75 $\times 10^4$ yr; row B are taken at 2.5 $\times 10^4$ yr. The white crossings show the positions of forming stars.

1.1.2 Competitive accretion models

According to competitive accretion models, gas that forms a massive star is drawn from a wider region in its parental molecular clouds (0.2 to $>$ 10 pc, Kuiper & Hosokawa 2018), without being a massive prestellar core. It is argued that most stars form in clusters and more massive stars form closer to the centre of clusters. Benefiting from the large gravitational potential of the whole cluster, stars near the centre of the cluster potential are able to gain more mass than those on outskirts or in isolation, and thus can grow into massive stars. Figure 1.2 shows the distribution of the gas that is ultimately accreted onto the most massive star. The central star accretes gas widely from its parsec-scale environment. Besides, stars with initial higher masses are also able to accrete more gas and become more massive than those with lower masses at the beginning. Competitive accretion models suggest that massive star formation should start with low-mass prestellar cores. These cores first evolve to low-mass protostars. The low-mass protostars then keep accreting gas at different rates in relation to various location/environment and initial masses, becoming massive protostars and eventually massive stars. In this scenario, massive prestellar cores are not necessary in the early stages of massive star formation. Bonnell et al. (2004) proposed an evolutionary trend of massive cluster formation, indicating that the (proto)cluster gains more stars while the most massive star hosted accretes more gas. The mass of the most massive star ($M_{\rm max}$) scales up with the total mass of stars within the host (proto)cluster ($M_{\rm stars}$) as $M_{\rm max} \propto M_{\rm stars}^{2/3}$. This relation can naturally reproduce the power-law part of the IMF (Bonnell et al. 2007).

1.2 Formation of stellar clusters

Stellar clusters and associations are groups of stars which are physically related (Lada & Lada 2003). It is found that ~70% of Galactic O-type stars are members of stellar clusters or OB associations (Gies 1987, Mason et al. 1998). Deep images revealing stellar companions and spectroscopy studies showing runaway kinematics can push the percentage even higher (e.g., de Wit et al. 2005, Selier et al. 2011, Bressert et al. 2012, Oey et al. 2013, Lamb et al. 2016). Therefore, a natural question is: how is the formation of high-mass stars connected with cluster formation? Answering this question requires a comprehensive understanding of the formation of massive stellar clusters. Two competing concepts have been proposed to account for the formation of massive clusters at parsec scale, which are monolithic formation models (Baumgardt & Kroupa 2007, Banerjee & Kroupa 2014, Banerjee & Kroupa 2015, Banerjee & Kroupa 2017) and hierarchical models (Bonnell et al. 2003, Allison et al. 2009, Vázquez-Semadeni et al. 2017). They separately provide distinguishing predictions in terms of the spatial distribution of high- and low-mass (proto)stars. In monolithic formation models, large-scale cloud clumps fragment to form prestellar cores which then collapse isolatedly into protostars. In this scenario, the protoclusters are likely more centrally concentrated than evolved clusters. While in the scenario of hierarchical cluster formation models, large- and small-scale collapses proceed concurrently (see Global Hierarchical Collapse model (GHC) in Vázquez-Semadeni et al. 2017). Stars form via collapses of small fragments which are widely distributed throughout their parental molecular clouds (MCs). Meanwhile, large-scale turbulence and gravitational

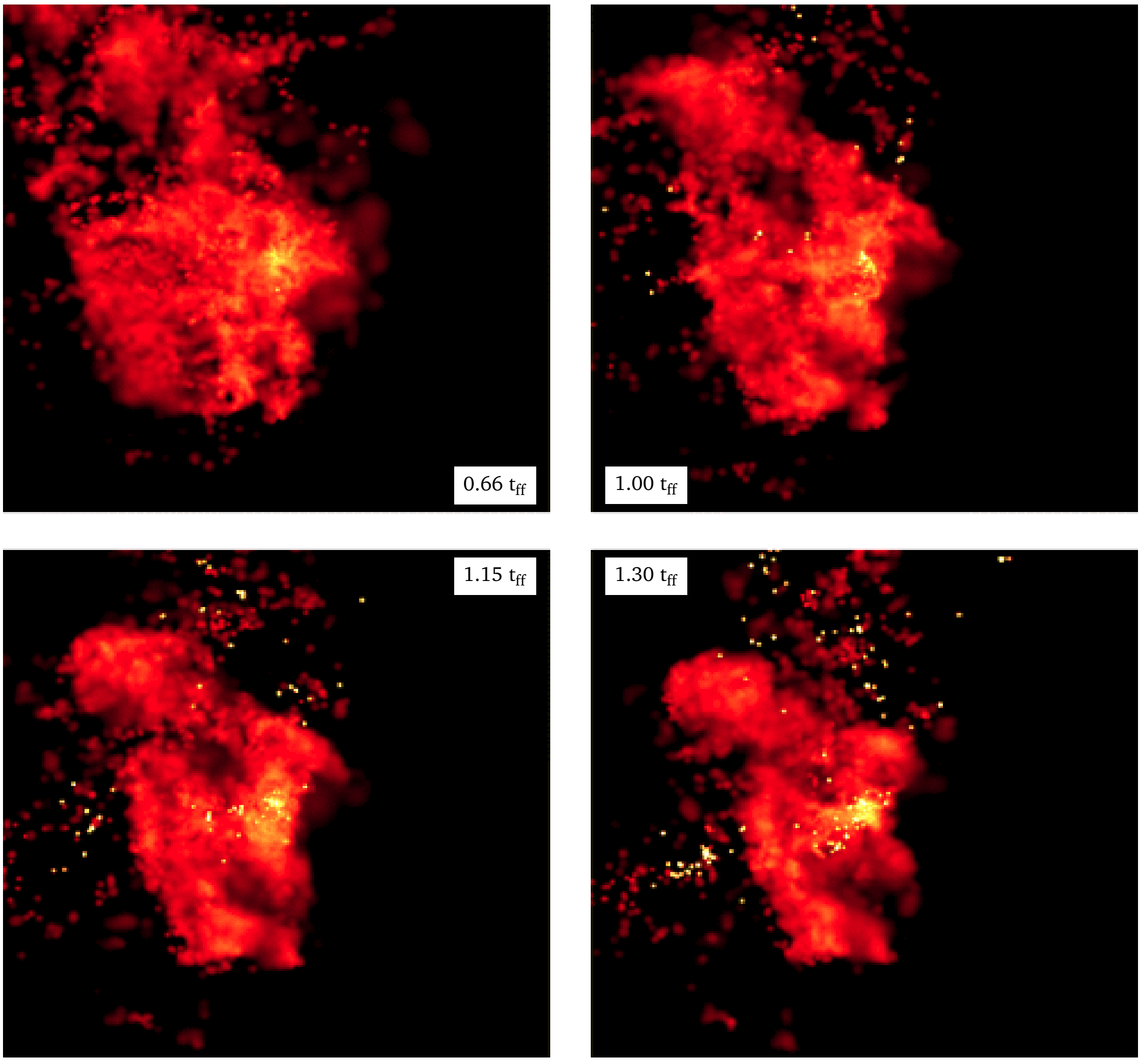

Figure 1.2: Snapshots of the gas distribution at different times of the simulation presented by Bonnell et al. (2004). The colorscale shows the column density distribution of the gas that is ultimately accreted onto the most massive star. The upper-left panel shows the gas distribution at the time that the star forms: 0.66 $t_{\rm ff}$, $\sim 1.26 \times 10^5$ yr, with the upper-right panel for 1 t_{ff}, lower-left for 1.15 t_{ff}, and lower-right for 1.3 t_{ff}. Each panel has a size of 0.8 pc with the concerned star in the centre.

collapses in MCs result in filamentary structures, through which gas from extended clouds accrete onto the small-scale star-forming sites. In this context, (proto)clusters prefer to be less centrally concentrated than unembedded clusters: high-mass protostars form in central hubs which are fed by filamentary accretion flows; low-mass protostars are distributed in wider and outer regions of protoclusters. Moreover, different hierarchical models give differing statements for the birth order of high- and low-mass (proto)stars. Maschberger et al. (2010) suggest that high-mass stars are born earlier than low-mass stars; while Vázquez-Semadeni et al.

(2017) argue that massive stars can only emerge at later times. To test these theoretical predictions, large-area high-resolution numerical simulations and multi-wavelength observations are both required (e.g., Motte et al. 2007, Smith et al. 2009, Cyganowski et al. 2017, Pillai et al. 2019, Avison et al. 2021).

1.3 Observations: history and prospect

1.3.1 Ultra-compact H II regions

To answer the questions about massive star formation (see section 1.1), observers have started to search for the precursors of high-mass stars using ground- and space-based observations since the 1980s (Benson et al. 1984, Reid & Mould 1985). As mentioned before, OB stars are known to be associated with developed HII regions. Classical HII regions produce copious emission lines at UV-optical, Infrared and radio wavelengths. Particularly, although massive protostars are deeply embedded in their parental molecular clouds, neutral gas and dust in surrounding envelopes appear to be optically thin at radio band. This allows radio centimeter and recombination lines as probes of the evolution of HII regions, which indicates the formation of linked massive stars. Based on the level of ionization expansion, Churchwell (2002) and Hoare et al. (2007) proposed an empirical evolutionary path, leading from hypercompact HII regions, and then ultra-compact HII regions, to compact HII regions, and then classical developed HII regions. The hypercompact HII regions (HCHIIs) and ultra-compact HII regions (UCHIIs) have relatively smaller sizes (0.1 pc and <0.05 pc, Hoare et al. 2007), and correspond to early phases of HII regions.

1.3.2 Infrared bright protostars

For an embedded massive protostar, dust in surrounding molecular clouds can absorb most of its radiation and thus make it invisible at optical wavelengths. Instead, the dust heated by the interior protostar can produce thermal emission which peaks at far-infrared (FIR) wavelengths. This is so-called the infrared-bright high-mass protostar. Wood & Churchwell (1989) search for young HII regions among the luminous infrared sources provided by the *Infrared Astronomical Satellite* (IRAS) point source catalog. They select bright IRAS sources satisfying log ($F_{60}\mu$m / $F_{12}\mu$m) > 1.3 and log ($F_{25}\mu$m / $F_{12}\mu$m) > 0.57, which generates a catalogue of 1646 objects distributed across the Galaxy. Most of these selected sources are confirmed to be

UCHII regions. The sources remaining undetected at centimetre wavelengths are suspected to be protostellar objects embedded within gas envelopes that have not yet created HII regions. To further examine whether these infrared sources are precursors of massive stars (i.e massive and dense enough to form high-mass stars), dense gas tracers (e.g. millimeter continuum, molecular lines, masers) have been applied to investigate their physical properties (Sridharan et al. 2002, Hill et al. 2005). Massive protostellar clumps (∼1 pc) are identified to be closely associated with the IRAS sources (Beuther et al. 2002), which are good candidates to host infrared-bright high-mass protostars.

1.3.3 Infrared dark clouds (IRDCs) and filamentary structures

In the past decade, efforts have been made to search for the precursors of infrared-bright high-mass protostars, which are speculated to be dense, cold, infrared-dark structures. Two different methods are proposed to find the candidates of infrared-dark high-mass protostars. The first one is to use dense gas tracers (e.g. (sub)millimeter continuum) to image the surrounding environment of infrared-bright high-mass objects, UCHIIs, or H_2O / CH_3OH masers. This method has yielded successful discoveries of dense cloud structures (0.1 pc to 1 pc) which remain undetected at mid-infrared wavelengths (Sridharan et al. 2005). The second method is to search for cold cloud structures seen in absorption against the diffuse mid-infrared backgraound emission observed with the *Infrared Space Observatory* (ISO), *Midcourse Space Experiment* (MSX), *Spitzer Space Telescope* (Spitzer) and *Herschel Space Observatory* (Herschel). These absorption features are so-called infrared dark clouds (IRDCs). Imaging IRDCs with dense gas tracers reveals large samples of infrared-dark fragments with sizes of 0.1 pc to 1 pc (Ragan et al. 2006, Sakai et al. 2008). These 0.1-1 pc structures discussed above are colder and less luminous than infrared-bright high-mass objects mentioned before. They could be either massive starless clumps or clumps harboring infrared-dark protostars, depending on the existence of the signatures of protostellar accretion. Figure 1.3 shows an example of IRDCs discussed in Peretto & Fuller (2010).

1.3.4 Search for massive prestellar cores

At the earliest stage of massive star formation, the existence of massive prestellar cores remains controversial. Based on a high-resolution multi-wavelength study of the molecular cloud complex NGC 6334, Tigé et al. (2017) propose an evolutionary track of high-mass star formation,

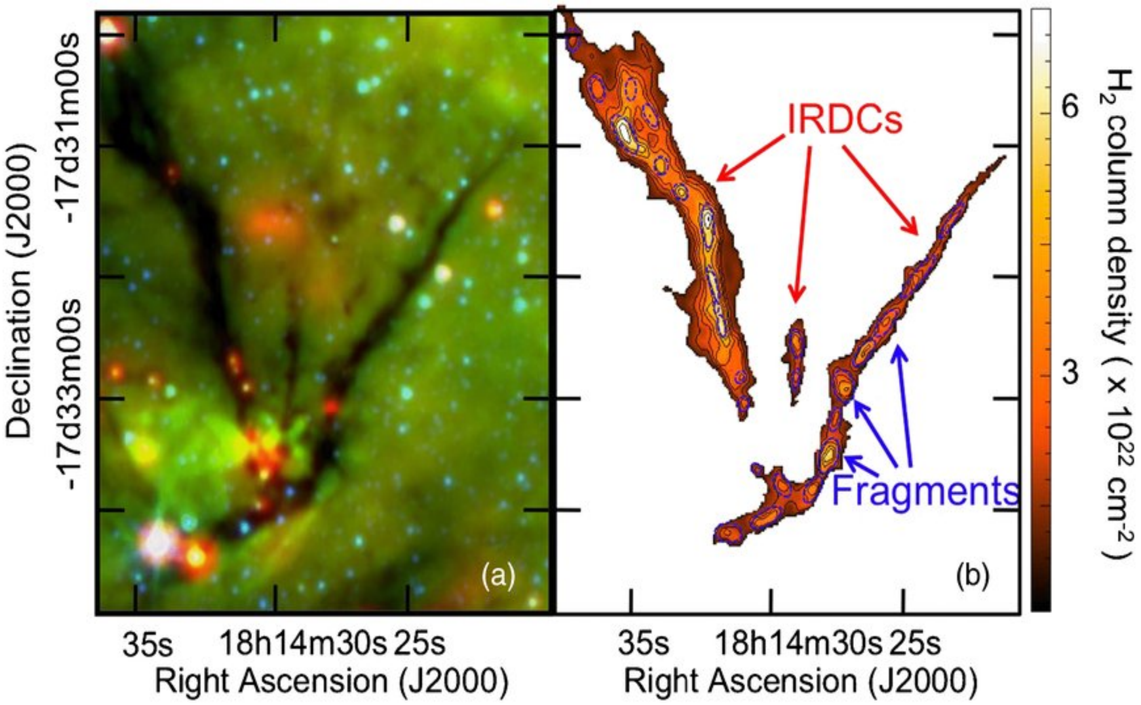

Figure 1.3: The Infrared Dark Clouds (IRDCs) presented in Peretto & Fuller (2010). Left panel shows the Spitzer IRAC three-colour image, where the IRDCs structure is indicated by extinction. Right panel shows the molecular hydrogen column density map of the IRDCs, which is inferred from the 8 micron extinction.

which starts from low-mass prestellar cores, to low-mass protostellar cores, and to high-mass protostars. A schematic view of the evolutionary stages is shown in Figure 1.4. Researchers have been looking for high-mass analogs of low-mass prestellar cores, which are supposed to be massive, small-scale (0.01-0.1 pc), gravitationally bound, dense ($n_{H_2} = 10^5 - 10^7$ cm^{-3}) cloud cores (André et al. 2000). With the improvement of detection sensitivity and spatial resolution, most of previous candidates of massive prestellar cores are disqualified. For example, G028C1-S, selected from a sample of IRDCs that have the highest contrast against the Galactic mid-infrared background (Butler & Tan 2009, Butler & Tan 2012), was found to contain ~60 M$_\odot$ within ~0.09 pc by Tan et al. (2013). However, follow-up studies revealed that G028C1-S consists of two protostars driving outflows (Tan et al. 2016). Similarly, G028C9A was first found to have a mass of ~80 M$_\odot$ within ~0.05 pc, but resolved to be two lower-mass cores (Kong et al. 2017). CygXN53-MM2, with a mass of ~25 M$_\odot$ within ~0.025 pc, had been one of the best massive prestellar core candidates (Bontemps et al. 2010). However, owing to the short distance from its neighbour protostar CygXN53-MM1, it is difficult to figure out which of them is driving the weak outflow detected (Duarte-Cabral et al. 2013, Duarte-Cabral et al. 2014). The relative locations of CygXN53-MM1 and CygXN53-MM2 are denoted with

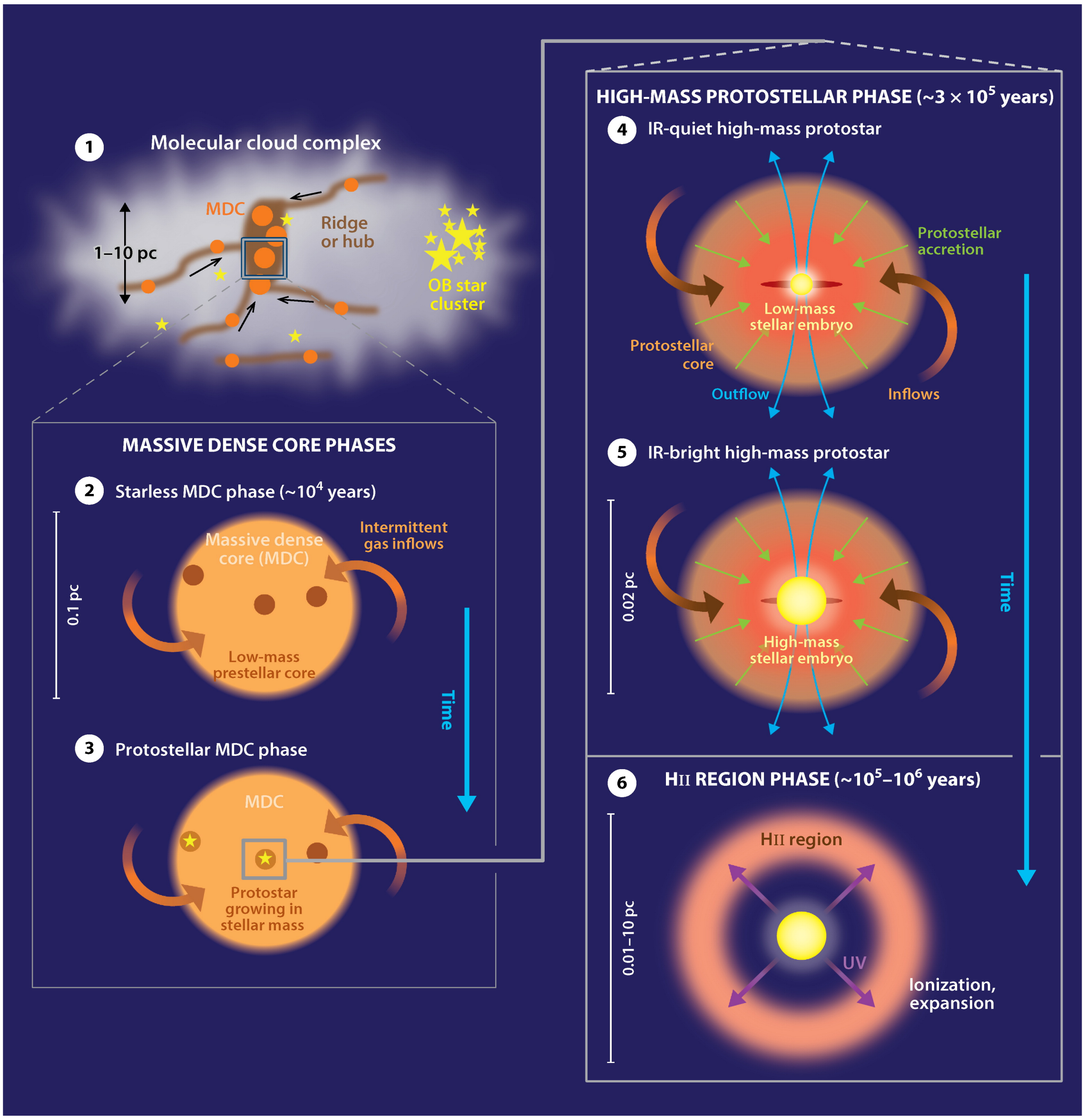
1
Molecular cloud complex
MDC
Ridge or hub
1–10 pc
OB star cluster
MASSIVE DENSE CORE PHASES
2
Starless MDC phase (~10^4 years)
0.1 pc
Massive dense core (MDC)
Intermittent gas inflows
Low-mass prestellar core
Time
3
Protostellar MDC phase
MDC
Protostar growing in stellar mass
HIGH-MASS PROTOSTELLAR PHASE (~3 × 10^5 years)
4
IR-quiet high-mass protostar
Protostellar accretion
Low-mass stellar embryo
Protostellar core
Outflow
Inflows
5
IR-bright high-mass protostar
0.02 pc
High-mass stellar embryo
Time
6
HII REGION PHASE (~10^5–10^6 years)
0.01–10 pc
HII region
UV
Ionization, expansion

Motte F, et al. 2018.
Annu. Rev. Astron. Astrophys. 56:41–82

Figure 1.4: A schematic diagram taken from Motte et al. (2018) displaying the evolutionary track of high-mass star formation proposed by Tigé et al. (2017).

green star symbols in Figure 1.5, with blue and red contours representing the CO outflows. The massive prestellar core candidates identified to date are G11P6-SMA1 ($\sim$30 M$_{\odot}$ within $\sim$0.02 pc, Wang et al. 2014), G11.92-0.61 MM2 ($\sim$30 M$_{\odot}$ within $\sim$0.005 pc, Cyganowski et al. 2014), W43-MM1 core 6 ($\sim$60 M$_{\odot}$, Nony et al. 2018, Molet et al. 2019), AG354 ($\sim$39 M$_{\odot}$, Redaelli et al. 2021), and G028.37+00.07 C2c1a ($\sim$23-31 M$_{\odot}$, Barnes et al. 2023). Their validity requires further examination using higher-resolution follow-up observations.

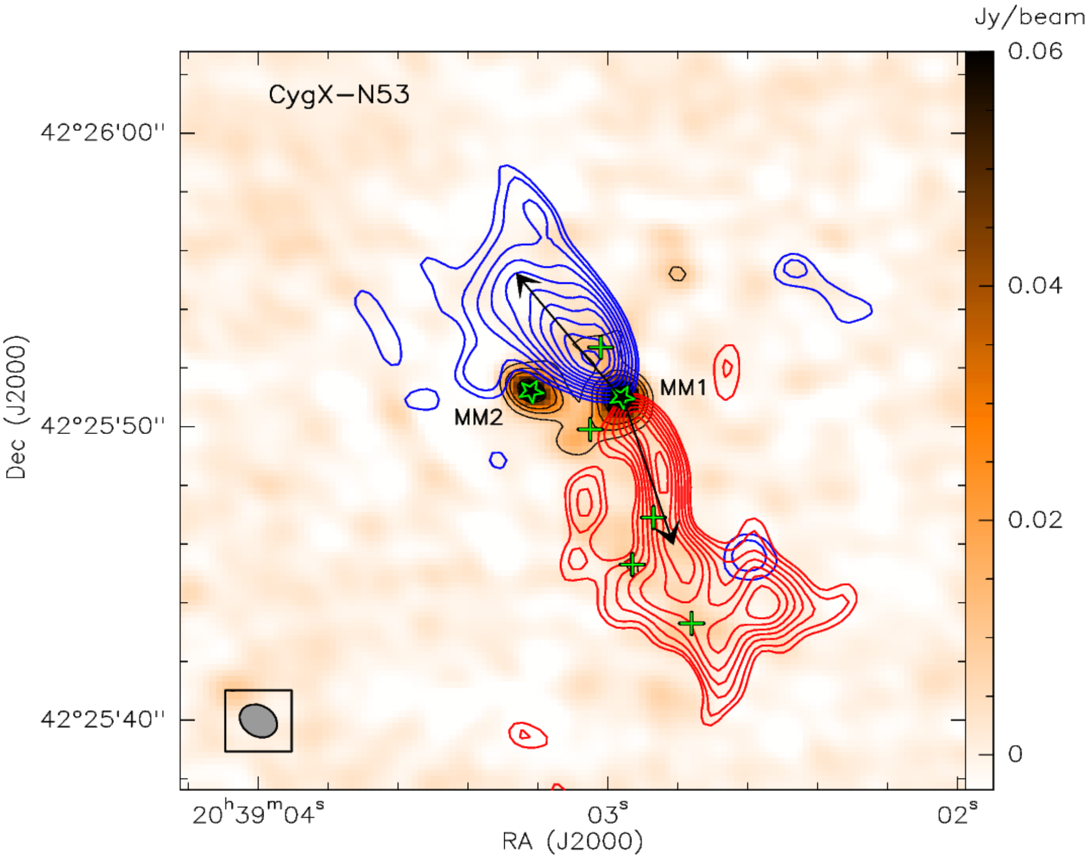

Figure 1.5: The PdBI 1.2 mm dust continuum image of CygX-N53 overlaid with the blue and red contours of the CO emission (adapted from Duarte-Cabral et al. 2013). The green star symbols mark the locations of the massive protostar CygXN53-MM1 and the high-mass prestellar core candidate CygXN53-MM2. The arrows indicate the directions of the CO outflows driven by CygXN53-MM1.

1.4 A brief introduction to submillimeter interferometry

1.4.1 Basics of interferometry

According to the diffraction theory, the angular resolution is proportional to λ/D, where λ is the wavelength; D is the aperture size of a radio telescope. Current ground-based telescopes working at submillimeter wavelengths have sizes of ∼10-30 m (e.g., APEX, JCMT, IRAM). For example, the James Clerk Maxwell Telescope (JCMT), has a diameter of 15 m and a typical angular resolution of 14$''$ at 350 GHz. This enable observations to resolve molecular clouds at 2 kpc down to the scale of 0.14 pc. For more distant sources and/or longer-wavelength observations, the angular resolution starts to decrease. A straightforward solution is to increase the diameter of telescopes. The largest fully steerable radio telescope is the Green Bank Telescope (GBT), which has a diameter of 100 m. To reach a one-arcsecond resolution at centimeter wavelengths, the diameter of a single dish telescope needs to go beyond a few to tens of kilometers, which is not practical with current techniques. The idea of interferometer is to synthesize a large aperture (of e.g., 10 km) with multiple pairs of small antennas which are located separatedly. Synthesizing a larger aperture through the combination of multiple separated pairs of antennas is the so-called Aperture Synthesis technique. The intensity distribution of the source on the sky is the Fourier Transform of the visibility (Van Cittert-Zernicke Theorem, Thompson et al. 2001). If an interferometer consists of N antennas, any two of these N antennas can be combined to form N×(N-1) unique baselines. Each baseline produces one Fourier component. As the number of antennas increases, one can resolve the structure of a source in more details; the observations can achieve a higher sensitivity.

1.4.2 Limitation: short spacing and missing flux problems

The interferometers are, however, limited by the short-spacing problem (Braun & Walterbos 1985). The largest spatial scale that an interferometer can resolve depends on the shortest baseline. Lacking short baselines, an interferometer cannot be sensitive to emission from large angular scales. This problem becomes unignorable when one tries to observe diffuse emission or extended sources. A common solution to this problem is to combine single dish observations with interferometric observations, because single dish telescopes can provide the short spacing information that is missed in interferometric observations. Adding single dish observations can help to recover the integrated flux density and diffuse emission. Figure 1.6 provides a schematic view of the range of spatial scales that single dishes and interferometers are sensitive to.

1.4.3 (Sub)millimeter interferometers: SMA and ALMA

In my thesis work, I mainly exploit (sub)millimeter interferometric data taken with the Submillimeter Array (SMA) and the Atacama Large Millimeter/submillimeter Array (ALMA). The details about the two interferometers are summarized in Table 1.1.

In Chapter 2, the ALMA Band 7 observations (targeting $H_2D^+(1_{1,0}-1_{1,1})$) were taken in multiple observing cycles including Cycle 3 to 5 with multiple configurations including C43-1, C43-2, C40-3, and C36-2/3. The proposed sensitivity of the ALMA observations was based on the requirement of detecting the $H_2D^+(1_{1,0}-1_{1,1})$ emission at the 3σ level at 0.1 km s^{-1} resolution in the most pessimistic plausible case, which gives an rms of 0.3 K. The requested

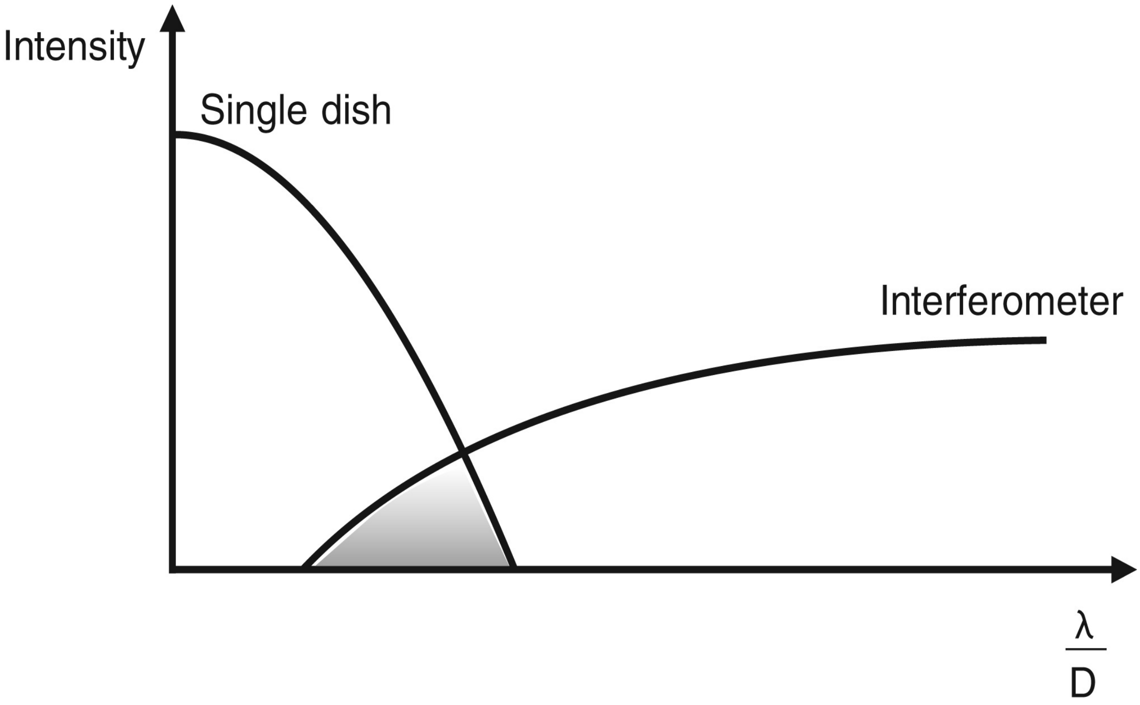

Figure 1.6: A schematic plot showing the spatial scales that a single dish telescope and an interferometer are sensitive to (adapted from Faridani et al. 2018). The shadowed area represents the overlapping region of spatial scales that both a single dish and an interferometer are sensitive to.

angular resolution (0.5″) was chosen to match to the expected size of the H_2D^+-emitting region to achieve sufficient brightness temperature sensitivity while avoiding beam dilution. We requested observations with the 12m antennas only to resolve the compact emission at the core scale. The maximum recoverable scale of this dataset is ∼5″. This means that we do not have information of larger-scale smooth structures due to missing short-spacing data (see section 1.4.2). In Chapter 4, the SMA 1.3 mm data were taken with extended configurations. The choices of configurations are designed to resolve the target with sufficient spatial resolution.

1.5 Thesis plan

In this thesis, I exploit (sub)millimeter interferometric observations towards high-mass star-forming regions in conjunction with synthetic observations to characterise the physical properties and kinematics of the early stages of high-mass star formation, where the parental molecular clouds have not been completely disrupted by the feedback of forming high-mass stars.

The thesis consists of an introduction chapter providing the research background of my PhD work, three science chapters describing my research projects, and a final chapter sum-

Table 1.1: A summary of the key information about the SMA and ALMA.

	SMA	ALMA
Site	Mauna Kea, Hawaii	Chajnantor, Chile
Altitude (m)	4207	5044
Diameter (m)	6	12 (7)
No. of antennas	8	54 (12)
Range of baselines (m)	25 - 508	160 - 16000
Highest angular resolution ($''$)	0.25	0.02
Frequency (GHz)	180 - 418	35 - 950
Bandwidth (GHz)	8	8
Spectral resolution (kHz)	140	3.8 - 15600

marising the main conclusions of this thesis work and future work plans. In Chapter 1, I present an introduction to the theory of (high-mass) star formation and cluster formation, a literature review on the major observational discoveries over the past decades, and a brief introduction to the (sub)millimeter interferometry. Chapter 2 provides a detailed description for the research project about investigating the gas kinematics around the high-mass prestellar core candidate G11.92-0.61 MM2 with ALMA 0.8 mm observations. In Chapter 3, I present my work on exploring the detectability of low-mass cores in massive protoclusters using synthetic observations. In Chapter 4, I describe my project about resolving the high-mass protostellar object G34.24+0.13MM with high-resolution SMA 1.3 mm observations. In Chapter 5, I summarise the main conclusions of my PhD projects and provide a plan of future work.

Chapter 2 and 4 provide provide direct observational evidence to constrain the star formation processes in particular high-mass star-forming regions. Chapter 3 provides theoretical predictions on the observable quantities of massive star-forming clumps. My PhD work investigates the relationship between the formation of Galactic high-mass stars and their environments, to ultimately answer the scientific questions addressed in section 1.1.

2

Gas kinematics around the high-mass prestellar core candidate G11.92-0.61 MM2

*In this project, I started with analysing the reduced ALMA data. As part of the main findings of this project, the discovery of an asymmetric bipolar molecular outflow traced by a low-excitation CH_3OH transition driven by MM2 has been incorporated into a journal paper presenting higher-resolution ALMA 1.3 mm observations towards MM2 (***Cyganowski et al. incl. Zhang, 2022***). Details of this work are described in Section 2.6.1.*

2.1 Background

2.1.1 How do high-mass stars assemble their masses?

One of the most important questions in the study of high-mass star formation is: how do high-mass stars obtain their masses? In particular, from what scale do the high-mass stars assemble their masses? Core accretion models (McKee & Tan 2002, McKee & Tan 2003) assume that the initial conditions of high-mass star formation are massive, gravitationally bound, centrally condensed, starless cores. The so-called high-mass prestellar cores are predicted to have a size of ≤0.1 pc, and are expected to have contained all the materials that are required to form high-mass stars. High-mass prestellar cores are assumed to be in nearly internal virial equilibrium, and in pressure equilibrium with their environment initially (see Tan et al. 2014). They will then experience ordered gravitational collapses to form high-mass stars or small multiple systems. This collapsing process is assumed to be relatively isolated from the environment of these cores. Search for the high-mass prestellar cores in observations has returned few good candidates for the past decade (see section 1.3.4). The high-mass prestellar core candidates known to date are G11P6-SMA1 ($\sim$30 $M_\odot$ within $\sim$0.02 pc, Wang et al. 2014), G11.92-0.61 MM2 ($\sim$30 $M_\odot$ within $\sim$0.005 pc, Cyganowski et al. 2014), W43-MM1 core 6 ($\sim$60 $M_\odot$, Nony et al. 2018, Molet et al. 2019), AG354 ($\sim$39 $M_\odot$, Redaelli et al. 2021), and G028.37+00.07 C2c1a ($\sim$23-31 $M_\odot$, Barnes et al. 2023).

In the contrast, competitive accretion models (Bonnell et al. 2001,Bonnell et al. 2003, Bonnell et al. 2004) connect the formation of high-mass stars with their environment. The authors propose that the protostars that are closer to the centre of protoclusters are more likely to form massive stars, with the advantage of getting fed by the gas materials that infall into the large-scale gravitational potential well. The precursors of massive stars are predicted to accrete gas widely from their large-scale surroundings (Bonnell et al. 2004), without being static massive starless cores. Recent observations reveal that hub-filament systems are probably the parsec-scale gas reservoirs where the high-mass stars are forming by filamentary accretion (e.g., Peretto et al. 2013, Yuan et al. 2018, Zhou et al. 2022, Xu et al. 2023).

2.1.2 G11.92-0.61 MM2: a massive prestellar core candidate

G11.92-0.61-MM2 was initially identified to be candidate of massive prestellar core when studying the GLIMPSE Extended Green Objects (EGOs; Cyganowski et al. 2008). It is located in the EGO G11.92-0.61, a massive protocluster containing three massive cores and 16 low-mass cores (Cyganowski et al. 2017). MM2 is a strong, compact dust continuum source, with an integrated flux density of $\sim$90±1 mJy at a spatial resolution of $\sim 0.5''$ (Cyganowski et al. 2017). However, MM2 is devoid of molecular line emission from hot core and star formation indicators. No line emission was detected toward MM2 across $\sim$24 GHz of bandwidth observed with SMA at 1.3, 1.1, 0.8 mm (Cyganowski et al. 2011b, Cyganowski et al. 2014). Other star

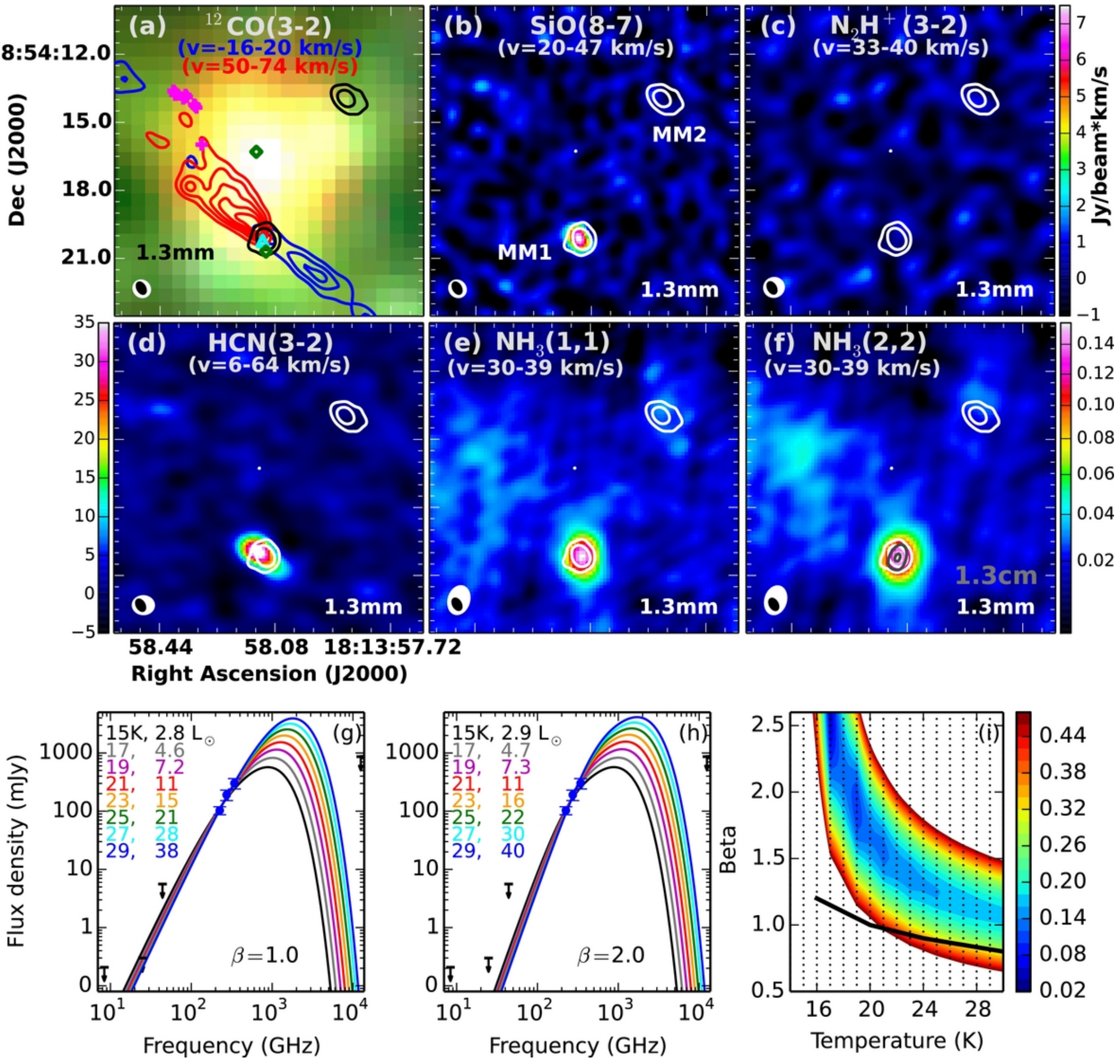

Figure 2.1: SMA 1.3 mm observations of the high-mass prestellar core candidate G11MM2 presented by Cyganowski et al. (2014). Panel (a): Spitzer three-color image (RGB: 8.0, 4.5, 3.6 μm) overlaid with continuum contours (black) and outflow contours (blue and red). The magenta and diamond markers indicate the locations of Class I and II CH_3OH masers. Panel (b) - (f): integrated intensity maps of submillimeter spectral lines (as marked on the top of each panel) overlaid with the SMA 1.3 mm continuum contours (white), with the VLA 1.3 cm continuum contours (grey) in Panel (f) only. Panel (g) and (h) show the observed MM2 SED overplotted with graybody fits. Panel (i) shows the χ^2 surface plot, where the black line indicates the 4σ 1.3 cm limit.

formation indicators including masers, and molecular outflows were also not detected at the position of MM2 (Cyganowski et al. 2009, Cyganowski et al. 2011b, Cyganowski et al. 2014). Figure 2.1 provides a summary of the SMA observations of MM2. A VLA imaging revealed that MM2 is marginally detected in 1.3 cm data and is undetected at 3 cm with a resolution of 0.25$''$ (Hunter et al. 2015). These signatures suggest very extreme physical properties within MM2: M > 30 M$_\odot$ within ∼1000 AU, and $n_{H_2} > 10^9$ cm^{-3}, T_{dust} ∼17-19 K, L ∼5-7 L$_\odot$(Cyganowski et al. 2014). To further explore the possible physical properties consistent with the dearth of molecular emission lines, Cyganowski et al. (2014) employ gas-grain astrochemical models using MONACO (Vasyunin et al. 2009) to model MM2. They find that under the extreme circumstances of $n_{H_2} \gg 10^8$ cm^{-3} and $T_{dust} < 20$ K, one would expect to have non-detection of (sub)millimeter line emission with SMA, due to extreme depletion of gas-species which freeze onto grains. Based on this, we propose to observe MM2 with ALMA targeting $H_2D^+(1_1,0\text{-}1_1,1)$ and N_2H^+(4-3), which are known to trace dense and depleted gas. We aim to test whether MM2's unusual properties were due to extreme physical conditions such as low temperature and high density. Recent high-resolution (∼160 AU) ALMA 1.3 mm observations reveal that MM2 is actually a protobinary system with a projected separation of 505 AU (Cyganowski et al. 2022).

2.2 Observations and data reduction

2.2.1 ALMA 0.82 mm observations

G11.92-0.61 MM2 was observed with the Atacama Large Millimeter/Submillimeter Array (ALMA) in Band 7 at 0.82 mm in cycle 3-5. The observations were performed on Apr 9 2016, Apr 22 and 26 2017, Jul 10 and Aug 16 2018, with configuration of C43-1, C43-2, C40-3, C36-2/3. The tuning was set up to centre at 358.02 GHz, with a bandwidth of 1.875 GHz and a spectral resolution of 0.977 MHz (corresponding to 0.8 km s^{-1}). The primary beam size is 17″. J1924–2914 was observed for bandpass calibration; J1911–2006 and J1733–1304 were observed for gain calibration; J1924–2914 and Titan were observed for absolute flux calibration. The projected baselines range from 14 to 583 kλ, resulting in a largest angular scale (LAS) of 5″.

Calibration and imaging

The 0.82 mm ALMA data was calibrated using the ALMA science pipeline with CASA 5.4.0. The line-free channels were identified following the procedure described in Brogan et al. (2016) and Cyganowski et al. (2017), and were used to construct a pseudo-continuum data set. The bandwidth of the resulting aggregate continuum is ∼0.44 GHz. The continuum data were iteratively self-calibrated, and the solutions were then applied to the line data. Continuum images were made using multi-frequency synthesis (which combines data from multiple closely spaced frequency channels to improve beam structures and signal-to-noise ratios, Conway et al.

1990), two Taylor terms (to account for the spectral index of the emission across the observed bandwidth), multiscale clean (which models the emission from extended objects that show complicated spatial structures using a combination of components of emission with different spatial scales, Cornwell 2008), and Briggs weighting with the robust parameter R = 0.5. The Briggs weighting scheme enables a continuous variation between natural weighting (R = 2), where the visibility measurements are weighted inversely with their variances to achieve better signal-to-noise ratios, and the uniform weighting (R = -2), where the measurements are weighted inversely with the density of the data points on *uv* plane to achieve higher spatial resolution and lower sidelobes (Briggs 1995, Thompson et al. 2017). R = 0.5 was chosen for a best trade-off between the rms noise and the resolution (see Fig. 10.3 in Thompson et al. 2017). The N_2H^+ (4-3) (372.672 GHz, E_{upper} =44.7 K) line and the DCO^+(5-4) (360.170 GHz, E_{upper} =51.9 K) line were imaged with R = 0.5 and a velocity resolution of 0.2 km s^{-1}. The $H_2D^+(1_{1,0}$-$1_{1,1})$ (372.421 GHz) line was imaged with R = 2 (to maximize the possibility to detect extended emission) and a velocity resolution of 0.4 km s^{-1}. The $CH_3OH(4_{-1,3}$-$3_{0,3})$ (358.606 GHz, E_{upper} =44 K) line was imaged with R = 0.5 and a velocity resolution of 1.0 km s^{-1}. All measurements were made from images corrected for the primary beam response.

In the 0.82 mm continuum image, we achieve a synthesised beam size of 0.575″ × 0.431″, equivalent to 1938 AU × 1452 AU at the distance of 3.37 kpc (the maser parallax distance for MM1, Sato et al. 2014); the rms noise level is measured to be 0.5 mJy beam^{-1}. For the N_2H^+ (4-3) cube, the beam size is 0.651″ × 0.442″ and the rms is 5.9 mJy beam^{-1}. For the DCO^+(5-4) cube, the beam size is 0.576″ × 0.433″. For the $CH_3OH(4_{-1,3}$-$3_{0,3})$ cube, the beam size is 0.574″ × 0.432″.

2.3 Results

Figure 2.2 shows a summary of the major results of the ALMA 0.82 mm observations. The panel (a) of Figure 2.2 shows the 0.82 mm continuum in colorscale overlaid with the contours of the integrated N_2H^+ emission. The locations of MM2, the proto-O star MM1, and a few millimeter sources identified in Cyganowski et al. (2017) are marked in white. The morphology of the 0.82 mm continuum is similar to that of the ALMA 1.05 mm continuum presented in Cyganowski et al. (2017). MM2 is located on a filamentary structure with a direction of north-southeast. The submillimeter emission extends from MM2 to its southeast, bridging MM2 and MM1. To the north of MM2, the extended emission connects MM2 with millimeter sources MM7/MM9. To the east of MM2, weak ($\sim 5\sigma$), extended emission connects the north-southwest dust ridge with MM5 and MM3, joining the main filamentary structure to the northeast of MM2. The white contours illustrate a markedly different morphology of the integrated N_2H^+ (4-3) emission, with a clear offset between the N_2H^+ local peaks and the peak of MM2 in the 0.82 mm map. The integrated N_2H^+ emission in the vicinity of MM2 peaks to the northwest and southwest of MM2, with an offset of $0.9''$ and $1.2''$ to the continuum peak respectively. The strongest integrated N_2H^+ emission is detected to the southeast of MM2, and is located on the direction of the molecular outflows driven by MM1 (Cyganowski et al. 2011c).

As shown in the panel (b) of Figure 2.2, H_2D^+ is undetected around MM2 at an rms noise level of 2.7 mJy beam^{-1} ($T_b \sim 0.06$ K) with a resolution of $0.65''$[1]. The H_2D^+ integrated intensity map shows a strong detection towards MM1. However, regarding that MM1 has been revealed to be a hot core associated with abundant molecular emission lines (see Figure 2 in Cyganowski et al. 2014) and host a proto-O star with a Keplerian disk(Ilee et al. 2016, Ilee et al. 2018), the detection in the integrated H_2D^+ map is likely to be the contamination of other lines within the velocity range used for integrating emission. Moreover, known as a dense and depleted gas tracer (< 20 K), $H_2D^+(1_{1,0}\text{-}1_1, 1)$ is unlikely to trace a proto-O star or its gaseous envelope. Therefore, we do not believe that the signals at MM1 shown on the H_2D^+ integrated intensity map are real $H_2D^+(1_{1,0}\text{-}1_1, 1)$ emission. Panel (c) of Figure 2.2 shows the integrated DCO^+(5-4) map overlaid with 0.82 mm continuum contours. Interestingly, the integrated DCO^+(5-4) emission appears to trace cooler structures such as the filamentary structures (e.g. to the south of MM2 and to the east of MM3). No DCO^+(5-4) is detected towards the cores with ongoing intermediate- or high-mass star formation reported (e.g. MM3 and MM1, Cyganowski et al. 2017). In addition, the CH_3OH ($4_{-1,3}\text{-}3_{0,3}$) line imaged using the wide spectral window (spw) of the ALMA 0.82 mm observation reveals an asymmetric bipolar molecular outflow associated with the protobinary system within MM2. This discovery has been published in Cyganowski et al. (2022).

In the ALMA images, extensive N_2H^+ emission is detected around MM2 with a $0.54''$[2] beam (~1800 AU). Panel (d), (e), (f) of Figure 2.2 show the integrated intensity map, peak intensity map, and velocity field map of the N_2H^+ (4-3) transition, respectively. The overlaying white

---

[1] The geometric mean

[2] The geometric mean

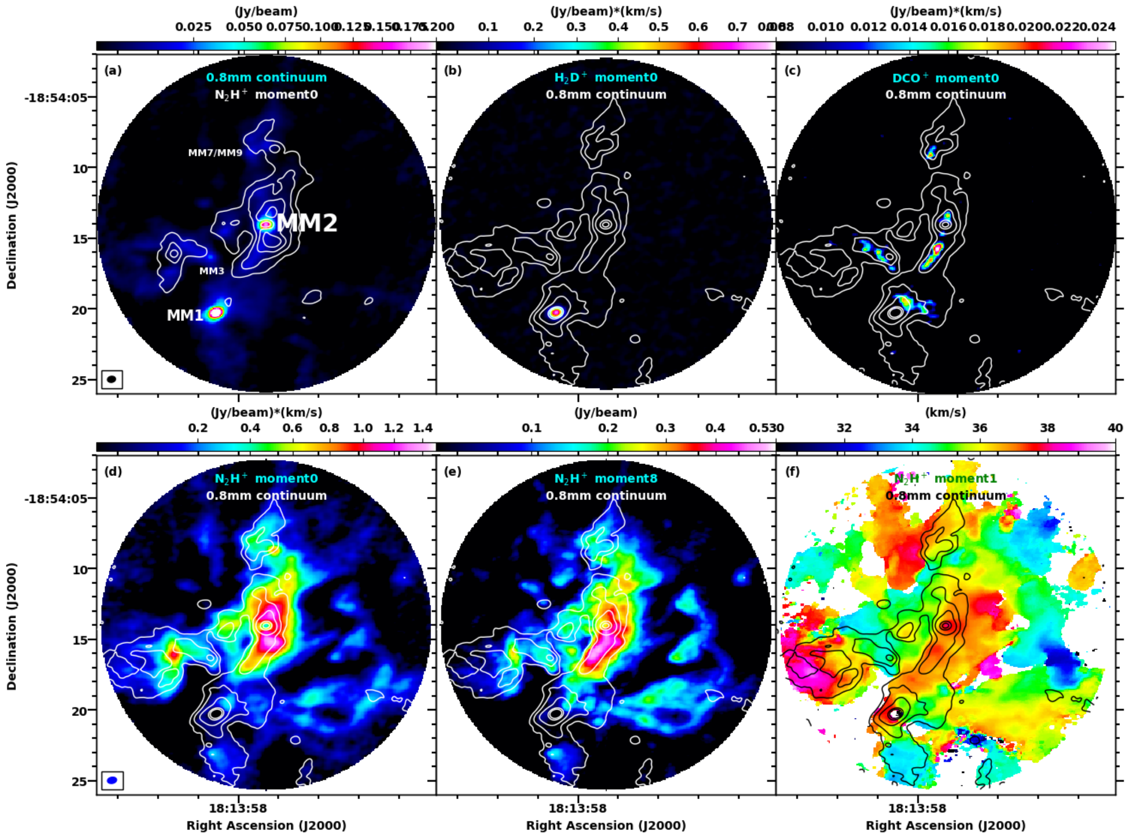

Figure 2.2: A summary of the observed results. Panel (a): the 0.8 mm continuum data in colorscale overlaid with the contours of the integrated N_2H^+(4-3) emission (velocity range: 27.0 - 42.0 km s^{-1}; contour levels: 0.06 × [5,10,15,20] Jy km s^{-1}). Panel (b): the integrated $H_2D^+(1_{1,0}\text{-}1_{1,1})$ emission (velocity range: 29.0 - 41.8 km s^{-1}) in colorscale overlaid with the 0.8 mm continuum contours (contour levels: 0.5 × [5,15,40,160,280] mJy $beam^{-1}$). Panel (c): the integrated DCO^+(5-4) emission (velocity range: 32.6 - 38.4 km s^{-1}) in colorscale overlaid with the 0.8 mm continuum contours. Panel (d): the integrated N_2H^+ emission in colorscale overlaid with continuum contours. Panel (e): the peak intensity map (i.e. moment 8 map) of the N_2H^+ emission in colorscale with continuum contours. Panel (f): the intensity-weighted velocity field map (i.e. moment 1 map) of the N_2H^+ emission in colorscale with continuum contours (velocity range: 27.0 - 42.0 km s^{-1}; cutoff: 4 $\times\sigma^*$, where $\sigma^* = 4.7$ mJy $beam^{-1}$ is measured with the N_2H^+ cube before primary beam correction).

contours represent the 0.82 mm continuum emission. A dip of the integrated N_2H^+ emission towards MM2 is clearly visible in panel (d). The morphology of the distribution of the peak N_2H^+ emission also differs from that of the 0.82 mm continuum, with a 2.3″ offset between the strongest N_2H^+ emission and the continuum peak (see panel (e)). The strongest N_2H^+ emission is detected on the filamentary structure to the south of MM2. The intensity-weighted velocity field map of the N_2H^+ cube is shown on panel (f). It suggests that a simple moment analysis is not sufficient to understand the complex kinematics of the N_2H^+-emitting gas.

Figure 2.3 provides a detailed view of the N_2H^+ emission. The integrated N_2H^+ (4-3)

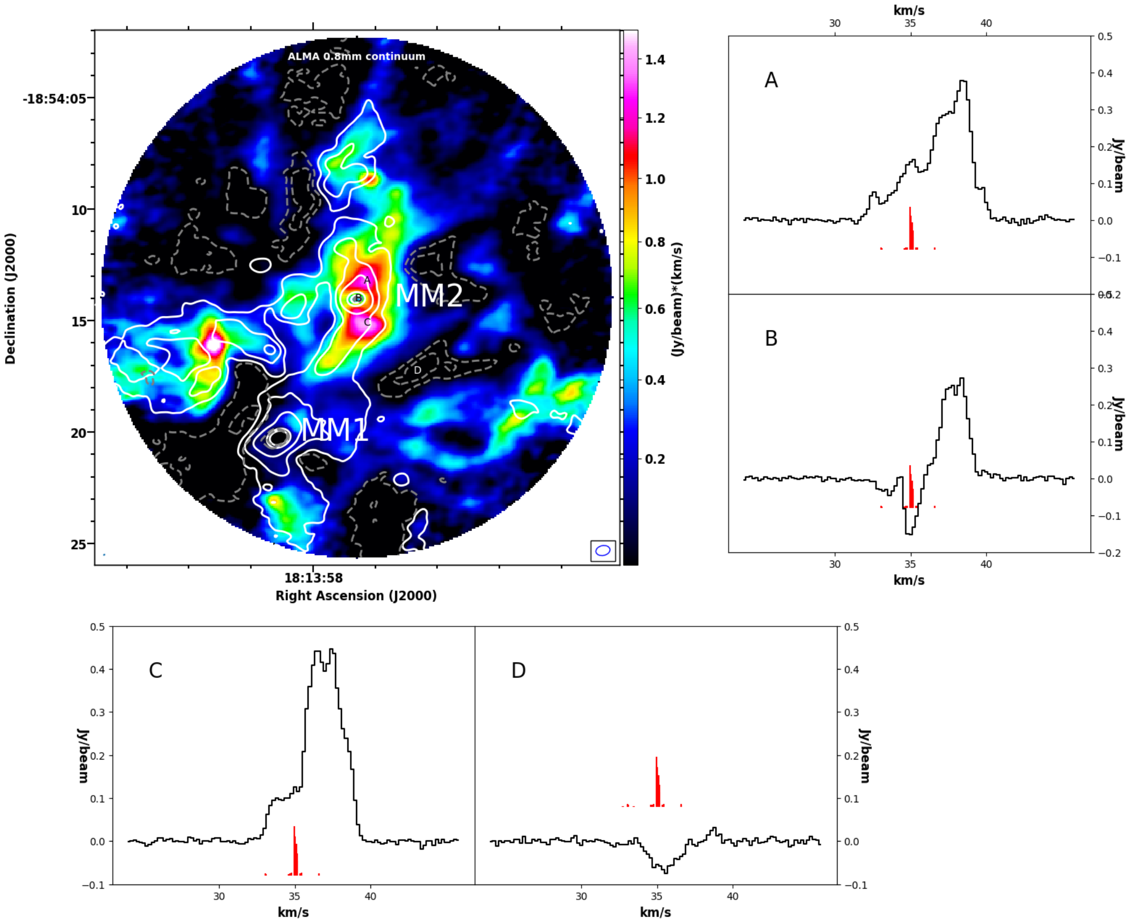

Figure 2.3: Top-left panel: integrated N_2H^+ (4-3) emission overlaid with the 0.82 mm continuum contours (velocity range: 27.0 - 42.0 km s^{-1}; contour levels: 0.06 × [5,10,15,20] Jy km s^{-1}). The right and bottom panels show the N_2H^+ (4-3) spectra extracted at the local peaks of the integrated intensity map to the north (labelled as A) and south (C) of MM2, the continuum peak of MM2 (B) and one of the negative bowls (D). The red vertical lines indicate the relative intensities of the hyperfine structures of this transition. The grey dashed contours show the negative bowls.

map is plotted in colorscale overlaid with the 0.82 mm continuum contours (velocity range: 27.0 - 42.0 km s^{-1}; contour levels: 0.06 × [5,10,15,20] Jy km s^{-1}). The right and bottom panels show the N_2H^+ (4-3) spectra that are extracted at the locations labelled with A, B, C, and D (including the local peaks of integrated N_2H^+, the continuum peak of MM2, and a pixel in one of the negative bowls). The N_2H^+ (4-3) spectra are complex, with multiple emission peaks and/or an absorption feature at the system velocity of 35 km s^{-1}. They also display a significant spatial variation across the map (e.g. vary from the northern N_2H^+ peak, the continuum peak, to the southern N_2H^+ peak). Based on the spectra, it is clear that the aforementioned dip of the integrated N_2H^+ emission towards MM2 is a result of the absorption against the continuum, where cooler gas in front of a hotter continuum source (along the line

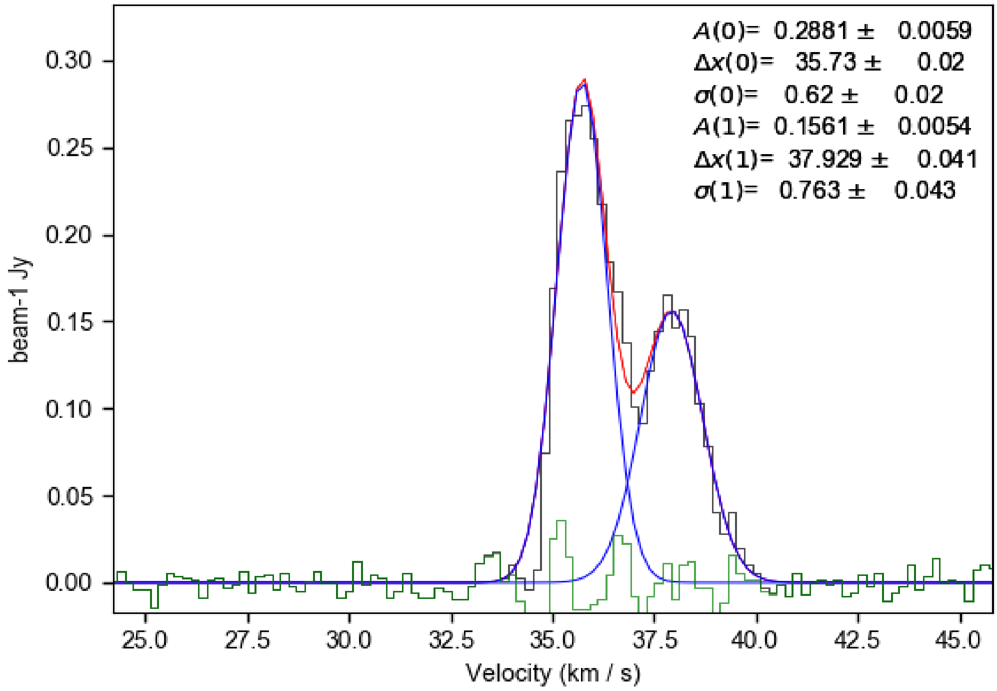

Figure 2.4: An example of performing Gaussian Decomposition to a N_2H^+ (4-3) spectrum with two velocity components. The observed spectrum is plotted in black, with the best-fitting Gaussian models in blue (individual) and red (overall). The best-fitting parameters along wih associated uncertainties are shown on the top right of the figure: peak intensity in Jy beam^{-1} ("A"), centroid velocity in km s^{-1} ("Δx"), and velocity dispersion in km s^{-1} (σ). The numbers in brackets refer to the indices of individual Gaussian models, which increases with ascending centroid velocities.

of sight) create an absorption feature in the continuous spectrum (see Rybicki & Lightman 1979). The N_2H^+ spectrum extracted at location D is an example showing the negative bowls. The red vertical lines on the bottom of the spectra indicate the relative intensities of the 38 hyperfine structures of the N_2H^+ (4-3) transition. It is reasonable to argue that the complexity of the N_2H^+ (4-3) spectra is due to a combination of the hyperfine structures and multiple velocity components within the N_2H^+-emitting gas surrounding MM2.

2.4 N_2H^+ (4-3) kinematics

2.4.1 Gaussian Decomposition using SCOUSEPY

Implement Gaussian Decomposition with SCOUSEPY

To study the gas kinematics in the vicinity of MM2, we first apply Gaussian Decomposition to the N_2H^+ cube to disentangle multiple velocity components along the line of sight using a tool called SCOUSEPY (Henshaw et al. 2016). Fig. 2.4 shows an example of performing Gaussian Decomposition to a N_2H^+ (4-3) spectrum with two velocity components. The observed spectrum is plotted in black, with the best-fitting Gaussian models in blue (individual) and red (overall). The best-fitting parameters along wih associated uncertainties are shown on the top right of the figure: peak intensity in Jy beam^{-1} ("A"), centroid velocity in km s^{-1} ("Δx"), and velocity dispersion in km s^{-1} (σ). SCOUSEPY is a Python implementation of the Semi-Automated multi-COmponent Universal Spectral-line fitting Engine (SCOUSE), designed to apply Gaussian Decomposition to large volumes of complex spectra in a semi-automated way. The SCOUSEPY version used in this work can be downloaded from github [3]. The workload consists of four stages, which are described as follows.

In stage 1), SCOUSEPY generates Spatially Averaged Areas (SAAs) and the spectra of SAAs. A 5σ mask ($\sim$ 54 mJy beam^{-1}) is applied to remove emission-free regions from the analyses that follow. Regarding the strong spatial variation of this dataset, the size of the SAAs is chosen to be 20 pixels with a filling factor of 0.6 [4]. Velocity range and pixel range are set to include the whole data cube. Other parameters are kept at default. By applying the above parameters to the N_2H^+ data cube, 452 SAAs are generated with a total number of 48141 individual spectra to fit.

In stage 2), the program applies Gaussian Decomposition to the spectra generated in stage 1). The SCOUSEPY version used in this work has introduced derivative spectroscopy (Lindner et al. 2015, Riener et al. 2019) to assist with multi-component Gaussian fitting. This technique measures the locations of spectral components by finding functional maxima and minima, producing accurate and consistent initial guesses for parameters (e.g. central velocity) in Gaussian Decomposition. To estimate maxima and minima, a spectrum will be filtered with

---

[3] `https://github.com/jdhenshaw/scousepy/tree/delta`

[4] The filling factor is used to select SAA of which more than 60 % enclosed pixels have significant emission. See details in Henshaw et al. (2016).

Table 2.1: A summary of the three sets of tolerance levels used in stage 3).

Parameter	version 0	version 1	version 2
T_0	2.0	2.0	2.0
T_1	3.0	3.0	3.0
T_2	1.0	1.0	1.0
T_3	2.5	4.0	2.5
T_4	2.5	2.5	1.0
T_5	0.5	0.5	0.5

a Gaussian kernel and the program will calculate derivatives of the smoothed spectra up to the fourth order (see details in Lindner et al. 2015). SCOUSEPY first fits the spectra based on measurements from derivative spectroscopy. The fits are controlled by two input parameters: signal-noise-ratio (SNR) and the size of the Gaussian kernel used for filtering. We vary SNR from 3 to 5 and kernel size from 1 to 3 to obtain satisfying fits for $\gtrsim$ 96% spectra. Only in four cases do we have to increase SNR to 7-9 to obtain reasonable fits. Additionally, we manually fit 2% spectra, for which derivative spectroscopy fitting fails. For example, derivative spectroscopy fits artificially broad red-shifted components in three spectra. We have to fit one or two more weak components to the red tail of these spectra to obtain reasonable fits. There is one spectrum which cannot be fitted well either by derivative spectroscopy and manual fitting. We flag the corresponding SAA at the end of stage (2) to make sure the problematic fit will not be passed on as initial guesses to fit individual spectra. Given the problematic SAA is overlapped with neighbors, SCOUSEPY will fit the spectra of the pixels within the flagged SAA based on the fits of its surrounding SAAs.

Stage 3) uses the fits for the spectra of SAAs as initial guesses to conduct Gaussian Decomposition for individual spectra. SCOUSEPY adopts the fits from stage (2) as initial guesses and applies automated Gaussian Decomposition to the individual spectra within each SAA. To control the process of automated Gaussian Decomposition, users have to set tolerance levels using six parameters: T_0, T_1, T_2, T_3, T_4 and T_5. T_0 is newly introduced to the SCOUSEPY version we are using. It limits the maximum difference between the number of fitted components for spatially averaged spectra and individual spectra. T_1 sets the threshold for amplitude, under which weak components are discarded before following analyses. T_2 and T_3 control the full width at half-maximum (FWHM) of fitted components; T_4 limits the centroid velocity. T_5 sets the minimum separation in centroid velocity between two adjacent Gaussian components. Detailed description about these parameters can be found in Henshaw et al. (2016a).

In the final stage, SCOUSEPY selects the best-fitting models with Akaike information criterion (AIC). As SAAs are Nyquist sampled, individual spectra may hold multiple solutions of Gaussian Decomposition. The program identifies locations with multiple models and chooses the models with the lowest AIC values as the best-fitting ones.

We first run SCOUSEPY with default tolerance levels in stage 3) (results referred as version 0). This version generates reasonable fits for $\sim 80\%$ spectra. However, given the complicated spectral structure and significant spatial variation of this dataset, automated fitting could miss or overfit components at certain regions. For example, in version 0 SCOUSEPY identifies two adjacent peaks as a single velocity component at a few pixels to the north of MM2. Therefore, a single set of tolerance levels may not be ideal for the whole dataset. To test the performance of automated fitting, we run stage 3) with another two sets of tolerance levels labelled as version 1, version 2. In version 1, we allow the velocity dispersion of fitted components to vary by more than 60% compared with version 0; in version 2, we restrict the range of fitted centroid velocity by 60% in contrast with version 0. Other tolerance levels are kept identical (as listed in Table 1). We compile all the results from the three versions and select the models with the lowest AIC values as the best-fitting ones. More than 79% of the final best-fitting models are adopted from version 0; while 8% are taken from version 1 and 3% from version 2. For $\sim 9.7\%$ of the pixels within the mask applied in stage 1), SCOUSEPY could not find best-fitting models which satisfy all the conditions mentioned above. The tolerance levels applied in each version are summarized in Table 2.1. The contribution of each version to the final results are shown on the left panel of Fig. 2.5.

We note that SCOUSEPY cannot handle the absorption structure of the N_2H^+ spectra. The Gaussian Decomposition is applied to the spectral emission only. The following analyses described in this chapter also focus on the emission feature only. To analyse the absorption feature, we invert the N_2H^+ data cube and perform Gaussian Decomposition to the inverted N_2H^+ cube around MM2's continuum peak, treating the inverted absorption feature as an emission feature. This analysis will be further discussed in section 5.2 of Chapter 5 as part of the future work.

Results and basic statistics

We obtain best-fitting models for 43079 spectra, and a total of 96157 Gaussian velocity components. This result in ~ 2.2 components per pixel on average. In fact, more than 66% of the spectra are fitted with models containing multiple velocity components. The right panel of

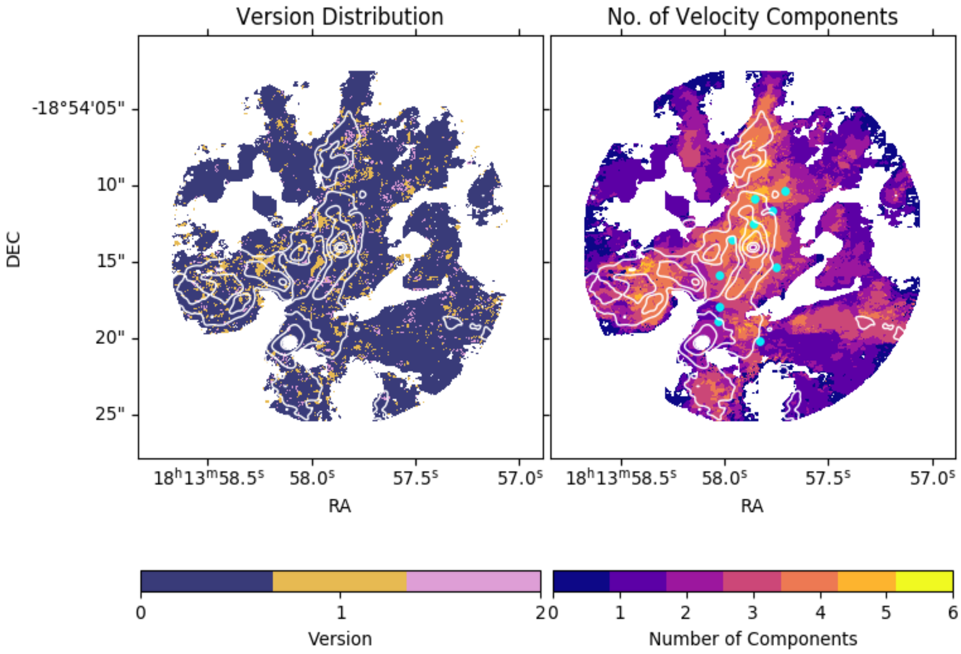

Figure 2.5: Left: the version of the best-fitting models employed in the final compiled solution. Different versions of tolerance levels are coded by color/number: darkblue/0 represents version 0; yellow/1 for version 1; pink/2 for version 2. Overlaid are the continuum contours. Right: the distribution of the number of velocity components of the best-fitting models. The cyan filled circles overlaid indicate the locations of the 10 spectra that are selected for hyperfine structure fitting.

Fig. 2.5 shows the distribution of the number of velocity components at each pixel. Pixels with zero components do not have accepted models (as mentioned in section 4.1). The minimum number of components is 1, while the maximum could go up to 6, with a median value of 2. We note that the complexity of the velocity structure also varies spatially. The vicinity of MM2 is one of the few regions with the most complex spectra. The median value of the number of the components reaches 4 at the places to the north of MM2, and 3 to the south.

Fig. 2.6a shows the histogram of centroid velocities of best-fitting components and the relation of flux density versus velocity. The velocities range from 27 to 42 km s^{-1}, with a mean velocity of 35.7 km s^{-1}, a standard deviation of 1.8 km s^{-1}, and an interquartile range of 2.7 km s^{-1}. The histogram of velocity deviates from Gaussian-like distributions by having at least two groups of peaks at $\sim$ 34.5 and $\sim$ 37 km s^{-1}. This possibly indicates the existence of large-scale velocity gradients across this region. Besides, sharp spikes and shoulders are also clearly visible on the velocity histogram, which reflect complex velocity substructures on small

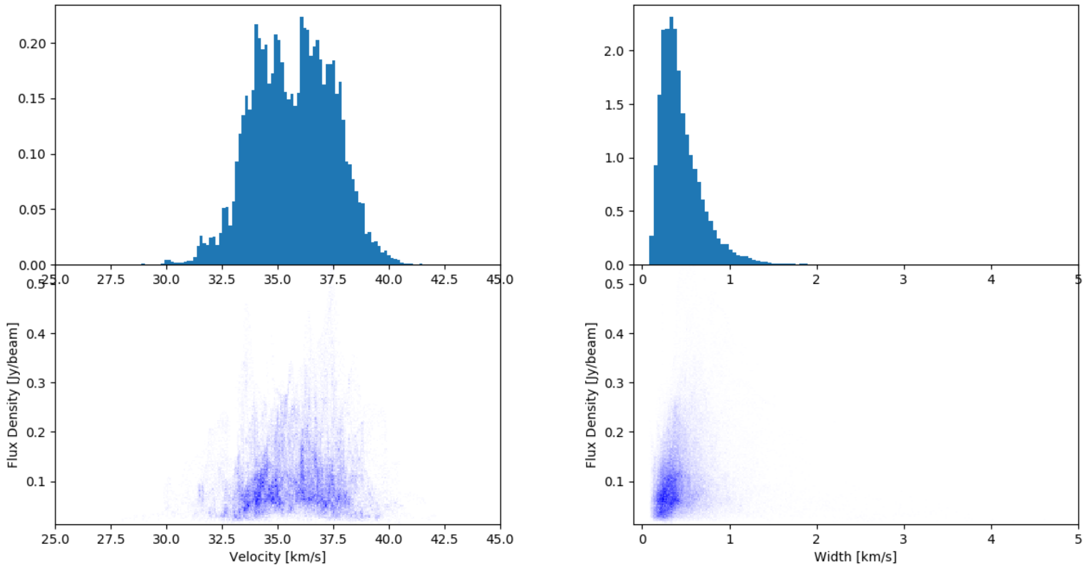

(a) (b)

Figure 2.6: (a) Top panel: the histogram of centroid velocities for the best-fitting components (bin size: 0.25 km s^{-1}). Bottom panel: the amplitude of velocity components versus centroid velocity. (b) Top panel: the histogram of velocity dispersion for the best-fitting components (bin size: 0.06 km s^{-1}). Bottom panel: the amplitude of velocity components versus velocity dispersion.

spatial scales. The bottom panel of Fig. 2.6a plots amplitude against central velocity for all fitted components. The median flux density value is ~ 0.09 Jy beam^{-1}. Most of the strongest components lie between the interquartile range of velocity. The components on the tails of velocity distribution are generally weaker.

Similarly, we plot the histogram of velocity dispersion (σ_v) and amplitude against σ_v for best-fitting velocity components in Fig. 2.6b. The velocity dispersion ranges from 0.08 to 4.6 km s^{-1}, with a median value of 0.39 km s^{-1}, and an interquartile range of 0.28 km s^{-1}. As shown in Fig. 2.6b, the histogram of σ_v is highly asymmetric, with a far-end tail reaching up to 12 times the median value. This asymmetry is also reflected by a positive skewness of ~ 2.6. Therefore we present median and interquartile values here instead of mean and standard deviation values to better describe the concentration and dispersion of velocity dispersion. We note that the $\sigma_v \gtrsim 3$ km s^{-1} are mainly contributed by the blue-shifted broad components that are spacially associated with the molecular outflows driven by protostars MM7/MM9.

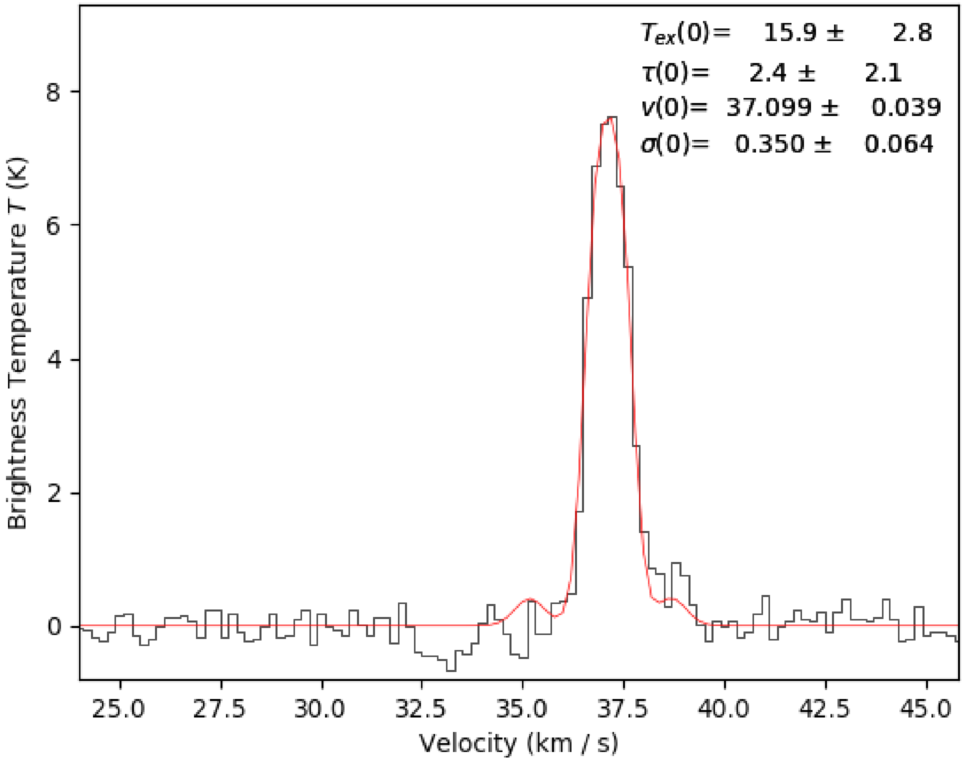

Figure 2.7: A one-component N_2H^+ (4-3) spectrum fitted with a single set of hyperfine structures. The spectrum is plotted in black, with the model in red. The fitted parameters are listed on the top right corner.

We point out that the line profile of the N_2H^+ data cube is shaped by at least three factors: missing short spacings, hyperfine structures (hfs), and multiple velocity components. Hacar et al.[5] demonstrate that missing short spacings can affect the relative intensities of the hyperfine components. This effect has so far been known to be highly non-linear, making it difficult to determine quantitatively. Our statistics on central velocity and velocity dispersion are to some degree biased by the fact that we only employ interferometric data for the analyses. Without short spacing correction applied, we are unable to recover the original line profile. In addition, the N_2H^+ (4-3) transition has 38 hyperfine lines which are spaced over a velocity range of $\gtrsim$ 4.5 km s^{-1}. However, the effects of the hyperfine structures of this transition have not been investigated yet. We conduct Gaussian Decomposition on the N_2H^+ data for the purpose of disentangling multiple velocity components and studying gas kinematics. But pure Gaussian Decomposition could overestimate the line width of velocity components. To investigate how much of the line width is overestimated by Gaussian Decomposition, we apply multi-component hyperfine structure fitting to 10 selected spectra using pyspeckit (Ginsburg & Mirocha 2011). The spectra are extracted from the pixels that are selected based on their number of fitted Gaussian components (see green circles on the right panel of Fig. 2.5). The pyspeckit package applies a uniform excitation temperature (T_{ex}) to all the hyperfine lines in the fitting. A one-component hfs fitting will fit four parameters: the centroid velocity, the velocity dispersion, T_{ex}, and the optical depth τ. An example of the one-component hfs fitting is shown in Figure 2.7. The number of fitted parameters in the multi-component hfs fitting will be four times of the number of components. To better constrain the multi-parameter fitting, we use the best-fitting Gaussian models as the initial guesses for the central velocity and the velocity dispersion. An initial test run returns good fits for spectra with one or two Gaussian component. As the number of components increase, it becomes difficult for the program to constrain T_{ex} and τ. To obtain reasonable fits, we have fixed the the T_{ex} of those unconstrained components to be the median value of the T_{ex} from initial good fits (which is 14 K). Fixing T_{ex} only leads to $\sim$ 0.1 % variation of other parameters, and thus is kept in the multi-component hyperfine structure fitting. Based on the statistics on a limited sample, Gaussian Decomposition can overestimate the line width by 37% on average. The fitted centroid velocity remains relatively consistent regardless of the methods used, with a subtle variation of $\leq$ 0.1%. The comparisons between the Gaussian Decomposition and hyperfine structure fitting are shown in Fig. 2.8.

---

[5] Hacar, A., The need for data combination in the ALMA era, EAS2020 - SS13a: Eight years of ALMA groundbreaking results: A joint venture between the ALMA user community and the ALMA Regional Centres, June 29 - July 3, 2020.

2.4.2 Hierarchical Clustering using ACORNS

Conduct hierarchical clustering with ACORNS

To further analyse the velocity structure within the N_2H^+-emitting gas, we conduct hierarchical clustering of the velocity components extracted in Section 4 using ACORNS[6] (Agglomerative Clustering for Organising Nested Structures, Henshaw et al. 2019). ACORNS is designed to characterise the hierarchical structure within discrete spectroscopic data (e.g. the data points in the position-position-velocity space) based on the hierarchical agglomerative clustering technique. A comprehensive description of the philosophy and parameters of this package can be found in Henshaw et al. (2019) Appendix B.

---

[6] ACORNS is a publicly available Python package, and can be downloaded from `https://github.com/jdhenshaw/acorns`.

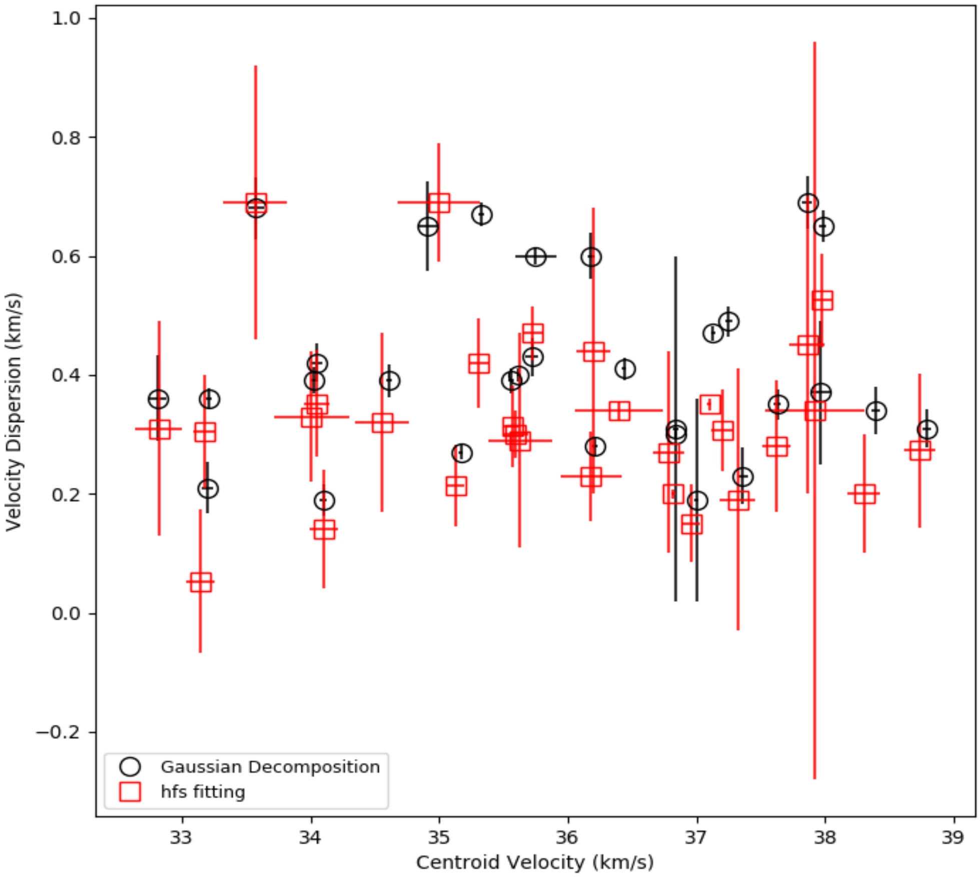

Figure 2.8: The comparison of the fitted parameters from Gaussian Decomposition (plotted with black circles) and hyperfine structure fitting (plotted with red squares). The y axis shows the velocity dispersion; the x axis shows the centroid velocity; the associated error is indicated by the length of the line.

Before running the ACORNS clustering, we perform a cleaning on the velocity components extracted by SCOUSEPY. We discard all pixels without fits (∼ 5% of total SCOUSEPY data), remove the components where the peak intensities are $< 3 \times$ rms (which is measured specifically for each spectrum), and remove the components where either the peak intensities or the velocity dispersion are smaller than their associated uncertainties. We conduct the ACORNS clustering only on the selected velocity components, which represent ∼ 94% of total extracted components.

We first perform the ACORNS clustering of the SCOUSEPY fits in the position-position-velocity space. The minimum radius of a cluster is set to 4 × the pixel size to ensure the minimum number of data points in a cluster is greater than the number of pixels of the synthesized beam (~ 52.3). The minimum height above the merge level is set to be 3 × the mean rms. The absolute velocity difference between two components which are identified as linked cannot be greater than 0.2 km s^{-1} (which is the channel width of the N_2H^+ data). We add an additional clustering criterion based on the linking of velocity dispersion: the absolute difference of velocity dispersion of two components must be smaller than 0.2 km s^{-1} to be considered as linked. These parameters are selected based on the spatial and spectral resolution of the N_2H^+ dataset. With these criteria applied, ACORNS identifies a total of 198 clusters, which contains $\sim$ 95% of the selected velocity components. We also try a few variants of the clustering described above to test our choices of parameters. We first experiment with a higher intensity cut-off during the selection of velocity components, and find that the clustering with a 5σ cut-off would discard a significant amount of data points ($\sim$ 23%), and thus cannot reflect the extended structure of clusters. We then test the clustering criteria for position, velocity, and velocity dispersion with different relaxation levels of linking lengths. We relax the linking criteria by 20% and 50% to enable to clusters to grow. However, the clustering results remain relatively robust against relaxation: the percentage of data points assigned into clusters only grows by $\sim$ 0.3% and $\sim$ 0.8% in the 20% and 50% relaxed versions respectively. This means that the vast majority of pixels have been clustered without the need for relaxing the criteria. Therefore, we decide to proceed with the original clustering with 3σ cut-off and without relaxing the linking criteria.

Results and statistics

Fig. 2.9 shows the hierarchical system (also referred as "forest") identified by the ACORNS PPV clustering. The forest consists of a number of trees; each tree may consist of substructure (which is referred as "branch" if with further substructure, or "leaves" if without). Note that the trees with no substructure will also be categorized as leaves. The ACORNS PPV clustering identifies a total of 70 trees, of which $\sim$23% (16/70) have branches or leaves (i.e. substructure). Among these trees, we select 8 most dominant trees based on the their assigned data points: Tree 0, Tree 17, Tree 1, Tree 4, Tree 9, Tree 7, Tree 30, Tree 57 (descending ranking). The 8 most dominant trees are plotted in rainbow colours in Fig. 2.9. These trees contain $> \sim$ 60% of all the data points used for clustering. In the rest of this chapter, we focus on the most dominant feature of this hierarchical system: Tree 0. Tree 0 contains the largest

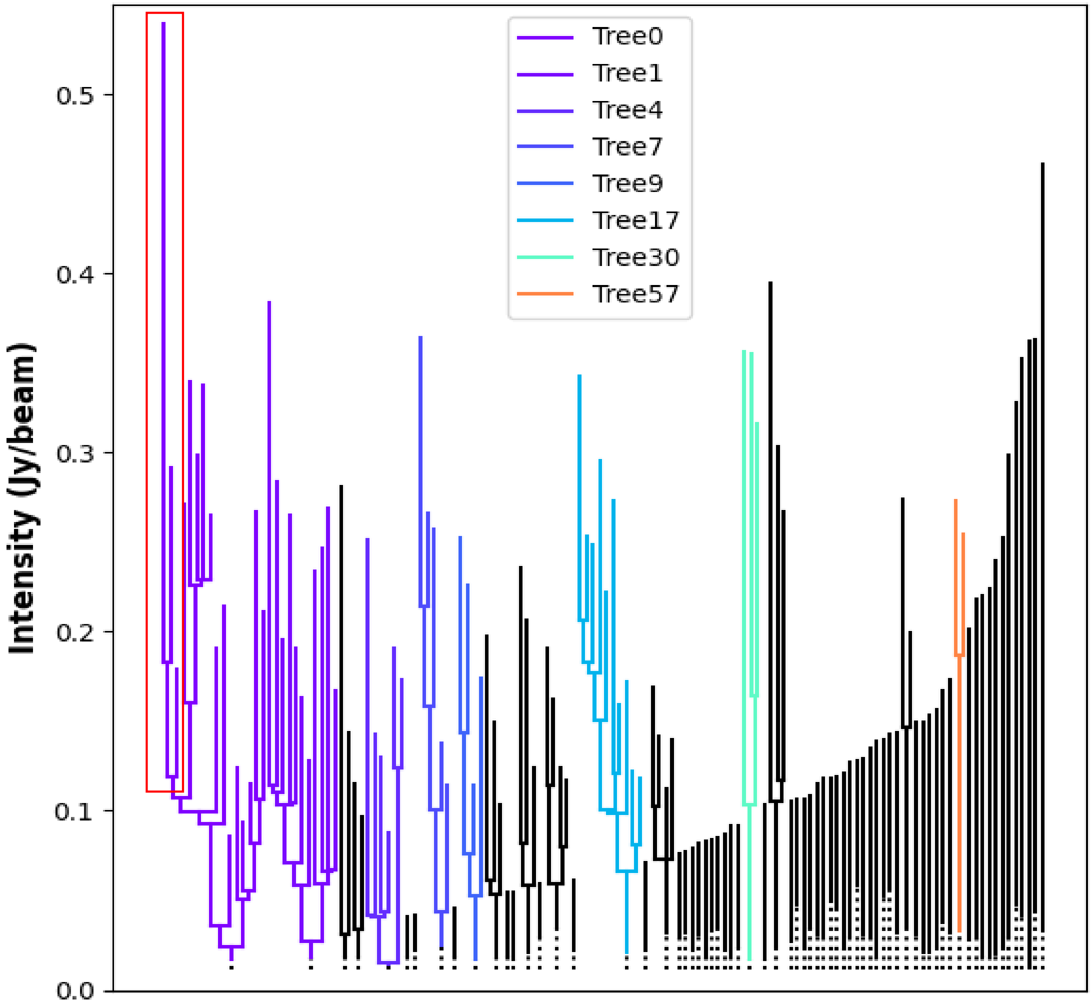

Figure 2.9: The dendrogram showing the structure of the ACORNS forest. The forest consists of 70 trees (i.e. the ACORNS clusters). ∼23% (16/70) of the trees have branches or leaves (i.e. substructure). The substructure is indicated by the short horizontal lines. The highest points of the leaves represent their peak intensities. The eight most dominant trees are plotted in rainbow colours (as labelled). The red rectangle marks Branch 8.

percentage of total velocity components (≃ 20%) and the components with the highest peak intensity. Fig. 2.10 plots Tree 0 in the Position-Position-Velocity (PPV) space, providing a direct view of the velocity structure within the tree. Each velocity component that is clustered into Tree 0 is plotted with a filled circle. The colours indicate the peak intensities of the velocity components. The 0.8 mm continuum emission is plotted in colourscale on the bottom, with a cutoff of $5 \times \sigma_{cont}$ ($\sigma_{cont} = 0.5$ mJy beam^{-1}) applied.

Fig. 2.11 shows the distribution of the peak intensities of the velocity components of Tree 0 (left), the centroid velocity map of Tree 0 (mid), and the velocity dispersion map of Tree

0 (right). The black contours show the 0.8 mm continuum emission (contour levels: 0.5 × [5,15,40,160,280] mJy beam^{-1}). Tree 0 has a peak intensity of 0.54 Jy/beam and a median intensity of 0.12 Jy/beam. The centroid velocities of the components in Tree 0 range from 34.96 km s^{-1} to 38.80 km s^{-1}, with a mean velocity of 36.95 km s^{-1}. The velocity dispersion of Tree 0 has a maximum value of 1.52 km s^{-1} and a median value of 0.45 km s^{-1}. The minimum velocity dispersion is below the channel width of the N_2H^+ data, so is not included here. Tree 0 appears to follow the major features of the moment 8 map (see panel (e) in Figure 2.2), including the main filamentary structure on the direction of north-southeast, and the extended emission from the southern end of the main filament to the west. The intensity peak ($\sim$ 0.54 Jy/beam) of Tree 0 is also located on the filamentary structure to the southeast of MM2 (see the left panel of Figure 2.11). The mid panel of Figure 2.11 shows the centroid velocity map of Tree 0, which indicates a velocity gradient along the main filamentary structure on the direction of roughly south-north. The velocity dispersion map of Tree 0 is plotted on the right panel, where an enhanced velocity dispersion ($\sim$ 50 - 70 %) is visible in the intermediate surroundings of MM2 (within a radius of $3''$). Fig. 2.12 shows the Probability Distribution Function (PDF) of the centroid velocities of the components in Tree 0 (plotted with filled circles). The dashed lines represent the best-fitting Gaussian model to the velocity PDF. The PDF of Tree does not agree with the Gaussian distribution, with excess at $\sim$ 36.3 km s^{-1} and $\sim$ 37.8 km s^{-1}, and moderation in the tails. The kurtosis of the velocity PDF of Tree 0 is estimated to be 2.3. This value being smaller than 3 (the kurtosis of the Gaussian distribution) implies lighter tails, which is consistent with the features of the PDF. Simulations of turbulence suggest a Gaussian-like PDF of the velocities (e.g. Federrath 2013), but observations do not always agree (e.g. Federrath et al. 2016). Federrath et al. (2016) interpret the deviation from Gaussian distribution as the result of systematic motions. Henshaw et al. (2019) argue that the deviation could also be due to the noise in the data and the excitation conditions of the tracer. For the velocity PDF of Tree 0, the double-peak feature can possibly be caused by a large-scale velocity gradient, as seen on the centroid velocity map in Figure 2.11.

2.5 Filamentary accretion flows

2.5.1 Velocity gradient

The centroid velocity map of Tree 0 implies a velocity gradient from south-west to north-east. This gradient goes through MM2 and extends to MM1 to the south of MM2 and MM7/MM9 to

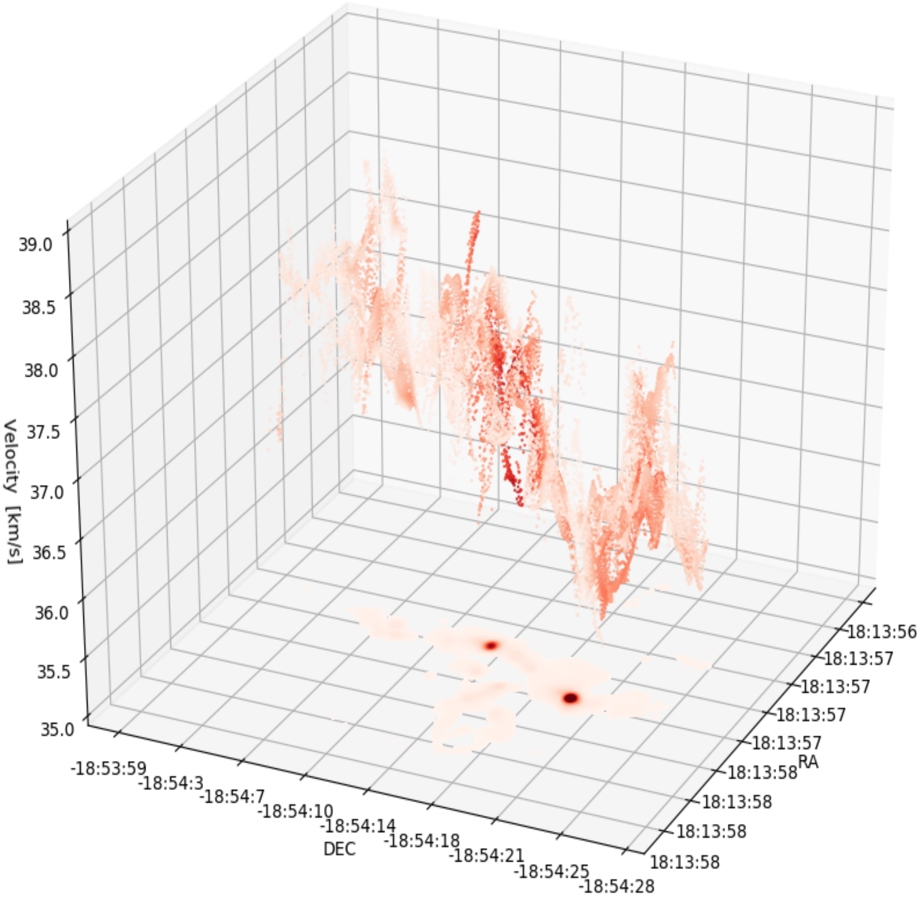

Figure 2.10: Tree 0 in Position-Position-Velocity (PPV) space. Each velocity component that is clustered into Tree 0 is plotted with a filled circle. The colours indicate the peak intensities of the velocity components. The 0.8 mm continuum emission is plotted in colourscale on the bottom, with a cutoff of $5 \times \sigma_{cont}$ ($\sigma_{cont} = 0.5$ mJy beam^{-1}) applied.

the north of MM2. To analyze the gas kinematics in the immediate environment of MM2, we select a branch of Tree 0 of which the morphology is coincident with that of the filamentary structure where MM2 is located in (numbered as Branch 8). This branch is marked with the red rectangle in Fig. 2.9. Fig. 2.13 shows the centroid velocity map of Branch 8, overlaid with the 0.8 mm continuum contours (black; contour levels: 0.5 × [5,15,40,160,280] mJy beam^{-1}), and the 1.3 mm continuum contours (grey; contour levels: 0.06 × [10,50,150] mJy beam^{-1}). We estimate the velocity gradient for Branch 8 using the methods proposed by Goodman et al. (1993). A linear gradient of centroid velocities is described by the equation

$$v = v_0 + a\Delta\alpha + b\Delta\delta, \tag{2.1}$$

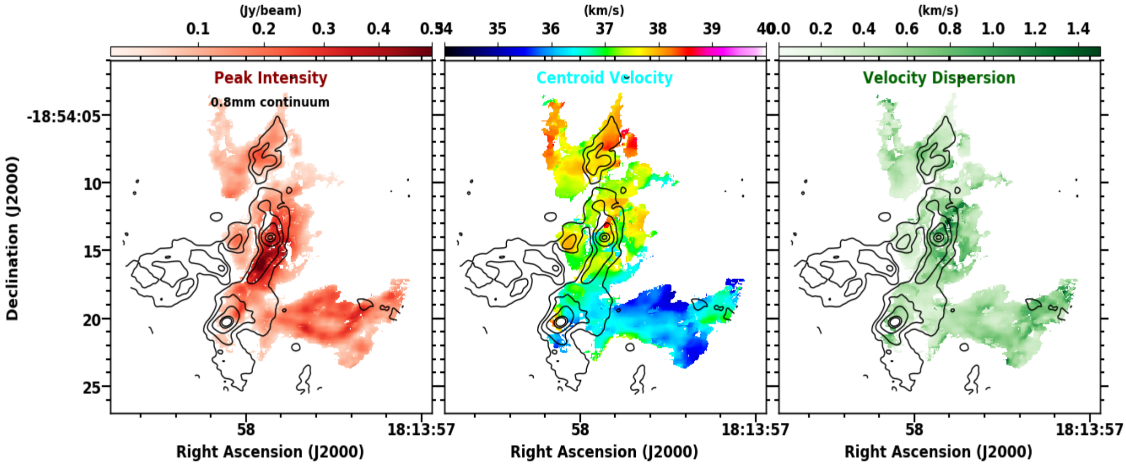

Figure 2.11: Left panel: the distribution of the peak intensities of the velocity components of Tree 0; black contours show the 0.8 mm continuum emission (contour levels: 0.5 × [5,15,40,160,280] mJy beam^{-1}). Mid panel: the centroid velocity map of Tree 0 overlaid with the continuum contours. Right panel: the velocity dispersion map of Tree 0 with the contours.

where $\Delta\alpha$ and $\Delta\delta$ are the variations in right ascension and declination; v_0 is the system velocity. The magnitude of the velocity gradient $|\nabla v|$ is given by

$$|\nabla v| = \frac{\sqrt{a^2+b^2}}{D}, \tag{2.2}$$

where D is the distance. The direction of increasing velocity (east of north) is

$$\Theta = \arctan(\frac{a}{b}). \tag{2.3}$$

We estimate the values of a and b by fitting a first-degree bivariate polynomical to the centroid velocity map of Branch 8 using LMFIT [7]. The uncertainties associated with the centroid velocities from SCOUSEPY are included to constrain the fitting.

The length of Branch 8 is measured to be ~0.17 pc. We estimate the velocity gradient exhibited by Branch 8 to be 10.5±0.2 km s^{-1} pc^{-1} in a direction of ~19° (east of north). The direction of the velocity gradient is shown by the black arrow on Fig. 2.13.

2.5.2 Mass

To determine the physical parameters of MM2, we fit one two-dimensional Gaussian model to the 0.82 mm continuum using CASA task imfit. We use the integrated flux of the fitted

---

[7] Lmfit is a Python package designed for non-linear least-squares minimization and curve-fitting based on scipy.optimize. The package is publically available via https://github.com/lmfit/lmfit-py.

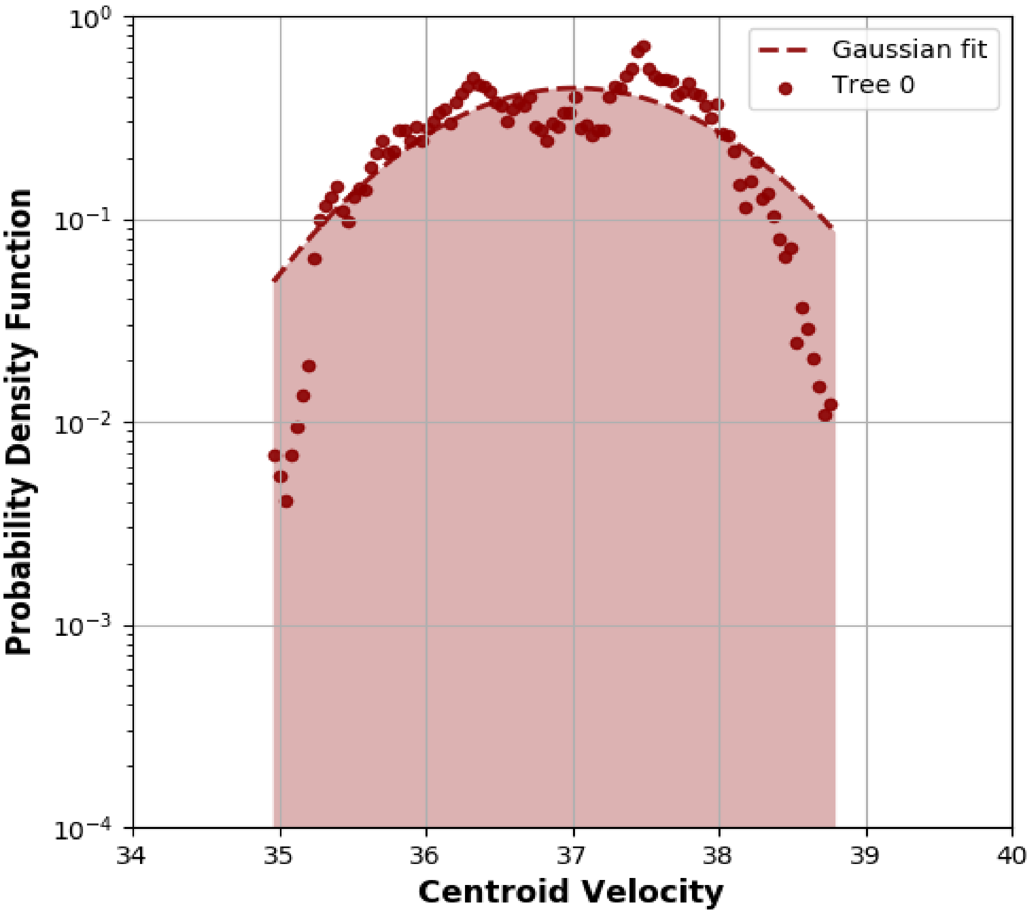

Figure 2.12: The filled circles show the Probability Distribution Function (PDF) of the centroid velocities of the components in Tree 0. The dashed lines represent the best-fitting Gaussian model to the velocity PDF.

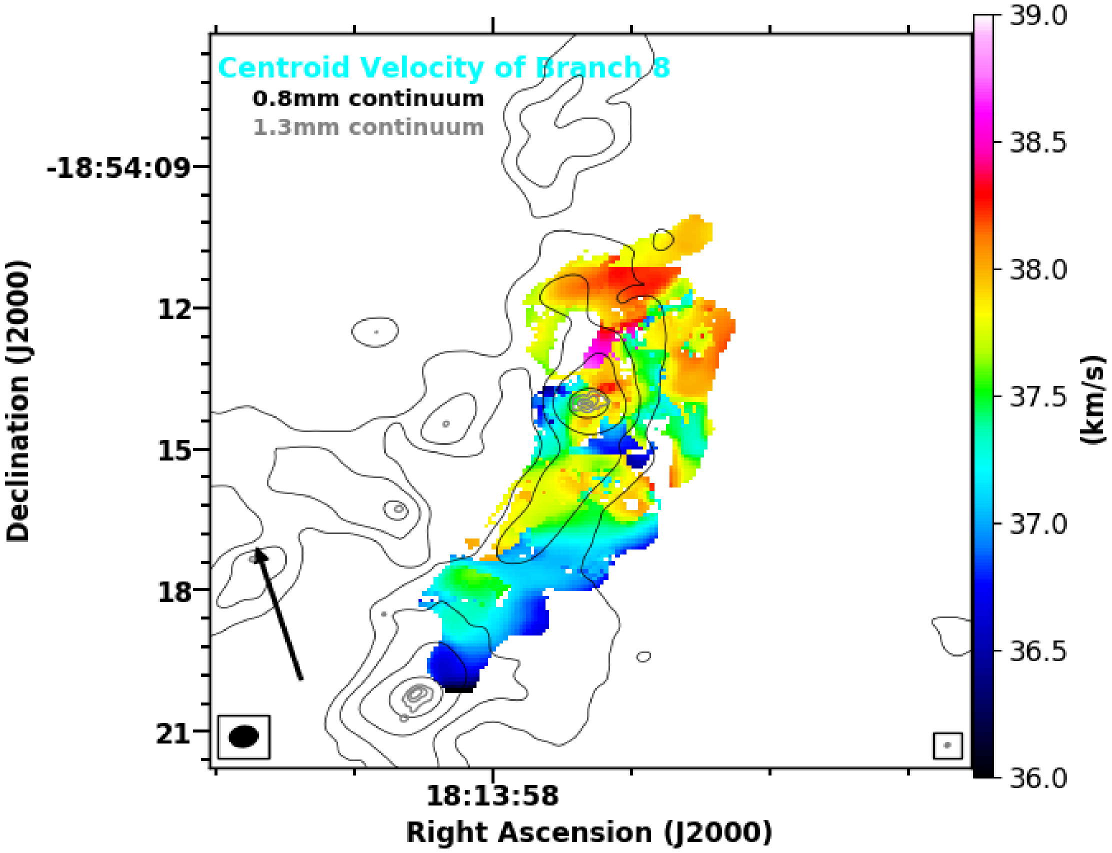

Figure 2.13: The centroid velocity map of Branch 8, overlaid with the 0.8 mm continuum contours (black; contour levels: 0.5 × [5,15,40,160,280] mJy beam^{-1}), and the 1.3 mm continuum contours (grey; contour levels: 0.06 × [10,50,150] mJy beam^{-1}). The synthesised beams of the 0.8 mm and 1.3 mm data are illustrated in the bottom left and right corners, respectively.

component to estimate the gas mass $M_{\rm gas}$ for this source, assuming an isothermal dust emission (as the FIR-submm SED of dust is usually described by an isothermal grey-body model) and including a correction for dust opacity. The equation we use is as below:

$$M_{\rm gas}({\rm M}_\odot) = \frac{4.79 \times 10^{-14} R S_\nu({\rm Jy}) D^2({\rm kpc}) C_{\tau_{\rm dust}}}{B(\nu, T_{\rm dust})\kappa_\nu}. \tag{2.4}$$

In this equation, R is the gas-to-dust mass ratio which is assumed to be 100; S_ν is the integrated flux of the source; D is the distance to MM2; $C_{\tau_{\rm dust}}$ is the correction factor of dust opacity defined by $C_{\tau_{\rm dust}} = \tau_{\rm dust}/(1-\exp(-\tau_{\rm dust}))$, where the dust opacity $\tau_{\rm dust}$ is estimated by $\tau_{\rm dust} = -\ln(1 - \frac{T_b}{T_{\rm dust}})$; κ_ν is set to be 2.3 cm^2 g^{-1}, a value linearly interpolated for 0.82 mm using the values listed in column 7 of table 1 of Ossenkopf & Henning (1994), which are calculated assuming dust grains are MRNs with thick ice mantles in a region where $n_{\rm H_2} = 10^6$ cm^{-3}. The brightness temperature T_b of MM2 is calculated using $T_b = \frac{\lambda^2}{2k\Omega}S$, where k is the Boltzmann constant, λ the wavelength, Ω the solid angle, and S the integrated flux of MM2. The dust temperature $T_{\rm dust}$ is assumed to range from 15 to 25 K. The mass of MM2 is estimated to be 16.8-47.2 M$_\odot$ with opacity correction, and 13.2-28.7 M$_\odot$without. Having obtained the gas masses, we calculate the molecular hydrogen density $n_{\rm H_2}$ and the column density $N_{\rm H_2}$ assuming a spherical geometry with a mean molecular weight per hydrogen molecule $\mu_{\rm H_2} = 2.8$ (Kauffmann et al. 2008). The $n_{\rm H_2}$ is estimated to be 10^8 - 10^9 cm^{-3}, with $N_{\rm H_2}$ 10^{24} - 10^{25} cm^{-2}.

We also estimate the mass of Branch 8 using equation (4). The integrated flux of the branch is measured using CASA task imstat. We measure the mean brightness temperature (0.35 K) of Branch 8 on the brightness temperature map converted from the intensity map, and adopt this value in the mass calculation. The dust temperature $T_{\rm dust}$ is also assumed to be 15-25 K for consistency. The mass of Branch 8 is estimated to be 29.8-65.4 M$_\odot$ with opacity correction, and 29.6-64.6 M$_\odot$ without. We note that these estimates should be taken as an upper limit, as Branch 8 is (partly) overlapping with other trees (e.g., Tree 9) along the line of sight, and thus is not the only contributor to the total gas mass estimated using the dust emission. However, the overlapping area between e.g., Branch 8 and Tree 9 is relatively small, and more importantly, the peak intensity of Branch 8 is more than two times higher than that of Tree 9. Though it is difficult to quantitatively determine the fraction of the total cloud mass in Branch 8 without radiative transfer modelling, it is reasonable to argue that the uncertainty of the branch mass is less dominant than that of the dust temperature.

As considering opacity correction will introduce extra uncertainties, we determine to proceed with the uncorrected masses assuming the dust emission is optically-thin at 0.82 mm. We note that the uncorrected masses should be taken as the lower limits.

2.5.3 Mass inflow rate

Velocity gradients along filaments are commonly interpreted as filamentary accretion flows (see Kirk et al. 2013). The observed velocity gradient in Tree 0 is probably caused by accelerating accretion flows towards MM2, if the filamentary structure is oriented with its southeast end further and the northwest closer to the observer. Rotation could also produce a velocity gradient similar to the observed one. Assuming the velocity gradient is caused by a Keplerian rotation, we derive the kinematic mass required to drive this rotation to be ∼72.5 $M_\odot$. This value is ∼2-3 factors higher than the upper limits of the mass estimates of MM2 using dust emission (see section 2.5.2). This suggest that MM2 is unlikely to be massive enough to drive a Keplerian rotation which can produce the observed velocity gradient pattern.

Based on the hypothesis of filamentary accretion flows, we can derive a mass inflow rate using the velocity gradient and branch mass following the procedure in Kirk et al. (2013). Assuming a simple cylindrical model with a length of L, a mass of M, and a projection angle to the plane of the sky of α, we can calculate the rate of the mass channelled towards MM2 $\dot{M}$ using the equation:

$$\dot{M} = \frac{|\nabla v| M}{\tan(\alpha)}. \tag{2.5}$$

The $\tan(\alpha)$ is a result of the projection effects of the true filament length and the true motions of velocities along the filament (see Kirk et al. 2013 for details of derivation). The Branch 8 is estimated to have a length of ∼0.17 pc. Taking the branch mass without opacity correction and assuming the inclination angle α to be $30^\circ - 60^\circ$, we derive a mass inflow rate of $0.2 \times 10^{-3} - 1.2 \times 10^{-3}$ $M_\odot$ yr^{-1}.

This mass inflow rate spans over almost an order of magnitude due to the uncertainties in the dust temperature and the inclination angle. We note that this range of mass inflow rates should still be taken as the lower limits for the masses are calculated assuming optically thin dust emission. Our $\dot{M}$ is $\geq$ one order of magnitude higher than the values reported in the few very first studies of filamentary accretion flows (e.g. Kirk et al. 2013, Henshaw et al.

2014, Peretto et al. 2014). In fact, our estimated velocity gradient ($\sim$ 10.5 km s^{-1} pc^{-1}) is already about one order of magnitude higher ($\sim$ 1 - 2 km s^{-1} pc^{-1}). Our mass inflow rates are also higher than the typical accretion rates of the NH_3 filaments in Lu et al. (2018) by a few factors. Yuan et al. (2018) discover that the most massive and densest clump located in the junction of the hub-filament system G22 is globally collapsing. They derive the mass infall rate as a result of clump-scale collapsing to be 7.2×10^{-4} M$_\odot$ yr^{-1}. Liu et al. (2016) estimate a similar mass infall rate of 9.6×10^{-4} M$_\odot$ yr^{-1} for the globally collapsing clump AFGL 5142. Though these values are covered in the range of the mass inflow rates that we derive for the filamentary accretion flows towards MM2, it is likely that similar $\dot{M}$ values are driven by different mechanisms. Liu et al. (2016) further discover a network of filaments traced by the NH_3 (1,1) emission, and estimate a typical velocity gradient of 10 km s^{-1} pc^{-1} for their filaments. The authors adopt the clump mass as a lower limit of the total mass of filaments, and derive a mass accretion rate of $\sim 2.1 \times 10^{-3}$ M$_\odot$ yr^{-1}. This value is $\sim$ 50% higher than ours, but is not surprising regarding the different methods used to estimate the masses of filaments.

2.6 Discussions

2.6.1 Filamentary accretion flows feeding the protobinary system

Combining Gaussian Decomposition and hierarchical analysis, we discover that a hierarchy of the N_2H^+ (4-3) emission probably traces filamentary accretion flows towards MM2. The filamentary accretion flows are funnelling gas onto MM2 at an estimated rate of $0.2\times10^{-3}-1.2\times10^{-3}$ M$_\odot$ yr^{-1}. Recent high angular resolution ALMA 1.3 mm data resolves MM2 into a protobinary system with a separation of 505 AU (Cyganowski et al. 2022). The authors estimate the current stellar masses of the binary members to be 1M$_\odot$ for each using the ^{13}CO (2-1) line detected in absorption. The CH_3OH line covered by the tuning of our 0.82 mm ALMA observations reveal an asymmetric bipolar molecular outflow associated with the protobinary system, indicating that the binary system is currently accreting gas from its surroundings. Located on the filamentary structure, the accreting protobinary probably benefit from the filamentary accretion flows traced by N_2H^+. Assuming the ongoing accretion is fed by the gas materials that are carried by the filamentary accretion flows, we can estimate the time for the binary members to double their masses to be $[0.3,\ 2]\times10^4$ yr, with an efficiency factor of transporting the gas carried by the filamentary inflows onto the stars of 50%. Similarly, the time for each member to reach 10 $M_\odot$ is estimated to be [3, 18]$\times 10^4$ yr. This timescale is consistent with the timescale of the 70 micron weak phase (5×10^4) which is derived with chemical clocks from Sabatini et al. (2021).

2.6.2 Non-detection of $H_2D^+(1_{1,0}$-$1_{1,1})$

In the ALMA 0.82 mm images, H_2D^+ ($1_{1,0}$-$1_{1,1}$) is undetected towards or around MM2 at an rms noise level of 2.7 mJy beam^{-1} with a resolution of 0.65″, which is equivalent to $T_b \sim 0.06$ K. The high sensitivity of the H_2D^+ map suggests that potential H_2D^+ signals below the ALMA detection limit are highly impossible. As discussed in section 2.3, the detection towards MM1 in the H_2D^+ integrated intensity map is likely to be the contamination of other lines within the velocity range ([29.0, 42.0] km s^{-1}) used to integrating emission.

As a dense and depleted gas tracer, $H_2D^+(1_{1,0}$-$1_1, 1)$ is found to be sensitive to temperature. When the gas temperature goes above 20 K, the frozen CO molecules start to evaporate into gas phase and react with H_2D^+, resulting in the decrease of the abundance of H_2D^+; if the temperature reaches > 30 K, the deuteration level will decrease (Redaelli et al. 2021). Cyganowski et al. (2022) employ the high-resolution (160 AU) ALMA data to derive the 1.3 mm brightness temperatures of 68.4/64.6 K for the binary members MM2E/MM2W, respectively. This suggests that these two sources are internally heated. The H_2D^+ ($1_{1,0}$-$1_1, 1$) line does not preferably trace sources with such temperatures, which is consistent with the non-detection towards MM2.

The non-detection of H_2D^+ at larger scales is likely to be the result of the spatial filtering of the interferometric observations. The Largest Angular Scale (LAS) of the ALMA 0.82 mm observations is 5″. Smooth structures with spatial scales larger than 5″ have been filtered out in our observations. Compared with the N_2H^+ (4-3) (with a critical density of $\sim 10^6$ cm^{-3}), $H_2D^+(1_{1,0}$-$1_1, 1)$ has a relatively lower critical density ($\sim 10^5$ cm^{-3}), which means the distribution of the H_2D^+ emission is expected to be more extended. Redaelli et al. (2021) report the first (and the only so far) interferometric (ALMA) detection of the $H_2D^+(1_{1,0}$-$1_1, 1)$ line in high-mass star-forming regions, with an LAS of 20″ and an rms of 0.3 K. They reveal extended large-scale structures as well as point sources traced by the H_2D^+ emission, with a massive H_2D^+ core being the candidate of high-mass prestellar core. In the future, single dish or ACA+TP observations may assist to detect the H_2D^+ ($1_{1,0}$-$1_1, 1$) in MM2's environment.

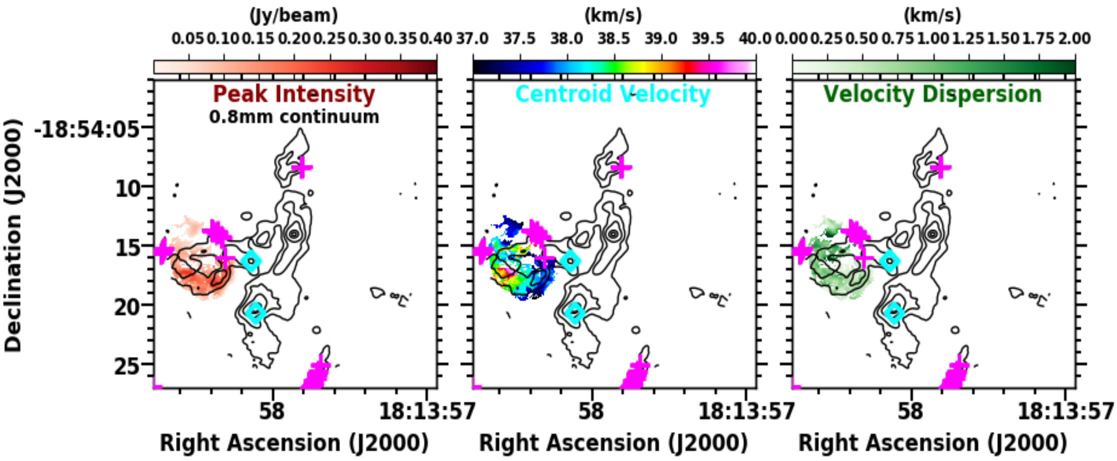

Figure 2.14: Left panel: the distribution of the peak intensities of the velocity components of Tree 7; black contours show the 0.8 mm continuum emission (contour levels: 0.5 × [5,15,40,160,280] mJy beam^{-1}). Mid panel: the centroid velocity map of Tree 7 overlaid with the continuum contours. Right panel: the velocity dispersion map of Tree 7 with the contours. The magenta crosses mark the locations of the class II 6.7 GHz methanol masers; the cyan diamonds mark the locations of the class I 44 GHz methanol masers (Cyganowski et al. 2009).

2.6.3 Impact of protostellar feedback traced by N_2H^+ (4-3)

Fig. 2.14 shows the distribution of the peak intensities of the velocity components of Tree 7 (left), the centroid velocity map of Tree 7 (mid), and the velocity dispersion map of Tree 7 (right). The black contours show the 0.8 mm continuum emission (contour levels: 0.5 × [5,15,40,160,280] mJy beam^{-1}). Tree 7 has a peak intensity of 0.36 Jy/beam and a median intensity of 0.11 Jy/beam. The centroid velocities of the components in Tree 7 range from 36.34 km s^{-1} to 39.94 km s^{-1}, with a mean velocity of 38.15 km s^{-1}. The velocity dispersion of Tree 7 has a maximum value of 2.40 km s^{-1} and a median value of 0.68 km s^{-1}. The minimum velocity dispersion is below the channel width of the N_2H^+ data. Located at the end of the secondary filamentary structure, Tree 7 appears to be a bubble-like structure which agrees well with the continuum emission. This bubble is located on the direction of the bipolar outflows driven by MM1 (see panel (a) in Figure 2.1) A group of class II 6.7 GHz methanol masers are detected at the edge of tree 7. The velocity dispersion map shows an enhancement towards the centre of Tree 7; the centroid velocities decrease from the centre to the edge. Based on these features, Tree 7 possibly trace the dense gas layers blown by the protostellar outflows driven by MM1, which can lead to the enhancement of velocity dispersion (i.e. elevated turbulence). In these cases, the N_2H^+ (4-3) emission can be employed to study the impact of the protostellar feedback on the ambient environment of massive protostars.

2.7 Conclusions

We present deep ALMA 0.82 mm observations towards the high-mass prestellar core candidate G11.92-0.61 MM2. Our ALMA observations, targeting $H_2D^+(1_1,0\text{-}1_1,1)$ and N_2H^+(4-3), were designed to trace dense and depleted gas to study MM2's properties. We detect extensive N_2H^+ emission around MM2 with a $0.54''$ beam ($\sim$1800 AU), while H_2D^+ is undetected at an rms noise level of 2.7 mJy beam^{-1} ($T_b \sim 0.06$ K) with a resolution of $0.65''$. The morphology of the N_2H^+ emission differs markedly from that of the 0.82 mm continuum, with a clear offset between the peak of the integrated N_2H^+ emission and the continuum peak. The N_2H^+ spectra are complex, with multiple velocity components present within the cloud. To analyze the kinematics of the gas surrounding MM2, we apply Gaussian decomposition to the N_2H^+ spectrum at each pixel using SCOUSEPY and then conduct hierarchical clustering of the extracted velocity components using ACORNS. We find that eight velocity- and position-coherent clusters in the N_2H^+-emitting gas describe $> 60\%$ of the fitted velocity components. The most dominant cluster ($> 20\%$ components) indicates a velocity gradient along the filamentary structure traced by the continuum in the south-west to north-east direction. The observed velocity gradient is ~ 10.5 km s^{-1} pc^{-1}, indicating filamentary accretion flows towards MM2. Based on the hypothesis of filamentary accretion flows, we derive a mass inflow rate of $2 \times 10^{-4} \sim 1.2 \times 10^{-3}$ M$_\odot$ yr^{-1}. The gas inflows are probably feeding the ongoing accretion onto MM2 and ultimately to the embedded protobinary system.

3

A parametric study of the observability of low-mass cores in massive protoclusters

3.1 Background

3.1.1 Isolated high-mass star formation

The vast majority (70-90%) of stars are observed to form in clustered environments (Lada & Lada 2003). In particular, ~70% of Galactic O-type stars are found to be members of stellar clusters or OB associations, while the remaining 30% are isolated high-mass stars in the Galactic field (Gies 1987, Mason et al. 1998). The mechanism of high-mass star formation has not been fully understood yet (see Chapter one). The competitive accretion models (Bonnell et al. 2003, Bonnell et al. 2004) propose that high-mass stars ($M_{zams} > 8\ M_{\odot}$) tend to form in the centre of stellar clusters. Fed by the gases falling into the central gravitational potentials of protoclusters, protostars close to the centre are able to grow in mass within shorter timescales (i.e. to accrete at higher rates) to form high-mass stars. By contrast, protostars that are initially located at the outskirts would be less likely to benefit from global gas infall, and are thus more likely to form low-mass stars. In this scenario, high-mass stars are born in the centre of stellar clusters, with low-mass stars forming in their vicinity. This claim is consolidated by both numerical simulations and observations for high-mass protoclusters (e.g. Motte et al. 2007, Smith et al. 2009, Cyganowski et al. 2017, Pillai et al. 2019, Avison et al. 2021). However, the origin of field OB stars cannot be explained using this clustered formation theory alone. Radiation-magnetohydrodynamic simulations (Commerçon et al. 2011, Myers et al. 2013, Rosen & Krumholz 2020) demonstrate that the combined effects of magnetic fields and radiative transfer can effectively suppress the initial fragmentation of massive dense cores. Through this mechanism, highly magnetized massive dense cores remain stable against fragmentation, so are able to form individual high-mass stars via gravitational collapse; while marginally magnetized ones form OB associations or small clusters. In this framework, large-scale gravitational potential is not necessary for high-mass star formation, which means that the formation of high-mass stars is not deeply involved in cluster formation. High-mass stars could form in isolation.

To investigate how field OB stars form, kinematics studies are conducted on selected samples of field OB stars using e.g. spectroscopic data (Rauw et al. 2012, Lamb et al. 2016) and proper motions measured with Gaia (Lennon et al. 2018). Most field OB stars are revealed to be runaways with high velocities (> 30 km s^{-1}, Gies & Bolton 1986), which probably arise from dynamical ejection from young clusters (de Wit et al. 2005, Gvaramadze et al. 2012, Rauw et al. 2012, Bressert et al. 2012, Lamb et al. 2016, Lennon et al. 2018). In the simulations performed by Lucas et al. (2018), OB stars can initially form in clusters and then disperse into the fields as their parent clusters are tidally disrupted in mergers with higher mass clusters. Additionally, higher- resolution and sensitivity observations can revolutionize previous identification of field OB stars. For example, Oey et al. (2013) show that 9 out of 14 selected OB field stars in the Small Magellanic Cloud (SMC) actually have accompanying low-mass stars. Similarly, Stephens et al. (2017) observed seven previously-identified “isolated” high-mass young stellar objects (MYSOs) in the Large Magellanic Cloud (LMC) with Hubble Space Telescope. They discovered that each MYSO is accompanied by $\gtrsim$100 pre-main-sequence stars which were too faint to be detected before. Although these studies suggest that most field OB stars are initially born in young clusters and ejected later, or are surrounded by stellar companions, there is a small fraction (2-6%) of field OB stars which are located $\gtrsim 10^1$-10^2 pc away from any stellar clusters, OB associations and giant molecular clouds (GMCs), moving at low velocities (see de Wit et al. 2005, Selier et al. 2011, Bressert et al. 2012, Oey et al. 2013, Lamb et al. 2016). Understanding the origin of these stars is crucial for testing different categories of high-mass star formation models.

In the past decades, researchers have been searching for the progenitors of high-mass stars at longer wavelengths (see section 1.4). Recent high-resolution ALMA observations reveal high-mass protostars forming in isolated environments (e.g. Csengeri et al. 2018, Harada et al. 2019). In particular, Csengeri et al. (2018) report the discovery of a single protostellar object which is expected to form an O-type star with a mass of $\sim$50 $M_{\odot}$ in the young massive clump 328.2551–0.5321 (rms noise level $\sim$1.3 mJy beam^{-1}, spatial resolution $\sim$400 AU). It is possible that low-mass protostars are present around the high-mass source, but are not detected under their observational limits (e.g. sensitivity, spatial resolution).

3.1.2 Synthetic Observations

The ability to detect low-mass protostars in a massive protocluster can be restricted by observational limits, including wavelength, sensitivity, spatial resolution and interferometric effects. It can also be influenced by stellar properties such as stellar mass and luminosity, and geometry such as the location of low-mass sources and projection effects. To investigate how the detectability is determined by these factors, we employ synthetic observations.

A synthetic observation is defined as the prediction of how an astrophysical source would perform in real observations based on theoretical models (Haworth et al. 2018). To generate a synthetic observation, one could first use (semi-)analytic models or the output from hydrodynamical simulations to prescribe the density and thermal structures (plus velocity structures for synthetic spectral line observations), and then solve the radiative transfer equation to compute the radiation received by an observer. Chemical compositions and instrumental effects are also important components that need to be taken into consideration in the studies of ISM and star formation. Synthetic observations have a wide range of applications, including estimating observational parameters (e.g. integration time and/or configuration of interferometers) required to detect an object, testing the accuracy and predictive capability of models, and determining models for direct interpretation of real observations of specific systems such as protoplanetary disc (e.g. Williams & Best 2014) and star-forming regions (e.g. Izquierdo et al. 2018).

Synthetic observations have been a popular tool for the purpose of predicting the observability and/or distinguishing observational features of individual star-forming cores (Saigo & Tomisaka 2011, Commerçon et al. 2012a) and their substructures (Commerçon et al. 2012b). Commerçon et al. (2012b) present synthetic ALMA continuum images of the first hydrostatic cores (Larson 1969), arguing that ALMA is capable of resolving fragmentation within the cores and distinguishing between magnetized and unmagnetized cores at a distance of $\leq$ 150 pc. Harries et al. (2017) run a numerical simulation of the formation of a single massive (25 $M_\odot$) star using Monte Carlo-based radiation hydrodynamics. They show that the spiral features in the circumstellar discs (with a characteristic radius of 1500 AU) are recovered in their computed ALMA 1 mm continuum images. Figure 3.1 shows the synthetic images based on a simulation of an accreting disk around a young massive star (Meyer et al. 2018). The synthetic dust continuum image and velocity map are similarly consistent with observations in Johnston et al. (2015). Jankovic et al. (2019) produce synthetic observations of circumstellar discs with substructure around massive young stellar objects (MYSOs) using semi-analytic models. They predict that spirals are detectable around MYSOs at <5 kpc with ALMA, if the discs are strongly self-gravitating. Recent very high-resolution ($\sim$100 AU) observations have successfully resolved (<500-1000 AU) spiral-like features around MYSOs (Maud et al. 2017, Chen et al. 2020).

Synthetic observations carried by Lomax & Whitworth (2018), Jankovic et al. (2019), and Meyer et al. (2019a) shed light on the physical properties and/or the observability of young multiple (massive) systems. In particular, Meyer et al. (2019a) compute synthetic dust continuum images of a gravitationally-collapsing prestellar core (100 $M_\odot$) modelled by gravito-radiation-hydrodynamics simulations. They demonstrate the possibility of direct imaging of nascent multiple massive protostellar systems. They predict that the multiplicity in the environment of young massive protostars can be revealed by ALMA with 10 minutes exposure and a beam of $0.015''$, for sources located at 1 kpc.

Synthetic observations have also been applied to investigate larger-scale structures ($\sim$ a few parsec), such as studying the dynamical evolution of filaments (Juvela et al. 2012) and characterizing the gas density distribution of magnetized turbulent molecular clouds (Burkhart et al. 2013a, Burkhart et al. 2013b). Figure 3.2 shows synthetic ALMA emission from a Giant Molecular Cloud (GMC) in the Milky Way. A few studies also discuss the observational properties of cores embedded in the filaments/clumps of turbulent molecular clouds (Smith et al.

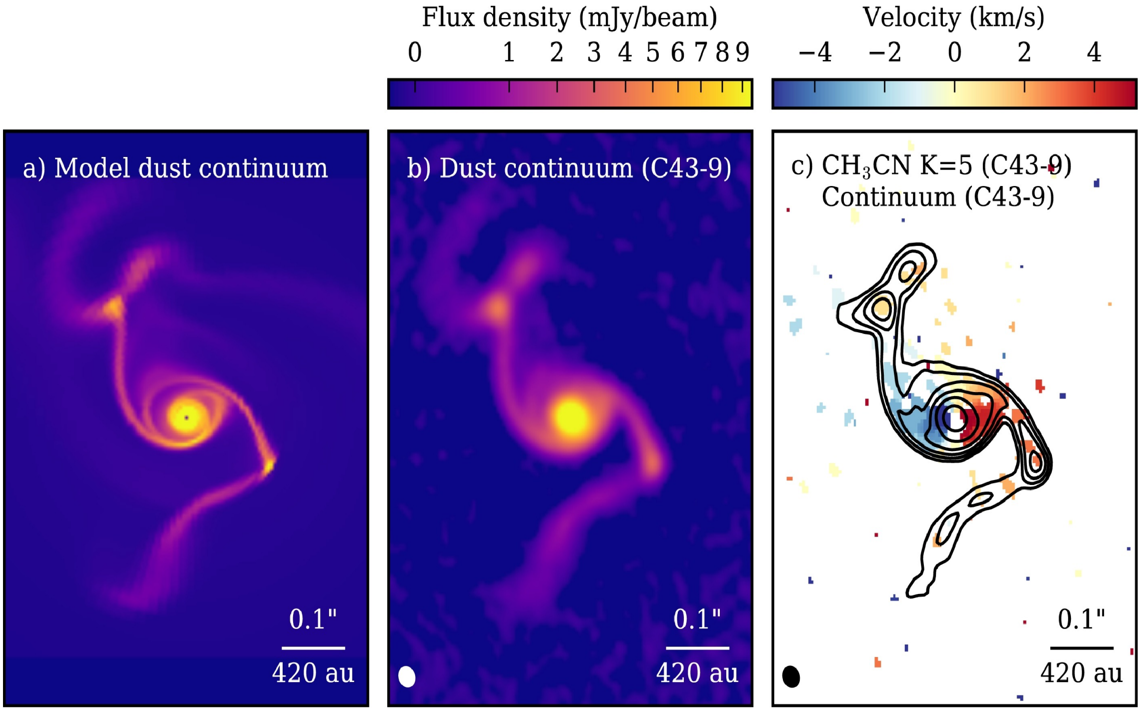

Figure 3.1: An example of synthetic observations of an accretion disk around a young high-mass star (Meyer et al. 2018). Left panel shows the synthetic image of dust continuum emission; Mid panel shows the continuum image that is expected if it is observed with ALMA; Right panel shows the CH_3CN velocity map that would appear in ALMA observations.

2009, Smith et al. 2012, Chira et al. 2014, Steinacker et al. 2016). Smith et al. (2009) run a smoothed particle hydrodynamic (SPH) simulation of a 10^4 $M_\odot$ molecular cloud (with a length of 10 pc and a radius of 3 pc) over ∼ 1 free-fall time, and present simulated interferometric 1.3 mm dust continuum images of three parsec-scale star-forming clumps at different evolutionary stages. These images show that the dust emission becomes dominant by the dense and hot cores forming in the center of clumps as they collapse. Smith et al. (2012) perform radiative transfer calculations of the cloud from the Smith et al. (2009) simulation, and computed synthetic CS (2-1), HCN (1-0) and N_2H^+ (1-0) lines. They demonstrate that the classic blue asymmetry feature expected in the optically thick line profiles of collapsing cores may not be observable in reality, where the cores are surrounded by asymmetric gas. Additionally, Offner et al. (2009) conduct radiation-hydrodynamic calculations of a turbulent molecular cloud (size ∼ 0.65 pc, mass ∼ 185 $M_\odot$) to simulate low-mass star formation. They compute synthetic dust continuum observations of the starless and protostellar cores from the numerical simulation, and predict that the protostellar companions of starless cores at a separation of ∼ 1000 AU should be detectable with CARMA (Offner et al. 2012). However, there have not been any studies considering both high- and low-mass cores and investigating a variety of parameter combinations.

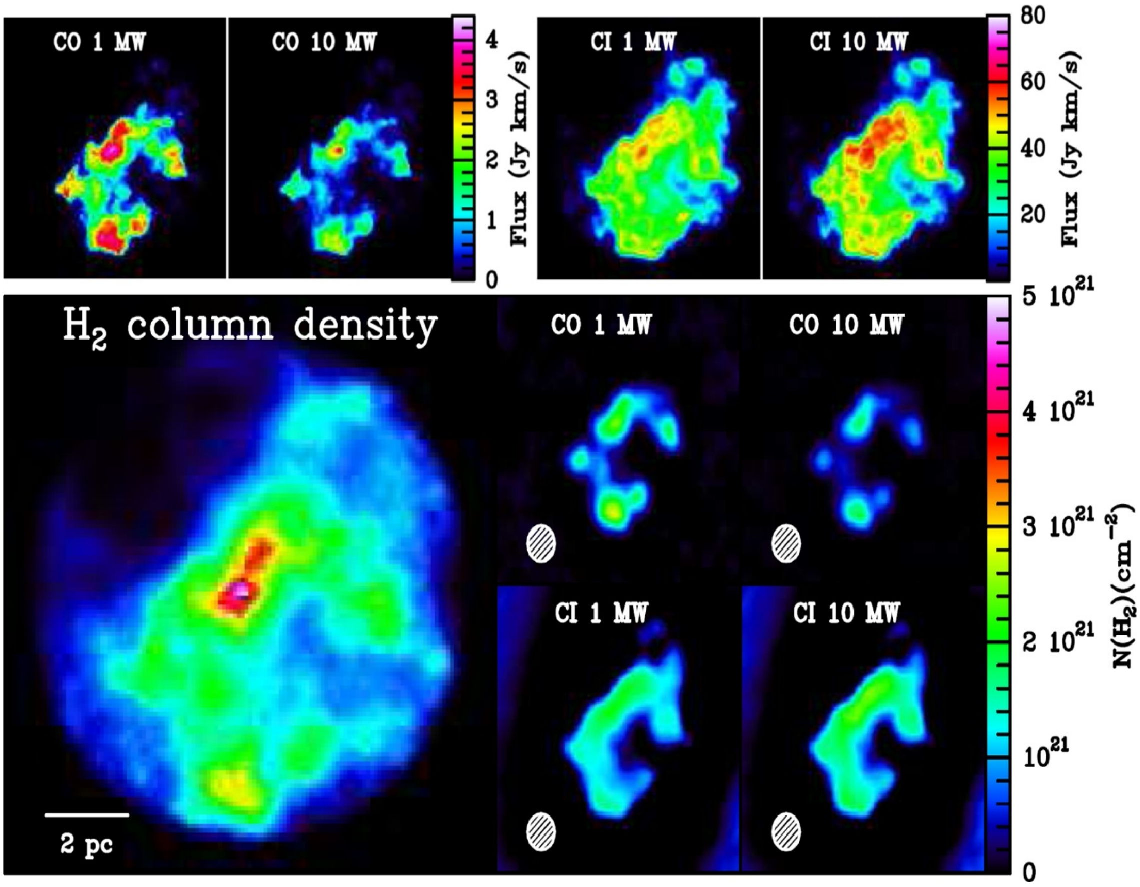

Figure 3.2: Synthetic ALMA observations of the CO(1-0) and [CI](1-0) emission from a typical Milky Way (MW) GMC (Haworth et al. 2018). Their models consider that the GMC is irradiated by an MW-average isotropic Far-UV radiation field and cosmic rays with a cosmic ray ionisation rate equal to 1 and 10 times the MW average. The top row shows the fluxes of CO(1-0) (left) and [CI](1-0) (right) with different cosmic ray ionisation rates (as labelled). Bottom left panel shows the true distribution of the molecular hydrogen column density of the GMC. The four small panels on the lower right show the distributions of the molecular hydrogen column density that are derived using the CO-to-H_2 and CI-to-H_2 conversion factors.

Here we construct a semi-analytic framework to generate synthetic observations for protostellar cores in a young massive protocluster, aiming to quantify the observability of low-mass protostars around high-mass young stellar objects at submillimeter wavelength. We choose parametric models instead of hydrodynamical ones for the sake of saving computational cost, which allows for the exploration of a large parameter space.

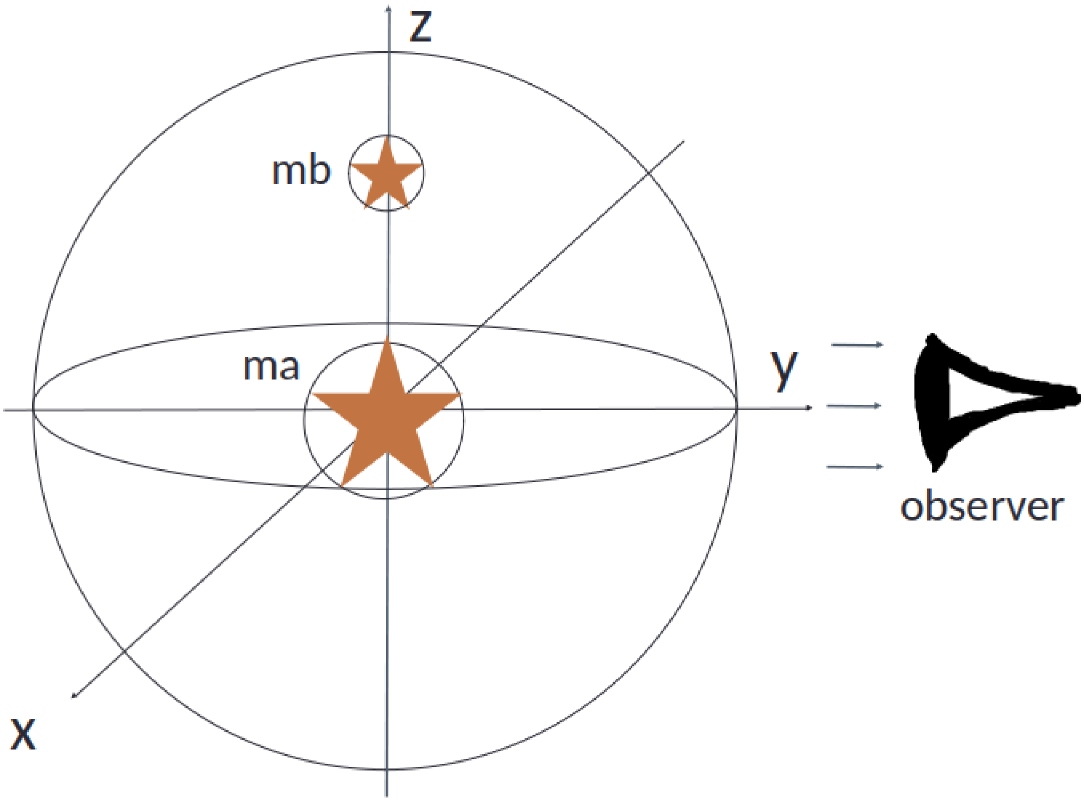

Figure 3.3: A cartoon showing the gas sphere described by a 3D Cartesian grid. The locations of protostars are plotted with orange stellar markers encompassed by black circles. The line of sight is parallel to the y axis.

3.2 Methodology

3.2.1 Model construction

We assume a massive protocluster embedded in a spherical gas clump with a diameter of 1.0 pc, which is the typical size of the massive clumps identified in the Herschel Infrared Galactic Plane Survey (Hi-GAL, Molinari et al. 2016, Elia et al. 2017a). To describe the model, we set up a 3D Cartesian grid with a cell size of 0.02 pc, corresponding to 0.2″ at a distance of 2 kpc (see Table 3.1). The high-mass protostar (A) is located at the centre ($\vec{a}$ = (0., 0., 0.)); the low-mass protostar (B) is separated from protostar A along the z axis ($\vec{b}$ = (0., 0., z_b)). We assume synthetic observations are taken along the y axis, with the line of sight perpendicular to the y = 0 plane on which the two protostars are located. The pre-defined geometry is demonstrated in Fig. 3.3.

Parameter	Symbol	Value
Mass of protostar A	m_a	
Mass of protostar B	m_b	
Clump radius	R	1.0 pc
Location of protostar A	$\vec{a}$	(0., 0., 0.) pc
Location of protostar B	$\vec{b}$	(0., 0., z_b) pc
Distance	D	2 kpc
Cell size	d	0.02 pc
Resolution	θ	$0.2''$
Frequency	ν	230 GHz
Wavelength	λ	1.3 mm
Dust opacity	κ_ν	0.7 $\mathrm{cm}^2\ \mathrm{g}^{-1}$
Gas-to-dust mass ratio	$R_{\mathrm{g/d}}$	100

Table 3.1: A summary of parameters.

Density prescriptions

We assume a spherically-symmetric power-law density distribution associated with each protostar. The density structure is described by

$$\rho(r) = \rho_0 \left(\frac{r}{r_0}\right)^{-p} \tag{3.1}$$

where ρ_0 is the reference density at the reference radius r_0. We choose the radius of the protostellar envelope r_{env} as the reference radius. r_{env} is set to be 5000 AU, which is within the typical range of fragmentation length-scale observed in star-forming regions (e.g. Longmore et al. 2006, Beuther et al. 2018a). The gas density at the envelope radius is determined by assuming the gas mass within the envelope to be $M_{\mathrm{env}} = \epsilon M_*$, where ϵ is a coefficient and M_* is the mass of the protostar embedded in the envelope. Previous studies combining large-sample observations with modelled protostellar evolutionary tracks show that protostars evolve from the envelope-dominant phase ($M_{\mathrm{env}} \gg M_*$) to the star-dominant phase ($M_{\mathrm{env}} < M_*$, André et al. 2008, Minier et al. 2009, Maury et al. 2011). Here we choose $\epsilon = 1$ to represent an intermediate stage of protostellar evolution. The power-law exponent p is assumed to be $p = 1.5$ when $r \leq r_{\mathrm{env}}$ and $p = 2$ when $r > r_{\mathrm{env}}$. This is based on the classic model of collapsing isothermal spheres, where $r^{-1.5}$ law describes the density distribution within the freely-falling protostellar envelope, and r^{-2} for the (nearly) static region outside the envelope (Larson 1969, Shu 1977). This assumption is often taken as the initial conditions of isolated low-mass star formation, and also appear consistent with the density profiles observed in high-mass star-forming regions (e.g. Mueller et al. 2002, Beuther et al. 2002, Li et al. 2019, Lin et al. 2021).

At each cell, the density is given by linearly adding up the densities contributed by the profiles of protostar A and protostar B:

$$\rho(r_i) = \rho(r_{i,a}) + \rho(r_{i,b}) \tag{3.2}$$

where $r_{i,a}$ and $r_{i,b}$ are the distances from location r_i to the two protostars respectively. To convert the gas density distribution to the dust density distribution, we adopt a gas-to-dust mass ratio ($\mathrm{R_{g/d}}$) of 100, which is the most commonly used value when only hydrogen molecule is considered (Draine et al. 2007).

Dust temperature prescription

We describe the dust temperature distribution due to the radiative feedback from young stars using a 1D temperature profile derived in Smith et al. (2009) (equation (3)):

$$T(r) = 100 \times \left(\frac{m}{10\ \mathrm{M_\odot}}\right)^{0.35} \times \left(\frac{r}{1000\ \mathrm{au}}\right)^{-0.45} \mathrm{K};\ m < 10\ \mathrm{M_\odot} \tag{3.3}$$

$$T(r) = 100 \times \left(\frac{m}{10\ \mathrm{M_\odot}}\right)^{1.11} \times \left(\frac{r}{1000\ \mathrm{au}}\right)^{-0.5} \mathrm{K};\ m > 10\ \mathrm{M_\odot} \tag{3.4}$$

where m is the stellar mass and r is the distance from the star. This 1D prescription is approximated based on a grid of pre-computed Monte Carlo radiative transfer models of young stars in Robitaille et al. (2006). We adopt the analytic prescription for dust temperature instead of performing Monte Carlo calculations to reduce the computational costs for exploring a large parameter space.

Consider the equilibrium of dust heating and cooling, the dust temperature at each cell is given by:

$$T(r_i) = (T^4(m_a, r_{i,a}) + T^4(m_b, r_{i,b}))^{\frac{1}{4}} \tag{3.5}$$

where $T(m_a, r_{i,a})$ and $T(m_b, r_{i,b})$ are the temperatures at location r_i due to the radiative feedback from protostar A and protostar B, with $r_{i,a}$ and $r_{i,b}$ being the distances from location r_i to the two protostars respectively.

3.2.2 Radiative transfer modelling

To generate synthetic dust continuum images of this star-forming clump, we conduct radiative transfer (RT) calculations to model the emission of photons and their propagation through the dusty medium based on the density and thermal structure detailed in section 4.2.1. Dust particles are known to absorb ultraviolet/optical photons, and re-emit them at infrared/submillimeter wavelengths (Steinacker et al. 2013). Considering the radiation feedback from protostars, we determine the dust temperature at a given location using equation (3.5). Dust is also effective in scattering light, especially for ultraviolet to near infrared regime (see e.g. Burgh et al. 2002). In the context of this work, we focus on the absorption and re-emission of dust grains, ignoring the scattering process as the dust scattering albedo at submillimeter wavelengths ($\sim 10^{-5}$) is much smaller than that at shorter wavelengths (e.g. $\sim 10^{-1}$ at NIR, Draine 2003). The dust emission can be determined by RT modelling or analytically with optically-thin assumptions (e.g. using equation A.31 in Kauffmann et al. 2008). We choose to model the emission with RT techniques instead of optically-thin calculations, as the effects of optical depth cannot be ignored, especially around the regions with high densities (e.g. τ can be ~ 0.3 at a few hundreds AU away from the high-mass source, for the most massive case). Moreover, it takes ~ 2 minutes to run RT, but ~ 10 minutes to calculate flux densities analytically for a single model. Therefore, RT techniques are also a better option regarding computational costs.

The main objective of RT modelling is to solve the radiative transfer equation (Rybicki & Lightman 1979):

$$\frac{dI_\nu}{d\tau_\nu} = S_\nu - I_\nu, \tag{3.6}$$

where I_ν is the intensity at frequency ν, τ_ν is the optical depth defined by

$$d\tau_\nu = \alpha_\nu ds, \tag{3.7}$$

and S_ν is the source function defined by

$$S_\nu = \frac{j_\nu}{\alpha_\nu}. \tag{3.8}$$

Note that j_ν and α_ν are the emission coefficient and absorption coefficient respectively. We assume the observations are taken at the frequency of 230 GHz (equivalent to 1.3 mm) In the modelling, the line of sight is parallel to the y direction; the distance between the clump and the observer is set to be 2 kpc. We assume a dust opacity at 1.3 mm for thin ice mantles with a classic MRN size distribution under a gas density of 10^5 cm^{-3} (Ossenkopf & Henning 1994, Mathis et al. 1977), and apply it uniformly to all the cells within the spherical clump. Values of these parameters are summarized in Table 3.1.

We run dust radiative transfer calculations using a software package called RADMC-3D (Dullemond et al. 2012). RADMC-3D is coded to model dust continuum radiative transfer and gas line transfer in 1D, 2D and 3D geometries (see the manual of RADMC-3D [1]). With the dust density and temperature distributions provided, RADMC-3D performs a ray-tracing computation to compute synthetic dust continuum images. Ray tracing follows the change of intensity in a particular direction. This technique is implemented by solving the first-order differential of the radiative transfer equation within a spatial grid cell along a given direction. If the emission and absorption properties within a medium are provided, it is relatively straightforward to calculate the intensity towards the observer using this method, because rays only have to be traced in one direction.

We convert the output data files from RADMC-3D into FITS images using a Python package called radmc3dPy [2]. The FITS images are originally in units of Jansky per pixel. To account for the finite spatial resolution of real astronomical observations, we then convolve the images with 2D Gaussian beams using the *imsmooth* task in CASA [3] (McMullin et al. 2007). In this work, we do not consider sophisticated instrumental effects such as spatial filtering or dynamic range of interferometry. In real interferometric observations, the incomplete sampling in spatial frequencies leads to the loss of information for e.g., short spacings (see section 1.4.2). The smooth extended emission with spatial scales larger than the maximum recoverable scale (MRS) of certain observation is expected to be filtered out by the interferometer. In addition, the dynamic range, defined as the ratio of the maximum intensity to the rms noise level in the image, is limited by instrumental response (Thompson et al. 2001). Achieving high dynamic range requires accurate visibility measurements, good *uv* coverage, and careful calibration and deconvolution (e.g., self-calibration). Further discussion on spatial filtering and a preliminary

---

[1] `https://www.ita.uni-heidelberg.de/~dullemond/software/radmc-3d/manual_radmc3d/index.html`

[2] radmc3dPy is a Python package coded for analyzing the results of RADMC-3D. This package is developed by Attila Juhasz. Details can be found at `https://www.ita.uni-heidelberg.de/~dullemond/software/radmc-3d/manual_rmcpy/index.html`

[3] CASA version 5.4.0

Parameter	Symbol	Value
Mass of protostar A ($M_\odot$)	m_a	[8,15,25,50]
Mass of protostar B ($M_\odot$)	m_b	[0.1,0.25,0.5,1,2,5]
Separation (pc)	S	[0.05,0.10,0.15,0.20,0.25,0.30]
Resolution ($'' \times ''$)	$\theta_{maj} \times \theta_{min}$	$[0.6'' \times 0.4'', 3.0'' \times 2.0'', 6.0'' \times 5.0'']$

Table 3.2: A summary of the parameter space we explore in this work.

test can be found in Chapter 5 section 5.2.

3.2.3 Parameter space

In our models, we set the mass of protostar A (m_a) to be 8, 15, 25, and 50 $M_\odot$; the mass range of protostar B (m_b) covers 0.1, 0.25, 0.5, 1.0, 2.0, 5.0 $M_\odot$. These values are among the typical range of the masses of the protostars identified in recent observations (e.g. high-mass protostars in Duarte-Cabral et al. 2013, Tigé et al. 2017). The lower limit of m_b is set to 0.1 $M_\odot$ to ensure that the mass of protostar B is above the stellar-substellar boundary (see Table 8 in Dieterich et al. 2014). We vary the separation between protostar A and B from 0.05 to 0.30 pc with a step size of 0.05 pc. These assumptions adopt the projected distances between high- and low-mass cores that are observed in massive protoclusters (e.g. Cyganowski et al. 2017). We choose the major and minor axis ($\theta_{\rm maj} \times \theta_{\rm min}$) of the Gaussian beam to be $0.6'' \times 0.4''$, $3.0'' \times 2.0''$, and $6.0'' \times 5.0''$, which are roughly the numbers of the characteristic angular resolution of ALMA (at C-3 or C-4 configuration), SMA (at compact configuration), and ACA at 230 GHz. A summary of the parameter space is listed in Table 3.2.

To understand how the observability of the low-mass core is influenced by the parameters discussed above, we explore the combinations of four masses of m_a, six masses of m_b, six separations (S), and three beam sizes ($\theta_{\rm maj} \times \theta_{\rm min}$) in the modelling. We have run 432 models in total, and the results are shown in the next section.

3.3 Results

3.3.1 A one-dimensional overview

We extract one-dimensional slices which go through the locations of the high- and low-mass sources from the synthetic images. The 1D slices provide a straightforward illustration of the significance of the low-mass source.

Fig.3.4 shows 1D slices of a subset of all results where $m_a = 8M_\odot$. Slices with different beam sizes are arranged in columns (left: $0.6'' \times 0.4''$; middle: $3.0'' \times 2.0''$; right: $6.0'' \times 5.0''$), with different separations in rows (from top to bottom panel: 0.05 pc, 0.10 pc, 0.15 pc, 0.20 pc, 0.25 pc, 0.30 pc). Slices with different masses of the low-mass source (m_b) are plotted in different colours (black: 0.1 $M_\odot$; blue: 0.25 $M_\odot$; red: 0.5 $M_\odot$; lime: 1.0 $M_\odot$; magenta: 2.0 $M_\odot$; green: 5.0 $M_\odot$). The central peak ($y = 0$) of each slice is dominated by the emission from the high-mass source (protostar A). The secondary peak with a separation from the centre is a result of the emission from the low-mass source (protostar B). To illustrate the effects of beam sizes, we first plot the slices in units of Jansky per square arcsecond area. To do this, we estimate how many square arcsecond areas a beam area (A_{beam}) is equivalent to (n_{arcs}), and then divide the intensities in Jansky per beam over n_{arcs} to obtain intensities in Jansky per square arcsecond area. Fig.3.5 - Fig.3.7 are the same as Fig.3.4 but for m_a equals to 15, 25, and 50 $M_\odot$ respectively.

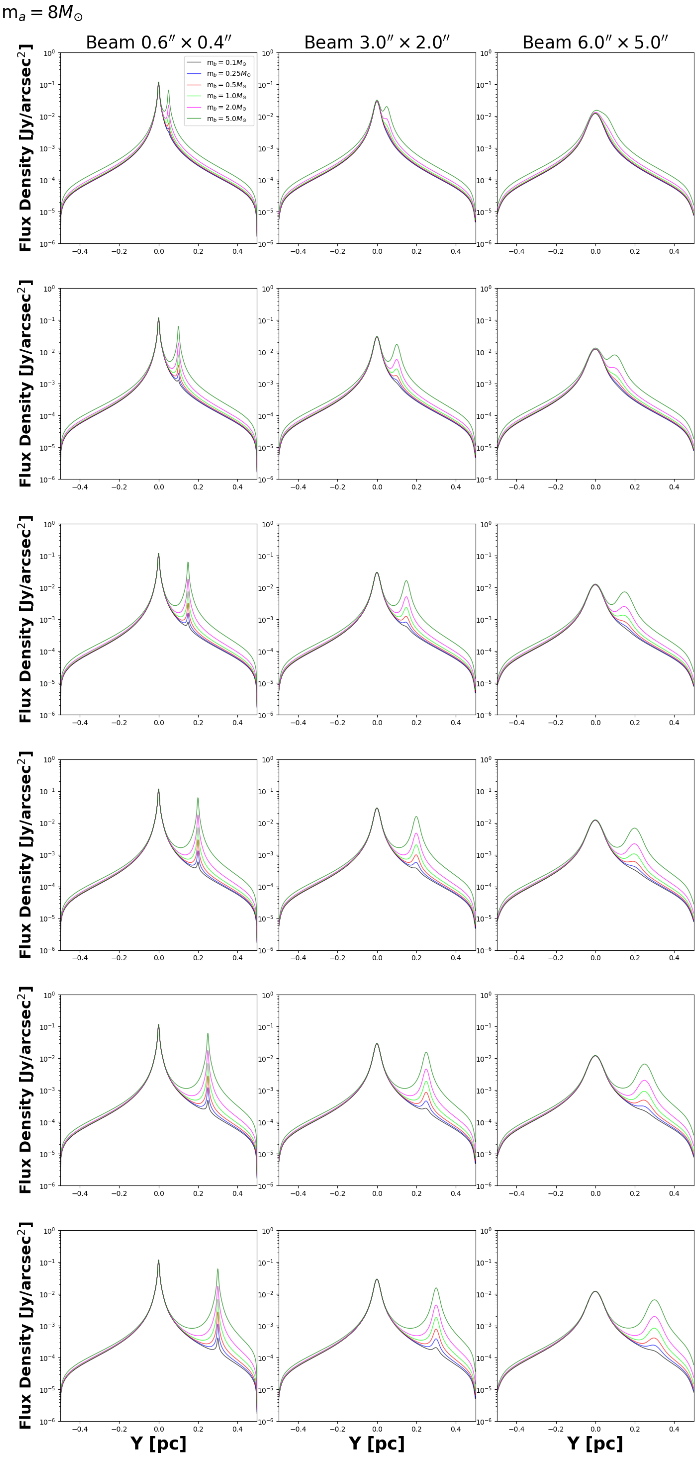

Figure 3.4: One-dimensional slices crossing the locations of the high- and low-mass sources extracted from the synthetic continuum images (where $m_a = 8$ M$_\odot$). The intensities are plotted in units of Jansky per square arcsecond area. Results with different resolution are plotted in different columns (left: 0.6″ × 0.4″; middle: 3.0″ × 2.0″; right: 6.0″ × 5.0″). Results with different separation are shown in rows (from top to bottom: 0.05 pc, 0.10 pc, 0.15 pc, 0.20 pc, 0.25 pc, 0.30 pc). The masses of the low-mass source (m_b) are colour-coded (black: 0.1 M$_\odot$; blue: 0.25 M$_\odot$; red: 0.5 M$_\odot$; lime: 1.0 M$_\odot$; magenta: 2.0 M$_\odot$; green: 5.0 M$_\odot$).

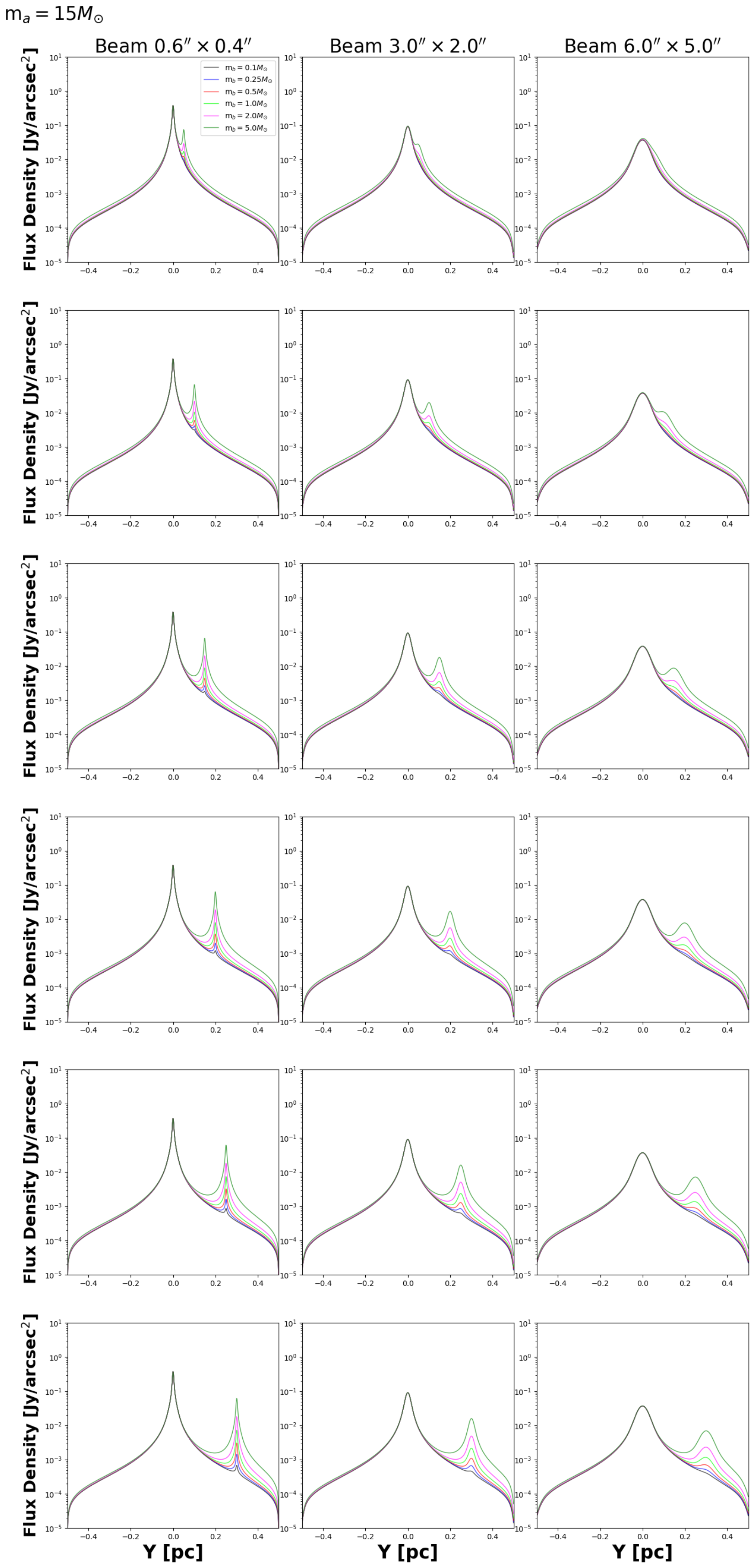

Figure 3.5: As Fig.3.4 with $m_a = 15\ M_\odot$.

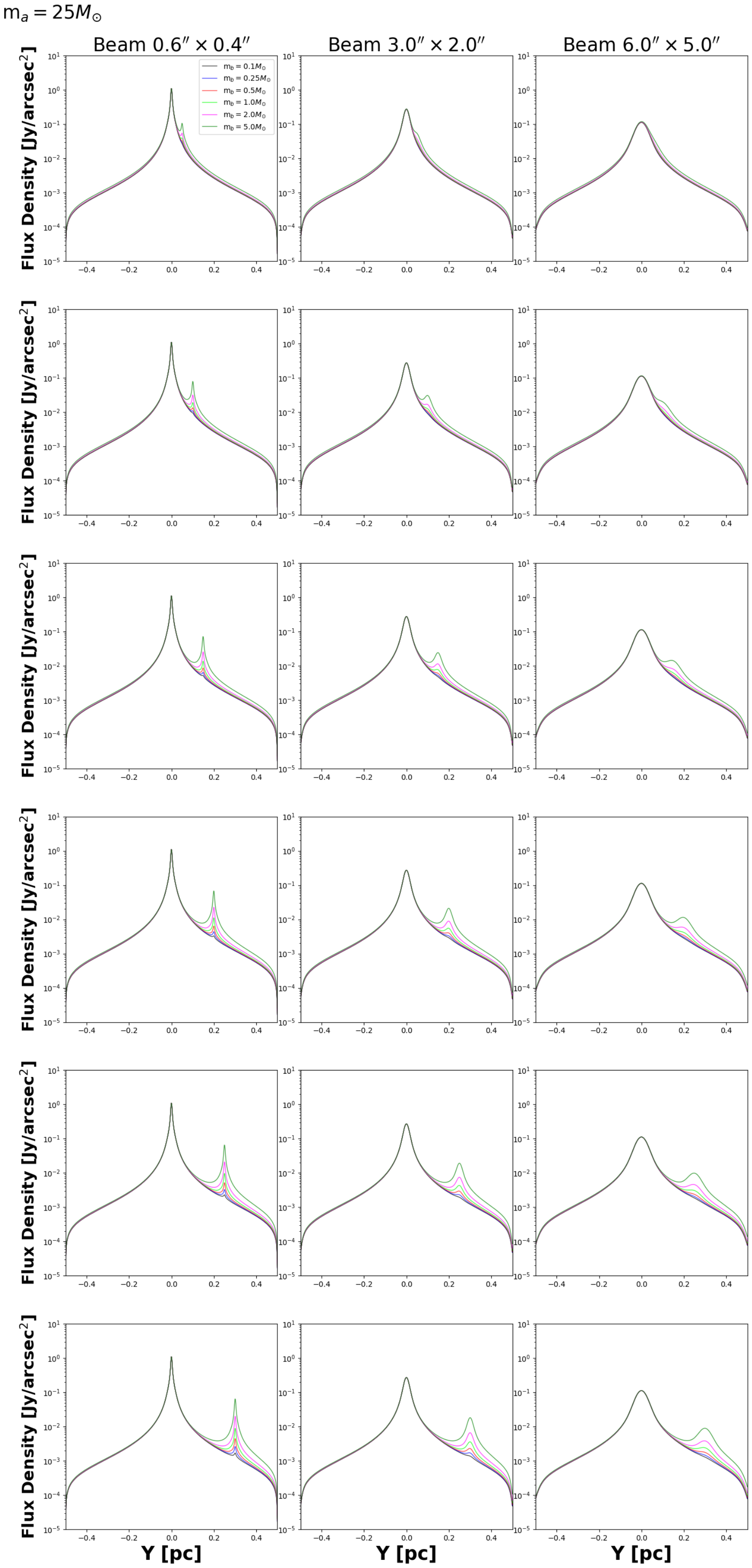

Figure 3.6: As Fig.3.4 with m_a = 25 $M_\odot$.

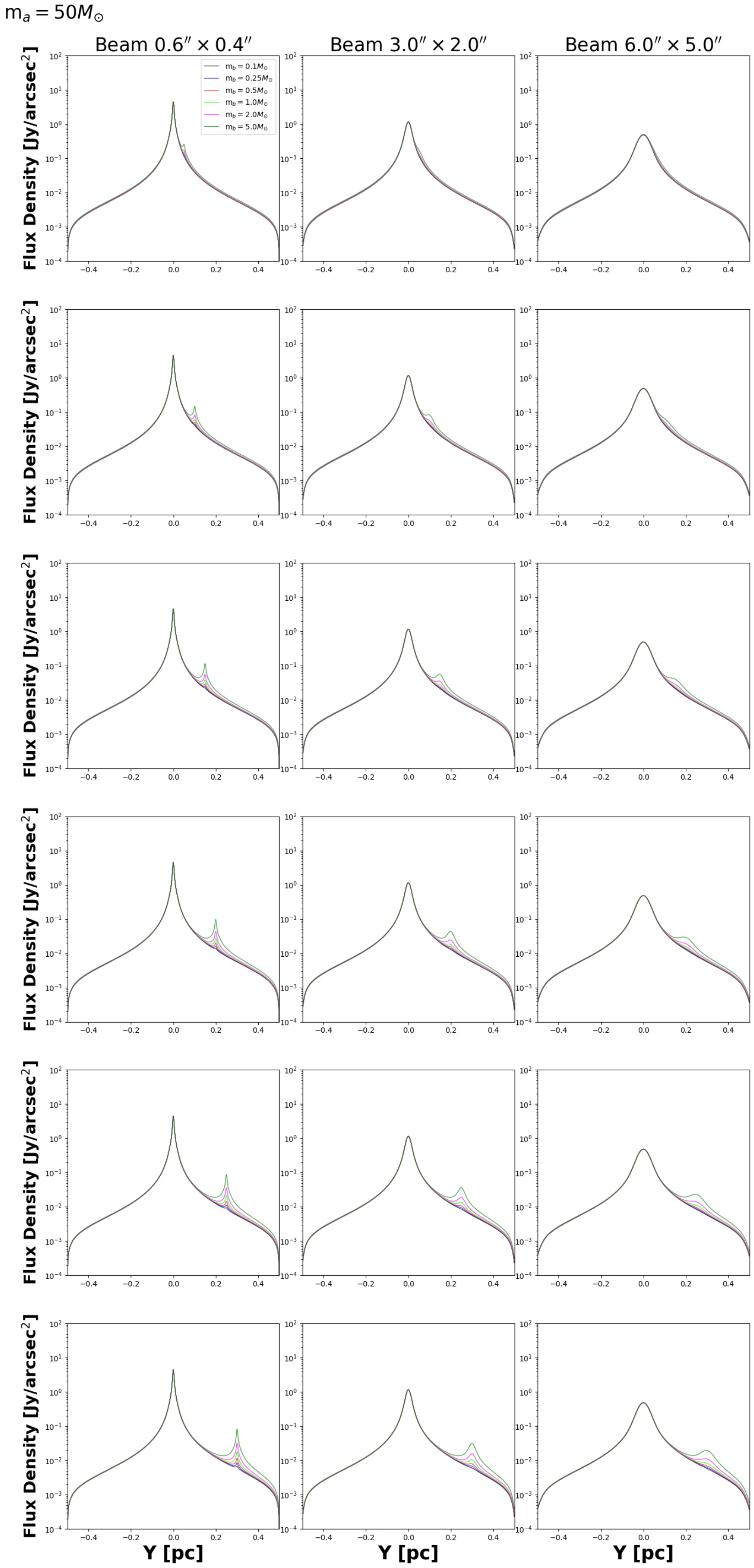

Figure 3.7: As Fig.3.4 with m$_a$ = 50 M$_\odot$.

In the regime of Jansky per square arcsecond area, we employ the relative height of the secondary peak to demonstrate how significant the low-mass source appears. Looking at individual panels of Fig.3.4 - Fig.3.7, we can first compare the slices of different masses of m_b for a particular m_a, separation and beam size. As m_b increases from 0.1 $M_\odot$ (black) to 5.0 $M_\odot$ (green), the secondary peak increases accordingly. For example, for the cases with smallest beam and separation and $m_a = 8$ $M_\odot$ (corresponding to the top left panel of Fig.3.4), the difference between the lowest and highest secondary peak is approximately an order of magnitude. The trend shows that the more massive the low-mass source is, the more emission it will generate. This is because the temperature and the density of the protostellar core will increase as the stellar mass increases, which will result in a higher intensity of the emission at sub-mm wavelengths. Observational studies of low-mass protostellar objects show similar trends (e.g. Tobin et al. 2019). Secondly, when comparing the slices with different separations (e.g. different rows in left/middle/right panel), we find that the secondary peak becomes more distinguishable from the central peak as the separation gets larger, as expected. Moreover, this effect is more influential on lower-mass sources. For example, on the left panel of Fig.3.4, the secondary peaks in black and blue ($m_b = 0.1$, 0.25 $M_\odot$) are almost dominated by the emission from the central high-mass source for $S = 0.05$ pc. As the separation increases, these peaks become more visible. The absolute height of the secondary, however, decreases as the separation increases. For example, the secondary peak in black decreases by about one order of magnitude when the separation increases from 0.05 to 0.30 pc. The descending trend of absolute height is in contrast to the illustration where the secondary peak appears more distinguishable with larger separation. The explanation behind this trend is probably that the emission within this clump is generally dominated by that from the high-mass source. When the separation gets smaller and the low-mass source is closer to the high-mass one, the emission at the location of the low-mass source becomes increasingly dominated by that from the high-mass source. The significance of the effects of the high-mass source also depends on the assumed density and thermal structure (e.g. $\rho \propto r^{-1.5}$ and $T \propto r^{-0.5}$ outside the protostellar envelope when $m > 10$ $M_\odot$, see details in section 4.2.1). With power-law assumptions, there is a dramatic attenuation in the intensity from the centre to the margin of the clump, which thus results in the attenuation of the secondary peak at larger separation. Thirdly, the beam size also has crucial influences on the visibility of the secondary peak. If we compare the three panels of each row of Fig.3.4, it is apparent that as the beam size gets larger, the secondary peak becomes blurred or even disappears with its height decreasing. For the cases with large beam sizes, small separation and low m_b (e.g. the top right panel of Fig.3.4), the secondary peak can join the central one, making a single broad asymmetric peak. This trend agrees with recent discoveries of high-resolution interferometric observations, where a single source reported in low-resolution observations can be resolved into multiple fragments in higher-resolution data (e.g., Hunter et al. 2014, Wang et al. 2014, Cyganowski et al. (2022), Barnes et al. (2023)).

To make it easier to inspect the effects of the mass of the high-mass source, we also plot the slices of different m_a values for a particular m_b, separation and beam size. Fig.3.8 shows slices of $m_b = 0.1$ $M_\odot$ with different separation in rows and beam sizes in columns. On each panel slices of different m_a are plotted in different colours (magenta: 8 $M_\odot$;blue: 15 $M_\odot$; red: 25 $M_\odot$; green: 50 $M_\odot$). The intensities are again converted into units of Jansky per square arcsecond area to display the effects of beam sizes. Fig.3.9 - Fig.3.13 are the same as Fig.3.8 but for $m_b = 0.25, 0.5, 1.0, 2.0, 5.0$ $M_\odot$. From a quick look at these results, it is evident that the high-mass source dominates the emission of this clump. When the mass of the high-mass source increases from 8 to 50 $M_\odot$, the intensity of the whole clump (including the location of the low-mass source) can increase by up to two orders of magnitude; the secondary peak, however, becomes less visible in the meantime. For example, on the bottom left panel of Fig.3.8, the evident secondary peak in magenta will become the little bump in green if m_a increases from 8 to 50 $M_\odot$, although the green bump is higher than the magenta peak. This suggests that the more massive the high-mass source, the more chances that the radiation from the high-mass source will dominate that from the whole star-forming clump, leading to accompanying low-mass sources less visible.

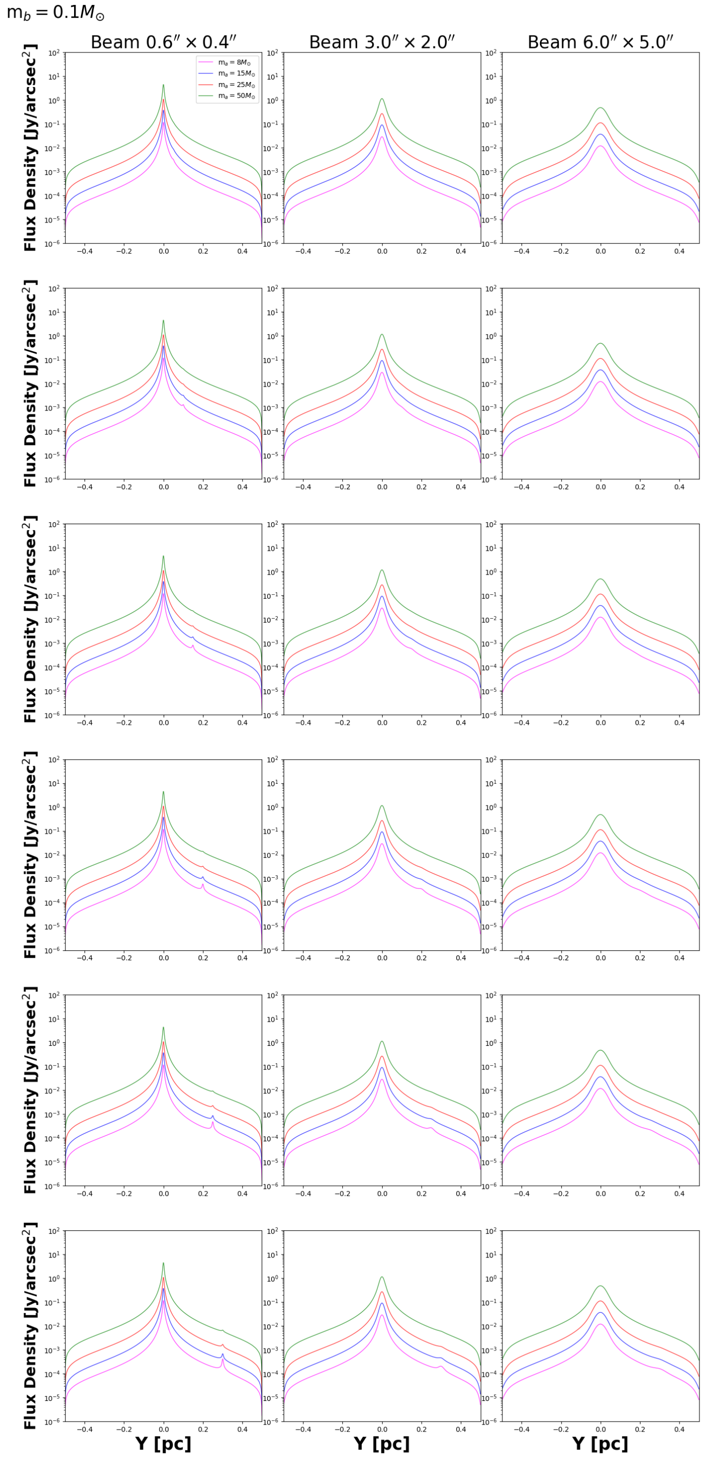

Figure 3.8: One-dimensional slices crossing the locations of the high- and low-mass sources extracted from the synthetic continuum images (where m$_b$ = 0.1 M$_\odot$). The intensities are plotted in units of Jansky per square arcsecond area. Results with different resolution are plotted in different columns (left: 0.6″ × 0.4″; middle: 3.0″ × 2.0″; right: 6.0″ × 5.0″). Results with different separation are shown in rows (from top to bottom: 0.05 pc, 0.10 pc, 0.15 pc, 0.20 pc, 0.25 pc, 0.30 pc). The masses of the high-mass source (m$_a$) are colour-coded (magenta: 8 M$_\odot$;blue: 15 M$_\odot$; red: 25 M$_\odot$; green: 50 M$_\odot$).

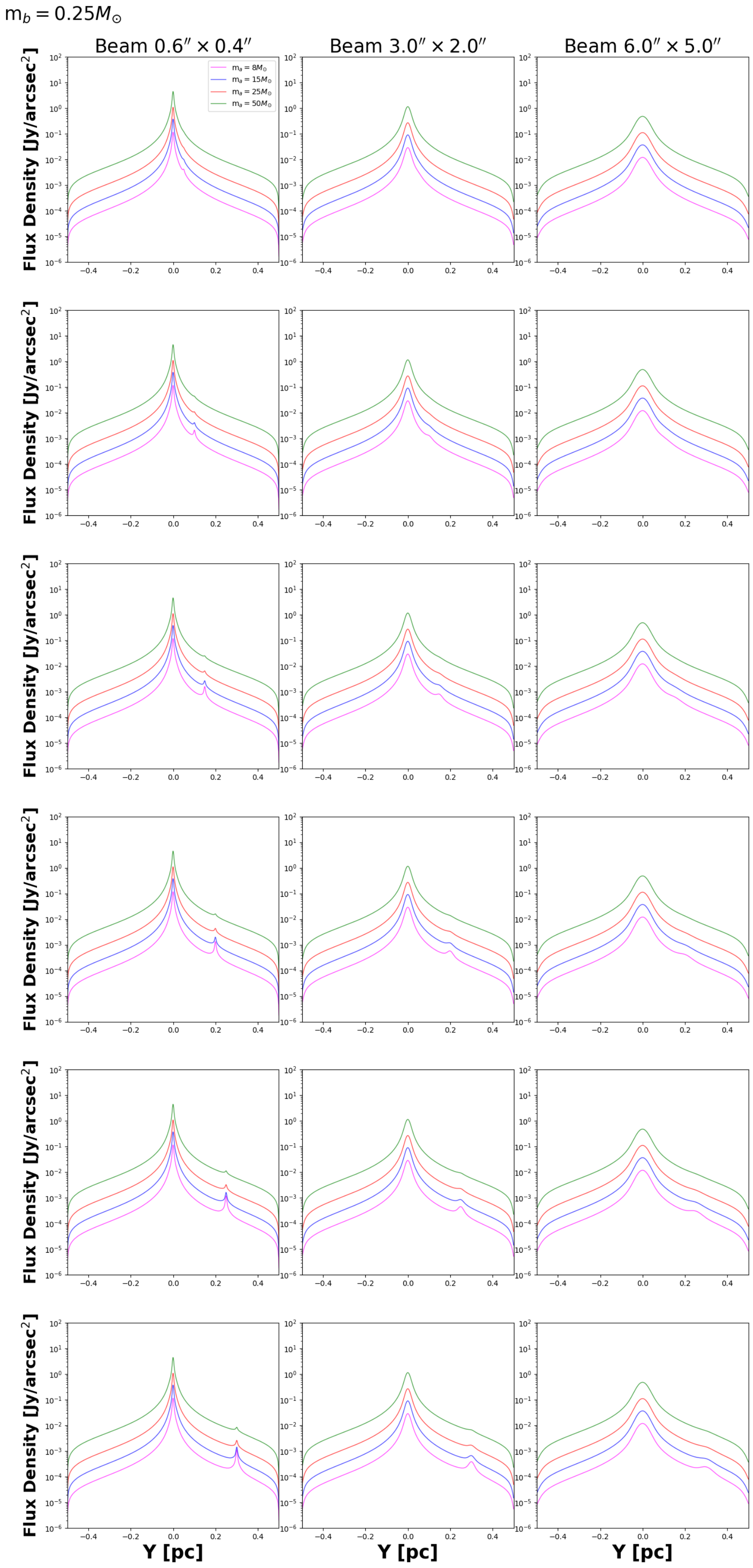

Figure 3.9: As Fig.3.8 with m$_b$ = 0.25 M$_\odot$.

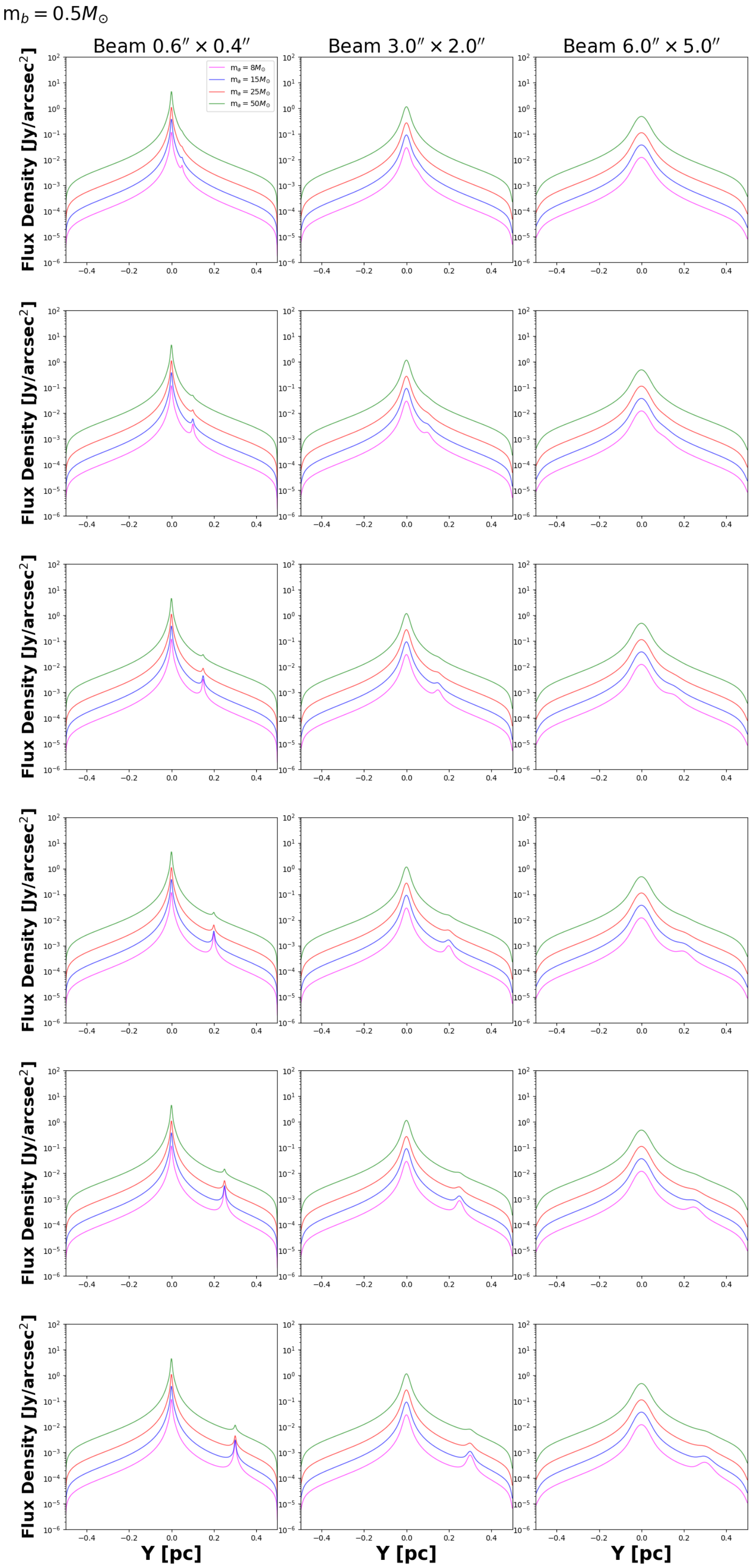

Figure 3.10: As Fig.3.8 with m$_b$ = 0.5 M$_\odot$.

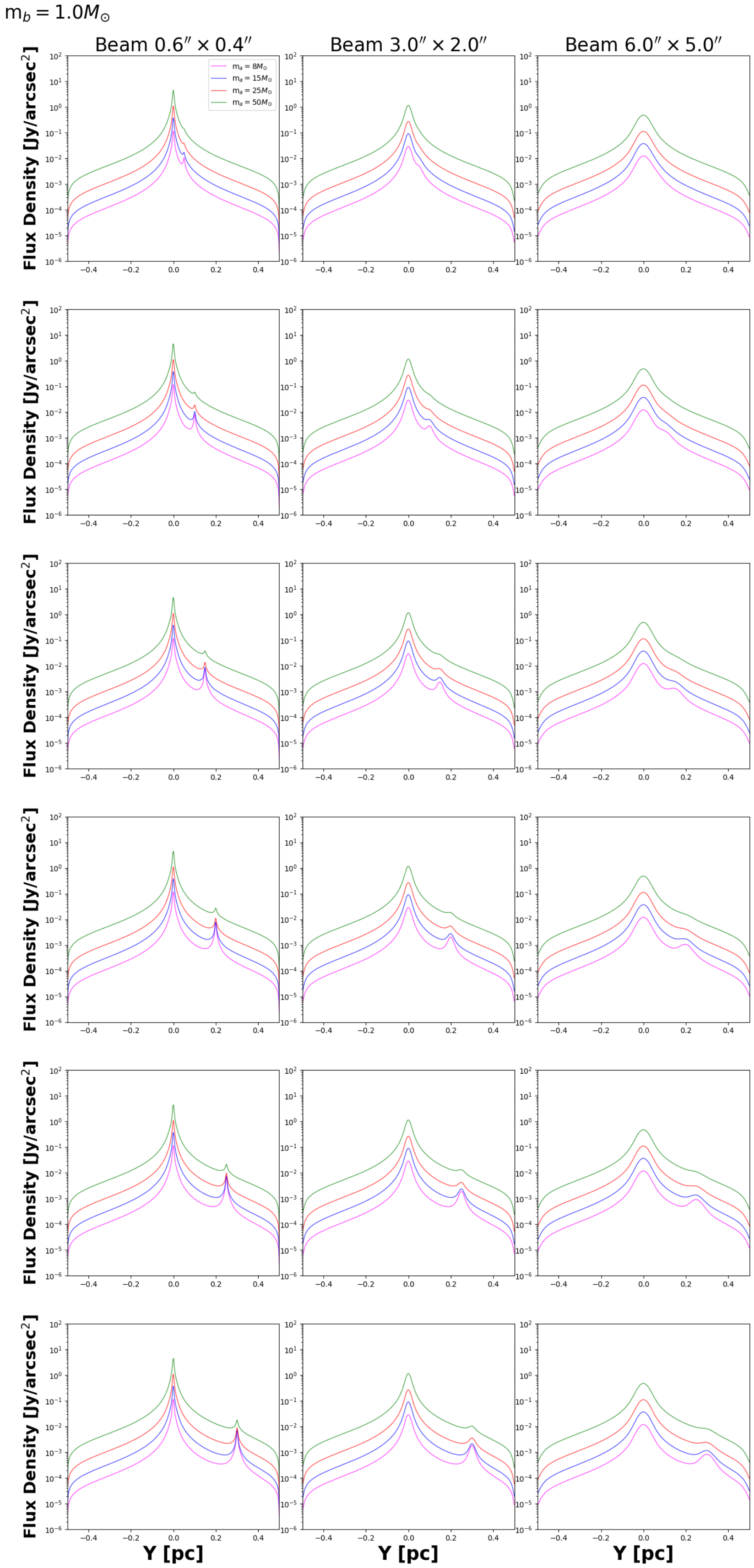

Figure 3.11: As Fig.3.8 with $m_b = 1.0\ M_\odot$.

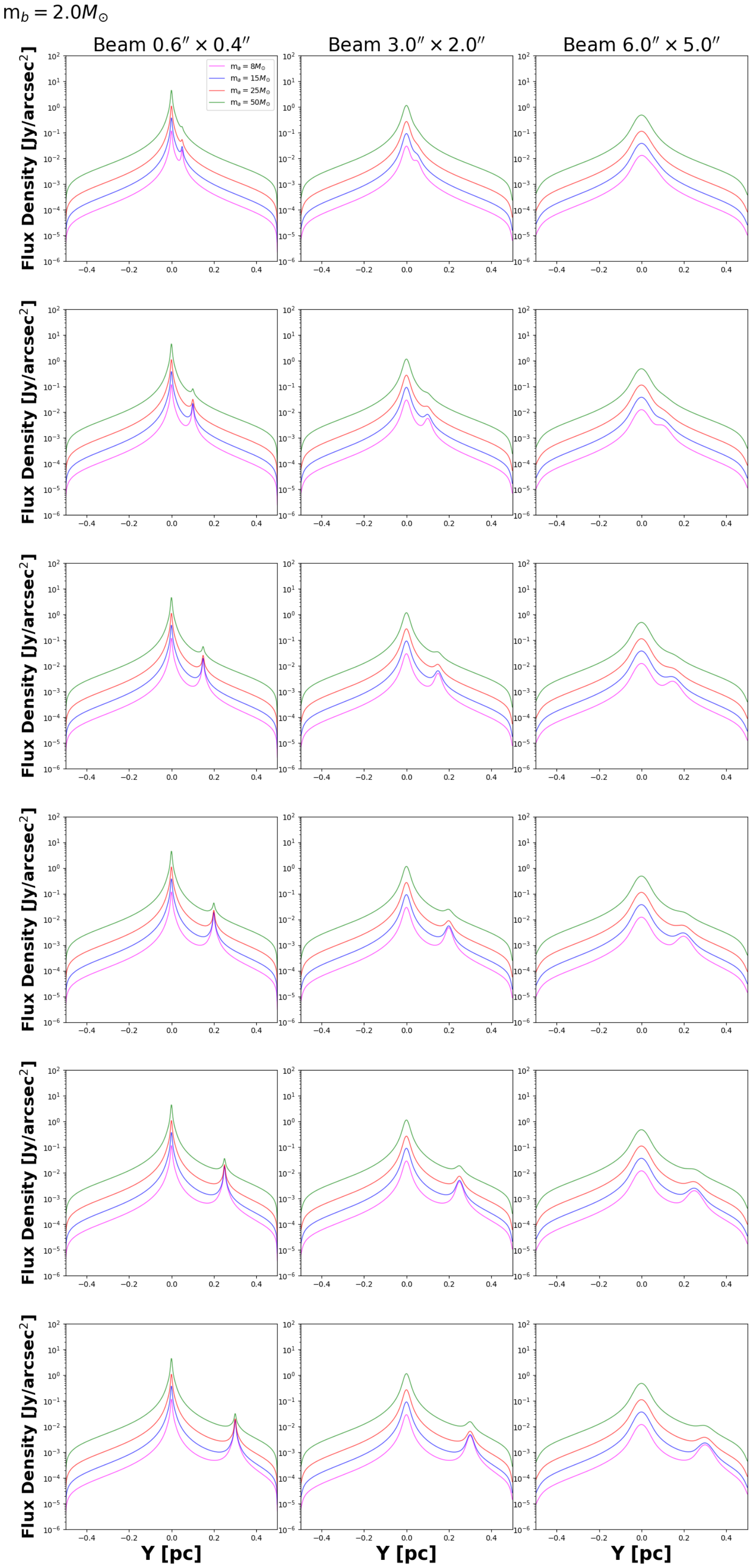

Figure 3.12: As Fig.3.8 with $m_b = 2.0\ M_\odot$.

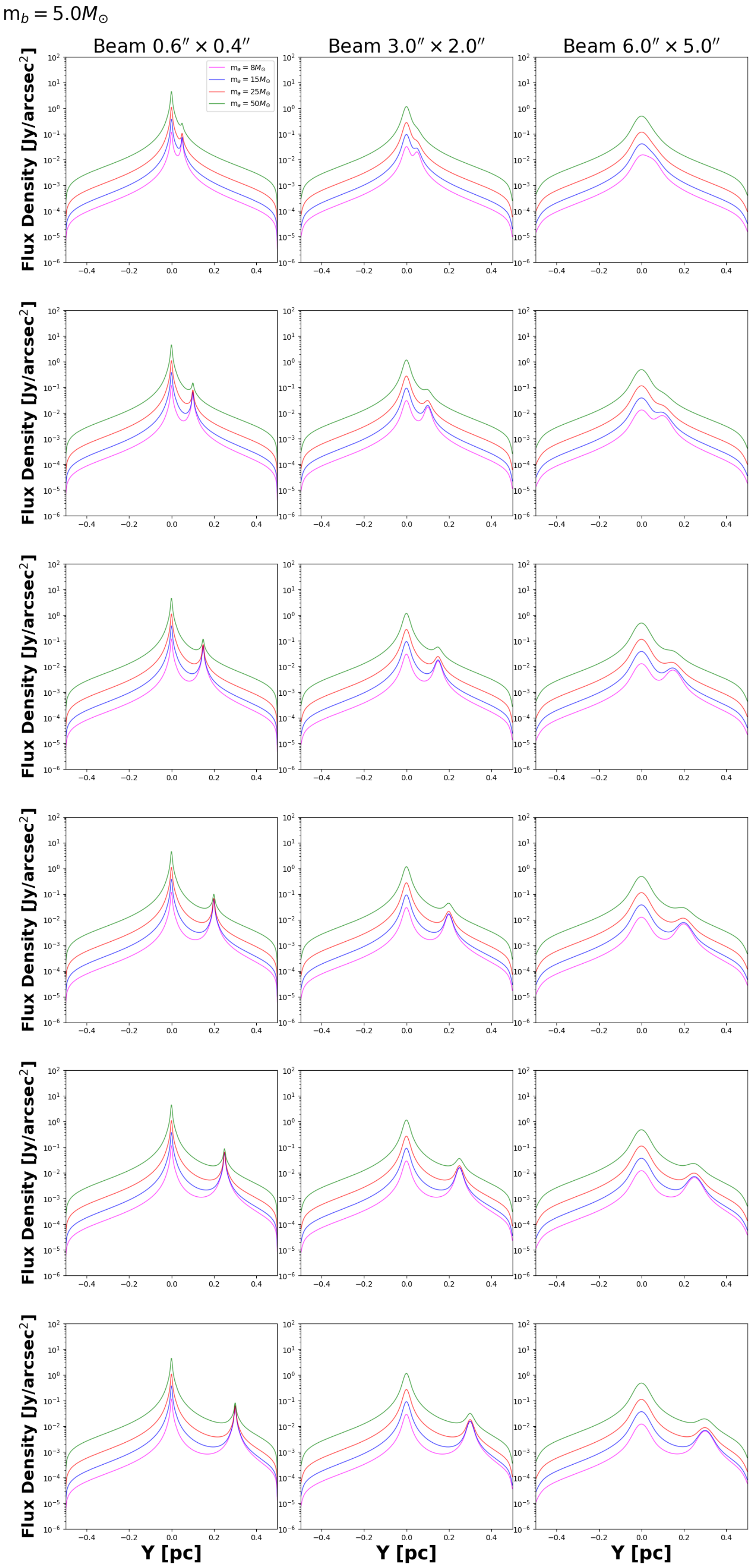

Figure 3.13: As Fig.3.8 with $m_b = 5.0\ M_\odot$.

Converting intensities in units of Jansky per square arcsecond area allows us to conduct direct comparisons between the results with different beam sizes. Nevertheless, analyses and discussions are usually carried out with data in units of Jansky per beam in practical observations. We make variants of those Jy/arcsec^2 figures where we keep the intensity unit as Jy/beam. Fig.3.14 is arranged in a similar way as Fig.3.4 is (e.g. columns, rows, colours), but with intensities in Jy/beam. The Jansky/beam slices vary with m$_a$, m$_b$ and S in the same way as the Jy/arcsec^2 ones do. However, the intensities in Jansky/beam are elevated as the beam size increases, which is opposite to the trend displayed on Jy/arcsec^2 figures. Note that the Jansky/beam slices are extracted from the 2D synthetic images convolved with beam sizes. The total emission within a beam area will increase if the size of the beam increases. Therefore, the secondary peaks are higher in the cases with larger beam sizes, but not necessarily more significant. It will be problematic if one discusses the significance of the low-mass source with different beam sizes by comparing the relative Jansky/beam intensity at the location of the low-mass source. Instead, we can compare the Jansky/beam slices with typical noise thresholds in real observations. The grey dotted lines on Fig.3.14 mark the levels of the noise thresholds, which are 5× the rms noise values. The rms noise values are adopted from published ALMA, SMA, and ACA 1.3 mm continuum surveys as representatives. The details of these observations are summarised in Table 3.3. Note that the listed continuum sensitivities are not measured under the exactly same circumstances as the assumptions in our models. For example, the corresponding physical size of the synthesised beam of G353.41 is greater than that of the smallest beam in our models by a factor of ∼2.6. We avoid to search for observational studies matching our assumptions accurately, as interferometry sensitivity depends on instrumental properties and observational parameters:

$$\sigma \propto \frac{T_{sys}}{\sqrt{t\Delta\nu}}, \tag{3.9}$$

where T$_{sys}$ is the system temperature, t is the time on source, and $\Delta\nu$ is the effective bandwidth (see section 9.7 of Wilson et al. 2013). Hsu et al. (2020) achieve a σ_{cont} of 13.5 mJy beam^{-1} with a total on-source integration time of 500 seconds and a bandwidth of 7.5 GHz. If the on-source integration time is doubled, the sensitivity will be increased to ∼ 9.5 mJy beam^{-1}. Fig.3.15 - Fig.3.17 are the same as Fig.3.14 but for m$_a$ = 15,25,50 M$_\odot$. The range of the intensities are limited to 10^{-6}-10^{0}, 10^{-5}-10^{1}, 10^{-5}-10^{1}, and 10^{-4}-10^{2} for Fig.3.14, Fig.3.15, Fig.3.16, and Fig.3.17 respectively for illustration. Fig.3.18 - Fig.3.23 are the Jansky/beam variants of Fig.3.8 - Fig.3.13 respectively, overlaid with the 5 $\times\sigma_{rms}$ threshold.

Table 3.3: A summary of the representative ALMA, SMA, and ACA 1.3 mm continuum observations.

Target	Distance	Synthesized Beam	σ_{rms} (mJy beam^{-1})	Telescope
G353.41[a]	2 kpc	$0.93'' \times 0.66''$	0.4	ALMA
G11.92-0.61[b]	3.37 kpc	$3.2'' \times 1.8''$	3.5	SMA
G208.68-19.20N1[c]	415 pc	$7.6'' \times 4.0''$	13.5	ACA

[a] Motte et al. (2021).

[b] Cyganowski et al. (2011c), Sato et al. (2014).

[c] Hsu et al. (2020).

The detectability of the low-mass source can be speculated using its intensity and the observed noise threshold. We extract the intensity at the location of the secondary source (I_b), and compare the value with the 5 $\times\sigma_{rms}$. If $I_b > 5 \times\sigma_{rms}$, the low-mass source is likely to be detected. With this criterion, the low-mass source with $m_b = 2.0$, 5.0 $M_\odot$ is detectable in all cases where $m_a = 8.0$ $M_\odot$. $m_b = 1.0$ $M_\odot$ is detectable only when the separation $\leqslant 0.10$ pc with the smallest and middle beam sizes. However, comparing the intensity at the location of the low-mass source with the noise does not take into consideration the distinguishableness of the low-mass source. For example, although the intensity at the location of the low-mass source is above the 5σ threshold for $m_b = 5.0$ $M_\odot$ on the top right panel of Fig.3.14, the secondary peak has been blended with the central peak and is not clearly visible. Therefore, we have to explore other criteria to quantitatively analyse the detectability of the low-mass source.

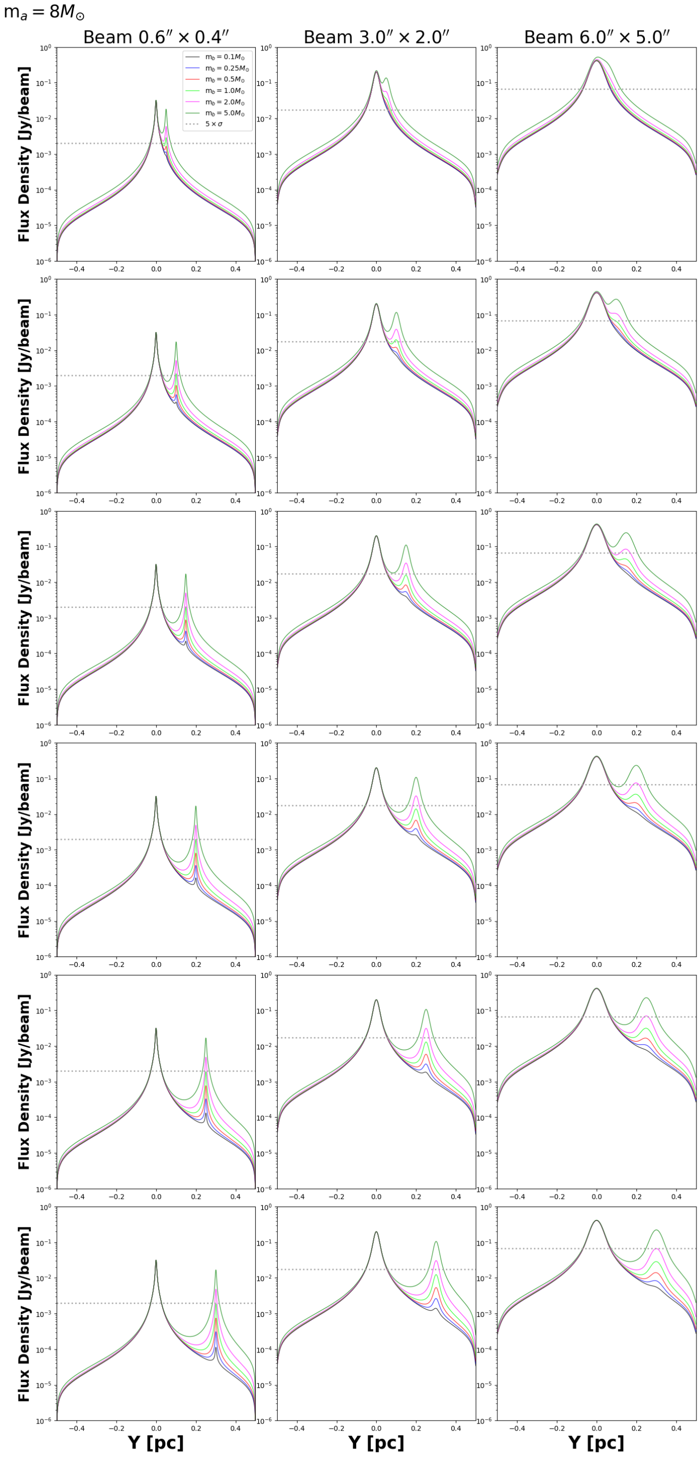

Figure 3.14: One-dimensional slices crossing the locations of the high- and low-mass sources extracted from the synthetic continuum images (where m$_a$ = 8 M$_\odot$). The intensities are plotted in units of Jansky per beam. Results with different resolution are plotted in different columns (left: 0.6″ × 0.4″; middle: 3.0″ × 2.0″; right: 6.0″ × 5.0″). Results with different separation are shown in rows (from top to bottom: 0.05 pc, 0.10 pc, 0.15 pc, 0.20 pc, 0.25 pc, 0.30 pc). The masses of the low-mass source are colour-coded (black: 0.1 M$_\odot$; blue: 0.25 M$_\odot$; red: 0.5 M$_\odot$; lime: 1.0 M$_\odot$; magenta: 2.0 M$_\odot$; green: 5.0 M$_\odot$). The grey dotted lines show the 5σ threshold in practical ALMA, SMA and ACA observations (taken from literature, see details in section 4.3.1).

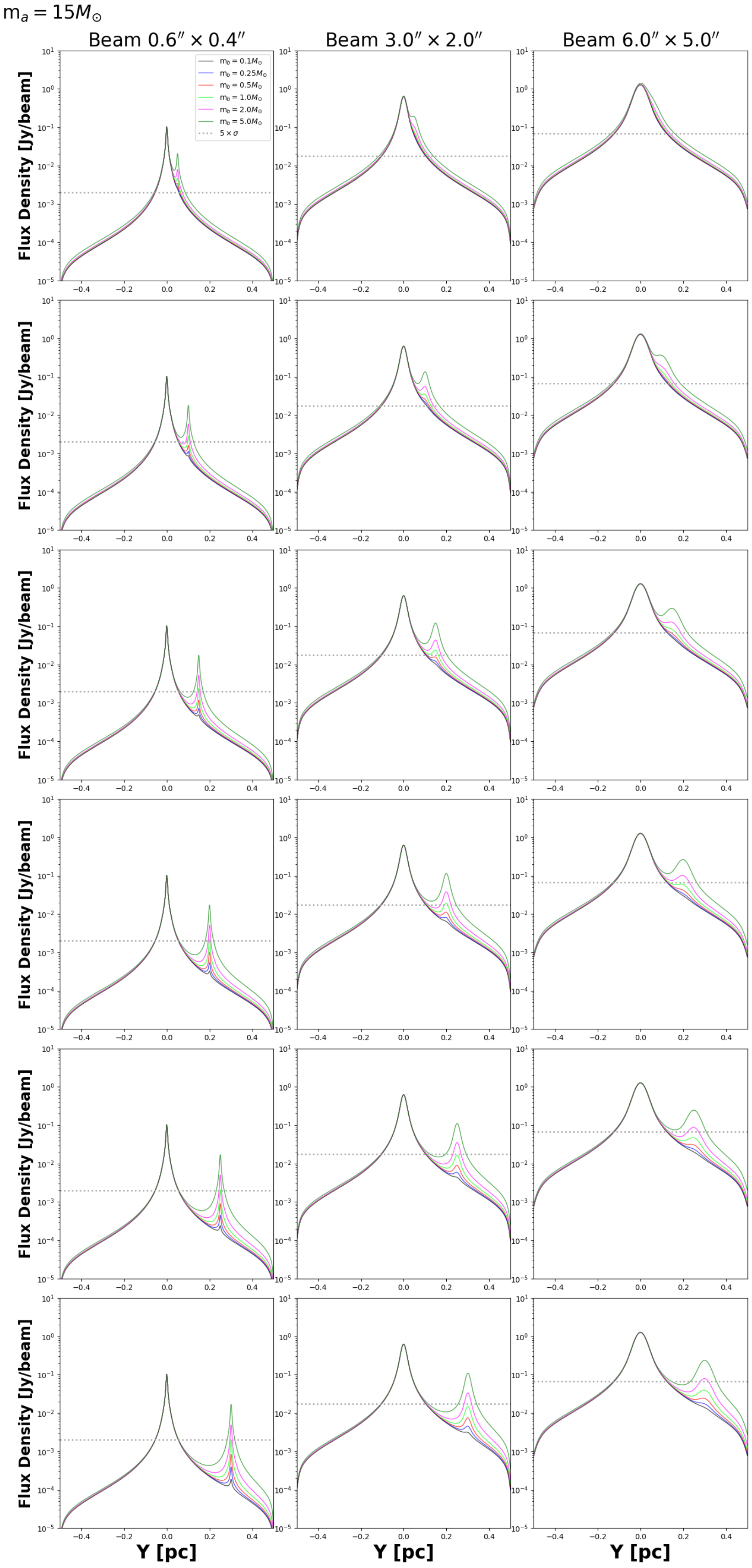

Figure 3.15: As Fig.3.14 with m$_a$ = 15 M$_\odot$.

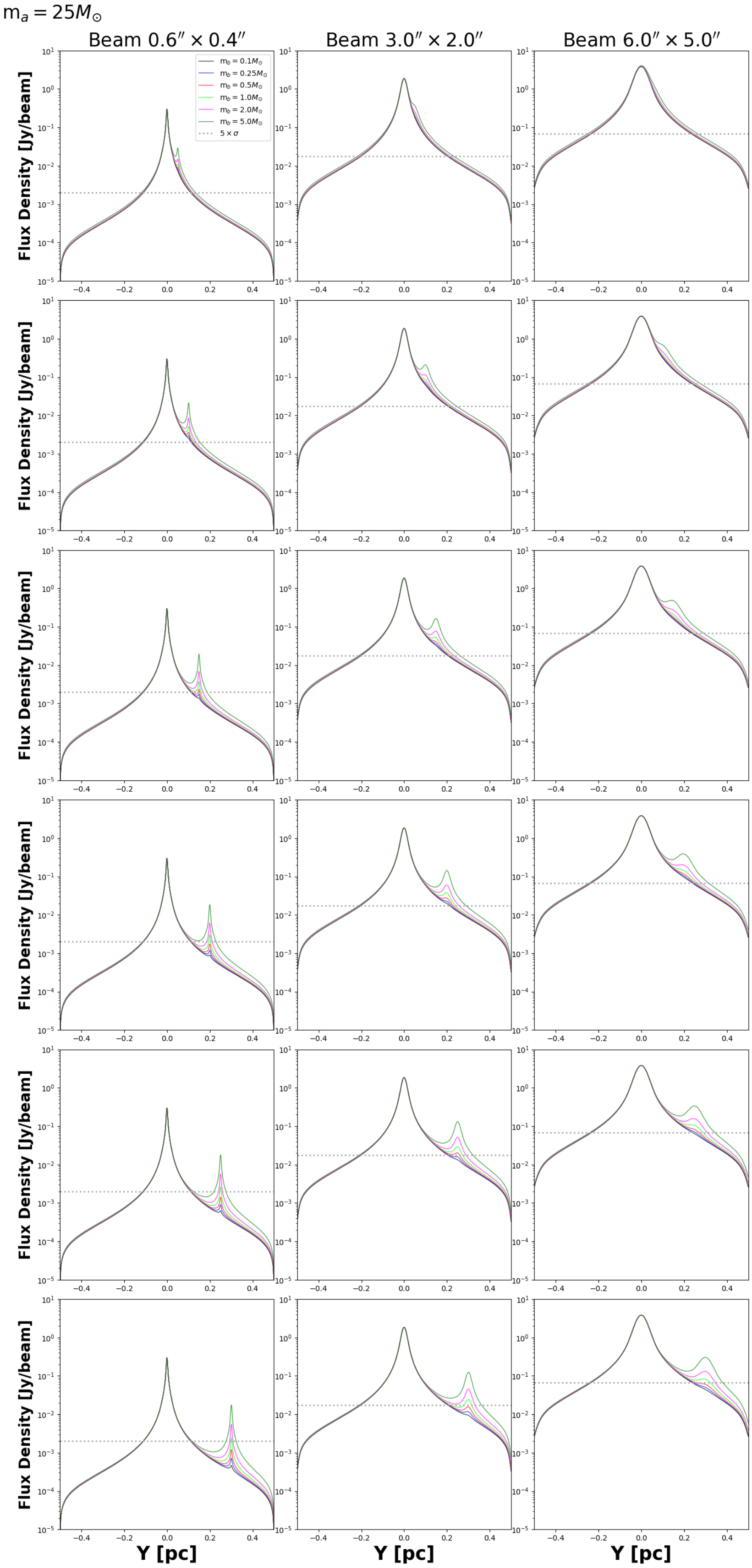

Figure 3.16: As Fig.3.14 with m$_a$ = 25 M$_\odot$.

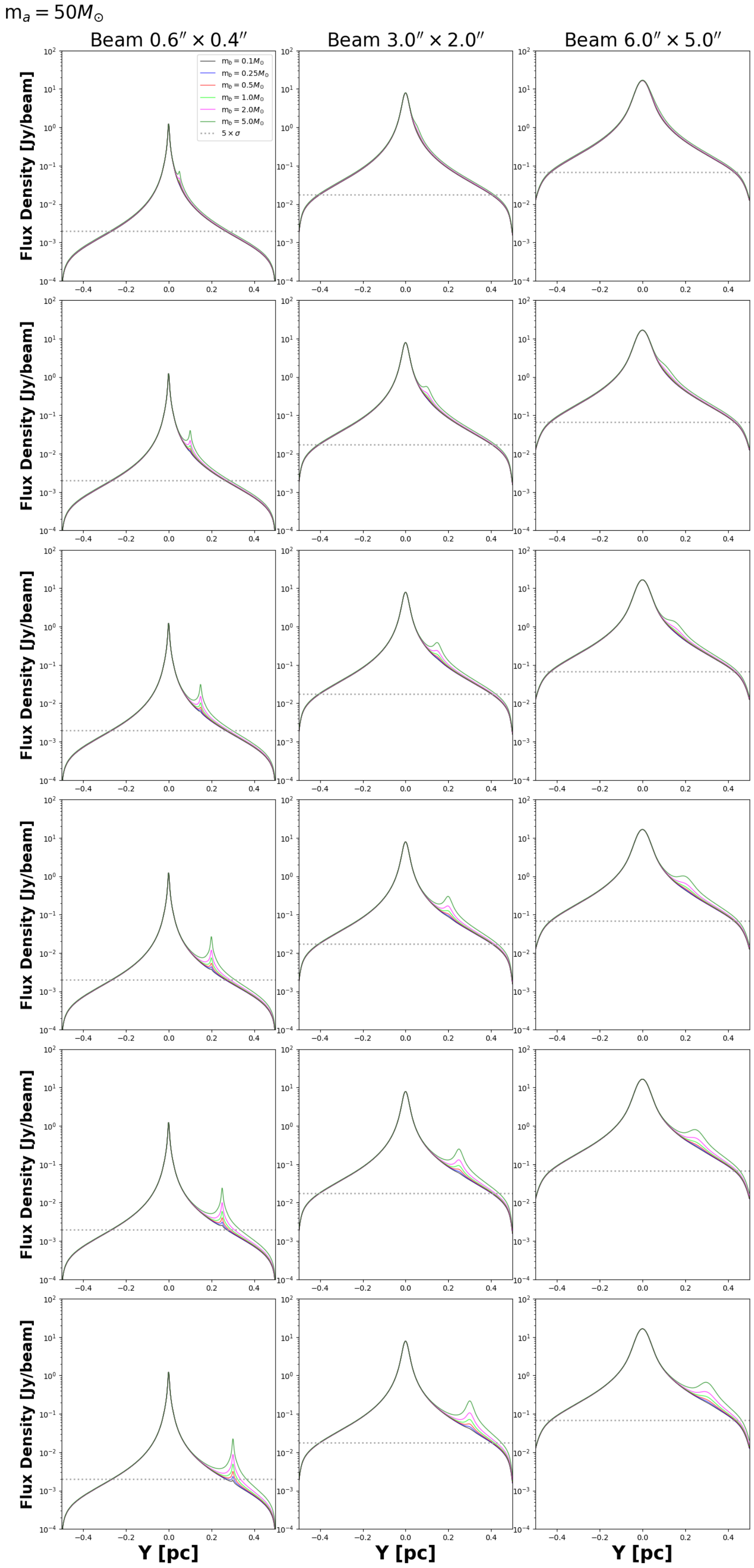

Figure 3.17: As Fig.3.14 with m$_a$ = 50 M$_\odot$.

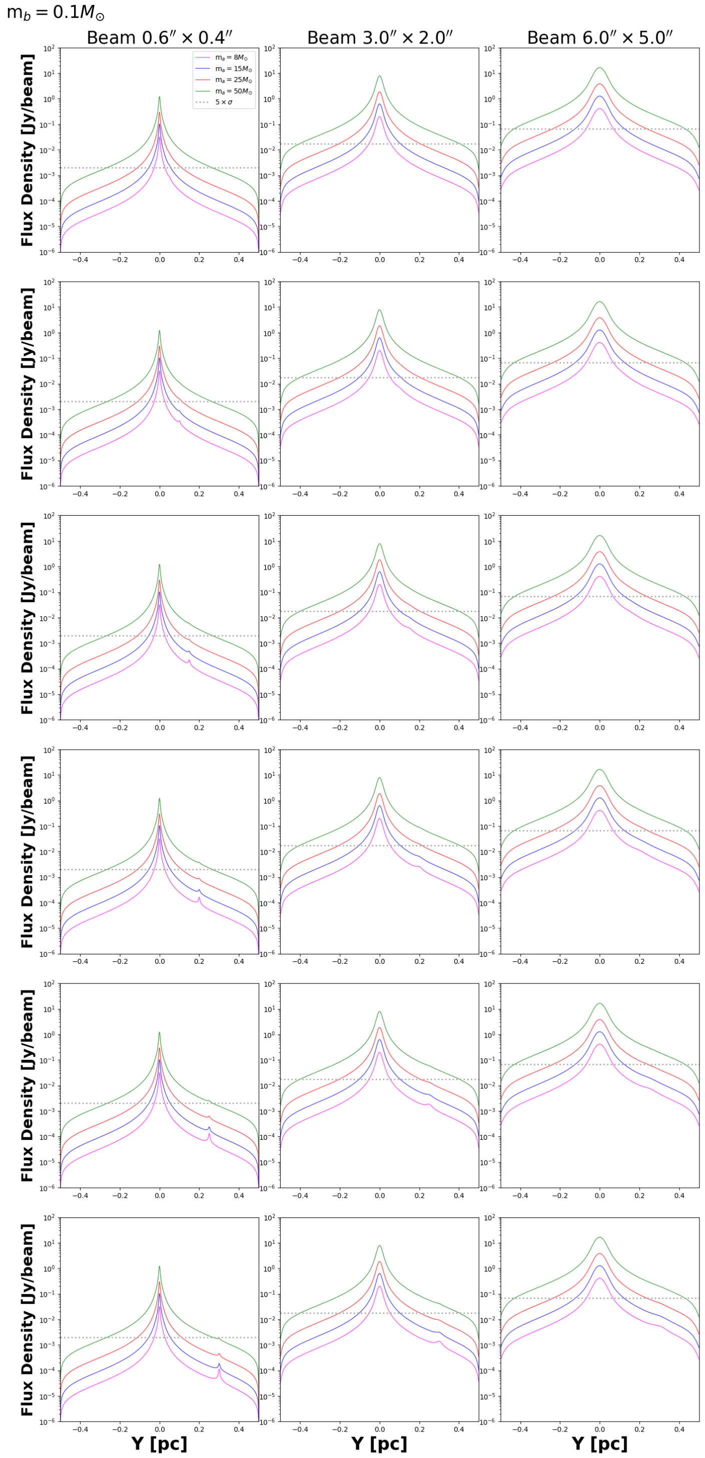

Figure 3.18: One-dimensional slices crossing the locations of the high- and low-mass sources extracted from the synthetic continuum images (where m$_b$ = 0.1 M$_\odot$). The intensities are plotted in units of Jansky per square arcsecond area. Results with different resolution are plotted in different columns (left: 0.6″ × 0.4″; middle: 3.0″ × 2.0″; right: 6.0″ × 5.0″). Results with different separation are shown in rows (from top to bottom: 0.05 pc, 0.10 pc, 0.15 pc, 0.20 pc, 0.25 pc, 0.30 pc). The masses of the high-mass source (m$_a$) are colour-coded (magenta: 8 M$_\odot$;blue: 15 M$_\odot$; red: 25 M$_\odot$; green: 50 M$_\odot$). The grey dotted lines show the 5σ threshold in practical ALMA, SMA and ACA observations (taken from literature, see details in section 4.3.1).

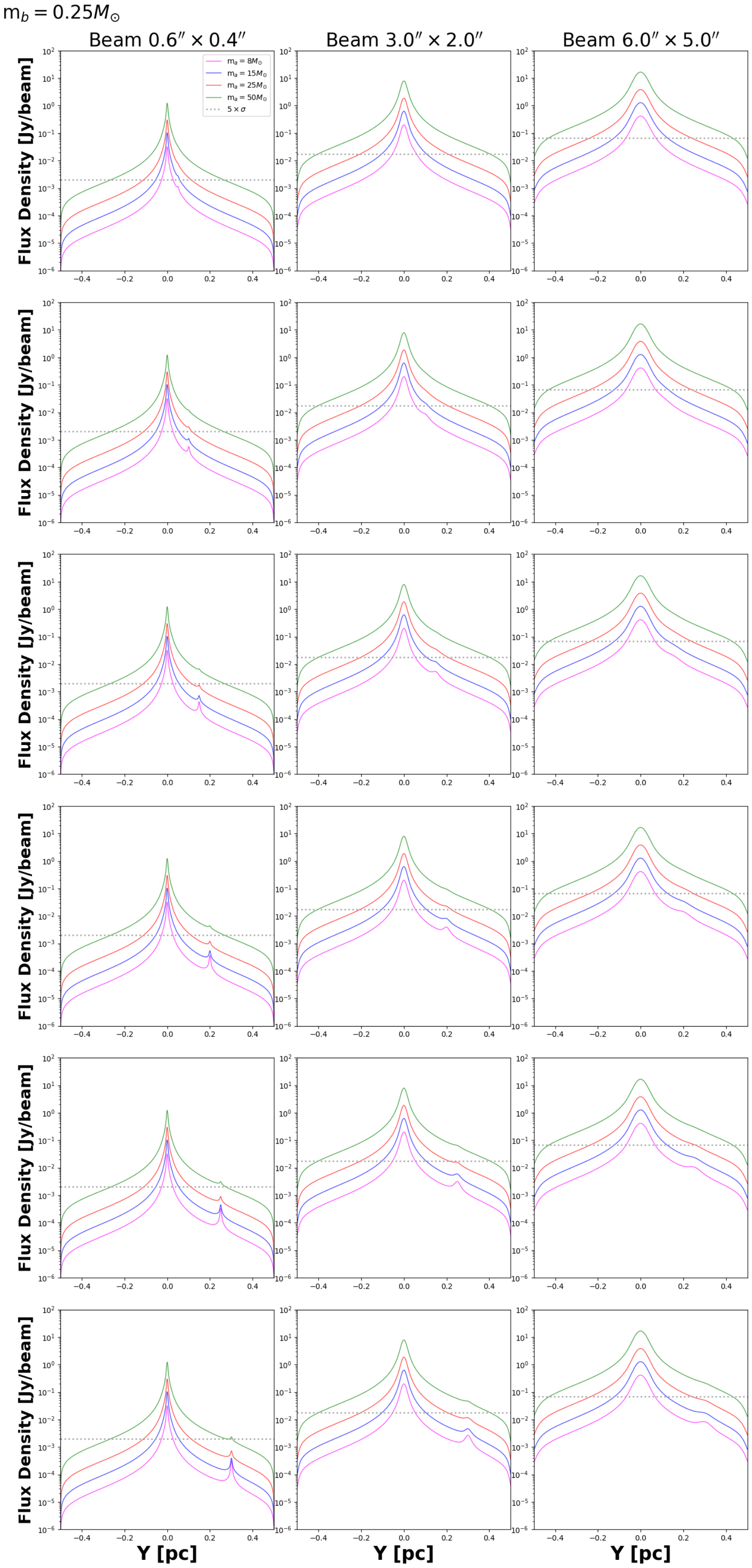

Figure 3.19: As Fig.3.18 with $m_b = 0.25$ $M_\odot$.

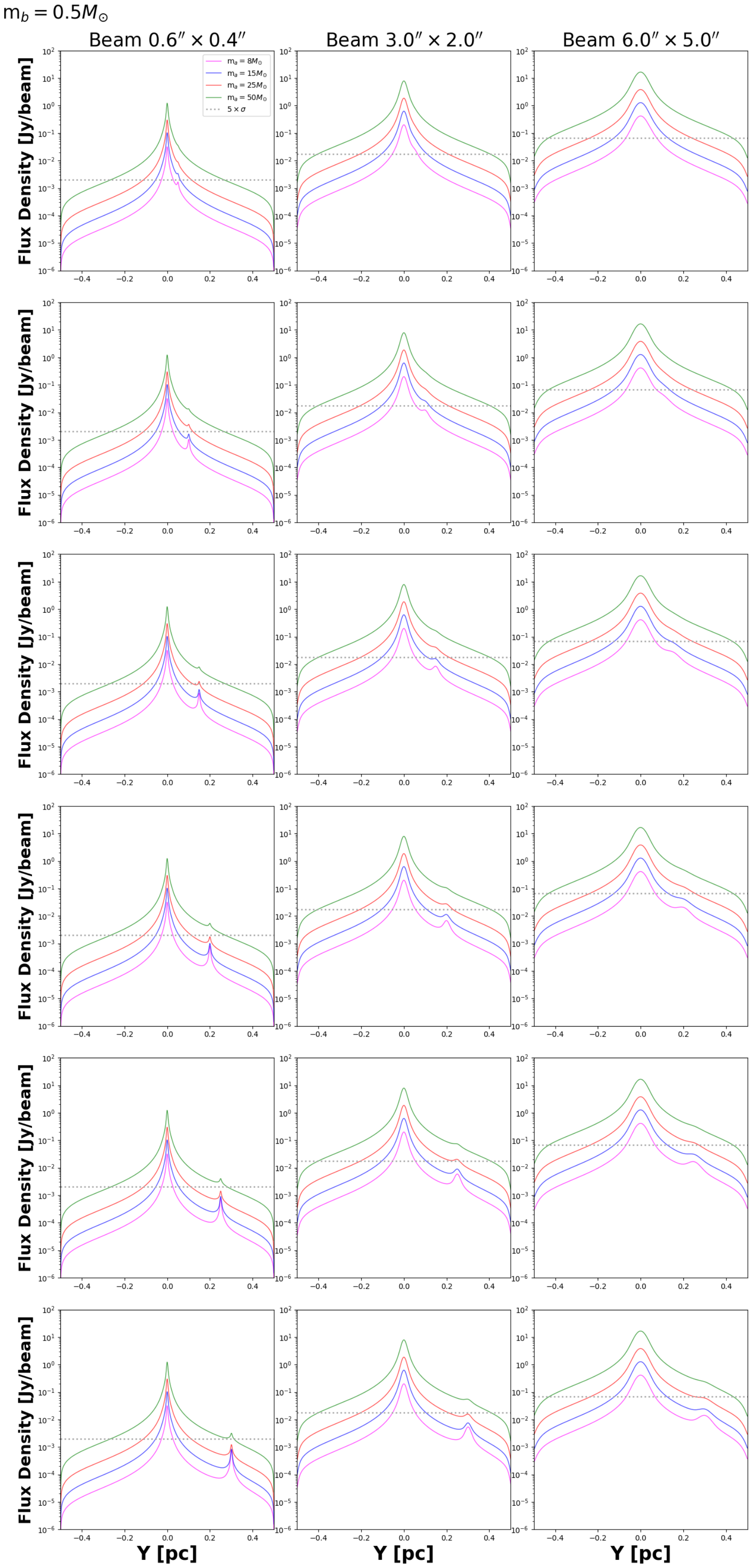

Figure 3.20: As Fig.3.18 with $m_b = 0.5$ M$_\odot$.

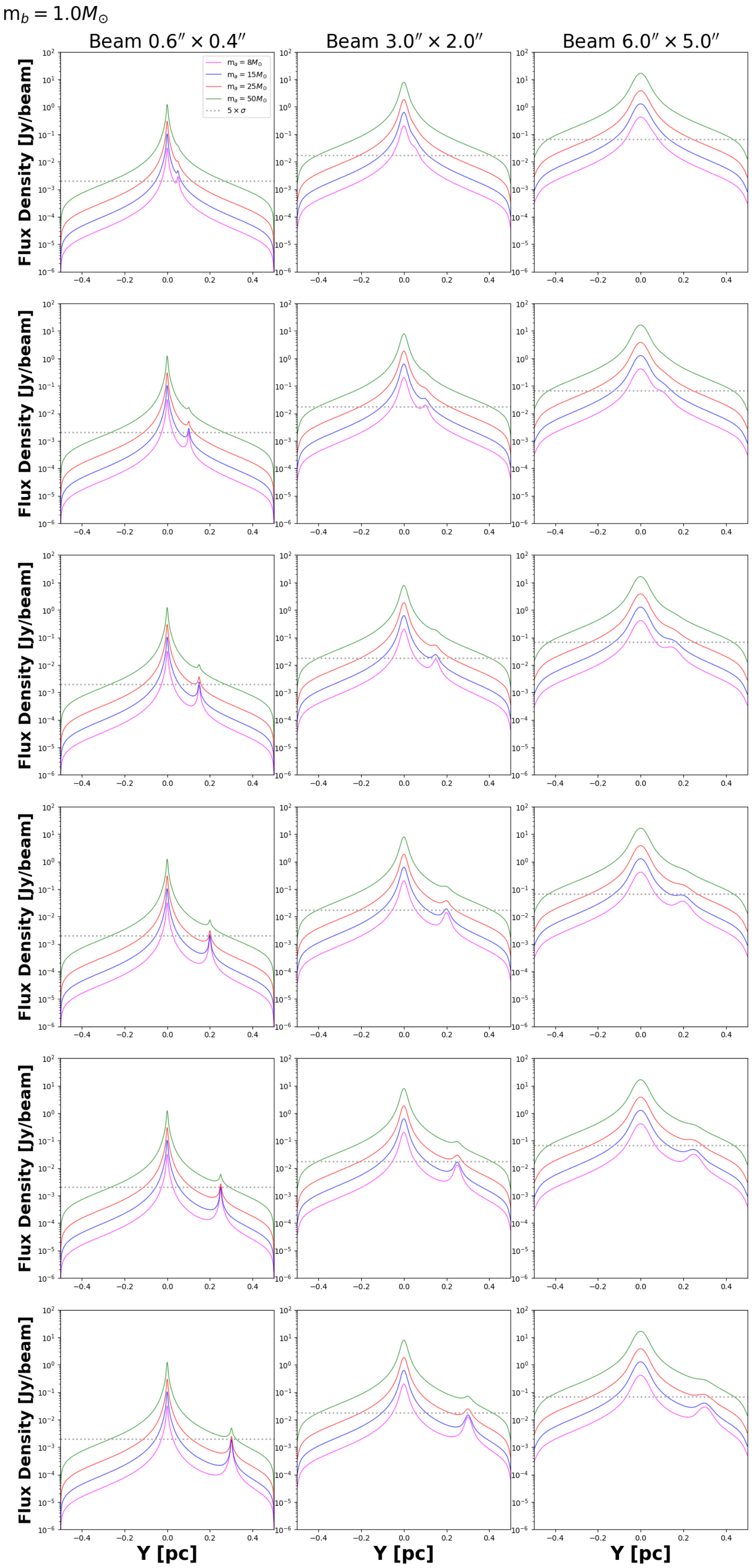

Figure 3.21: As Fig.3.18 with $m_b = 1.0$ $M_\odot$.

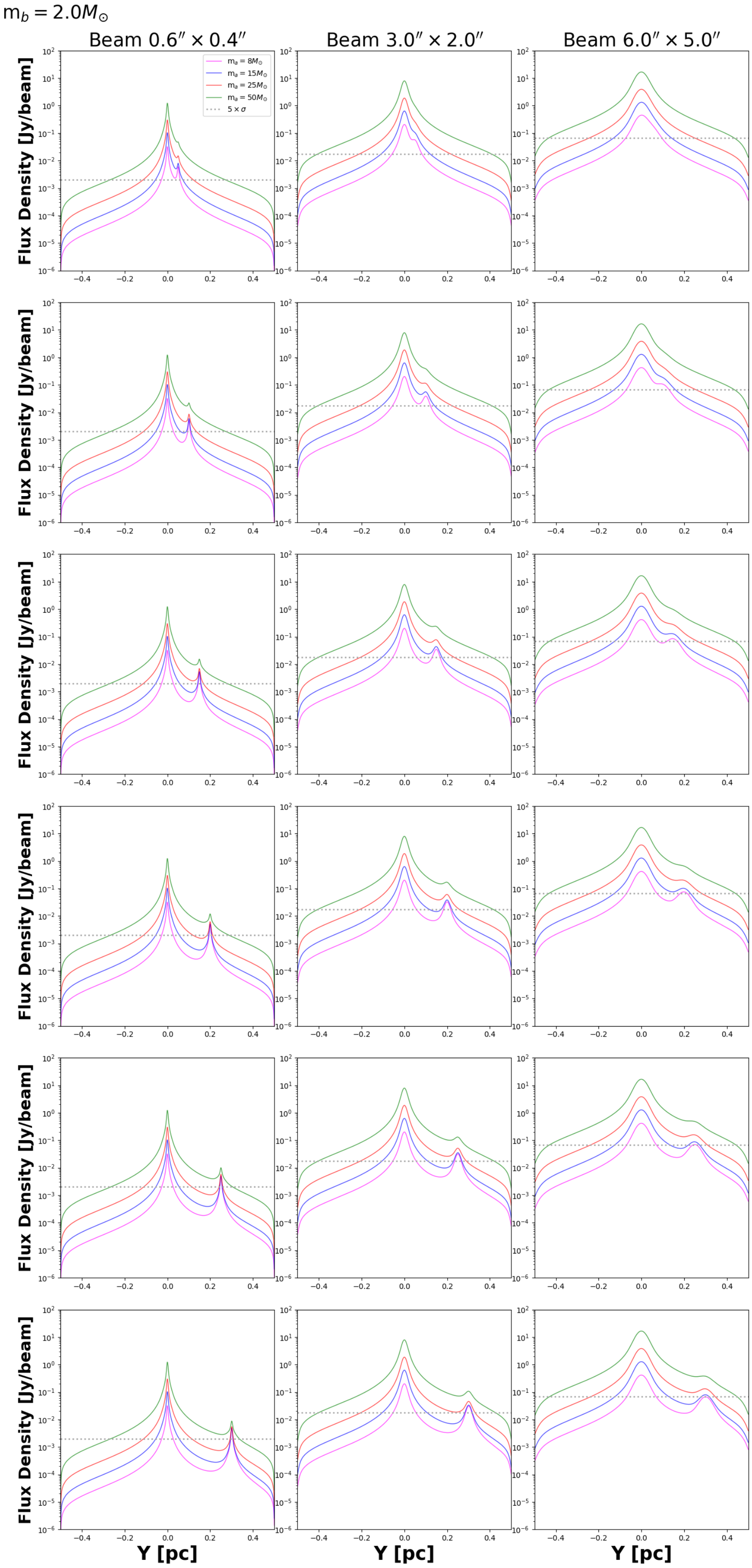

Figure 3.22: As Fig.3.18 with $m_b = 2.0$ M$_\odot$.

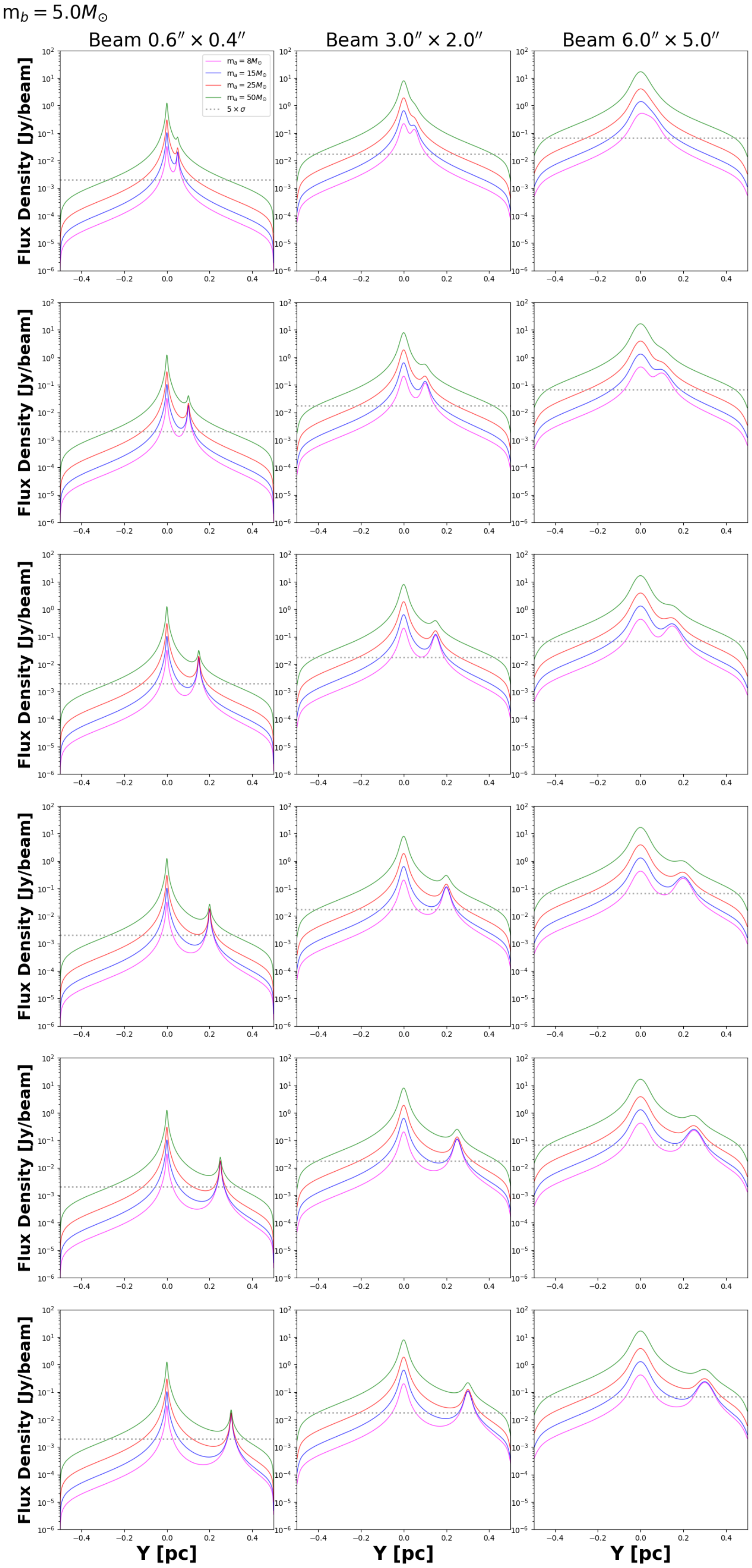

Figure 3.23: As Fig.3.18 with m$_b$ = 5.0 M$_\odot$.

3.3.2 Excess Flux

To quantitatively determine the visibility of the secondary peak, we introduce a quantity called Excess Flux (I_{ex}). The Excess Flux is defined to be the intensity at the location of the low-mass source (I_b) minus the minimum intensity between the locations of the high- and low-mass sources (I_{min}):

$$I_{ex} = I_b - I_{min}. \tag{3.10}$$

The Excess Flux value describes how significant the emission from the low-mass source is in contrast with the intermediate environment of the high- and low-mass sources. Thus it can be employed to analyse the detectability of the low-mass source.

We estimate the Excess Flux values for all of the 432 models, and visualise their distribution against assumed parameters. We first convert the Excess Flux in unit of Jansky per square arcsecond area to provide an overview of the distribution. Fig.3.24 shows the Excess Flux values for all models in colourscale. Results of different m_a are organised from top to bottom rows ($m_a = 8,15,25,50\ M_\odot$ respectively), with three columns showing the three different beam sizes (from left to right: $0.6'' \times 0.4''$, $3.0'' \times 2.0''$, $6.0'' \times 5.0''$)). For each panel, the y axis shows the masses of the low-mass source (from bottom to top: $m_b = 0.1,0.25,0.5,1.0,2.0,5.0\ M_\odot$); the x axis shows the six different separations (S = 0.05,0.10,0.15,0.20,0.25,0.30 pc from left to right). The black "x" symbols mark the cases where $I_{ex} = 0$, which implies there is no local minimum between the high- and low-mass sources (i.e. the intensity decreases monotonically from the centre to the location of the low-mass source). Under these circumstances, the secondary peak has joined the central main peak, disappearing completely, or appearing as a shoulder of the central peak rather than a separate peak. Accordingly, the low-mass source is not visible intrinsically, or in the context of Excess Flux values. Fig.3.24 shows that cases with higher m_a, lower m_b, smaller separations, and larger beam sizes are more likely to have $I_{ex} = 0$. This is consistent with the trends indicated by the Jy/arcsec^2 1D slices (see Section 4.3.1): the low-mass source might be invisible with a high m_a, low m_b, large separation and beam.

Fig.3.24 allows a systematic comparison of the visibility of the low-mass source between cases with different separations, m_b, and beam sizes. First, the Excess Flux increases as the separation increases. For example, for the cases with $m_a = 8\ M_\odot$, $m_b = 5\ M_\odot$, and the smallest beam (corresponding to the top row of the top left panel), the Excess Flux increases by ∼9 mJy/arcsec^2 (∼ 17 %) when the separation varies from 0.05 pc to 0.30 pc. Second, the Excess

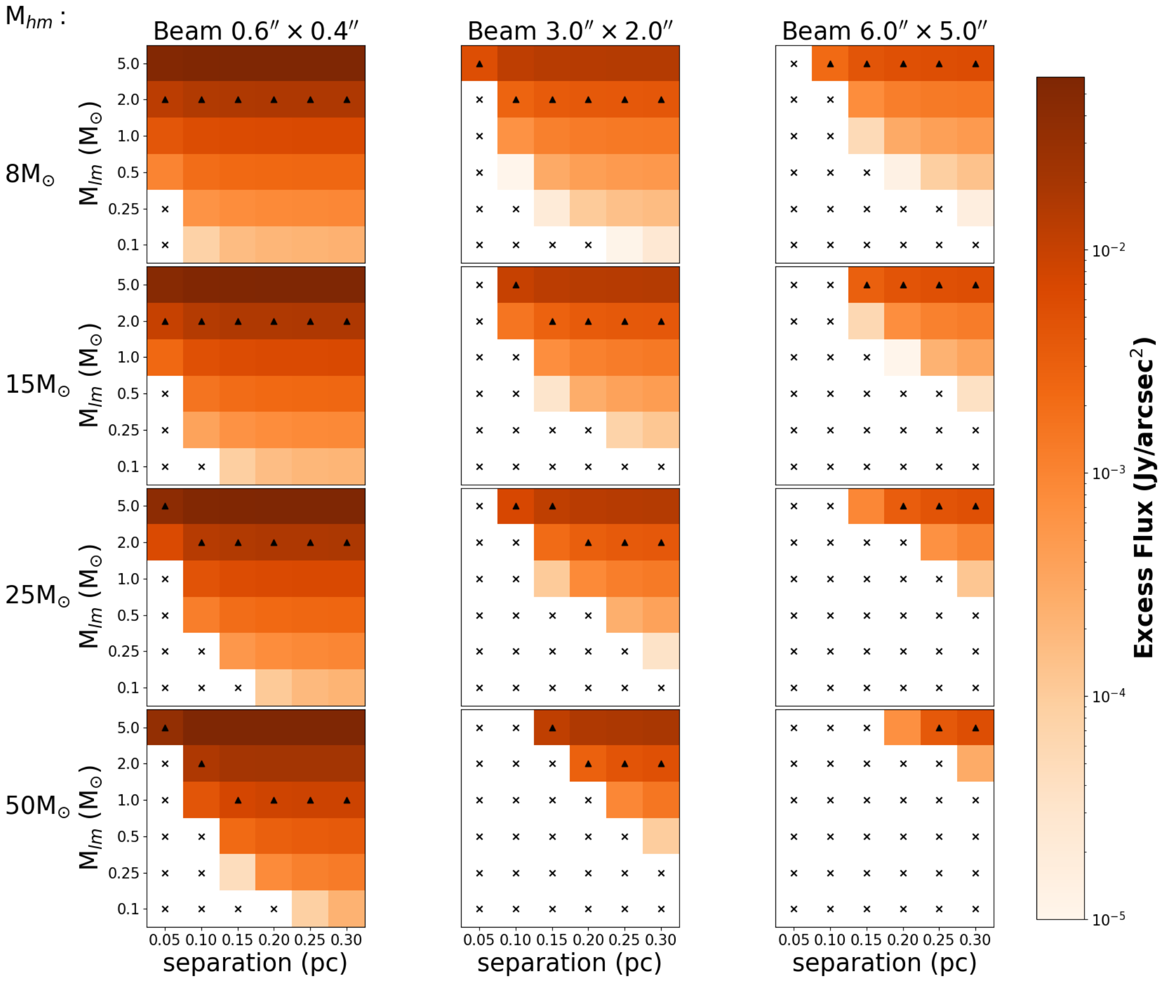

Figure 3.24: colourscale: the excess flux versus the mass of the low-mass source (y axis) and the separation (x axis) for different masses of the high-mass source (each row). The excess flux is calculated by the secondary peak minus the valley between the two sources, with a unit of Jansky per square arcsecond area. The cases where the calculated excess flux equals zero are marked with “x” symbols. The upward triangles mark the boundary above which the excess flux values are greater than 5 $\times\sigma_{rms}$.

Flux increases when the mass of the low-mass source increases. For the cases with $m_a = 8$ M$_\odot$, S = 0.3 pc, and the smallest beam (corresponding to the right column of the top left panel), the Excess Flux increases by ~59 mJy/arcsec^2 (~ a factor of 258) when m_b increases from 0.1 M$_\odot$ to 5 M$_\odot$. Thirdly, the Excess Flux decreases as the beam becomes larger. For the cases with $m_a = 8$ M$_\odot$ (corresponding to the top panel), the maximum Excess Flux (corresponding to the case with $m_a = 8$ M$_\odot$, $m_b = 5$ M$_\odot$, S = 0.3 pc; the top right pixel of each subplot) decreases by ~54 mJy/arcsec^2 (~ 90 %) when the beam area varies from the smallest size to the largest one. The variations of the Excess Flux against the m_b, separation and beam size are in agreement with the trends demonstrated by the Jy/arcsec^2 1D slices. To conclude, the low-mass source is more visible with a higher m_b, larger separation and smaller beam size. Moreover, the values of the Excess Flux variations indicate that the mass of the low-mass source has the most dominant influence on its visibility, while the beam size is the second dominant factor and the separation is the least important effect. Note that the importance of these parameters are only discussed for the assumed parameter space.

The variation of the Excess Flux versus the mass of the high-mass source, however, is not consistent with the general trends implied by the 1D slices. Based on Fig.3.8 - Fig.3.13, the low-mass source becomes less visible when the mass of the high-mass source increases. But Fig.3.24 does not indicate a monotonic decrease in Excess Flux with increasing m_a. For example, for the cases with the largest beam (corresponding to the right panel), the maximum Excess Flux (corresponding to the case with $m_b = 5$ $M_\odot$, $S = 0.3$ pc; the top right pixel of each subplot) decreases from ~5.7 to ~5.4 and ~5.0 mJy/arcsec^2 when m_a increases from 8 to 15 and 25 $M_\odot$. When m_a increases from 25 to 50 $M_\odot$, however, the maximum Excess Flux starts to increase from ~5.0 to ~5.7 mJy/arcsec^2, indicating that the low-mass source is roughly as visible as in the case with $m_a = 8$ $M_\odot$. This is probably due to the fact that the emission from the high-mass source is so strong in the most massive case that it reshapes the distribution of the intensity in the intermediate environment of the two sources. Therefore, we must be careful when discussing the effects of the mass of the high-mass source on the visibility of the low-mass source in the context of Excess Flux.

We plot the distribution of the Excess Flux values in units of Jansky per beam to compare with practical observations and then to derive the detectability of the low-mass source. Fig.3.25 is the same as Fig.3.24 but with values in Jansky per beam. The lightblue circles mark the cases where the intensity at the location of the low-mass source is above the $5 \times \sigma_{rms}$ threshold. The upward triangles mark the boundary above which the Excess Flux values are greater than $5 \times \sigma_{rms}$ (i.e. for each column of each subplot, the pixel with or above the upward triangle is the case where the Excess Flux $> 5 \times \sigma_{rms}$). The low-mass source will be regarded as detectable if two criteria are met:

- 1) The intensity at the location of the low-mass source is $> 5 \times \sigma_{rms}$.
- 2) The Excess Flux is $> 5 \times \sigma_{rms}$.

If only criterion 1) is met, the emission at the pre-defined location of the low-mass source will be above the representative sensitivity threshold, but the source itself may or may not appear distinguishable. If only criterion 2) is met, the emission from the low-mass source will make itself significant against its intermediate environment intrinsically, but signals might be wiped out by the rms noise in practical observations. Therefore, we strictly require the low-mass source to meet both criteria to be considered as detectable. On Fig.3.25, the cases that have met criterion 1) (maked by lightblue circles) encompass the cases that have met criterion 2). Thus, the upward triangles can further indicate the detectability of the low-mass source in the context of Excess Flux. To conclude, for $\mathrm{m}_a = 8$, the low-mass source is detectable:

- for all separations if $\mathrm{m}_b \geqq 2.0\ \mathrm{M}_\odot$ with the smallest beam;
- for separations $\geqq 0.1$ pc if $\mathrm{m}_b \geqq 2.0\ \mathrm{M}_\odot$ and separation $= 0.05$ pc if $\mathrm{m}_b \geqq 5.0\ \mathrm{M}_\odot$ with the middle beam;
- for separations $\geqq 0.1$ pc if $\mathrm{m}_b \geqq 5.0\ \mathrm{M}_\odot$ with the largest beam.

For $\mathrm{m}_a = 15$, the low-mass source is detectable:

- for all separations if $\mathrm{m}_b \geqq 2.0\ \mathrm{M}_\odot$ with the smallest beam;
- for separation $\geqq 0.15$ pc if $\mathrm{m}_b \geqq 2.0\ \mathrm{M}_\odot$ and separation $= 0.1$ pc if $\mathrm{m}_b \geqq 5.0\ \mathrm{M}_\odot$ with the middle beam;
- for separation $\geqq 0.15$ pc if $\mathrm{m}_b \geqq 5.0\ \mathrm{M}_\odot$ with the largest beam.

For $\mathrm{m}_a = 25$, the low-mass source is detectable:

- for separation $\geqq 0.1$ pc if $\mathrm{m}_b \geqq 2.0\ \mathrm{M}_\odot$ and separation $= 0.05$ pc if $\mathrm{m}_b \geqq 5.0\ \mathrm{M}_\odot$ with the smallest beam;
- for separation $\geqq 0.20$ pc if $\mathrm{m}_b \geqq 2.0\ \mathrm{M}_\odot$ and separation $= 0.1, 0.15$ pc if $\mathrm{m}_b \geqq 5.0\ \mathrm{M}_\odot$ with the middle beam;
- for separation $\geqq 0.20$ pc if $\mathrm{m}_b \geqq 5.0\ \mathrm{M}_\odot$ with the largest beam.

For $\mathrm{m}_a = 50$, the low-mass source is detectable:

- for separation $\geqq$ 0.15 pc if $\mathrm{m}_b \geqq 1.0\ \mathrm{M}_\odot$, separation = 0.1 pc if $\mathrm{m}_b \geqq 2.0\ \mathrm{M}_\odot$, and separation = 0.05 pc if $\mathrm{m}_b \geqq 5.0\ \mathrm{M}_\odot$ with the smallest beam;
- for separation $\geqq$ 0.20 pc if $\mathrm{m}_b \geqq 2.0\ \mathrm{M}_\odot$ and separation = 0.15 pc if $\mathrm{m}_b \geqq 5.0\ \mathrm{M}_\odot$ with the middle beam;
- for separation $\geqq$ 0.25 pc if $\mathrm{m}_b \geqq 5.0\ \mathrm{M}_\odot$ with the largest beam.

Note that a significant fraction of cases (194, $\sim$ 45%) are discarded according to the $I_{ex} = 0$ criterion before the detectability determination. It is reasonable to conclude that the low-mass source is not detectable if $I_{ex} = 0$ in the context of Excess Flux. However, this does not exclude the possibility of detecting the low-mass source in those cases using other methods. For example, for the case with $\mathrm{m}_a = 50\ \mathrm{M}_\odot$, $\mathrm{m}_b = 5\ \mathrm{M}_\odot$, separation = 0.15 pc, and the largest beam size, the 1D slice shows that the secondary peak is blended with the central peak with a shoulder remaining at the location of the low-mass source. There is no local minimum between the high- and low-mass sources, so that no detectability can be derived using Excess Flux. However, it may still be possible to decompose the secondary peak from the profile by 1D multi-component fitting such as Gaussian Decomposition. Moreover, 2D multi-Gaussian fitting might also help to dissentangle the low-mass source from the environment of the high-mass source if 2D images are employed. To summarise, the detectability inferred with Excess Flux is supposed to be considered as a lower limit. If the low-mass source is detectable in the context of Excess Flux, it is probably also detectable with various other methods. If the low-mass source is close to the Excess Flux detection boundary, but not detectable based on criterion 1) and 2), it might become detectable with more sophisticated methods.

3.3.3 Contrast

To assist the quantitative determination of the detectability of the low-mass source, we introduce a quantity called contrast C, which is defined by:

$$C = \frac{I_b - I_{min}}{I_{min}}, \tag{3.11}$$

where I_b is the intensity at the location of the low-mass source, I_{min} is the minimum intensity between the locations of the high- and low-mass sources. The contrast values are calculated using Equation 3.11 for all the 432 models, and then compared with the contrast values translated from the 5 $\times\sigma_{rms}$ thresholds.

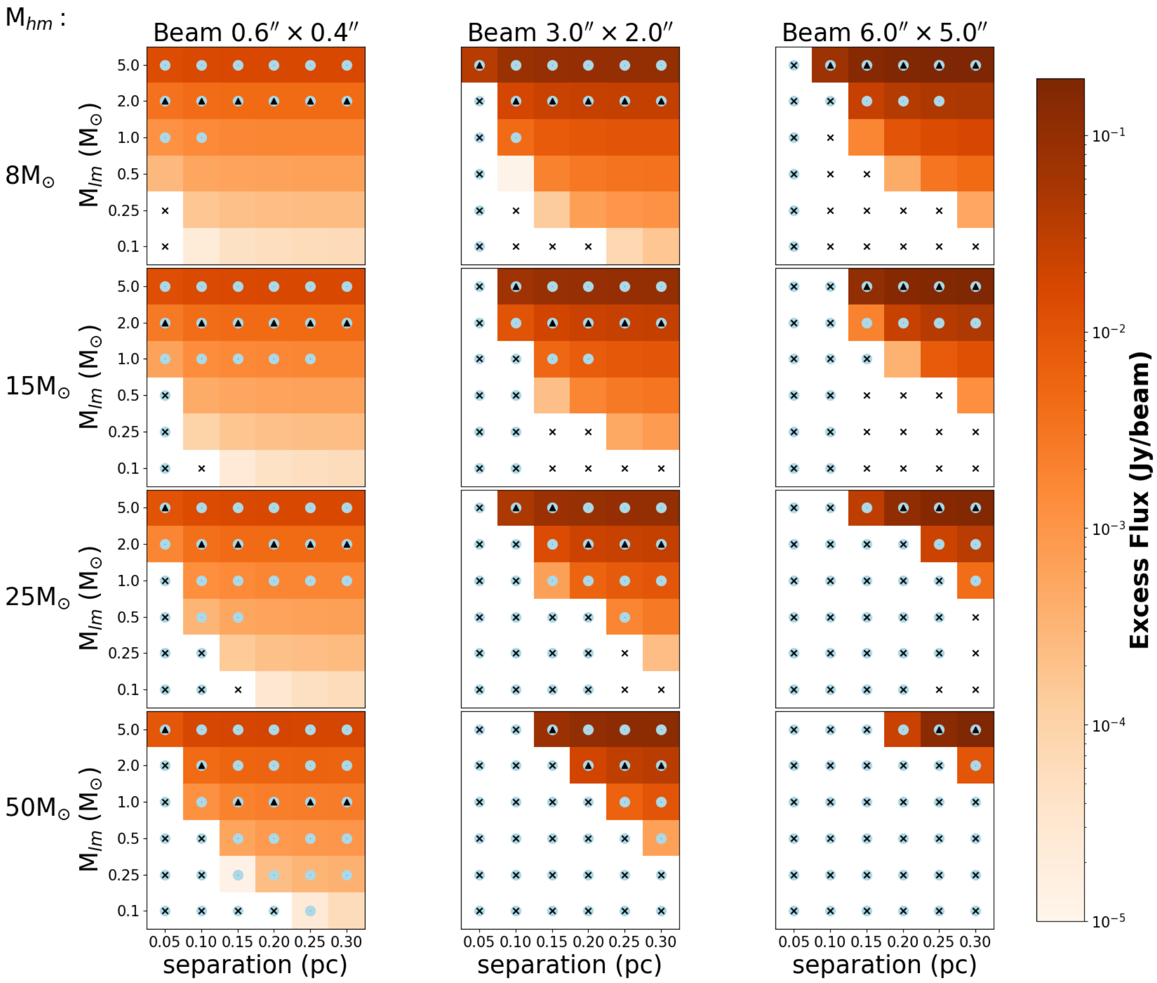

Figure 3.25: This figure is the same as Fig.3.24 but the excess flux is in unit of Jansky per beam. The lightblue circles mark the cases where the intensity at the location of the low-mass source is above the 5 $\times\sigma_{rms}$ threshold. The upward triangles mark the boundary above which the Excess Flux values are greater than 5 $\times\sigma_{rms}$.

Fig.3.26 shows the contrast values with units of Jansky per beam in colourscale. Values with different m_a are organised from top to bottom rows (m_a = 8,15,25,50 M$_\odot$ respectively), with three columns showing the three different beam sizes (from left to right: $0.6'' \times 0.4''$, $3.0'' \times 2.0''$, $6.0'' \times 5.0''$). For each panel, the y axis shows the masses of the low-mass source (from bottom to top: m_b = 0.1,0.25,0.5,1.0,2.0,5.0 M$_\odot$); the x axis shows the six different separations (S = 0.05,0.10,0.15,0.20,0.25,0.30 pc from left to right). The black “x” symbols mark the cases where C = 0 (i.e. $I_b = I_{min}$), which are the same as those where $I_{ex} = 0$ on Excess Flux figures (see Section 4.3.2). The low-mass source is not detectable in the context of contrast under these circumstances. The black filled circles mark the cases where the contrast of the secondary peak is greater than that converted from the 5 $\times\sigma_{rms}$ threshold: C > $C_{5\sigma}$, where $C_{5\sigma}$ is given by

$$C_{5\sigma} = \frac{5 \times \sigma_{rms}}{I_{min}}, \tag{3.12}$$

with I_{min} the minimum intensity between the locations of the high- and low-mass sources. Again, these cases are the same as those with $I_{ex} > 5 \times \sigma_{rms}$ on Fig.3.25. Fig.3.27 is the same figure as Fig.3.26 but with contrast values in units of Jansky per square arcsecond area.

Unlike the Jansky/beam figures for 1D slices or Excess Flux, the Jansky/beam contrast figure provides a comprehensive comparison of the visibility of the low-mass source between cases with different m_a, m_b, separations, and beam sizes. In particular, Fig.3.26 shows that the contrast value decreases by an order of magnitude as the beam size increases from $0.6'' \times 0.4''$ to $6.0'' \times 5.0''$, indicating that the low-mass source is less visible with lower spatial resolution. The Jy/arcsec^2 contrast figure implies the same trends as the Jansky/beam one does, but with greater differences between the contrast values under different resolution. For example, the contrast value in Jy/arcsec^2 can decrease by two orders of magnitude, if the beam size is increased from $0.6'' \times 0.4''$ to $6.0'' \times 5.0''$.

The low-mass source is considered to be detectable in the context of contrast only if the contrast value satisfies $C > C_{5\sigma}$. The cases where the low-mass source is detectable are marked with the black filled circles on Fig.3.26 and Fig.3.27. To conclude, the detectability of the low-mass source determined with contrast values is consistent with that of Excess Flux. Compared with Excess Flux, contrast allows a more comprehensive and systematic comparison of the visibility of the low-mass source within the parameter space that is explored.

3.4 Discussion

3.4.1 Radiative transfer modelling vs. optically-thin calculation

If the dust continuum emission is optically-thin ($\tau \ll 1$) at 1.3 mm, the flux density can also be determined analytically with a given density, temperature and opacity. To examine whether the optically-thin assumption is applicable to our models, we estimate the optical depth of this clump for the most massive case with $m_a = 50\ M_\odot$, $m_b = 5\ M_\odot$, and separation $= 0.15$ pc using the “tracetau” command in RADMC-3D. Fig.3.28 shows the distribution of optical depth on the projection plane in colourscale. The mean optical depth of this clump is ~ 0.003, indicating that the optical depth in the most massive case is small in general.

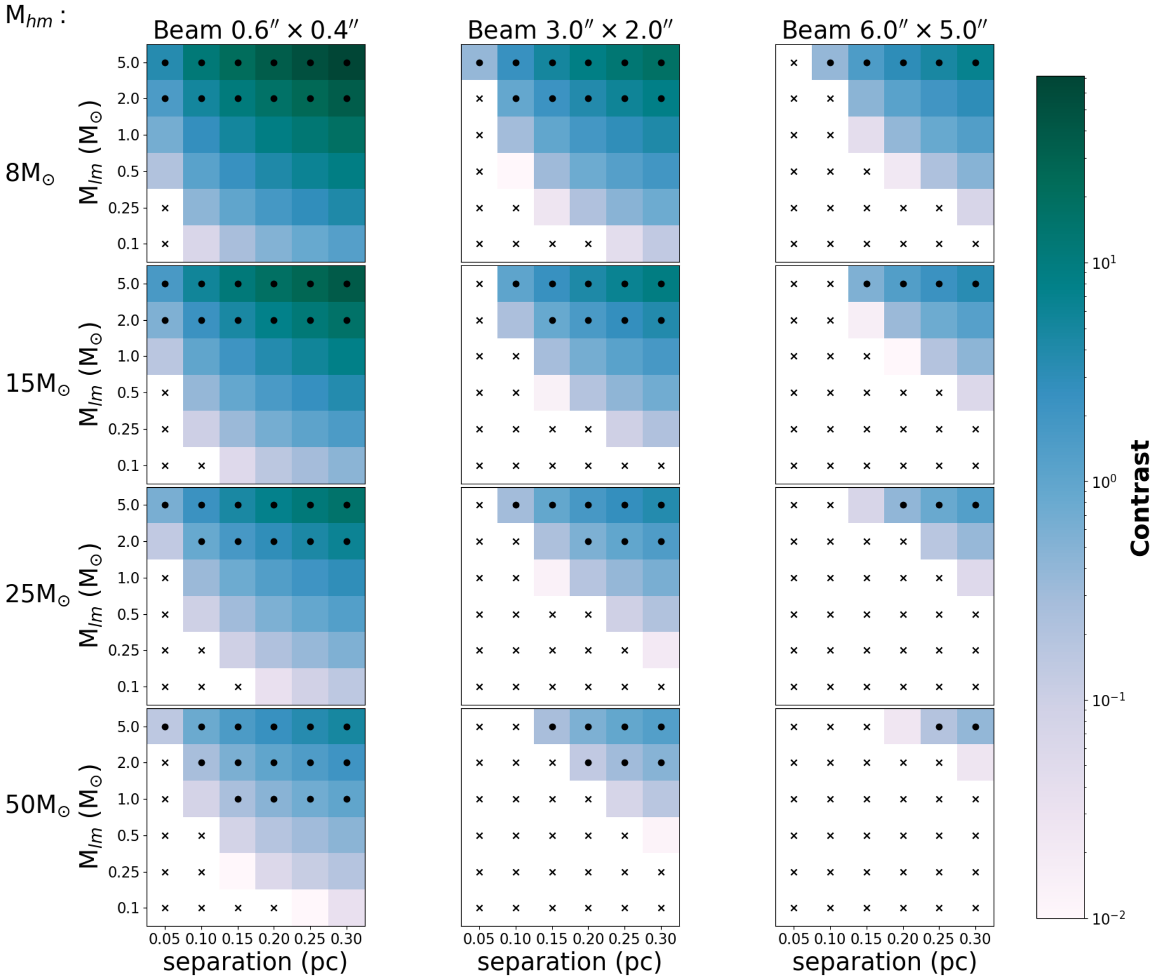

Figure 3.26: colourscale: the contrast versus the mass of the low-mass source (y axis) and the separation (x axis) for different masses of the high-mass source (each row). The contrast is given by (the secondary peak - the valley)/the valley, where the intensity is in unit of Jansky per beam. The black filled circles mark the cases where the contrast of the secondary peak is greater than that converted from 5σ noise. Cases where the secondary peak equals the valley are marked with X symbols.

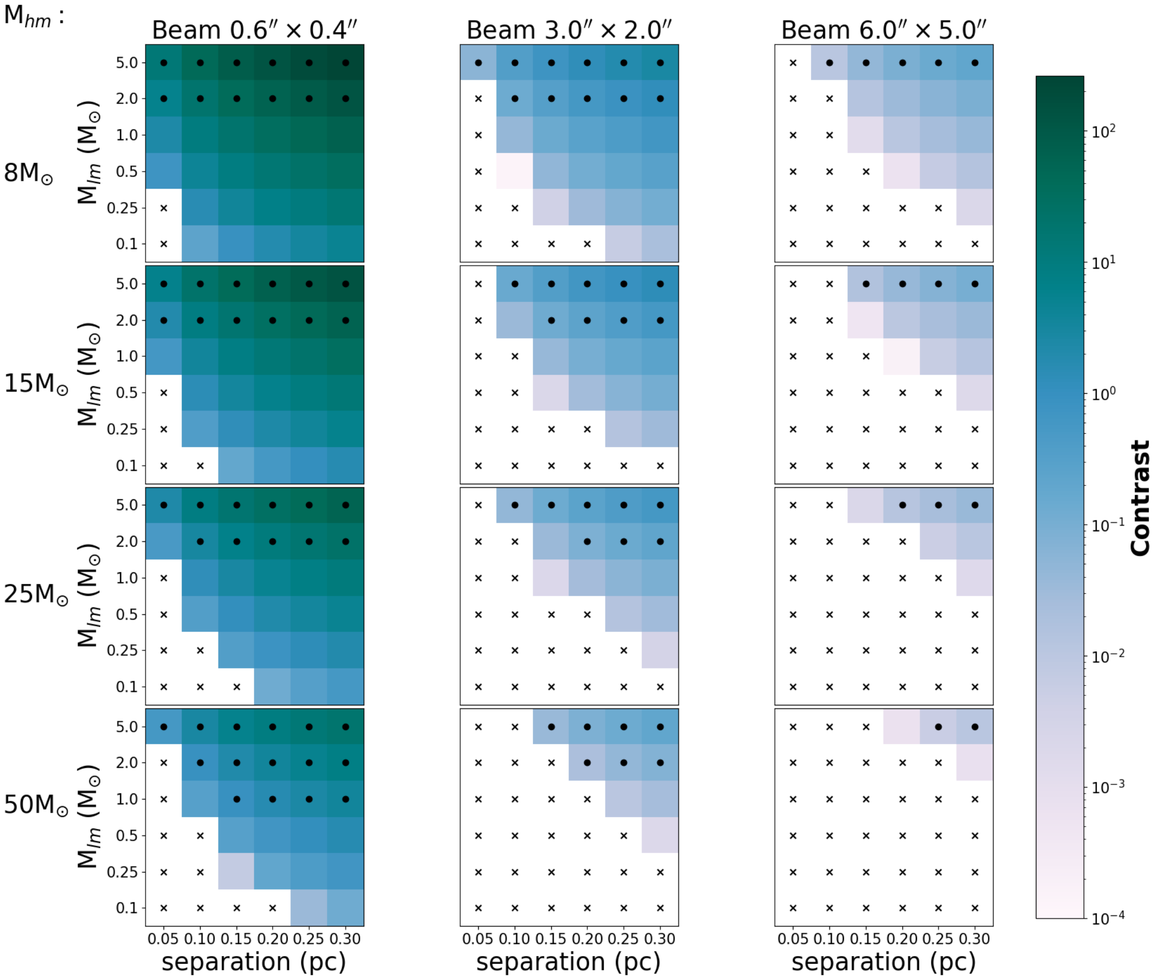

Figure 3.27: colourscale: the contrast versus the mass of the low-mass source (y axis) and the separation (x axis) for different masses of the high-mass source (each row). The contrast is given by (the secondary peak - the valley)/the valley, where the intensity is in unit of Jansky per square arcsecond area. The black filled circles mark the cases where the contrast of the secondary peak is greater than that converted from 5σ noise. Cases where the secondary peak equals the valley are marked with X symbols.

However, at the clump centre where the high-mass source is located, the optical depth reaches its maximum value which is ∼ 0.3. We also calculate the dust emission for the most massive case assuming optically-thin using equation A.27 in Kauffmann et al. (2008). We extract a 1D slice along the locations of the high- and low-mass sources from the 2D image, and compare it with the 1D slice from RT modelling. Fig.3.29 shows the fractional difference of the two slices, which is defined by (optically-thin - RT)/RT. The difference is ∼ 2% at the location of the low-mass source and > 10% at the location of the high-mass source, implying that the optically-thin calculation can overestimate the dust emission by up to 10% for the most massive case. Therefore, RT modelling is more appropriate than optically-thin calculation for this work as the effects of optical depth cannot be completely ignored.

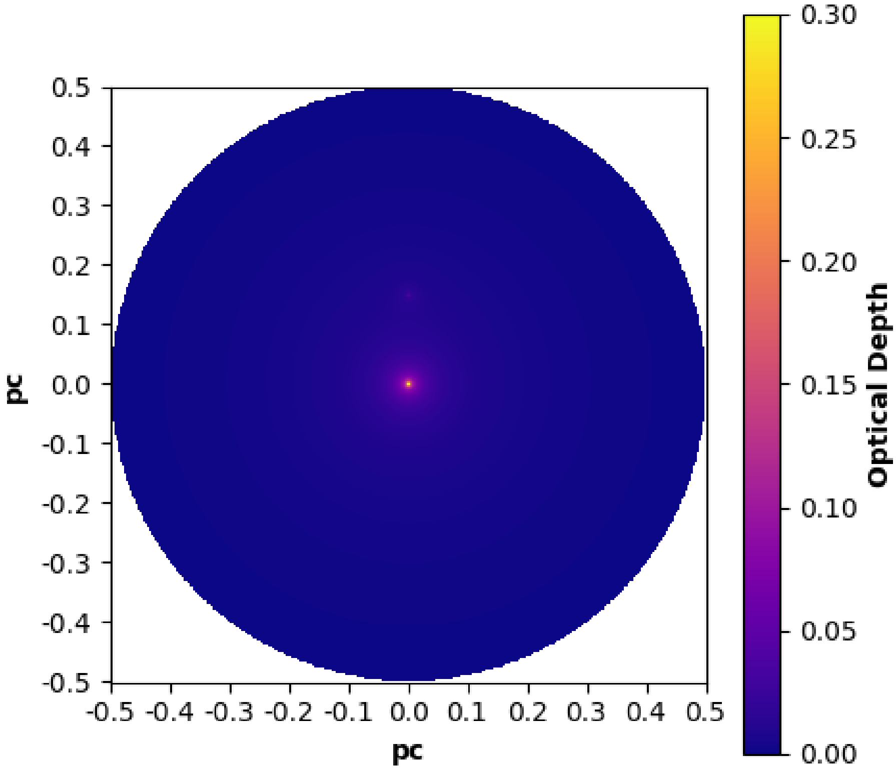

Figure 3.28: The distribution of optical depth on the projection plane for the case with m_a = 50 $M_\odot$, m_b = 5 $M_\odot$, separation = 0.15 pc.

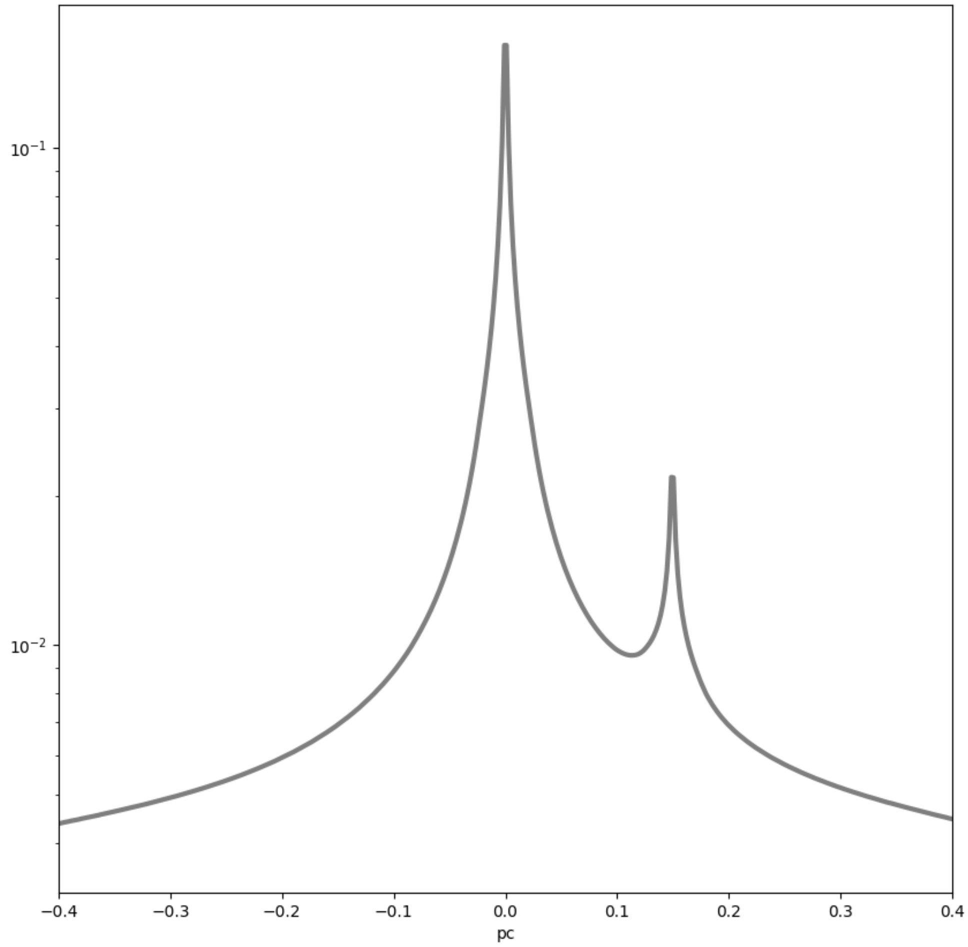

Figure 3.29: The fractional difference of the 1D slices between the optically-thin calculation and the RT modelling. The fraction is given by (OT - RT)/RT.

3.4.2 Observability of prestellar cores

The earliest phases of low-mass stars are known to be self-gravitating, centrally condensed, starless cores, so called low-mass prestellar cores. These cores are cold (7-15 K), dense ($n_{H^2} \sim 10^4$-10^6 cm^{-3}), with no evidence of on-going star-forming activities such as molecular outflows (see the review in Caselli & Ceccarelli 2012). The lifetime of low-mass prestellar cores is $\sim 10^5$ yr, making them statistically prevalent in star-forming regions. Surveys of nearby star-forming regions have identified a significant population of sources as low-mass prestellar cores, indicating the evolutionary stages of young low-mass stars (e.g. Enoch et al. 2008).

The semi-analytic framework of this work can also be employed to explore the observability of low-mass prestellar cores. We model the emission of prestellar cores by removing the thermal structure but keeping the density structure associated with the low-mass source (i.e. assuming the radiative feedback from the low-mass source equals to zero). We first run a test with $m_a = 25\ M_\odot$, $m_b = 0.5\ M_\odot$, $S = 0.1$ pc, and the highest resolution. The peak intensity of the low-mass prestellar core is $\sim$ 97% of that of the protostellar core. This suggests that the modelled emission from low-mass cores is dominated by density rather than temperature. We then run a few tests by varying separation from 0.05, 0.1 to 0.3 pc with $m_b = 0.5\ M_\odot$ and $m_b = 0.5, 0.25, 0.1\ M_\odot$ with $S = 0.3$ pc. We find that the difference between the intensities of proto- and pre-stellar cores decreases from 4%, 3% to 2% as the separation increases. This again indicates the significant influence of the high-mass source on the emission of low-mass both proto- and pre-stellar cores in its surroundings. The intensity difference decreases from 1.9%, 1.5% to 1.1% as m_b decreases, again implying that the mass of the low-mass source is the predominant factor of its emission.

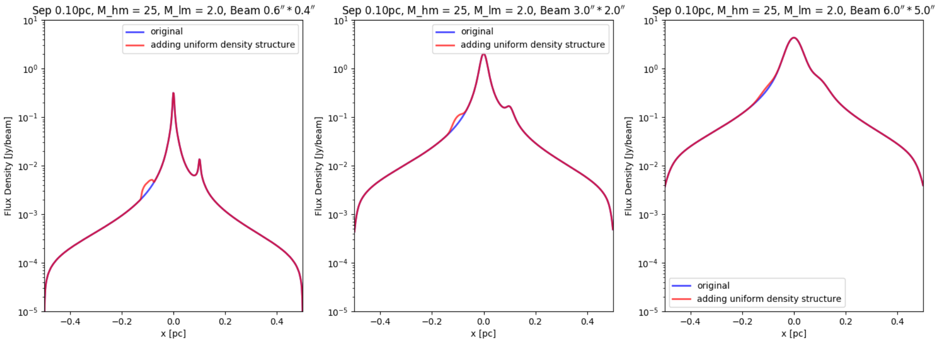

Figure 3.30: The 1D slices along the locations of high- and low-mass sources (red: with a uniform density sphere; blue: without). The separation is set to 0.1 pc, with $m_a = 25\ M_\odot$ and $m_b = 2\ M_\odot$. The three panels show the three different beam sizes (from left to right: $0.6'' \times 0.4''$, $3.0'' \times 2.0''$, $6.0'' \times 5.0''$).

We also run a test by adding a sphere of uniform density on the opposite side of the low-mass source with the same separation from the high-mass source. The sphere is set to have a radius equivalent to the assumed protostellar envelope radius (i.e. 5000 AU). The sphere density is calculated by assuming the mass within the sphere equivalent to the stellar mass of the low-mass source m_b. In the test, the separation is set to 0.1 pc, with $m_a = 25\ M_\odot$ and $m_b = 2\ M_\odot$. Similarly, we extract a 1D slice along the locations of the sphere, the high-mass source, and the low-mass source from the modelled images. Fig.3.30 shows the slices with the sphere (red) and without (blue) in different resolution (from left to right: $0.6'' \times 0.4''$, $3.0'' \times 2.0''$, $6.0'' \times 5.0''$). The added density structure appears as a separate peak in addition to the central and secondary peaks, which agrees with the expectation that a sphere density structure can be misleading in the identification of low-mass sources. However, the profile of the emission of the sphere is not similar to that of the real low-mass source, which is a natural result of modifying the density structure (power-law versus uniform). This indicates that we can potentially distinguish low-mass pre-/proto-stellar cores from other non-centrally-condensed density structure by investigating the radial profiles of their emission.

3.4.3 Caveats and future work

We note that there are caveats in our models. When constructing models, we have adopted pre-defined geometry for this protocluster. Both the high- and low-mass sources are assumed to be located at the $y = 0$ plane, with the same distance to the observer. However, protostars may in fact be located at different distances even if they are born in the same protocluster. The offset in the distance along the line of sight can affect the intensity of the low-mass source, and thus bring complexity to the discussion of its observability. This problem could potentially be avoided by post-processing hydro simulations instead of constructing analytic models. But hydro simulations are computationally expensive if a large parameter space is considered. Additionally, most high-mass stars are known to be born in binary or small multiple systems. We assume a single high-mass star in our models for simplicity. A potential improvement of this work is to replace the high-mass protostar with e.g. a high-mass protobinary, to see how the binarity would affect the observability of the low-mass source. The youngest high-mass protobinary system observed to date is G11.92-0.61 MM2 with a projected separation of $\sim$500 AU (Cyganowski et al. 2022). Note that the current set-up of our models has a cell size of 400 AU. It would be sufficient to model high-mass protobinaries if we improve the resolution of the models by e.g., 10 times (i.e. to achieve a cell size of e.g. 40 AU). Moreover, we model the protostellar density structure using power-law spherical envelopes, which describe the early phase of protostellar evolution. As a protostar grows in mass, it will accrete materials via the accretion disc and eject materials via bipolar molecular outflows. Outflows will push the protostellar envelope away and cause cavities. Robitaille (2017) present a set of models of young stellar objects which covers broad stages of protostellar evolution. Recent high-resolution ALMA observations reveal discs around proto-O stars with radii of $\sim$ 1000 - 2000 AU (e.g., Ilee et al. 2018, Williams et al. 2022). It would be useful to improve the assumed density structure especially for the protostellar cores with e.g. a powerlaw envelope plus a disc and/or cavities in the future work. Also, the assumed density structure in our models is smooth, which is a reasonable idealisation. To model the star-forming clump more realistically, we could potentially consider to construct a fractal density structure (Walch et al. 2015). The uniform sphere test discussed in section 4.4.2 demonstrates that an assumed density structure can behave similarly to real sources. It would be interesting to see how a random density structure would affect the identification of real sources.

When analysing these models, we have so far focused on the extracted 1D slices, which is convenient for the quantitative determination of observability and the comparison between the results of different parameters. The synthetic images are, however, unignorable information as main analysis is conducted on the 2D plane in practical observations. In the future, we can take the instrumental noise into consideration by e.g. simulating how the image will look like if observed by an interferometer (e.g. ALMA) using CASA task simobserve; we can extract sources by fitting 2D Gaussian models to the images using CASA task imfit, and then compare the flux densities with the noise values measured on the maps. We can potentially calculate the masses of the identified protostellar cores as if in observations (e.g. Cyganowski et al. 2017). When setting up models, we have fixed the mass of the protostellar core to be $M_{\rm env} = M_*$, which is not always true when the protostar evolves. It would be interesting to see how the calculated core mass differs from the assumption, and the peak value of the observed Core Mass Functions (CMFs).

3.5 Conclusions

We employ analytic prescriptions and radiative transfer modelling to generate synthetic 1.3 mm dust continuum images for parsec-scale star-forming clumps. We aim to investigate what parameters may affect the detectability of the low-mass source near a high-mass protostar, and if so, how the effects are happening. A total of 432 models with different combinations of stellar masses, separations of sources, and beam sizes are considered in this work. We extract 1D slices along the locations of protostars to visualise the visibility of the low-mass source. We derive Excess Flux and contrast values to compare with representative rms noise thresholds in practical observations, to determine the detectability of the low-mass source.

This is the very first work to explore the detectability of low-mass sources near bright high-mass protostars on parsec-scale and to consider a large parameter space. The main conclusions are summarised below:

- The 1D slices in units of Jansky per square arcsecond area and the contrast figures provide systematic and comprehensive views of the visibility of the low-mass source. The visibility of the low-mass source is affected by the resolution, the separation between the high- and low-mass source, and the mass of the low-mass source, as expected. The low-mass source is less visible if: 1) the observations are taken with a lower spatial resolution; 2) the low-mass source is located closer to the high-mass source; 3) the mass of the low-mass source is lower. In particular, the mass of the high-mass source can predominately affect the visibility of nearby low-mass sources. The low-mass source is more difficult to distinguish if the nearby high-mass source is more massive.
- The detectability of the low-mass source can be determined by comparing the Excess Flux or the contrast value with representative rms noise thresholds. The low-mass source with $m_b \leqq 1$ $M_\odot$ will not be detectable if it is located $\leqq 0.1$ pc away from a 50 $M_\odot$ protostar, even with a half-arcsecond spatial resolution.
- The derived detectability largely depends on the rms noise thresholds that are adopted for comparison. The values chosen for this work are representative values taken from recent surveys of high-mass star-forming regions.
- Next steps of this work could be e.g. to consider disc and outflow cavities for the density structure and to investigate the detectability of the low-mass source directly on the synthetic images.

4

Resolving the high-mass protostellar object G34.24+0.13 MM

In this project, I started with the raw SMA data and carried out calibration, imaging, and analysis.

4.1 Background

This chapter presents a case study for the high-mass protostellar object G34.24+0.13MM using the high-resolution 1.3 mm observations taken with the Submillimeter Array (SMA). G34.24+0.13MM was initially discovered in a $\sim 10''$ 350 μm continuum imaging survey that was carried out with the Submillimeter High Angular Resolution Camera (SHARC) at the Caltech Submillimeter Observatory (CSO), with the aim to search for high-mass protostars near UCHII regions (Hunter 1997). G34.24+0.13MM is located $84''$ (corresponding to 1.5 pc at the distance of 3.8 kpc[1]) from the cometary UCHII region G34.26+0.15 (Keto et al. 1987) to its southeast, and associated with a class II methanol maser detected at the frequencies of 6.7 and 12.2 GHz by Caswell et al. (1995a) and Caswell et al. (1995b). Higher-resolution ($\sim 2.5''$[2]) interferometric observations taken with the Owens Valley Radio Observatory (OVRO) at 1.3 mm reveal that G34.24+0.13MM is a single millimeter source with a size of $2''$ ($\sim$ 7600 AU, Hunter et al. 1998). To further characterise the nature of this source, the authors imaged G34.24+0.13MM at near- to mid-infrared wavelengths (including 1.0, 1.2, 1.6, 2.2, 3.7, 10, and 20 μm) with the Hale 200 inch telescope at Palomar Observatory. No emission was detected towards G34.24+0.13MM at these wavelengths. Combining the (sub)millimeter fluxes with the upper limit at 20 μm, Hunter et al. (1998) fit the spectral energy distribution (SED) of G34.24+0.13MM with a modified blackbody model, and derive a dust temperature of 50 K, a gas mass of 100 $M_\odot$, and a bolometric luminosity of 1600 - 6300 $L_\odot$ for this source (which has a diameter of 7600 AU). This luminosity range is similar to that of the zero-age main-sequence (ZAMS) stars with spectral types B1 - B3 (Panagia 1973). Based on these inferred properties in conjunction with the non-detection of the centimeter continuum (see the 2 cm continuum map in Fig. 2 of Fey et al. 1994), G34.24+0.13MM is speculated to be a high-mass dusty core hosting a deeply embedded proto–B star (Hunter et al. 1998).

---

[1] A distance of 3.8 kpc from the kinematics measurements by Wienen et al. (2015) is adopted for the analysis in this work.

This source remains to be dark in the 2MASS K_s (2.2 μm) image (Skrutskie et al. 2006) and the Spitzer 8 μm image. Subsequent far-infrared observations taken with the Kuiper Airborne Observatory towards the G34.3+0.2C complex reveal the extended 95 μm emission at the location of G34.24+0.13MM (Campbell et al. 2004). In the 70 and 160 μm images from the Herschel Hi-GAL survey (Molinari et al. 2010), G34.24+0.13MM is detected as a point source on an extended ridge. In addition, (sub)millimeter continuum surveys with single dish telescopes have reported multiple detections towards G34.24+0.13MM at the wavelength from 350, 450, 850, and 870 μm, to 1.2 mm over the past decades, and revealed the presence of larger-scale ($\sim$ 0.3 - 0.8 pc) gas clumps associated with the compact core G34.24+0.13MM (Hill et al. 2005, Thompson et al. 2006, Di Francesco et al. 2008, Urquhart et al. 2014, Merello et al. 2015, Lin et al. 2019). In particular, G34.24+0.13MM is found to be associated with the parsec-scale gas clump AGAL G034.243+00.132 identified in the ATLASGAL survey (Urquhart et al. 2014), with an offset of $\sim 9''$ between the fitted component peak of the 1.3 mm data (Hunter et al. 1998) and the 870 μm continuum peak. Urquhart et al. (2018) employ the 870 μm flux density in conjunction with the far-infrared data from the Herschel Hi-GAL survey

---

[2] The geometric mean of the size of the synthesized beam at 1.3 mm.

(Molinari et al. 2010) to fit the SED of this clump, obtaining a dust temperature of 33.3 K, a gas mass of 346 $M_{\odot}$, and a bolometric luminosity of 33189 $L_{\odot}$. The left panel of Figure 4.1 shows G34.24+0.13MM (at the centre) and the nearby UCHII region G34.26+0.15 (to the northwest of G34.24+0.13MM) in the Spitzer IRAC three-color image (red 8 μm, green 4.5 μm, blue 3.6 μm) overlaid with the Herschel 70μm contours and 6 cm contours from the VLA CORNISH survey (Hoare et al. 2012). G34.24+0.13MM is shown as a single point source in dark against the background Spitzer 8 μm emission (in red), and is located within the narrow extended 70μm emission in the direction of east-west. G34.24+0.13MM and the UCHII region G34.26+0.15 are located on the edges of an infrared bubble which is traced by the Spitzer 8 μm emission. The right panel is a zoomed view to the white rectangular area. The OVRO 1.3 mm and the APEX 870 μm data are plotted with black and blue contours, respectively (contour levels: black [15, 40] mJy beam^{-1}; blue [400, 900, 1750] mJy beam^{-1}).

Molecular line emission has been detected towards the compact core G34.24+0.13MM with the CSO and SEST, including H_2CO $3_{1,2}-2_{1,1}$, CS (2–1), HCO^+ (1–0), HCN (1–0), CH_3CN (6-5), and $C^{34}S$ (2–1) (Hunter et al. 1998, Sridharan et al. 1999, Sobolev et al. 2003). The integrated intensity map of the CS (2–1) emission shows that G34.24+0.13MM is located at the boundary between a cavity (of which the morphology is similar to the aforementioned IR bubble) and a clump (Sobolev et al. 2003). Follow-up spectral line observations towards the (sub)millimeter clumps associated with G34.24+0.13MM reveal the HCO^+ (1–0), $H^{13}CO^+$ (1–0), HCN (1–0), and $C^{18}O$ (2-1) emission (López-Sepulcre et al. 2010, López-Sepulcre et al. 2011). In particular, López-Sepulcre et al. (2011) detect SiO (2–1) and SiO (3–2), which are known as the tracers of molecular outflows from accreting protostars, at the clump scale. Based on the similarity between the spectra of SiO and HCO^+ lines, the authors argue that this clump may host the molecular outflows that are oriented close to the plane of the sky. Caswell et al. (1995a) and Caswell et al. (1995b) have reported the detection of the class II methanol maser emission towards G34.24+0.13MM, indicating the existence of a high-mass protostar within the core. High-resolution VLBI observations have resolved the maser emission into a single maser with a size of $0.1''$ ($\sim$ 370 AU, Yi et al. 2002). Szymczak et al. (2002) report that the 6.7 GHz methonal maser associated with G34.24+0.13MM has a peak velocity of 55.4 km s^{-1} and a velocity range of [54, 62] km s^{-1}. The maser source has recently been imaged with the European VLBI Network (EVN) with a sensitivity of σ_{rms} = 5 - 10 mJy beam^{-1}, a spatial resolution of $\sim$ 6 milliarcsecond (the geometric mean of the synthesized beam), and a spectral resolution of ~ 0.1km s^{-1} (Bartkiewicz et al. 2016). The authors report a peak velocity of 55 km s^{-1} and a velocity range of [54.5, 62.7] km s^{-1}. A clear separation can be seen on the sky of the blue- (< 58.5 km s^{-1}, west) and redshifted (> 58.5 km s^{-1}, east) emission with a spatial separation of 170 AU and a separation in velocity of 4 km s^{-1}. This pattern is interpreted as a combined result of the expansion and rotation around a young stellar object, as detailed in Sanna et al. (2010). Interestingly, in contrast to the UCHII region G34.26+0.15 which is associated with a cluster of H_2O and OH masers, no H_2O or OH maser emission has been detected towards G34.24+0.13MM (Fey et al. 1994, Szymczak & Gérard 2004).

To examine whether the estimated luminosity for G34.24+0.13MM (1600 - 6300 $L_{\odot}$, Hunter et al. 1998) arises from a single high-mass protostar or a protocluster, we proposed to observe G34.24+0.13MM with the Submillimeter Array (SMA) at 1.3 mm. Details about the observational parameters and the data reduction process are described in section 4.2. A summary of observed results is in section 4.3. Discussion about the mass calculation, the luminosity-mass ratio, masers and molecular lines, fragmentation properties and potential future work can be found in section 4.4.

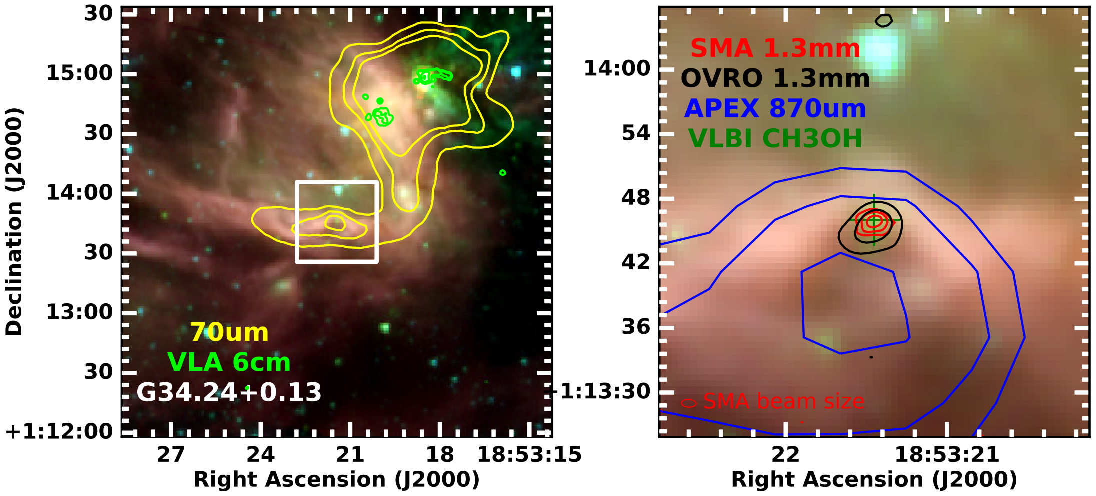

Figure 4.1: Spitzer IRAC 3-color image (red 8 μm, green 4.5 μm, blue 3.6 μm) overlaid in the left panel with Herschel 70μm contours and 6 cm contours (6, 15, 75, 300 mJy beam^{-1}) from the VLA CORNISH survey (Hoare et al. 2012) showing the UCHII region G34.26+0.15 located 1.5 pc from the target. The right panel is a zoomed view to the white rectangular area targeted by the SMA primary beam, overlaid with contours from the SMA 1.3 mm observations (resolution$\sim$1 $''$, red), OVRO 1.3 mm data from Hunter et al. (1998) (resolution $\sim$2.5 $''$, black) and 870 μm contours (400, 900, 1750 mJy beam^{-1}) from the ATLASGAL survey (resolution $\sim$19.2 $''$, blue, Csengeri et al. 2014). The 6.7 GHz methanol maser position from Bartkiewicz et al. (2016) is marked by a green cross.

4.2 Observations and data reduction

4.2.1 SMA 1.3 mm observations

G34.24+0.13MM was observed at 1.3 mm using the Submillimeter Array (SMA) located on Mauna Kea, Hawaii. Only 6 antennas were available in our observation period. The observations were conducted on May 25 2015 with extended configuration. ∼5 hours on-source time were obtained in total. Considering the small size of G34.24+0.13MM (∼1 ″) and its sitting 84″ away from UCHII region G34.26, we took only one pointing with a field of view of 60″ × 60″, which is equivalent to 1.1 pc at the distance of G34.24+0.13MM (3.8 kpc, from Fish et al. 2003). The maximum recoverable scale (MRS) in extended configuration is ∼6″. The ASIC correlator was used to cover 48 spectral windows (spws). Each channel had a bandwidth of 812.5 kHz.The total bandwidth of the data is 8 GHz. 3c279 was observed for bandpass calibration; 1751+096 and J1851+0035 were observed for gain calibration; Callisto was observed for absolute flux calibration. The weather worsened after 19:00, causing larger data scattering in the last three scans.

In this project, I started with the raw SMA data and carried out calibration, imaging, and analysis.

Calibration

The SMA data were calibrated and imaged using the CASA 5.4.0 version. Due to the fact that J1851+0035 was much weaker compared to 1751+096, we decided to use only 1751+096 as gain calibrator to obtain a better signal-to-noise ratio. J1851+0035 was calibrated as the science data. 3c279 was used as bandpass calibrator, for it's a bright point source with relatively flat spectrum. However, part of the band was affected by strong atmospheric ozone, which increased the noise level of our data.

Imaging

After the calibration was applied, the science target data were split off and re-sampled to velocity axis. Then the line-free channels were identified and used to construct a (pseudo-)continuum data set. The (pseudo-)continuum data were iteratively self-calibrated to remove atmosphere variation on long baselines. These solutions were applied to the emission line data cubes. The final SMA continuum image was made using multi-frequency synthesis and a robust weighting parameter of 0.5. The line image cubes were made using the continuum subtracted channels with a robust weighting parameter of 1.0. This was to achieve the best compromise between sensitivity and confusion from missing short spacing information. The line cubes were imaged with a velocity resolution of 1.1 km s^{-1}. All measurements were made from images corrected for the primary beam response.

4.2.2 Archive data

In order to gain a comprehensive understanding of G34.24+0.13MM, we incorporated archival data from Near-Infrared to radio observations. For example, the 3.6 μm, 4.5 μm, 8.0 μm images from Spitzer are combined to make a three-color image, indicating the distribution of dust and gas clouds; 70 μm image from Herschel and 870 μm from ATLASGAL survey (Csengeri et al. 2014) are overlaid to show the distribution of the parental cloud clump of G34.24+0.13MM, within which the protostars are forming; 6 cm image from VLA are used to trace the UCHII regions near the G34.24+0.13MM.

4.3 Results

4.3.1 1.3mm continuum

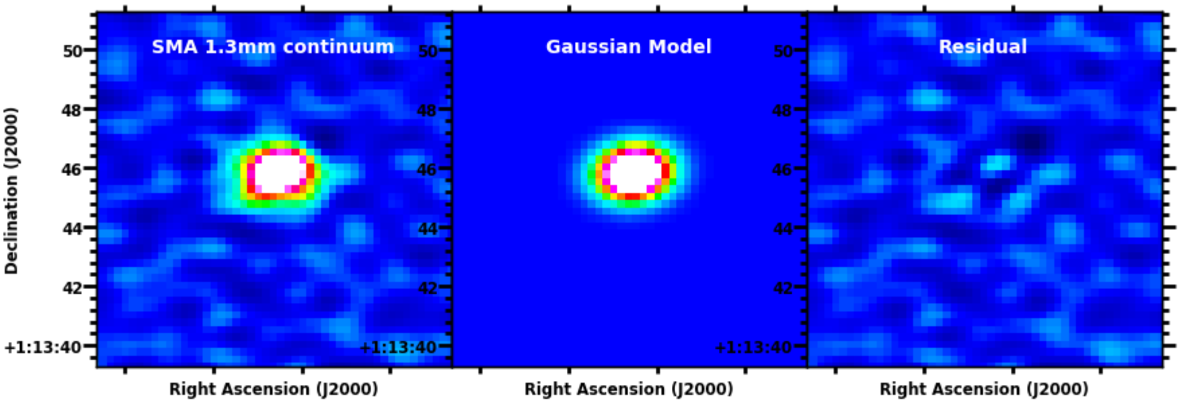

Figure 4.2: A zoom-in view of the SMA 1.3 mm dust continuum emission from G34.24+0.13MM (left panel), the best-fitting 2D Gaussian model (mid panel), and the residual image (right panel).

We achieve a synthesised beam size of 1.40″ × 0.72″ (equivalent to 5360 au × 3240 au at 3.8 kpc) and a sensitivity of $\sigma = 1.3$ mJy beam^{-1} in the SMA 1.3 mm continuum image. As shown on the right panel of Figure 4.1, G34.24+0.13MM is resolved to be a single millimeter source with a tiny tail extending towards the direction of southeast (red contour levels: [6, 15, 35] mJy beam^{-1}). It is located within the previously discovered 1.3 mm OVRO source

Source	G34.24+0.13MM
Telescope	SMA
λ (mm)	1.3
R.A.	$18^h53^m21^s.452$
decl.	$+01^\circ13'45''.847$
Peak Intensity (mJy beam^{-1})	55.5±1.4
Integ. Flux Density (mJy)	132.3±4.4
Deconv. Size ($'' \times ''$)	1.18×1.09
Deconv. Size (AU×AU)	4905×4518

Table 4.1: A summary of the fitted parameters of the 1.3 mm SMA continuum image for G34.24+0.13MM.

in Hunter et al. (1998) (black contour levels: [15, 40] mJy beam^{-1}). No other millimeter sources are detected in the vicinity of G34.24+0.13MM at 5σ level. The SMA source has a peak intensity of 57.1 mJy beam^{-1} at 1.3 mm. To quantify the parameters of G34.24+0.13MM, we fit a two-dimensional Gaussian model to the SMA continuum image using the CASA task imfit. The 2D Gaussian fitting returns a deconvolved size of 1.18″ × 1.09″ (equivalent to 4905 AU × 4518 AU), and an integrated flux density of 132±4 mJy. The best-fitting component has a peak intensity of 55.5±1.4 mJy beam^{-1}. The fitted parameters for G34.24+0.13MM are summarised in Table 4.1. The residual image shows two emission peaks at the $\sim 4\sigma$ level, with one coincident with the peak of the 1.3 mm SMA continuum and the other associated with the tiny tail (see the right panel of Figure 4.2). These features suggest that the morphology of G34.24+0.13MM deviates from a pure Gaussian. Smaller-scale substructures may exist, but cannot be resolved under the spatial resolution of the current SMA data.

4.3.2 Spectral lines

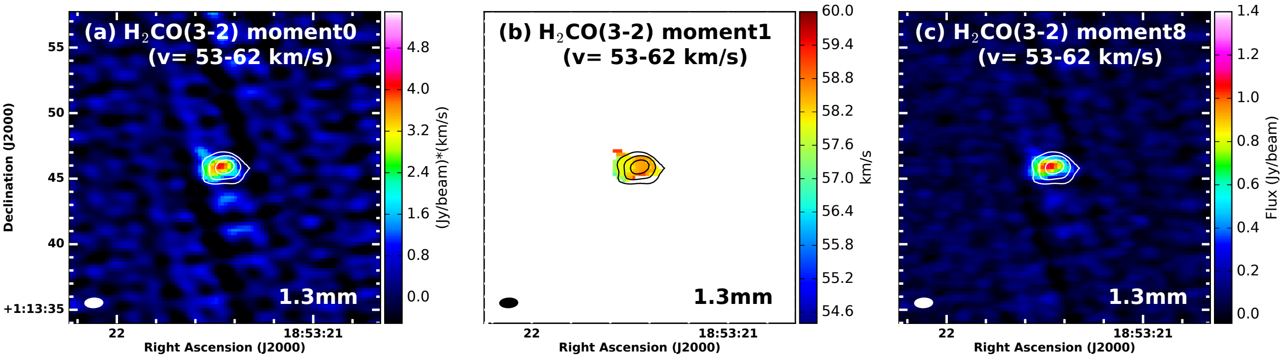

Figure 4.3: Moment maps of H$_2$CO $3_{1,2}-2_{1,1}$ (225.698 GHz, E_{upper} =33.4 K) emission overlaid with SMA 1.3 mm continuum contours: **Left:** moment 0 (integrated intensity), **Center:** moment 1, **Right:** moment 8 (peak map). Continuum contour levels: (0.2, 0.4, 0.6, 0.8)×peak intensity (=55.5 mJy beam^{-1}).

Several molecular emission lines are detected towards G34.24+0.13MM in the SMA 1.3 mm observations. H_2CO ($3_{1,2}-2_{1,1}$) (225.698 GHz, $E_{upper} = 33.4$ K) is detected to be the strongest emission line with a peak intensity of 860±44 mJy beam^{-1} at a rms level of ∼45 mJy beam^{-1} (i.e a signal-to-noise ratio of ∼20). The moment maps of the formaldehyde (H_2CO) data cube are shown in Figure 4.3. The H_2CO ($3_{1,2}-2_{1,1}$) emission is well coincident with the 1.3 mm dust continuum, implying that this line of formaldehyde mainly traces the compact structure. It is worth mentioning that the peak of the formaldehyde line shifts 0.3$''$ (equivalent to 1100 AU) from the continuum peak, which may indicate unknown substructures within the source. The velocity field map (the mid panel of Fig. 4.3) displays a velocity gradient across the continuum contours in a roughly east-west direction. This probably implies either 1) ordered motions of the gaseous envelope such as rotation, or 2) unresolved multiplicity inside the core.

In addition to the strongest formaldehyde line, several weaker emission lines have also been identified. For example, the HC_3N (J = 25-24) transition (227.419 GHz, E_{upper} = 141.9 K) is detected with a peak intensity of 200 mJy beam^{-1} at a rms level of ∼43 mJy beam^{-1} (i.e SNR∼5). The moment maps of this emission line is shown in Figure 4.4. The HC_3N emission appears to be overlapping with the continuum emission, with a tail-like morphology which bends towards the north-east. The peak HC_3N emission is seen on the centre of the tail for both the integrated intensity map and the peak intensity map. The peak HC_3N emission is slightly offset to the east of the continuum peak, implying the existence of substructure and/or inner motions within the core.

At $\sim 3\sigma$ level, we detect the CH_3CN (13-12) ladder (239.0-239.1 GHz, E_{upper} = 80.3-258.9 K), CH_3OH $5_{1,5}-4_{1,4}$ (239.746 GHz, $E_{upper} = 49.1$ K), H_2CS $7_{1,7}-6_{1,6}$ (236.727 GHz, E_{upper} = 58.6 K), HC_3N (J = 26-25) (236.513 GHz, E_{upper} = 153.3 K), $C^{17}O$ (J = 2-1) (224.714 GHz, $E_{upper} = 16.2$ K), and CN (2-1) (226.874 GHz, $E_{upper} = 16.3$ K). The detection of high-E_{upper} transitions of CH_3CN and CH_3OH supports the existence of a hot molecular core (HMC). HMCs are hot and dense molecular cores with a typical temperature of >100 K, a size of ≤0.1 pc, a density of $\geq 10^7$ cm^{-3}, masses of ∼10-1000 $M_\odot$, and luminosities of $>10^4$ $L_\odot$ (Araya et al. 2005, Cesaroni 2005). HMCs are believed to be the site of high-mass star formation which is in an earlier phase than the stage of UCHII regions (Kurtz et al. 2000). The radiation from a newly-born massive star can heat its surrounding envelope, evaporating molecules that are formed on dust grains into gas phase. HMCs are usually observed in highly excited emission lines of complex molecules such as CH_3CN and CH_3OH (e.g., Millar & Hatchell 1997, Sánchez-Monge et al. 2013, Cesaroni et al. 2014, Hernández-Hernández et al. 2014, Kirsanova

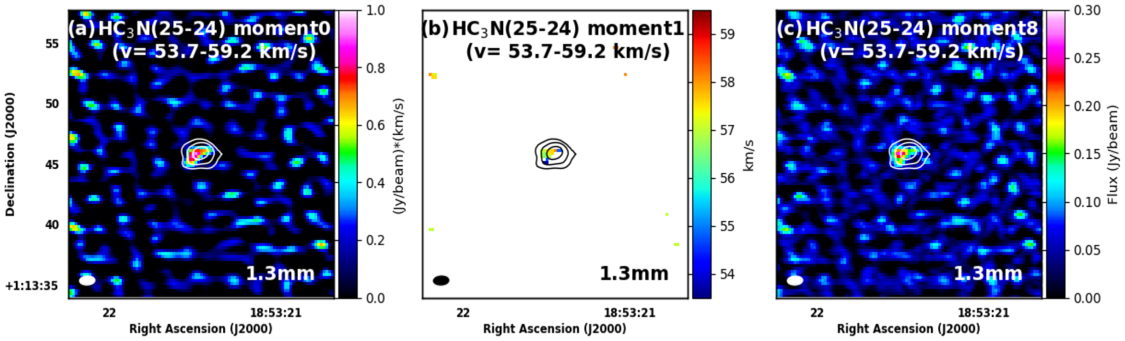

Figure 4.4: Moment maps of HC_3N (J = 25-24) emission overlaid with SMA 1.3 mm continuum contours: **Left:** moment 0 (integrated intensity), **Center:** moment 1, **Right:** moment 8 (peak map). Continuum contour levels: (0.2, 0.4, 0.6, 0.8)×peak intensity (=55.5 mJy beam^{-1}). The velocity range is 53.7-59.2 km s^{-1}.

et al. 2021). We do not include the lines detected at $\sim 3\sigma$ in the discussion of this chapter. Note that extra uncertainties may be introduced into line identification by a difference of morphology between the line emission and dust continuum. For these weak lines, I perform line identification using the spectra extracted from both the locations of line peaks and the region within the 40% contour of the continuum peak.

4.4 Discussions and future work

4.4.1 Mass calculation

Using the integrated flux density obtained in the 2D Gaussian fitting for the SMA 1.3 mm data, we calculate the gas mass of G34.24+0.13MM using a simple model of isothermal dust emission:

$$M_{gas} = \frac{d^2 F_{\nu,tot} R}{B_\nu(T)\kappa_\nu}, \tag{4.1}$$

where $F_{\nu,tot}$ is the observed integrated flux density, R is the gas-to-dust mass ratio, $B_\nu(T)$ is the Planck function at a specified temperature T and κ_ν is the dust absorption coefficient. A κ_ν of 1.0 cm^2 g^{-1} is adopted from Ossenkopf & Henning (1994) for the case of MRN with thick ice mantles and a gas density of 10^8 cm^{-3} (which is consistent with the average volume density derived by Hunter et al. (1998)). The temperature is assumed to be 50 K, which is consistent with the dust temperature given by the SED fitting in Hunter et al. (1998). This assumed temperature is higher than or similar to the upper energy levels of most molecular lines detected towards G34.24+0.13MM with the SMA. Assuming a gas-to-dust mass ratio R of 100, we obtain a gas mass of 12.5±0.4 $M_\odot$ for G34.24+0.13MM. The continuum sensitivity corresponds to a 5σ mass detection limit of 1.8 $M_\odot$ for a $T_{\rm dust}$ of 20 K. The mass estimate using the SMA data is important for calculating the luminosity-to-mass ratio of G34.24+0.13MM, which is frequently used to diagnose the evolutionary stages of massive young stellar objects (e.g., Towner et al. 2019). This metric will be further discussed in section 4.4.2. The maximum recoverable scale (MRS) of the SMA observations is $\sim 6''$ ($\sim$23000 AU), which means that structures with spatial scales larger than the MRS have been filtered out. Hunter et al. (1998) analyse the OVRO 1.3 mm dust continuum data (beam size $2.7'' \times 2.4''$) and obtain a deconvolved size of $2.7'' \times 1.4''$ (equivalent to 11223 AU × 5819 AU) and an integrated flux density of 143±29 mJy for G34.24+0.13MM. They estimate a dust temperature of $\sim$50 K, a total gas mass of 100 $M_\odot$, and a luminosity of 1600 - 6300 $L_\odot$ by performing an SED fitting. If adopting the OVRO flux to calculate the gas mass using equation 4.1, we obtain a gas mass of 13.5±2.7 $M_\odot$ (assuming a κ_ν of 1.0 cm^2 g^{-1} and a dust temperature of 50 K, same as in the mass calculation using the SMA data). When calculated in the same way, the OVRO mass is only 8% larger than the SMA mass, despite its beam size being a factor of two larger. This suggests that both interferometric data consistently trace the dense compact structure (i.e. the star-forming core of G34.24+0.13MM).

4.4.2 L_{bol}/M ratio of G34.24+0.13MM

The luminosity-to-mass ratio L_{bol}/M has been demonstrated to be a good probe of the evolutionary stages of pre-/proto-stellar objects (see Elia et al. 2017b, Urquhart et al. 2018). This is possibly a result of dramatic changes in luminosity as a massive young stellar object evolves as described in Hosokawa & Omukai (2009). The relation of bolometric luminosity versus gas mass for G34.24+0.13MM can be updated using the mass derived with new SMA 1.3 mm data. Hunter et al. (1998) perform an SED fitting for the source using the isothermal greybody dust model (Rathborne et al. 2010) with a combined dataset of the 1.3, 2.7, 3.2 mm OVRO flux densities, the 350μm CSO flux density, and the 20 μm Hale upper limit. They obtain a dust temperature of $\sim$ 50 K, a bolometric luminosity of 1600 - 6300 $L_\odot$, and a mass of 100 $M_\odot$, resulting in a corresponding luminosity-mass ratio of 16 - 63. With the updated mass value, we calculate the luminosity-mass ratio to be 128 - 504. We note that these should be taken as an upper limit, as the measured flux of the core e.g. at 350μm is likely to be contaminated by those of nearby sources due to the low angular resolution of the CSO data ($12''$), which can possibly lead to an overestimate for L_{bol} and thus an overestimate for L_{bol}/M.

Recent far-infrared and submillimeter surveys of high-mass star-forming regions provide constraints on the physical properties (e.g. dust temperature T_d, bolometric luminosity L_{bol}, and gas mass M) at the scale of $\sim$ 0.1 pc. Tigé et al. (2017) perform an imaging survey towards the molecular cloud complex NGC 6334 with Herschel at the wavelengths of 70, 160, 250, 350, and 500 μm. Combining the Herschel images with the JCMT (450 μm, 850 μm), APEX (870 μm), and SEST (1.2 mm) data, the authors extract $\sim$ 0.1 pc dense cores, construct the spectral energy distributions (SEDs) for these cores, and estimate the temperature, luminosity and mass from the SED of each core. After applying a mass cut-off of 75 $M_\odot$ (based on the association with two indicators of high-mass star formation: Class II methanol masers and/or compact centimeter sources), they identify 46 massive dense cores (MDCs) with a median temperature of $\sim$ 17 K, an L_{bol} of 320 $L_\odot$, and an M of 120 $M_\odot$. They further divide the MDCs into four categories: IR-bright protostellar , IR-quiet protostellar, starless, and undefined, based on their 1) mid-infrared fluxes, 2) associations with compact emission at 70 μm, and 3) morphology of the emission at submillimeter wavelengths (e.g. whether or not centrally-peaked). The IR-bright MDCs are reported to have a median size of 0.08 pc, a T_d of 29 K, an L_{bol} of 9500 $L_\odot$, and an M of 140 $M_\odot$; while the IR-quiet MDCs have a size of 0.1 pc, a T_d of 16 K, an L_{bol} of 760 $L_\odot$, and an M of 106 $M_\odot$ (note all the numbers listed are median values). Using the parameters listed in Table 3 of Tigé et al. (2017), we estimate a median L_{bol}/M ratio of 70±28 for the IR-bright group, and 3.1±2.8 for IR-quiet. Following the same procedure of Tigé et al. (2017), Russeil et al. (2019) identify 23 MDCs in NGC 6357, with only one IR-quiet candidate with an estimated L_{bol}/M ratio of $\sim$ 0.5. With a smaller mass threshold (35 $M_\odot$), Cao et al. (2019) identify 151 MDCs in the Cygnus X molecular cloud complex using a consortium of the Herschel, JCMT and IRAM data. The L_{bol}/M ratios of their IR-bright MDCs peak at $\sim$ 10, with IR-quiet at $\sim$ 1 (based on an inspection on their Figure 8). We note that the MDCs have a typical size of 0.1 pc, which is $\sim$ 5 times larger than that of G34.24+0.13MM.With the different scales in mind, it is not surprising to see differences in temperature, luminosity and mass between MDCs and G34.24+0.13MM. Interestingly, our estimated L_{bol}/M ratio for G34.24+0.13MM is significantly higher than the typical L_{bol}/M values for MDCs in literature: the L_{bol}/M of G34.24+0.13MM is about two orders of magnitude higher than the median L_{bol}/M of the IR-quiet MDCs reported by Tigé et al. (2017), Russeil et al. (2019), Cao et al. (2019), and one order of magnitude higher than the peak L_{bol}/M value of the IR-bright MDCs in Cao et al. (2019). Comparing with the IR-bright MDCs identified in

Tigé et al. (2017), G34.24+0.13MM has an L_{bol}/M ratio that is higher by a factor of 2 - 7. The high L_{bol}/M ratio for G34.24+0.13MM is probably due to 1) a potential overestimate for L_{bol}, and/or 2) the fact that it is estimated at a much smaller spatial scale ($\sim$ 0.02 pc). However, it is still unclear how the L_{bol}/M ratio will be affected by different spatial scales at which the measurement is performed. Lin et al. (2019) compare their $\leq$ 0.2 pc SABOCA sources with the ATLASGAL clumps ($\sim$ 1 pc, Urquhart et al. 2018), and find no significant difference in the distribution of the L_{bol}/M ratios between the two samples (see Figure 1 in Lin et al. 2019). Besides, with current data, we cannot rule out the possibility that this unique L_{bol}/M value implies a distinct physical nature of G34.24+0.13MM.

At a larger scale ($\sim$ 1 pc), the parental clump of G34.24+0.13MM, AGAL G034.243+00.132, has been studied in detail regarding the L_{bol}/M ratio. Urquhart et al. (2018) employ the 870μm data from the ATLASGAL survey with APEX and the [70, 160, 250, 350, 500] μm data from the Hi-GAL survey with Herschel (Molinari et al. 2010) to fit the SED of the clump. The clump dust temperature, luminosity, and mass are estimated to be 33.3 K, 33189 $L_\odot$, and 346 $M_\odot$ respectively, which yields a L_{bol}/M of $\sim$ 96. As AGAL G034.243+00.132 is resolved (with a size of $\sim$0.8 pc) in the ATLASGAL and Hi-GAL maps (spatial resolution $\sim$ 20 $''$, equivalent to $\sim$0.37 pc), the L, M, and L_{bol}/M values are reliable indicators for the clump-scale physical properties. López-Sepulcre et al. (2011) report a T_d of 48 K, an M of 51 $M_\odot$, and an L_{bol} of 31700 $L_\odot$ towards the 1.2 mm clump identified by Hill et al. (2005). Note that the 1.2 mm peak is 1.5$''$ from the 870μm peak, which is smaller than the pointing uncertainty of APEX ($\sim$4 $''$, Urquhart et al. 2014). The L_{bol}/M ratio is estimated to be $\sim$622. This is an upper limit of the clump L_{bol}/M , as multiple sources could sit within the beam (120 $''$) of the 100μm IRAS data that they use for the SED fitting. The updated L_{bol}/M ratio for G34.24+0.13MM using the SMA data is higher than that of the associated ATLASGAL clump in Urquhart et al. (2018) by a factor of $\sim$ 1.3 - 5.3. This might indicate the existence of unresolved substructure that is less dominant in the far-infrared regime than G34.24+0.13MM within the parental clump. Lacking of systematic investigation on L_{bol}/M ratios at different spatial scales, it is difficult to speculate the fragmentation properties of AGAL G034.243+00.132 based on its L_{bol}/M value. Higher-resolution (e.g. at the core scale), higher-sensitivity multi-wavelength studies are required to explain the difference of the L_{bol}/M ratios between G34.24+0.13MM and AGAL G034.243+00.132.

Large-sample multi-wavelength studies suggest that the L_{bol}/M ratios reflect a protostellar evolutionary trend. Elia et al. (2017b) show that the L_{bol}/M ratios of the prestellar sources identified in the Hi-GAL survey peak at $\sim 10^{-0.6}$, with protostellar at $10^{0.4}$. Sridharan et al. (2002) find that the UCHII region has a higher bolometric luminosity than the younger high-mass protostellar object with the same mass. Urquhart et al. (2018) suggest that the L_{bol}/M ratios of their massive star-forming clumps range from 1 to 100, while sources with $L_{bol}/M >$ 40 are more likely to host compact HII regions. Towner et al. (2019) investigate the physical properties of a sample of 12 Extended Green Objects (EGOs) using the data taken with the Stratospheric Observatory for Infrared Astronomy (SOFIA, Temi et al. 2014) at 19.7 and 37.1 μm, along with other archival data taken with Spitzer, Herschel, and APEX. The authors construct SEDs for these EGOs at the wavelengths of near-IR to submillimeter, and derive a median L_{bol}/M ratio of 24.7±8.4. The highest L_{bol}/M value recorded is associated with G35.03+0.35 ($L_{bol}/M \sim$ 80 - 200), which is known to host at least an ultracompact HII region and probably a hypercompact HII region (Cyganowski et al. 2011a). The L_{bol}/M of G35.03+0.35 overlaps well with the lower half of the G34.24+0.13MM range, indicating the possibility that G34.24+0.13MM might be on a similar or even later evolutionary stage to G35.03+0.35. For example, despite no compact centimeter source has been detected towards G34.24+0.13MM yet, it is possible that a hypercompact HII region has developed within the core, but is small and difficult to detect e.g. due to being gravitationally trapped (Keto 2007). On the other hand, high L_{bol}/M ratios could be due to the formation of most massive stars (Ma et al. 2013). To further investigate the nature of G34.24+0.13MM, we will require high-resolution, deep centimeter observations.

In addition to asking for high-resolution submillimeter observations, an immediate next step of work is to re-fit the SED of G34.24+0.13MM with recently published far-infrared and submillimeter images that are mentioned in section 4.1. The available data is summarised in Table 4.2. Measurements at the wavelengths near the peak of the SED are expected to better contrain the fitting, and thus provide a more accurate estimate to the L_{bol}/M ratio of G34.24+0.13MM.

4.4.3 Kinematics

Bartkiewicz et al. (2016) report an accurate detection of the 6.7 GHz Class II methanol maser associated with G34.24+0.13MM, and present a milliarcsecond map for the maser source. Interestingly, the methanol maser map illustrates a separation between the blue- ($<$ 58.5 km s^{-1},

Telescope	λ (μm)	Beam ($''$)	References
Herschel/PACS	70	5.9	Molinari et al. (2010)
Herschel/PACS	160	11.7	Molinari et al. (2010)
APEX/LABOCA	350	8.5	Lin et al. (2019)
JCMT/SCUBA-2	450	8.5	Di Francesco et al. (2008)
JCMT/SCUBA-2	850	15.0	Di Francesco et al. (2008)
APEX (ATLASGAL)	870	19.2	Urquhart et al. (2014)
SEST/SIMBA	1200	24	Hill et al. (2005)
SMA	1300	1	This work

Table 4.2: A summary of the observational parameters of recently published far-infrared and submillimeter data that is available for the SED fitting for G34.24+0.13MM.

west) and redshifted ($>$ 58.5 km s^{-1}, east) emission, with a spatial separation of 170 AU and a separation in velocity of 4 km s^{-1}. The spots of the blueshifted emission form an arc-like shape with a size of $\sim$ 200 AU. These features possibly indicate the ordered motions of the internal of G34.24+0.13MM at the scale of the accretion disc around massive protostars ($\sim$ 500 AU, Peters et al. 2010). In fact, the spatial- and velocity-separation pattern has been observed towards G23.01000.411, and is explained as a combination of expansion and rotaion around a YSO of 20 M$_\odot$ by Sanna et al. (2010). Polushkin & Val'Tts (2011) further interpret the maser kinematic pattern in G23.01000.411 as a tracer of the rotating protoplanetary disk, and derive a similar mass for the central protostar to Sanna et al. (2010).

The reported methanol maser at G34.24+0.13MM has a peak velocity of 55.0 km s^{-1} and a velocity range of [54.5, 62.7] km s^{-1} centred at 58.5 km s^{-1}. Their Fig.A.1. shows the spectrum of the methanol maser, illustrating a secondary peak at $\sim$ 61.2 km s^{-1} (red-shifted), and a third peak at $\sim$ 57.0 km s^{-1} (blue-shifted). The velocity of the H_2CO $3_{1,2}-2_{1,1}$ emission from our 1.3 mm SMA observations spans over an interval of [56.9, 59.1] km s^{-1} (measured using the emission above 5σ), with a peak velocity of 58.0 km s^{-1}. The formaldehyde velocity range overlaps with the interval between the central velocity ($\sim$ 58.5 km s^{-1}) and the blue-shifted third peak of the maser emission ($\sim$ 57.0 km s^{-1}). No peak is found in the maser spectrum at the peak velocity of the formaldehyde line. The HC_3N (J = 25-24) emission has a peak velocity of 57.0 km s^{-1}, which is coincident with the blue-shifted third peak of the maser emission. The velocity of significant HC_3N emission (i.e. $>$ 5σ) ranges from 53.7 to 58.1 km s^{-1}. This is consistent with the blue-shifted emission of the methanol maser ($<$ 58.5 km s^{-1}), covering its major (55.0 km s^{-1}) and third peak (57.0 km s^{-1}).

However, despite the overlapping in velocity range, it is unlikely that the maser emission traces the same component of G34.24+0.13MM as the thermal lines do. The peak formaldehyde emission is located $\sim 0.5''$ (1900 AU) to the southeast of the maser source, while the extent of the maser emission is ≤ 600 AU. The peak HC_3N emission is even $\sim 0.24''$ further to the east of the peak formaldehyde. The H_2CO emission displays a velocity gradient across the continuum contours on the direction of roughly east-west, while the maser map shows a roughly west-east velocity gradient at a much smaller scale. The H_2CO emission could possibly trace the ordered motions (e.g. rotation) of the outer envelope of G34.24+0.13MM, or reflect the presence of unresolved multiple sources within the core, while the maser emission probably trace the inner motions associated with protostellar accretion. High angular resolution (sub)millimeter line observations will assist to study the gas kinematics of thermal lines and masers, and understand the relation between them.

The SMA 1.3 mm continuum source G34.24+0.13MM is located within the 900 mJy beam^{-1} contour of the 870μm continuum emission of AGAL G034.243+00.132 (with the 1.3 mm continuum peak offset $\sim$9.3$''$ from the 870μm peak), as shown on the right panel of Figure 4.1. Several follow-up molecular line surveys have targeted this clump, which include tracers of dense gas, outflows, and photodissociation region (PDR) (e.g. Wienen et al. 2012, Kim et al. 2017, Yang et al. 2018, Kim et al. 2020). The system velocity of AGAL G034.243+00.132 inferred using optically-thin lines is 57.2 km s^{-1} (López-Sepulcre et al. 2011, Urquhart et al. 2018), which is 0.2 km s^{-1} higher than the velocity of G34.24+0.13MM (57.0 km s^{-1}). Wienen et al. (2012) observe AGAL G034.243+00.132 with Parkes, targeting the NH_3 (1,1), (2,2), (3,3) inversion lines. They derive a kinetic temperature of 30.4±2.4 K and a column density of NH_3 of $\sim 10^{15}$ cm^{-2}. Yang et al. (2018) employ the ^{13}CO (3-2) and C^{18}O (3-2) lines from the CHIMPS survey (Rigby et al. 2016) at the James Clerk Maxwell Telescope (JCMT) to search for outflow candidates associated with ATLASGAL clumps. They identified blue- and red-shifted wings with velocity ranges of [51.9, 55.4] km s^{-1} and [57.4, 62.9] km s^{-1} respectively at AGAL G034.243+00.132 by subtracting the Gaussian fits of scaled C^{18}O spectra from the ^{13}CO spectra [3]. The velocity interval of the blue-shifted wing sits within the range of the blue-shifted 6.7 GHz methanol maser emission in Bartkiewicz et al. (2016), and covers the highest maser peak at 55.0 km s^{-1}. The red-shifted wing covers the red-shifted secondary maser peak at $\sim$ 61.2 km s^{-1}. However, the comparison needs to be performed with caveats that 1) the CO spectra are extracted at the 870 μm continuum peak, which is offset to the maser source; 2) the channel width of CO spectra is 0.5 km s^{-1}, which is about an order of magnitude larger than that of the maser spectrum. Yang et al. (2018) do not include AGAL G034.243+00.132 into further outflow analysis, for its outflow contours have complex morphology. Besides, the well-known outflow tracers SiO (2–1) and (3–2) are also detected towards the location of AGAL G034.243+00.132 by López-Sepulcre et al. (2011). The authors argue that the similar line widths at zero power between SiO and HCO^+ (1–0) (López-Sepulcre et al. 2010) may indicate the existence of an molecular outflow with its orientation close to the plane of the sky. Based on the data to date, it is difficult to conclude whether the outflow arises from the compact core G34.24+0.13MM or is associated with other unresolved sources within the AGAL G034.243+00.132 clump. In addition, Kim et al. (2020) detect a series of PDR tracers (HCO, C_2H, c-C_3H_2, CN,$HC^{15}N$, $H^{13}CN$, $HN^{13}C$) plus $C^{18}O$ (1-0) and $H^{13}CO^+$ (1-0) towards this clump. They report column densities of $\sim 10^{13} - 10^{15}$ $cm^{-2}$for the PDR tracers. The abundance of HCO is estimated to be $\geq 10^{10}$ for AGAL G034.243+00.132, indicating on-going FUV chemistry in the PDR.

---

[3] The spectra are extracted at the peak of the clump AGAL G034.243+00.132.

4.4.4 Fragmentation and multiplicity

It is known that a large fraction (> 90 %) of OB stars in clustered environment are found to be in multiple systems (see the review of Offner et al. 2022). In particular, Offner et al. (2022) estimate that $\sim$ 68% of O-type stars are in triple and higher-order multiple systems. The high frequency of multiplicity in high-mass stars is speculated to originate from the early stages of high-mass star formation. Therefore, characterising the multiplicity properties in early high-mass star-forming regions is crucial to better understand the formation of high-mass multiple systems. G34.24+0.13MM remains as a single source with a size of $\sim$ 4700 AU in the SMA 1.3 mm continuum image. The 1.3 mm continuum has a linear resolution of $\sim$ 4200 AU, which is not sufficient to resolve possible binarity or multiplicity. Williams et al. (2022) suggest the existence of an unresolved high-mass binary system within $\sim$ 4000 AU in G19.01–0.03 based on the fact that the estimated bolometric luminosity ($\sim 10^4$ $L_\odot$) is $\sim$ one order of magnitude lower than the expected luminosity ($> 10^5$ $L_\odot$) of a single star at its mass ($\sim$ 33 - 65 $M_\odot$). Ilee et al. (2018) report a low-mass ($<$ 0.6 $M_\odot$) companion located $\sim$ 2000 AU from the proto-O star G11.92-0.61 MM1a (enclosed mass $\sim$ 40 $M_\odot$) at the spatial resolution of $\sim$ 300 AU. Despite a small sample to date, observations of high-mass protobinary systems suggest a separation of $\sim$ 200 to $\sim$ 800 AU (Beltrán et al. 2016, Beuther et al. 2017, Kraus et al. 2017, Zapata et al. 2019, Zhang 2019, Cyganowski et al. 2022). To investigate the fragmentation properties in high-mass star-forming regions, Beuther et al. (2018b) observe a sample of 20 high-mass star-forming regions with the IRAM Northern Extended Millimeter Array (NOEMA) with a linear resolution of $\lessapprox$ 1000 AU at 1.3 mm (also known as the CORE program). They find that the observed targets are resolved to vary from a single high-mass source to a group of 20 fragments, with the mean separation between cores ranges from $\sim$ 1500 AU to $\sim$ 32000 AU. In particular, under a resolution of a few hundreds of AU, IRAS 21078 is resolved into a small cluster of 20 cores with a maximum separation of $<$ 2500 AU; while CepAHW2 consists of only two cores within $<$ 2400 AU. However, the authors do not rule out the possibility of further fragmentation at smaller spatial scales ($\lessapprox$ 100 AU). In fact, $< 0.01\,''$ resolution ALMA observations suggest fragmentation proceeds in a hierarchical way down to the scale of a few tens of AU (Beuther et al. 2019). To conclude, although G34.24+0.13MM appears to be a single compact core in our $\sim 1\,''$ SMA image, higher resolution data is required to establish whether G34.24+0.13MM is indeed a single source, a multiple system, or a small cluster. We proposed to observe G34.24+0.13MM using SMA at 1.3 mm with its highest resolution of $\sim$ 1900 AU at 3.8 kpc and a high sensitivity of 0.23 mJy beam^{-1} to resolve substructures such as protostellar disc similarly to those found in Hunter et al. (2014). The observations were taken under unsatisfactory weather conditions. A possible next step is to resolve G34.24+0.13MM with ALMA at even higher resolution. Meyer et al. (2019b) perform synthetic observations to demonstrate that substructures such as spiral arms and gaseous clumps located at a few hundreds of AU from the protostar can be resolved with the C43-8 and C43-10 configurations at 1.2 mm in ALMA Cycle 7. They estimate the exposure time required to resolve the sources at the distance of 2 kpc to be 30 minutes.

5

Summary and Future Work

5.1 Summary

This thesis is motivated by the unanswered question in the field of high-mass star formation: what is the relation between the formation process of a high-mass star and its environment? Aiming to answer or constrain this question, my PhD research is focused on studying the progenitors of high-mass stars, which are denoted as high-mass (pre-/)proto-stellar cores, together with their environment, using both observations and synthetic observations at submillimeter wavelengths. Chapter 1 provides an overview of the field of high-mass star formation, including an introduction to the theoretical models and a summary of observational discoveries. Chapter 2 presents a case study of ALMA observations of the high-mass prestellar core candidate G11.92-0.61 MM2. Chapter 3 includes the results from a parametric study of synthetic observations of high-mass star-forming clumps. Chapter 4 summarises the SMA observations of the high-mass protostellar core G34.24+0.13MM.

Both observations and synthetic observations play crucial roles in broadening and deepening the knowledge of high-mass star formation. The real observations allow us to examine the physical, chemical, and kinematic properties of these sources, providing direct evidence of the early phases of high-mass star formation. We perform two case studies with:

- ALMA 0.8 mm observations of the high-mass prestellar core candidate G11.92-0.61 MM2, to understand the relation between this source and its environment;
- SMA 1.3 mm observations of the high-mass protostellar core G34.24+0.13MM, to unveil its fragmentation state under a high luminosity-mass ratio.

The synthetic observations connect the theoretical models with real observations, making it feasible to compare observations with model predictions. We construct a semi-analytic framework to model a simple high-mass star-forming clump, and use it to conduct a parametric investigation on the detectability of low-mass protostellar cores around young massive protostars. The idea is to test whether the isolatedly-forming high-mass stars found in recent observations could be a result of limited detection capability.

In the ALMA 0.82 mm observations towards the high-mass prestellar core G11.92-0.61 MM2, we detect extensive N_2H^+ emission around MM2 with a $0.54''$ beam ($\sim$1800 AU), while H_2D^+ is undetected at an rms noise level of 2.7 mJy beam^{-1} ($T_b \sim 0.06$ K) with a resolution of $0.65''$. The N_2H^+ spectra are complex, with multiple velocity components present within the cloud. We apply Gaussian decomposition to the N_2H^+ spectrum at each pixel using SCOUSEPY (Henshaw et al. 2016) and then conduct hierarchical clustering of the extracted velocity components using ACORNS (Henshaw et al. 2019). We find that eight velocity- and position-coherent clusters in the N_2H^+-emitting gas describe $> 60\%$ of the fitted velocity components. The most dominant cluster ($> 20\%$ components) indicates a velocity gradient along the filamentary structure traced by the continuum in the south-west to north-east direction. The observed velocity gradient is $\sim$ 10.5 km s^{-1} pc^{-1}, and is possibly caused by a filamentary accretion flow towards MM2. Based on the hypothesis of filamentary accretion flows, we derive a mass inflow rate of $2 \times 10^{-4} \sim 1.2 \times 10^{-3}$ $M_\odot$ yr^{-1}. The infalling gas is probably feeding the ongoing accretion onto the protobinary system and its surrounding core.

The SMA 1.3 mm observations (with an angular resolution of $1''$) towards the high-mass protostellar object G34.24+0.13MM reveal a single dusty compact core with a size of 4700 AU and a mass of 12.5 $M_\odot$. Several molecular emission lines are also detected towards the source, while only the H_2CO ($3_{1,2}$—$2_{1,1}$) line is detected with a high signal-noise ratio. The morphology of the H_2CO emission generally agrees with that of the continuum emission, with a slight offset between the peak of the integrated H_2CO emission and the continuum peak. The intensity-weighted velocity map shows a velocity gradient across the continuum source on the east-west direction, which possibly indicates ordered motions of the gaseous envelope or unresolved multiplicity. The luminosity-mass ratio of G34.24+0.13MM is updated to be 128 - 504 using the gas mass estimated with the SMA data. This uniquely high luminosity-mass ratio requires future higher-resolution multi-wavelength observations to properly explain.

In the parametric study with synthetic observations, we explored a total of 432 models with different combinations of stellar masses, separations of sources, and beam sizes. We extract 1D slices along the locations of protostars to visualise the visibility of the low-mass source, and derive Excess Flux and contrast values to compare with representative rms noise thresholds in practical observations, to determine the detectability of the low-mass source. We find that the 1D slices in units of Jansky per square arcsecond area and the contrast figures provide systematic and comprehensive views of the visibility of the low-mass source. The low-mass source is less visible if: 1) the observations are taken with a lower spatial resolution; 2) the low-mass source is located closer to the high-mass source; 3) the mass of the low-mass source is lower. In particular, the mass of the high-mass source can predominately affect the visibility of nearby low-mass sources. We determine the detectability of the low-mass source by comparing the Excess Flux or the contrast value with representative rms noise thresholds from observations. We conclude that the low-mass source with $m_b \leqq 1\ M_\odot$ will not be detectable if it is located $\leqq 0.1$ pc away from a 50 $M_\odot$ protostar, even with a half-arcsecond spatial resolution.

5.2 Future Work

Based on the work that have been done, we find a few directions of future work that would be interesting to develop.

In Chapter 2, we discover 70 velocity- and position-coherent structures (i.e. trees) in the N_2H^+-emitting gas. Among these trees, Tree 0 is the most dominant tree regarding peak intensity and/or number of components, and is spatially associated the filamentary structure where MM2 is located. Thus, in the majority of Chapter 2, we focus on analysing the kinematic features of Tree 0, for the purpose of understanding the relation between MM2 and its immediate environment. We also mentioned Tree 7 in section 2.6.3 as a tracer of the impact of the molecular outflows driven by a proto-O star on its ambient gas. We plan to further examine the physical and kinematic properties of the N_2H^+ bubble traced by Tree 7, to quantitatively determine the influence of the protostellar feedback activities to the environment. For example, we can estimate the enhancement of turbulence of this region using the velocity dispersion of Tree 7 (which is evidently elevated compared with other trees).

In addition to Tree 0, Tree 9 also displays a velocity gradient along the filamentary structure in a north-south direction. Fig. 5.1 shows the distribution of the peak intensities of the velocity components of Tree 9 (left), the centroid velocity map (mid), and the velocity dispersion map (right). The black contours show the ALMA 0.8 mm continuum emission. The peak intensities of the components in Tree 9 have a maximum value of 0.25 Jy/beam and a median value of 0.075 Jy/beam. The centroid velocities of the components in Tree 9 range from 32.7 km s^{-1} to 35.2 km s^{-1}, with a median value of 34 km s^{-1}. The velocity dispersions have a maximum value of 1.4 km s^{-1} and a median value of 0.5 km s^{-1}. Though the peak intensities of Tree 0 are about a factor of two higher than those of Tree 9, their velocity dispersions are comparable. The distinct ranges of the centroid velocities suggest that the two trees are kinematically separate structures, with Tree 0 being relatively red-shifted and Tree 9 blue-shifted. We are currently working on measuring the velocity gradient in Tree 9 following the procedures described in section 2.5.1. In addition, Tree 9 displays a “hole” near the continuum peak of MM2, which is probably associated with the absorption feature that is discussed in section 2.3 of Chapter 2. As mentioned in section 2.4.1, we have inverted the N_2H^+ data cube and performed Gaussian Decomposition to analyse the absorption feature. In the future, we plan to combine Tree 9 and the inverted absorption feature to analyse their connections in e.g. morphology and kinematics.

Moreover, based on quick inspections, we also find abundant kinematic information in some other trees which are spatially connected to other cores in the protocluster G11.92. For example, velocity gradients along the filamentary structure where the intermediate-mass core MM3 (Cyganowski et al. 2017) is located are clearly visible in tree 17 and tree 1. We could potentially measure the velocity gradients and estimate the mass inflow rates onto MM3 in a similar way as for MM2 in Chapter 2. In addition, tree 19 and tree 69 are spatially associated with the dusty tail extending to the South of MM1, displaying velocity gradients in the direction of south-west to north-east. These structures are possibly the relics of MM1’s early accretion

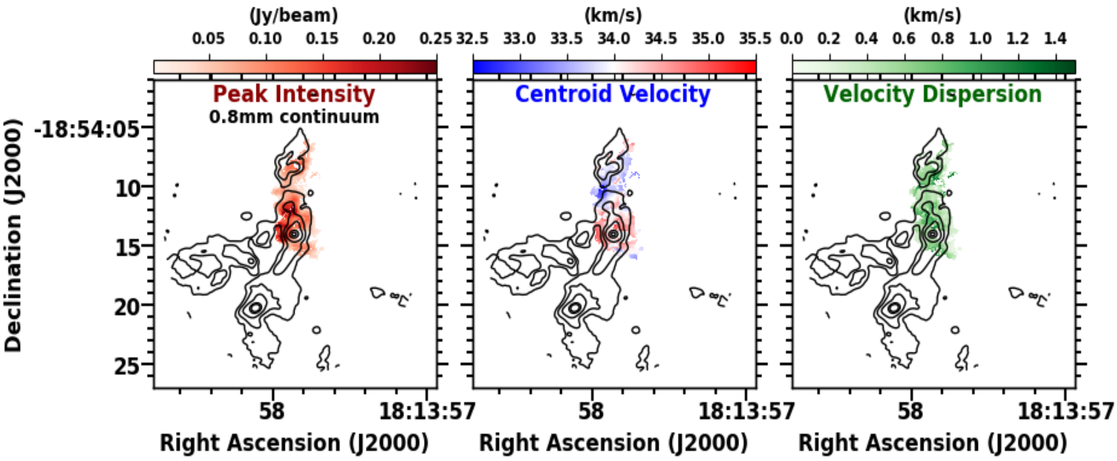

Figure 5.1: Left panel: the distribution of the peak intensities of the velocity components of Tree 9; black contours show the 0.8 mm continuum emission (contour levels: 0.5 × [5,15,40,160,280] mJy beam^{-1}). Mid panel: the centroid velocity map of Tree 9 overlaid with the continuum contours. Right panel: the velocity dispersion map of Tree 9.

from the clumpy environment. Further investigation is required to understand their origin.

Besides, we have addressed the potential impact of the short-spacing problem on the analysis about the kinematics of MM2's environment. To comprehensively unveil the gas kinematics of up to parsec-scale environment of G11.92-0.61 MM2, short-spacing corrections to the current ALMA 0.8 mm data are required. A natural follow-up would be applying for the Atacama Compact Array (ACA) along with the total power observations of N_2H^+ (4-3) for G11.92-0.61 MM2. Combining these new observations with the data taken with the ALMA 12 m array, we will be able to study the gas kinematics of MM2's environment at the spatial scales from $\sim 0.1\ pc$ to $\sim 1\ pc$, and recover the missing fluxes in 12 m only observations.

Chapter 2 demonstrates a successful case of using N_2H^+ (4-3) emission to uncover the kinematics of dense cold gas in the surroundings of the high-mass prestellar core candidate G11.92-0.61 MM2. It has proven to be practical to examine the validity of high-mass prestellar core candidates by investigating their relations with their environment using gas kinematics. This method can be applied to study other high-mass prestellar core candidates. We could potentially apply for high-resolution ALMA N_2H^+ observations of a large sample of high-mass prestellar core candidates for a systematic study. It would be interesting to visualise the environment of these sources to see whether they are actually located within dense filamentary structures, which have been observed to be universal in high-mass star-forming regions and to funnel gas onto the cores within (see e.g. Zhou et al. 2022). In particular, lower-J N_2H^+ transitions, such as N_2H^+ (1-0), are probably better choices to target than N_2H^+ (4-3), due

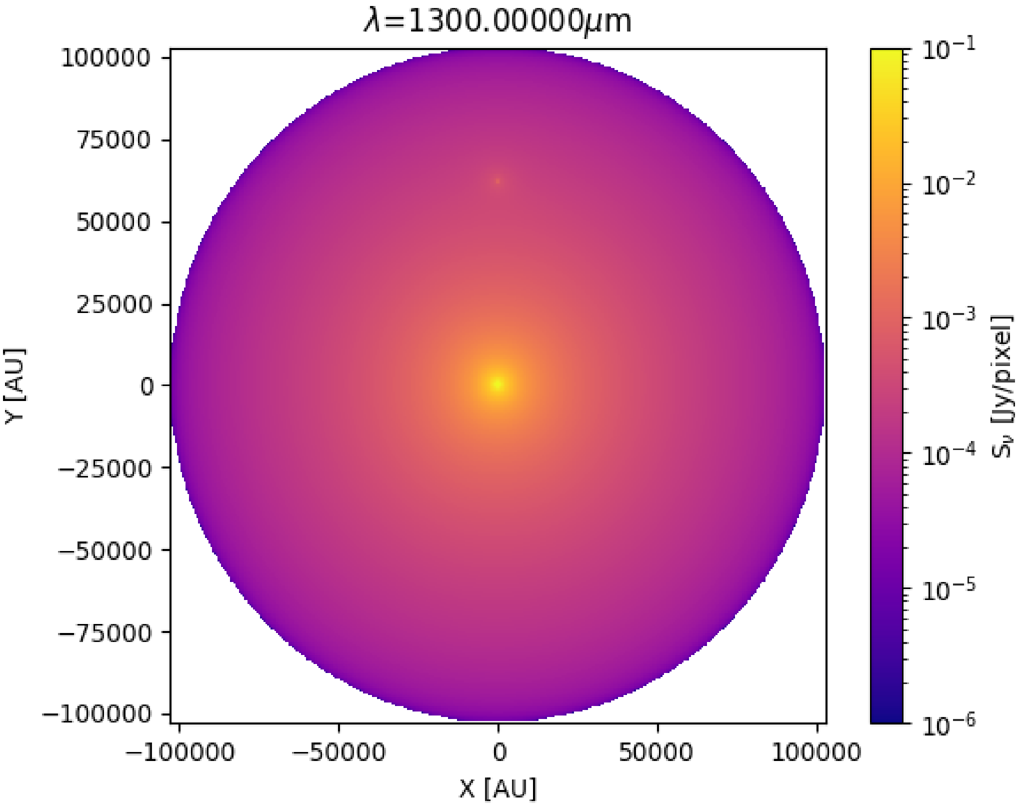

Figure 5.2: An example of the synthetic 1.3 mm continuum images generated by RADMC-3D. This image shows the result of the model with separation = 0.3 pc, the mass of the high-mass protostar $m_a = 50\ M_\odot$, and the mass of the low-mass protostar $m_b = 2\ M_\odot$. The high-mass source is located in the centre, while the low-mass source is 0.3 pc above.

to the fact that 1) N_2H^+ (1-0) has less hyperfine structures than 4-3, which makes it easier to disentangle the effects of multiple velocity components from that of hyperfine lines; 2) N_2H^+ (4-3) transition has a rest frame frequency of 372 GHz, which is located near the edge of atmosphere window, so usually it is not easy to observe this transition.

A potential improvement to the work in Chapter 3 is to make the synthetic observations closer to real observations taken with telescopes such as ALMA. Large-scale smooth structures will be filtered out through the limited sampling to spatial scales in real interferometric observations. This effect has not yet been considered in our framework. In the future, we plan to put the synthetic images produced by RADMC-3D (as shown in Figure 5.2) directly into the ALMA simulator (e.g. simobserve task in CASA) to model the instrumental effects. We have performed preliminary tests and show an example in Figure 5.3. In this specific case, the input image is for a model with a separation of 0.1 pc, a mass of the high-mass protostar of 25 $M_\odot$, and a mass of the low-mass protostar of 2 $M_\odot$. We simulate single-pointing ALMA observations

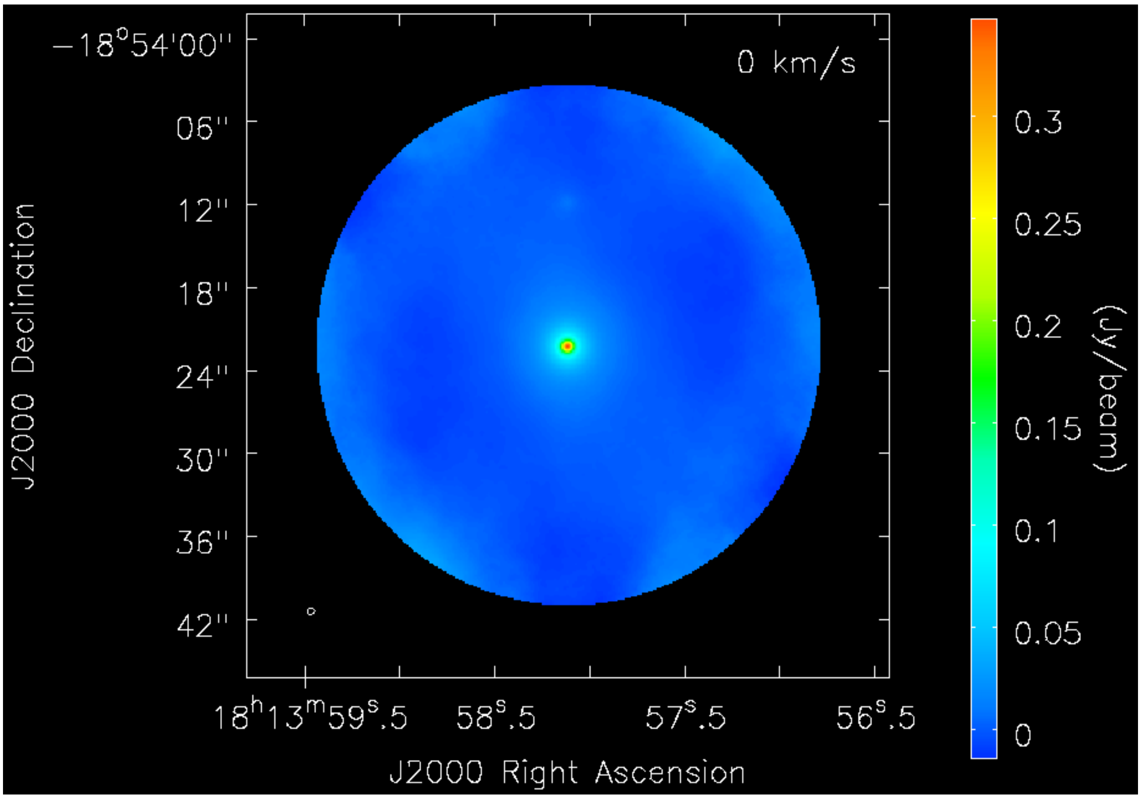

Figure 5.3: A synthetic ALMA 1.3 mm dust continuum image simulating 43-antenna observations using the CASA task *simobserve*. The model is set up with separation = 0.1 pc, the mass of the high-mass protostar $m_a = 25\ M_\odot$, and the mass of the low-mass protostar $m_b = 2\ M_\odot$. The simulations consider single pointing observations centred at 231 GHz with a bandwidth of 1.875 GHz at the C43-4 configuration of ALMA Cycle 6. The assumed phase centre is (18h13m58.11s, -18d54m22.141s).

centred at 231 GHz with a bandwidth of 1.875 GHz. The simulated observations are taken at the C43-4 configuration of ALMA Cycle 6, where the minimum and maximum baselines are 15 and 784 metres respectively, giving an angular resolution of $\sim$0.9$''$ and a maximum recoverable scale (MRS) of $\sim$11$''$. As in real observations, we clean the simulated observations using the CASA task *tclean* with a Briggs weighting (R = 0.5) and a continuum mode. Figure 5.3 shows the cleaned 1.3 mm dust continuum image with the primary beam response corrected. We can see the smooth extended emission e.g., associated with the central high-mass protostar at spatial scales of $\lesssim$10$''$. Larger-scale smooth emission has been filtered out due to the $\sim$11$''$ MRS of the simulated observations. On the other hand, we could work on making the synthetic observations more realistic. The current set-up of our models assume a single high-mass protostar in the centre of a gas clump with power-law density profiles. The analytic models make it possible to perform a parametric study with a large parameter space. However, the assumptions do not agree with the high percentage of binarity of high-mass protostars, nor the filamentary and fractal nature of dense gas clumps that are found in recent observations.We could potentially perform a similar analysis on the images from e.g. hydrodynamic simulations, which are better representatives of observed high-mass star-forming clumps.

As mentioned in section 4.4 of chapter 4, we have proposed to image G34.24+0.13MM with SMA at its highest angular resolution ($0.5''$) at 1.3 mm to further investigate the physical and fragmentation properties of this source. We requested six hours for both extended and very extended configuration to achieve a sensitivity of 2 mJy beam^{-1} to detect lower-mass objects. The proposed tuning covers a frequency range of 214-246 GHz, including outflow tracers such as CO and SiO and hot core tracers such as CH_3CN and CH_3OH. The proposed observations at very extended configuration were taken on June 21, 2019 and June 25, 2019. For the observations on June 21, the Tau was good but the phase was not very stable. Regarding G34.24+0.13MM is bright enough for self-calibration, the longest baselines would still possibly be useful. For the observations on June 25, the Tau was too high but the phase was not too bad. In the future, we plan to calibrate, image, and analyse this new dataset using methods similar to those described in Chapter 4. Based on the results from the new SMA data, we can decide either to re-submit the SMA proposal (to obtain observations at both configurations in better weather) or to request higher-resolution ALMA observations. In addition, it would be useful to re-fit the SED of G34.24+0.13MM with recently published far-infrared and submillimeter images, as measurements at the wavelengths near the peak of the SED (e.g. the 70 μm data from the Hi-GAL survey, Molinari et al. 2010) are expected to better constrain the fitting, and thus provide a more accurate estimate to the L_{bol}/M ratio of G34.24+0.13MM.

Furthermore, it would be interesting to generate synthetic observations based on models of filamentary star-forming clouds (e.g. the hub-filament systems, Tigé et al. 2017). This would help to examine whether filamentary accretions flows can cause the kinematics patterns that are similar to what have been observed in e.g. G11.92-0.61.

Bibliography

Allison, R. J., Goodwin, S. P., Parker, R. J., de Grijs, R., Portegies Zwart, S. F., & Kouwenhoven, M. B. N. 2009, ApJ, 700, L99, 0906.4806

André, P. et al. 2010, A&A, 518, L102, 1005.2618

——. 2008, A&A, 490, L27, 0809.3968

André, P., Ward-Thompson, D., & Barsony, M. 2000, in Protostars and Planets IV, ed. V. Mannings, A. P. Boss, & S. S. Russell, 59, astro-ph/9903284

Araya, E., Hofner, P., Kurtz, S., Bronfman, L., & DeDeo, S. 2005, ApJS, 157, 279

Avison, A. et al. 2021, A&A, 645, A142, 2012.08948

Banerjee, S., & Kroupa, P. 2014, ApJ, 787, 158, 1403.4601

——. 2015, arXiv e-prints, arXiv:1512.03074, 1512.03074

——. 2017, A&A, 597, A28, 1510.04293

Barnes, A. T. et al. 2023, A&A, 675, A53, 2303.15499

Bartkiewicz, A., Szymczak, M., & van Langevelde, H. J. 2016, A&A, 587, A104, 1601.03197

Baumgardt, H., & Kroupa, P. 2007, MNRAS, 380, 1589, 0707.1944

Beltrán, M. T., Cesaroni, R., Moscadelli, L., Sánchez-Monge, Á., Hirota, T., & Kumar, M. S. N. 2016, A&A, 593, A49, 1606.03943

Benson, P. J., Myers, P. C., & Wright, E. L. 1984, ApJ, 279, L27

Beuther, H. et al. 2019, A&A, 621, A122, 1811.10245

Beuther, H., Linz, H., Henning, T., Feng, S., & Teague, R. 2017, A&A, 605, A61, 1705.06246

Beuther, H. et al. 2018a, A&A, 617, A100, 1805.01191

——. 2018b, A&A, 617, A100, 1805.01191

Beuther, H., Schilke, P., Menten, K. M., Motte, F., Sridharan, T. K., & Wyrowski, F. 2002, ApJ, 566, 945, astro-ph/0110370

Bonnell, I. A., & Bate, M. R. 2006, Mon. Not. Roy. Astron. Soc., 370, 488, astro-ph/0604615

Bonnell, I. A., Bate, M. R., Clarke, C. J., & Pringle, J. E. 2001, MNRAS, 323, 785, astro-ph/0102074

Bonnell, I. A., Bate, M. R., & Vine, S. G. 2003, Mon. Not. Roy. Astron. Soc., 343, 413, astro-ph/0305082

Bonnell, I. A., Larson, R. B., & Zinnecker, H. 2007, in Protostars and Planets V, ed. B. Reipurth, D. Jewitt, & K. Keil, 149, astro-ph/0603447

Bonnell, I. A., Vine, S. G., & Bate, M. R. 2004, Mon. Not. Roy. Astron. Soc., 349, 735, astro-ph/0401059

Bontemps, S., Motte, F., Csengeri, T., & Schneider, N. 2010, A&A, 524, A18, 0909.2315

Braun, R., & Walterbos, R. A. M. 1985, A&A, 143, 307

Bressert, E. et al. 2012, A&A, 542, A49, 1204.3628

Briggs, D. S. 1995, PhD thesis, New Mexico Institute of Mining and Technology

Brogan, C. L., Hunter, T. R., Cyganowski, C. J., Chandler, C. J., Friesen, R., & Indebetouw, R. 2016, ApJ, 832, 187, 1609.07470

Burgh, E. B., McCandliss, S. R., & Feldman, P. D. 2002, ApJ, 575, 240, astro-ph/0204156

Burkhart, B., Lazarian, A., Goodman, A., & Rosolowsky, E. 2013a, ApJ, 770, 141, 1206.4703

Burkhart, B., Ossenkopf, V., Lazarian, A., & Stutzki, J. 2013b, ApJ, 771, 122, 1304.3131

Butler, M. J., & Tan, J. C. 2009, ApJ, 696, 484, 0812.2882

——. 2012, ApJ, 754, 5, 1205.2391

Campbell, M. F., Harvey, P. M., Lester, D. F., & Clark, D. M. 2004, ApJ, 600, 254

Cao, Y., Qiu, K., Zhang, Q., Wang, Y., Hu, B., & Liu, J. 2019, ApJS, 241, 1, 1901.06475

Caselli, P., & Ceccarelli, C. 2012, A&A Rev., 20, 56, 1210.6368

Caswell, J. L., Vaile, R. A., Ellingsen, S. P., & Norris, R. P. 1995a, MNRAS, 274, 1126

Caswell, J. L., Vaile, R. A., & Forster, J. R. 1995b, MNRAS, 277, 210

Cesaroni, R. 2005, in Massive Star Birth: A Crossroads of Astrophysics, ed. R. Cesaroni, M. Felli, E. Churchwell, & M. Walmsley, Vol. 227, 59–69

Cesaroni, R., Galli, D., Neri, R., & Walmsley, C. M. 2014, A&A, 566, A73

Chen, X. et al. 2020, Nature Astronomy, 4, 1170

Chira, R.-A., Smith, R. J., Klessen, R. S., Stutz, A. M., & Shetty, R. 2014, MNRAS, 444, 874, 1402.5279

Churchwell, E. 2002, ARA&A, 40, 27

Commerçon, B., Hennebelle, P., & Henning, T. 2011, ApJ, 742, L9, 1110.2955

Commerçon, B., Launhardt, R., Dullemond, C., & Henning, T. 2012a, A&A, 545, A98, 1207.0656

Commerçon, B., Levrier, F., Maury, A. J., Henning, T., & Launhardt, R. 2012b, A&A, 548, A39, 1210.1023

Conway, J. E., Cornwell, T. J., & Wilkinson, P. N. 1990, MNRAS, 246, 490

Cornwell, T. J. 2008, IEEE Journal of Selected Topics in Signal Processing, 2, 793

Csengeri, T. et al. 2018, A&A, 617, A89, 1804.06482

——. 2014, A&A, 565, A75, 1312.0937

Cyganowski, C. J., Brogan, C. L., Hunter, T. R., & Churchwell, E. 2009, ApJ, 702, 1615, 0907.1089

——. 2011a, ApJ, 743, 56, 1109.1829

Cyganowski, C. J., Brogan, C. L., Hunter, T. R., Churchwell, E., & Zhang, Q. 2011b, ApJ, 729, 124, 1012.0851

——. 2011c, ApJ, 729, 124, 1012.0851

Cyganowski, C. J. et al. 2014, ApJ, 796, L2, 1410.2605

Cyganowski, C. J., Brogan, C. L., Hunter, T. R., Smith, R., Kruijssen, J. M. D., Bonnell, I. A., & Zhang, Q. 2017, MNRAS, 468, 3694, 1701.02802

Cyganowski, C. J., Ilee, J. D., Brogan, C. L., Hunter, T. R., Zhang, S., Harries, T. J., & Haworth, T. J. 2022, ApJ, 931, L31, 2204.09163

Cyganowski, C. J. et al. 2008, AJ, 136, 2391, 0810.0530

de Wit, W. J., Testi, L., Palla, F., & Zinnecker, H. 2005, A&A, 437, 247, astro-ph/0503337

Di Francesco, J., Johnstone, D., Kirk, H., MacKenzie, T., & Ledwosinska, E. 2008, ApJS, 175, 277, 0801.2595

Dieterich, S. B., Henry, T. J., Jao, W.-C., Winters, J. G., Hosey, A. D., Riedel, A. R., & Subasavage, J. P. 2014, AJ, 147, 94, 1312.1736

Draine, B. T. 2003, ARA&A, 41, 241, astro-ph/0304489

Draine, B. T. et al. 2007, ApJ, 663, 866, astro-ph/0703213

Duarte-Cabral, A., Bontemps, S., Motte, F., Gusdorf, A., Csengeri, T., Schneider, N., & Louvet, F. 2014, A&A, 570, A1, 1407.6400

Duarte-Cabral, A., Bontemps, S., Motte, F., Hennemann, M., Schneider, N., & André, P. 2013, A&A, 558, A125, 1308.6490

Dullemond, C. P., Juhasz, A., Pohl, A., Sereshti, F., Shetty, R., Peters, T., Commercon, B., & Flock, M. 2012, RADMC-3D: A multi-purpose radiative transfer tool, 1202.015

Elia, D. et al. 2017a, MNRAS, 471, 100, 1706.01046

——. 2017b, MNRAS, 471, 100, 1706.01046

Enoch, M. L., Evans, Neal J., I., Sargent, A. I., Glenn, J., Rosolowsky, E., & Myers, P. 2008, ApJ, 684, 1240, 0805.1075

Faridani, S., Bigiel, F., Flöer, L., Kerp, J., & Stanimirović, S. 2018, Astronomische Nachrichten, 339, 87, 1709.09365

Federrath, C. 2013, MNRAS, 436, 1245, 1306.3989

Federrath, C. et al. 2016, ApJ, 832, 143, 1609.05911

Fey, A. L., Gaume, R. A., Nedoluha, G. E., & Claussen, M. J. 1994, ApJ, 435, 738

Fish, V. L., Reid, M. J., Wilner, D. J., & Churchwell, E. 2003, ApJ, 587, 701

Gies, D. R. 1987, ApJS, 64, 545

Gies, D. R., & Bolton, C. T. 1986, ApJS, 61, 419

Ginsburg, A., & Mirocha, J. 2011, PySpecKit: Python Spectroscopic Toolkit, 1109.001

Goodman, A. A., Benson, P. J., Fuller, G. A., & Myers, P. C. 1993, ApJ, 406, 528

Gvaramadze, V. V., Weidner, C., Kroupa, P., & Pflamm-Altenburg, J. 2012, MNRAS, 424, 3037, 1206.1596

Harada, R. et al. 2019, PASJ, 71, 44, 1901.08250

Harries, T. J., Douglas, T. A., & Ali, A. 2017, MNRAS, 471, 4111, 1706.04017

Haworth, T. J., Glover, S. C. O., Koepferl, C. M., Bisbas, T. G., & Dale, J. E. 2018, New A Rev., 82, 1, 1711.05275

Henshaw, J. D., Caselli, P., Fontani, F., Jiménez-Serra, I., & Tan, J. C. 2014, MNRAS, 440, 2860, 1403.1444

Henshaw, J. D. et al. 2019, MNRAS, 485, 2457, 1902.02793

——. 2016, MNRAS, 457, 2675, 1601.03732

Hernández-Hernández, V., Zapata, L., Kurtz, S., & Garay, G. 2014, ApJ, 786, 38, 1402.2682

Hill, T., Burton, M. G., Minier, V., Thompson, M. A., Walsh, A. J., Hunt-Cunningham, M., & Garay, G. 2005, MNRAS, 363, 405, astro-ph/0506402

Hoare, M. G., Kurtz, S. E., Lizano, S., Keto, E., & Hofner, P. 2007, in Protostars and Planets V, ed. B. Reipurth, D. Jewitt, & K. Keil, 181, astro-ph/0603560

Hoare, M. G. et al. 2012, PASP, 124, 939, 1208.3351

Hosokawa, T., & Omukai, K. 2009, ApJ, 691, 823, 0806.4122

Hsu, S.-Y. et al. 2020, ApJ, 898, 107, 2006.15850

Hunter, T. R. 1997, PhD thesis, Smithsonian Astrophysical Observatory

Hunter, T. R., Brogan, C. L., Cyganowski, C. J., & Schnee, S. 2015, in EAS Publications Series, Vol. 75, EAS Publications Series, 285–286

Hunter, T. R., Brogan, C. L., Cyganowski, C. J., & Young, K. H. 2014, ApJ, 788, 187, 1405.0496

Hunter, T. R., Neugebauer, G., Benford, D. J., Matthews, K., Lis, D. C., Serabyn, E., & Phillips, T. G. 1998, ApJ, 493, L97

Ilee, J. D., Cyganowski, C. J., Brogan, C. L., Hunter, T. R., Forgan, D. H., Haworth, T. J., Clarke, C. J., & Harries, T. J. 2018, ApJ, 869, L24, 1811.05267

Ilee, J. D., Cyganowski, C. J., Nazari, P., Hunter, T. R., Brogan, C. L., Forgan, D. H., & Zhang, Q. 2016, MNRAS, 462, 4386, 1608.05561

Izquierdo, A. F., Galván-Madrid, R., Maud, L. T., Hoare, M. G., Johnston, K. G., Keto, E. R., Zhang, Q., & de Wit, W.-J. 2018, MNRAS, 478, 2505, 1804.09204

Jankovic, M. R. et al. 2019, MNRAS, 482, 4673, 1810.11398

Johnston, K. G. et al. 2015, ApJ, 813, L19, 1509.08469

Juvela, M., Malinen, J., & Lunttila, T. 2012, A&A, 544, A141, 1207.3635

Kauffmann, J., Bertoldi, F., Bourke, T. L., Evans, N. J., I., & Lee, C. W. 2008, A&A, 487, 993, 0805.4205

Keto, E. 2007, ApJ, 666, 976, astro-ph/0603856

Keto, E. R., Ho, P. T. P., & Reid, M. J. 1987, ApJ, 323, L117

Kim, W. J., Wyrowski, F., Urquhart, J. S., Menten, K. M., & Csengeri, T. 2017, A&A, 602, A37, 1702.02062

Kim, W. J., Wyrowski, F., Urquhart, J. S., Pérez-Beaupuits, J. P., Pillai, T., Tiwari, M., & Menten, K. M. 2020, A&A, 644, A160, 2009.14238

Kirk, H., Myers, P. C., Bourke, T. L., Gutermuth, R. A., Hedden, A., & Wilson, G. W. 2013, ApJ, 766, 115, 1301.6792

Kirsanova, M. S., Salii, S. V., Kalenskii, S. V., Wiebe, D. S., Sobolev, A. M., & Boley, P. A. 2021, MNRAS, 503, 633, 2102.09145

Kong, S., Tan, J. C., Caselli, P., Fontani, F., Liu, M., & Butler, M. J. 2017, ApJ, 834, 193, 1609.06008

Kraus, S. et al. 2017, The Messenger, 170, 45

Krumholz, M. R., Klein, R. I., McKee, C. F., Offner, S. S. R., & Cunningham, A. J. 2009, Science, 323, 754, 0901.3157

Kuiper, R., & Hosokawa, T. 2018, A&A, 616, A101, 1804.10211

Kurtz, S., Cesaroni, R., Churchwell, E., Hofner, P., & Walmsley, C. M. 2000, in Protostars and Planets IV, ed. V. Mannings, A. P. Boss, & S. S. Russell, 299–326

Lada, C. J., & Lada, E. A. 2003, ARA&A, 41, 57, astro-ph/0301540

Lamb, J. B., Oey, M. S., Segura-Cox, D. M., Graus, A. S., Kiminki, D. C., Golden-Marx, J. B., & Parker, J. W. 2016, ApJ, 817, 113, 1512.01233

Larson, R. B. 1969, MNRAS, 145, 271

Lennon, D. J. et al. 2018, A&A, 619, A78, 1805.08277

Li, S., Zhang, Q., Pillai, T., Stephens, I. W., Wang, J., & Li, F. 2019, ApJ, 886, 130, 1909.08916

Lin, Y., Csengeri, T., Wyrowski, F., Urquhart, J. S., Schuller, F., Weiss, A., & Menten, K. M. 2019, A&A, 631, A72, 1909.01011

Lin, Y., Wyrowski, F., Liu, H. B., Izquierdo, A., Csengeri, T., Leurini, S., & Menten, K. M. 2021, arXiv e-prints, arXiv:2112.01115, 2112.01115

Liu, T. et al. 2016, ApJ, 824, 31, 1604.03548

Lomax, O., & Whitworth, A. P. 2018, MNRAS, 475, 1696, 1711.07385

Longmore, S. N., Burton, M. G., Minier, V., & Walsh, A. J. 2006, MNRAS, 369, 1196, astro-ph/0604257

López-Sepulcre, A., Cesaroni, R., & Walmsley, C. M. 2010, A&A, 517, A66

López-Sepulcre, A. et al. 2011, A&A, 526, L2, 1011.5419

Lu, X. et al. 2018, ApJ, 855, 9, 1801.05955

Lucas, W. E., Rybak, M., Bonnell, I. A., & Gieles, M. 2018, MNRAS, 474, 3582, 1711.09927

Ma, B., Tan, J. C., & Barnes, P. J. 2013, ApJ, 779, 79, 1211.6492

Maschberger, T., Clarke, C. J., Bonnell, I. A., & Kroupa, P. 2010, MNRAS, 404, 1061, 1002.4401

Mason, B. D., Gies, D. R., Hartkopf, W. I., Bagnuolo, William G., J., ten Brummelaar, T., & McAlister, H. A. 1998, AJ, 115, 821

Mathis, J. S., Rumpl, W., & Nordsieck, K. H. 1977, ApJ, 217, 425

Maud, L. T., Hoare, M. G., Galván-Madrid, R., Zhang, Q., de Wit, W. J., Keto, E., Johnston, K. G., & Pineda, J. E. 2017, MNRAS, 467, L120, 1701.06958

Maury, A. J., André, P., Men'shchikov, A., Könyves, V., & Bontemps, S. 2011, A&A, 535, A77, 1108.0668

McKee, C. F., & Tan, J. C. 2002, Nature, 416, 59, astro-ph/0203071

——. 2003, Astrophys. J., 585, 850, astro-ph/0206037

McKee, C. F., & Tan, J. C. 2003, ApJ, 585, 850, astro-ph/0206037

McMullin, J. P., Waters, B., Schiebel, D., Young, W., & Golap, K. 2007, in Astronomical Society of the Pacific Conference Series, Vol. 376, Astronomical Data Analysis Software and Systems XVI, ed. R. A. Shaw, F. Hill, & D. J. Bell, 127

Merello, M., Evans, Neal J., I., Shirley, Y. L., Rosolowsky, E., Ginsburg, A., Bally, J., Battersby, C., & Dunham, M. M. 2015, ApJS, 218, 1, 1501.05965

Meyer, D. M. A., Kreplin, A., Kraus, S., Vorobyov, E. I., Haemmerle, L., & Eislöffel, J. 2019a, MNRAS, 487, 4473, 1906.02015

——. 2019b, MNRAS, 487, 4473, 1906.02015

Meyer, D. M. A., Kuiper, R., Kley, W., Johnston, K. G., & Vorobyov, E. 2018, MNRAS, 473, 3615, 1710.01162

Millar, T. J., & Hatchell, J. 1997, Commmunications of the Konkoly Observatory Hungary, 100, 207

Minier, V. et al. 2009, A&A, 501, L1, 0907.3031

Molet, J. et al. 2019, A&A, 626, A132, 1905.12463

Molinari, S. et al. 2016, A&A, 591, A149, 1604.05911

——. 2010, PASP, 122, 314, 1001.2106

Motte, F. et al. 2021, arXiv e-prints, arXiv:2112.08182, 2112.08182

Motte, F., Bontemps, S., & Louvet, F. 2018, ARA&A, 56, 41, 1706.00118

Motte, F., Bontemps, S., Schilke, P., Schneider, N., Menten, K. M., & Broguière, D. 2007, A&A, 476, 1243, 0708.2774

Mueller, K. E., Shirley, Y. L., Evans, Neal J., I., & Jacobson, H. R. 2002, ApJS, 143, 469, astro-ph/0207322

Myers, A. T., McKee, C. F., Cunningham, A. J., Klein, R. I., & Krumholz, M. R. 2013, ApJ, 766, 97, 1211.3467

Nony, T. et al. 2018, A&A, 618, L5, 1810.01404

Oey, M. S., Lamb, J. B., Kushner, C. T., Pellegrini, E. W., & Graus, A. S. 2013, ApJ, 768, 66, 1303.1550

Offner, S. S. R., Capodilupo, J., Schnee, S., & Goodman, A. A. 2012, MNRAS, 420, L53, 1111.4209

Offner, S. S. R., Klein, R. I., McKee, C. F., & Krumholz, M. R. 2009, ApJ, 703, 131, 0904.2004

Offner, S. S. R., Moe, M., Kratter, K. M., Sadavoy, S. I., Jensen, E. L. N., & Tobin, J. J. 2022, arXiv e-prints, arXiv:2203.10066, 2203.10066

Ossenkopf, V., & Henning, T. 1994, A&A, 291, 943

Panagia, N. 1973, AJ, 78, 929

Peretto, N., & Fuller, G. A. 2010, ApJ, 723, 555, 1009.0716

Peretto, N. et al. 2014, A&A, 561, A83, 1311.0203

——. 2013, A&A, 555, A112, 1307.2590

Peters, T., Klessen, R. S., Mac Low, M.-M., & Banerjee, R. 2010, ApJ, 725, 134, 1005.3271

Pillai, T., Kauffmann, J., Zhang, Q., Sanhueza, P., Leurini, S., Wang, K., Sridharan, T. K., & König, C. 2019, A&A, 622, A54, 1901.07582

Polushkin, S. V., & Val'Tts, I. E. 2011, Astronomy Reports, 55, 445

Ragan, S. E., Bergin, E. A., Plume, R., Gibson, D. L., Wilner, D. J., O'Brien, S., & Hails, E. 2006, ApJS, 166, 567, astro-ph/0606284

Rathborne, J. M., Jackson, J. M., Chambers, E. T., Stojimirovic, I., Simon, R., Shipman, R., & Frieswijk, W. 2010, ApJ, 715, 310, 1003.3193

Rauw, G., Morel, T., & Palate, M. 2012, A&A, 546, A77, 1209.2606

Redaelli, E., Bovino, S., Giannetti, A., Sabatini, G., Caselli, P., Wyrowski, F., Schleicher, D. R. G., & Colombo, D. 2021, A&A, 650, A202, 2104.06431

Reid, N., & Mould, J. 1985, ApJ, 299, 236

Rigby, A. J. et al. 2016, MNRAS, 456, 2885, 1512.08235

Robitaille, T. P. 2017, A&A, 600, A11, 1703.05765

Robitaille, T. P., Whitney, B. A., Indebetouw, R., Wood, K., & Denzmore, P. 2006, ApJS, 167, 256, astro-ph/0608234

Rosen, A. L., & Krumholz, M. R. 2020, AJ, 160, 78, 2006.04829

Russeil, D. et al. 2019, A&A, 625, A134

Rybicki, G. B., & Lightman, A. P. 1979, Radiative processes in astrophysics

Sabatini, G. et al. 2021, A&A, 652, A71, 2106.00692

Saigo, K., & Tomisaka, K. 2011, ApJ, 728, 78

Sakai, T., Sakai, N., Kamegai, K., Hirota, T., Yamaguchi, N., Shiba, S., & Yamamoto, S. 2008, ApJ, 678, 1049, 0802.3030

Sánchez-Monge, Á. et al. 2013, A&A, 552, L10, 1303.4242

Sanna, A., Moscadelli, L., Cesaroni, R., Tarchi, A., Furuya, R. S., & Goddi, C. 2010, A&A, 517, A78, 1004.5578

Sato, M. et al. 2014, ApJ, 793, 72, 1408.0513

Selier, R., Heydari-Malayeri, M., & Gouliermis, D. A. 2011, A&A, 529, A40, 1102.1257

Shu, F. H. 1977, ApJ, 214, 488

Skrutskie, M. F. et al. 2006, AJ, 131, 1163

Smith, R. J., Longmore, S., & Bonnell, I. 2009, MNRAS, 400, 1775, 0908.3910

Smith, R. J., Shetty, R., Stutz, A. M., & Klessen, R. S. 2012, ApJ, 750, 64, 1201.6275

Sobolev, A. M., Salii, S. V., Ellingsen, S. P., Zinchenko, I. I., Johansson, L. E. B., & Sutton, E. C. 2003, Astronomical and Astrophysical Transactions, 22, 7

Sridharan, T. K., Beuther, H., Saito, M., Wyrowski, F., & Schilke, P. 2005, ApJ, 634, L57, astro-ph/0508421

Sridharan, T. K., Beuther, H., Schilke, P., Menten, K. M., & Wyrowski, F. 2002, ApJ, 566, 931, astro-ph/0110363

Sridharan, T. K., Menten, K. M., Wyrowski, F., & Schilke, P. 1999, in Star Formation 1999, ed. T. Nakamoto, 183–184

Steinacker, J., Bacmann, A., Henning, T., & Heigl, S. 2016, A&A, 593, A6, 1606.07942

Steinacker, J., Baes, M., & Gordon, K. D. 2013, ARA&A, 51, 63, 1303.4998

Stephens, I. W. et al. 2017, ApJ, 834, 94, 1609.04399

Szymczak, M., & Gérard, E. 2004, A&A, 423, 209, astro-ph/0405316

Szymczak, M., Kus, A. J., Hrynek, G., Kěpa, A., & Pazderski, E. 2002, A&A, 392, 277

Tan, J. C., Beltrán, M. T., Caselli, P., Fontani, F., Fuente, A., Krumholz, M. R., McKee, C. F., & Stolte, A. 2014, in Protostars and Planets VI, ed. H. Beuther, R. S. Klessen, C. P. Dullemond, & T. Henning, 149–172, 1402.0919

Tan, J. C., Kong, S., Butler, M. J., Caselli, P., & Fontani, F. 2013, ApJ, 779, 96, 1303.4343

Tan, J. C., Kong, S., Zhang, Y., Fontani, F., Caselli, P., & Butler, M. J. 2016, ApJ, 821, L3, 1601.07043

Temi, P. et al. 2014, ApJS, 212, 24, 1405.7390

Thompson, A. R., Moran, J. M., & Swenson, George W., J. 2001, Interferometry and Synthesis in Radio Astronomy, 2nd Edition

——. 2017, Interferometry and Synthesis in Radio Astronomy, 3rd Edition

Thompson, M. A., Hatchell, J., Walsh, A. J., MacDonald, G. H., & Millar, T. J. 2006, A&A, 453, 1003, astro-ph/0604208

Tigé, J. et al. 2017, A&A, 602, A77, 1703.09839

Tobin, J. J. et al. 2019, ApJ, 886, 6, 1910.00605

Towner, A. P. M., Brogan, C. L., Hunter, T. R., Cyganowski, C. J., & Friesen, R. K. 2019, ApJ, 875, 135, 1903.06808

Urquhart, J. S. et al. 2014, A&A, 568, A41, 1406.5741

——. 2018, MNRAS, 473, 1059, 1709.00392

Vasyunin, A. I., Semenov, D. A., Wiebe, D. S., & Henning, T. 2009, ApJ, 691, 1459, 0810.1591

Vázquez-Semadeni, E., González-Samaniego, A., & Colín, P. 2017, MNRAS, 467, 1313, 1611.00088

Walch, S., Whitworth, A. P., Bisbas, T. G., Hubber, D. A., & Wünsch, R. 2015, MNRAS, 452, 2794, 1109.3478

Wang, K. et al. 2014, MNRAS, 439, 3275, 1401.4157

Wienen, M. et al. 2015, A&A, 579, A91, 1503.00007

Wienen, M., Wyrowski, F., Schuller, F., Menten, K. M., Walmsley, C. M., Bronfman, L., & Motte, F. 2012, A&A, 544, A146, 1208.4848

Williams, G. M. et al. 2022, MNRAS, 509, 748, 2110.06262

Williams, J. P., & Best, W. M. J. 2014, ApJ, 788, 59, 1312.0151

Wilson, T. L., Rohlfs, K., & Hüttemeister, S. 2013, Tools of Radio Astronomy

Wood, D. O. S., & Churchwell, E. 1989, ApJ, 340, 265

Xu, F.-W. et al. 2023, MNRAS, 520, 3259, 2301.01895

Yang, A. Y., Thompson, M. A., Urquhart, J. S., & Tian, W. W. 2018, ApJS, 235, 3, 1712.04599

Yi, J., Phillips, C. J., & Booth, R. S. 2002, in Cosmic Masers: From Proto-Stars to Black Holes, ed. V. Migenes & M. J. Reid, Vol. 206, 159–162

Yuan, J. et al. 2018, ApJ, 852, 12, 1711.08951

Zapata, L. A., Garay, G., Palau, A., Rodríguez, L. F., Fernández-López, M., Estalella, R., & Guzmán, A. 2019, ApJ, 872, 176, 1901.04896

Zhang, Y. 2019, in ALMA2019: Science Results and Cross-Facility Synergies, 142

Zhou, J.-W. et al. 2022, MNRAS, 514, 6038, 2206.08505